Conception, fabrication and study of optical metasurfaces

Adelin Patoux

Université Fédérale
Toulouse Midi-Pyrénées

THÈSE

En vue de l'obtention du
DOCTORAT DE L'UNIVERSITÉ DE TOULOUSE
Délivré par l'Université Toulouse 3 - Paul Sabatier

Présentée et soutenue par

Adelin PATOUX

Le 31 mars 2022

Conception, fabrication et étude de métasurfaces optiques.

Ecole doctorale : **SDM - SCIENCES DE LA MATIERE - Toulouse**

Spécialité : **Nanophysique**

Financement CIFRE:
AIRBUS DEFENCE AND SPACE

Unités de recherche:
CEMES - Centre d'Elaboration de Matériaux et d'Etudes Structurales
LAAS - Laboratoire d'Analyse et d'Architecture des Systèmes

Thèse dirigée par

Arnaud ARBOUET (CEMES)

Co-encadrement par

Guilhem LARRIEU (LAAS)
Paul JOUGLA (AIRBUS DS)

Jury

Mme Béatrice DAGENS, Rapporteure
M. Patrice GENEVET, Rapporteur
M. Patrick FERRAND, Examinateur
M. ADNEN MLAYAH, Examinateur
M. Antoine MONMAYRANT, Examinateur
M. Guilhem LARRIEU, Co-encadrant
M. Paul JOUGLA, Co-encadrant
M. Arnaud ARBOUET, Directeur de thèse

Contents

Remerciements

Pour inaugurer ces remerciements, je vais tout d'abord commencer par remercier Airbus Defence and Space et la convention CIFRE d'avoir financé cette thèse, car sans ça, eh bah... y aurait pas eu de thèse !
Pour ce qui suit, je vais tenter ici de remercier tous les gens qui ont fait en sorte que ces trois années se soient (super très chouette) bien passées ! (pardon par avance pour tous les oublis, même si c'est pas mon genre...).
Je vais commencer par remercier les personnes avec qui j'ai pu travailler au CEMES. Et pour cela il me faut débuter par celui qui m'a choisi pour faire cette thèse et qui m'a accompagné pendant ces trois années, mon directeur de thèse : le "Superman Arnaud Arbouet". Je pense sincèrement que j'ai eu beaucoup de chance de t'avoir comme directeur de thèse. Tu as toujours su être disponible malgré un emploi du temps parfois plus que chargé ! Ce qui m'a rapidement marqué (et que j'ai beaucoup apprécié), c'est ta diplomatie et ta gentillesse. Je suis consciente que j'ai parfois tendance à m'emporter avec les idées que je peux avoir, et que cela peut être difficile à gérer. Et donc le fait que tu aies toujours eu une approche ludique à mon égard m'a vraiment motivé à vouloir m'améliorer. Je tiens donc à te remercier, en toute sincérité, pour l'aide extrêmement précieuse que tu as pu m'apporter tout au long de cette thèse, tant d'un point de vue scientifique que social (et ce malgré le covid !).
Je vais poursuivre avec "The Incredible Peter Wiecha". Quel bonheur d'avoir pu travailler avec toi également ! Ce qui m'a vraiment fait plaisir, c'est l'intérêt que tu as pu porter à certaines de mes idées, merci beaucoup pour cela car cela me motivait toujours à vouloir réfléchir à d'autres innovations ! J'ai toujours apprécié discuter avec toi (quel qu'en soit le sujet d'ailleurs) !
Toujours du côté du CEMES, je tiens à remercier particulièrement Christian Girard, Vincent Paillard, Jean-Marie Poumirol, Gonzague Agez, Aurélien Cuche et Sébastien Weber pour toutes les discussions et les bons moments passés ensemble ! Je remercie également Robin Cours, Cécile Marcelot, Frederic Neumayer, Gregory Seine et Sébastien Moyano, et plus généralement le groupe NEO et le service Optique pour votre aide durant ma thèse et également pour votre sympathie !
Je vais maintenant passer aux collègues doctorants (et post-doctorants), et pour cela je vais commencer par remercier un gars que je ne m'attendais pas à rencontrer pendant ma thèse, eh ouais, c'est toi Clément ! Franchement, je pense que tu es l'un des facteurs qui a le plus contribué à rendre ma thèse si agréable du début à la fin. Bien sûr, le fait que nous étions tous les deux dans le même bureau n'était pas toujours idéal pour optimiser le travail (et optimiser le compte en banque aussi...), mais en tout cas cela motivait vraiment de venir travailler le matin ! Merci pour ton aide pour tous ces choses pour lesquelles j'avais parfois la flemme (comme le template LateX pour écrire la thèse qui est toujours dans le dossier "Cadeau Clément"). Il y a tant de choses que je pourrais écrire pour dire que c'était vraiment sympa, mais bon, on va laisser de la place pour les autres ! En tout cas, le hasard (les choix aussi) fait qu'on va se retrouver à Nice très bientôt, et en vrai ça c'est grave stylé !
Bon, pour les suivants je tiens à remercier tout d'abord Mélodie. Certes, tu n'étais présente que

par morceaux, mais on a quand même réussi à sympathiser et puis surtout tu es la seule à être restée jusqu'à mon sacre ! (Bon, par contre moi je suis parti en t'abandonnant *tousse*). Merci également à Julien, pour les sorties burgers et ces magnifiques moves de babyfoot ! Merci aussi à Romain, on n'a pas pu échanger énormément, mais c'était toujours un plaisir de discuter avec toi (pardon si parfois j'étais trop bavard, faut dire que t'as pris la place de Clément après qu'il soit parti !). Merci aussi Martin, on s'est aussi connu un peu sur le tard (le covid n'a pas aidé des masse), mais c'était vraiment chouette d'échanger avec toi, d'ailleurs quand tu veux je me dévoue pour goûter ta cuisine ! Je tiens également à remercier mon prédécesseur, Giuseppe ! On s'est certes croisé assez rapidement, mais vu que t'es un mec super cool on a direct sympathisé et je me suis tout de suite bien senti au CEMES en faisant ta connaissance. Si jamais je passe vers chez toi ça sera un plaisir de te revoir (et j'avoue que j'aimerais bien voir ta collection de figurines héhé) ! Enfin, je remercie Nicolas (Bello), Ségolène, Daniela et tout le groupe pour m'avoir accueilli à mon arrivée au laboratoire ! Même si je ne me suis pas montré très démonstratif, sachez que la démarche m'a beaucoup touché !
On passe maintenant aux extras (mais toujours au CEMES). Et pour accueillir les extras, évidemment je vais commencer par Elodie ! Quelle rencontre trop cool en vrai ! Une giga fan de Dragon Ball, déjà quand j'avais appris ça j'étais sûr qu'on allait bien s'entendre ! En vrai merci beaucoup pour toutes ces discussions qui m'aidaient beaucoup à décompresser (même si des fois, étant un peu bavard quand je suis lancé, je décompressais peut-être un peu trop) !
Je vais finir en citant le groupe Babyfoot du laboratoire, où je faisais mon sport ! Merci donc à Christophe, Abdel, Clément, Julien, Marc, Hilal et Seb. Merci pour tous ces efforts fournis pour tenter de me détrôner, c'était mignon (bon je ne compte pas Hilal on était kif-kif) ! EH BIM !!

Ayant fait le tour du côté du CEMES, je vais maintenant poursuivre avec le LAAS. Je tiens donc tout d'abord à remercier Guilhem Larrieu qui a participé à mon encadrement. Quand bien même j'attends toujours ton invitation pour faire une réunion au Japon, j'ai vraiment apprécié travailler avec toi et ça sera avec plaisir de poursuivre par la suite ! Je voudrais ensuite exprimer mes remerciements à Franck Carcenac. Merci beaucoup pour tout le temps que tu as pu me consacrer et pour toutes ces discussions hyper intéressantes sur des sujets ma foi très variés ! Merci également à Aurélie Lecestre, Nicolas Mallet, Demba Ba, Laurent Bouscayrol, Benjamin Reig, et tout le service TEAM et le Groupe MPN en général pour leur aide et leur sympathie tout au long de ma thèse !
Je souhaite également remercier un collègue doctorant du LAAS (mais également ex-Supop) : Ivàn Esparza ! Merci beaucoup de m'avoir logé pendant quelques jours quand je suis arrivé à Toulouse et pour ton aide pour mes premières insolations !

Poursuivons du côté d'Airbus, où je tiens out d'abord à remercier Paul Jougla et Joël Boyadjian pour leur encadrement ! Merci beaucoup de m'avoir intégré dans le groupe, pour votre tolérance malgré certains retards de ma part (cette remarque vaut pour pas mal de gens en fait), et pour votre sympathie tout au long de ces trois années de thèse ! Je remercie d'ailleurs plus généralement tout le groupe Optique d'Airbus DS pour m'avoir intégré comme membre permanent, et ce malgré mes 1% de présence sur site !
Côté Airbus, je tiens également à remercier les membres de la médiathèque où j'étais bénévole. Là aussi j'ai pu faire de super rencontres, en particulier Zoé Bivort et Le Chef (Roger Pasqualini). Merci beaucoup pour ces instants de détente et euh de culture bien entendu. Cependant, si je puis me permettre, je pense qu'il faudrait que vous appreniez à râler un peu plus !

Ce que je retiens particulièrement, c'est que je me sens vraiment chanceux d'avoir pu travailler avec trois groupes différents au sein desquels toutes les personnes avec qui j'ai pu échanger étaient vraiment très sympathiques et accueillantes.
J'exprime également ma reconnaissance à Béatrice Dagens, Patrice Genevet, Patrick Ferrand, Antoine Monmayrant et Adnen Mlayah de s'être intéressés à mon travail de thèse en participant à mon jury de thèse ainsi que pour leur relecture précise du manuscrit.

Pour ce qui suit, je vais continuer avec les remerciements extra-professionnels, en commençant par les amis ! Tout d'abord les amis de Supop (+ Discord Waifu Hunters) : Dieu (Marcel), Aurélien, Yvan, Bambou, Glaey, Victor, Alexandre, Cédric et Grégoire ! Il y a eu des hauts et des bas (V***rant), mais avoir la possibilité de se faire des ptites parties rigolotes c'était vraiment chouette pour moi ! Merci aussi aux Poulets Master Race pour votre délicatesse. Bref, on a fait pleins de trucs, et je me suis bien marré, et ça, eh bah c'est cool !
Merci également à Nico man yeah man c'était trop cool que t'arrives à Toulouse mec ouahahouuuuh j'aurais jamais espéré ça la fête yeah ! Non en vrai ouais c'était vraiment inattendu et trop stylé qu'on puisse se retrouver à 2km de distance après 8 ans ! Merci de m'avoir motivé pour me mettre à la boxe et pour manger des cookies !
Merci aussi à tous les amis du groupe P3 ! Dans un ordre totalement aléatoire : Lois, Anaelle, Clarisse, Natacha, Victor, Victor, Vanille, Cédric, Julien, Caroline, Laurène, Elvina, François, Hugo, Juliette, Marion, Morane, Nathanaël, Sacha, Taoufik, Ulysse, et les oubliés si jamais y en a (vous êtes beaucoup aussi) ! Merci beaucoup d'avoir persisté à m'inviter aux événements malgré ma faible participation pendant ces trois dernières années, ça m'a toujours beaucoup touché !
Pour les amis, je vais finir en citant encore quelques noms un peu à la volée : Manon, Paul, Kosta, Thibault, Romain (Louligi), Maguelone, Charlène et probablement encore d'autres que j'oublie (désolé !). Merci à vous tous pour ces petits échanges qu'on a eus et qui m'ont fait plaisir !

Je vais finir avec un cercle un peu plus proche, ma famille, en commençant par mes parents : Daniel et Béatrice. Merci de m'avoir soutenu durant ces trois années de thèse, en m'aidant à emménager, à déménager, en occupant de moi pendant mes vacances, et tout particulièrement pendant mon rush final de rédaction où j'étais hébergé et bien chouchouté ! Je sais que vous serez toujours là en cas de besoin, je vous fais des gros bisous, merci beaucoup ! Merci aussi aux Brothers, Florian et Alexis ! En vrai c'est tellement cool d'avoir des frangins avec qui je m'entends si bien ! Alex, merci pour les dessins du Chapitre 4 qui sont vraiment canons ! On n'a pas beaucoup avancé le projet game sinon, mais bon ça va le faire, d'ailleurs passe le merci à Risa ! Et Flo, bah on n'a pas vraiment de projet et puis toi t'en as déjà un assez imposant, mais bougoudounoune quand même (et gloire à Instrumia). J'en profite pour remercier aussi mes neveux Martin, Simon et Natsume, et ma nièce Ayumi. Certes je pense qu'au moment où j'écris ces lignes, vous ne comprenez pas bien ce que ça représente, mais je tiens quand même à vous remercier pour vos mougnounous mignons oudoudoudous !
Merci aussi Mamir et Bidoune (Thérèse et Valérie) ! Vous étiez souvent les plus promptes à répondre à mes appels le midi, et c'était vraiment chouette de discuter avec vous à chaque fois ! Ah, mon bidou aussi vous dit merci ! Ensuite je remercie aussi toute la famille Simoes (Brigitte, Carlos, Aurélien, Fanny) pour votre soutien et suivi pendant ma thèse ! Et puis enfin merci aussi à la famille Piette (Patrick, Rolande, Marie-Audrey, Éric (même si pas officiellement Piette je te compte quand même), Alexandre, et euh... Non c'est tout c'est bien ça !

HEHE JE T'AI EU ROMAIN GHI !
Bon oui ptite dédicace particulière. T'es quand même venu une fois à Toulouse, et ça oh oui merci c'était beau ! Non en vrai merci aussi pour tous ces trajets à l'aéroport les lundis à 6h du mat pour que j'aille à Toulouse ! Merci pour les délires passés, présents et futurs (je ne rentre pas dans les détails tu ne m'en voudras pas). Et pour te dire à quel point c'est puissant, même les 15 autres s'accordent à te dire merci ! Ghi.

Pour conclure je finirai en te remerciant, toi qui lis ces lignes, pour ton intérêt pour mes travaux, et je te souhaite bien du courage dans ta lecture !
En toute honnêteté, avant de commencer cette thèse, mon moral n'étais pas vraiment au plus haut, et donc, quand bien même ça peut paraître étrange, je me sens bien mieux en sortie de thèse qu'en entrée de thèse, et ça je vous le dois à tous. Merci.

Introduction

Since the beginning of the 21st century, the optical properties of nanostructured materials have aroused a great interest. The first studies concerned *metamaterials*, that are made of a 3D arrangement of structures, and give access to unnatural properties, such as a negative refractive index. Over time, metamaterials studies evolved into *metasurfaces*, made up of subwavelength structures arranged on a surface. Due to their strong interaction with light, metasurfaces allow to considerably modify the properties (amplitude, polarization, phase) of the incoming radiation. As a result, they have enabled the development of flat and light optical components that can also combine multiple functionalities (*e.g.* wavefront modulation and polarization control). Due to their great potential, the study of metasurfaces has been an increasingly active research field. The development of optical components based on ever more complex metasurfaces then required an ever greater level of control over the accuracy of both numerical simulations and nanofabrication processes.
It is within this context that this PhD, funded by Airbus Defence and Space, has been set up to study the design, fabrication and characterization of optical metasurfaces. Thus, we present in this manuscript a detailed study of these three steps, focusing on the identification and minimization of fabrication errors on the performance of metasurfaces.
In the first chapter, after an introduction on the history of metasurfaces, we present the simulation tools GDM (Green Dyadic Method) and FDTD (Finite Difference Time Domain), which allow the simulation of the optical response of nanostructures.
In the second chapter, the design method used is presented. It involves the creation of a database of optical responses of various nanostructures, obtained by FDTD simulations. Then, we present the fabrication process, involving structuration by electron beam lithography. We also introduce the measurement tools used to characterize the fabricated components.
In the third chapter, we detail the design, the fabrication and the characterization of a metasurface acting as a light deflector operating at 750 nm composed of silicon nanodiscs of varying diameters, arranged on a periodic grid. Then, we focus on the identification of the origin of the differences between the measured performances and those predicted by the simulations. Thus, we study the impact of nanofabrication errors on the optical performances of the fabricated metadeflector. First, TEM observations allow us to characterize precisely the fabricated nanostructures and to compare them with the theoretical design. We then study the impact of these differences on the optical performances of the fabricated metadeflector by means of numerical simulations. We study the case in which the errors are systematic (*i.e.* identically applied to all structures) and statistical.
In the fourth chapter, we use an optical characterization method based on phase imaging called ptychography. This method consists of a numerical processing of a large number of diffraction images, acquired following the illumination of different portions of an object. First, a history of the technique and its operating principle are presented. Then, we describe the experimental bench used while justifying how to optimize the final resolution of reconstruction. Finally, we show the efficiency of the method by characterizing two metasurfaces, including a metalens

for which we extract the complex amplitude in order to evaluate its performance.
Finally, in the fifth chapter, we present a new approach for the design of metasurfaces using ptychography. This method consists in using the accuracy of the ptychography phase imaging to overcome the influence of systematic fabrication defects. Thus, we design, fabricate and characterize by ptychography a first reference metasurface. This metasurface is then used as a new database from which we design a new metalens. We then compare the optical response of the latter with the one of chapter 4.
To conclude, we detail the advantages and disadvantages of this approach compared to the traditional one, and discuss the numerous perspectives that it brings to improve the performances of metasurfaces.

1 Introduction to the study of metasurfaces and associated simulation tools

This first chapter will serve as an introduction to the field of metasurfaces. The first part summarizes the state of the art of this very active field. In a second part, we will present the theoretical tools that we have used in this thesis to describe the optical response of individual nanostructures to visible light. Finally, we will study the optical response of an assembly of several nanostructures.

1.1 Introduction to optical metasurfaces

In this section, we will first describe what is a metasurface using several examples. We will also go back in history to trace how research in optics has evolved to give birth to metasurfaces. Finally, we will discuss the current state of metasurfaces in terms of applications and limitations, and review their potential.

Definition of a metasurface

As we will see, the term *metasurface* inherits directly from the name *metamaterials*. Thus, to provide a definition of metasurfaces, we will first describe what metamaterials are.
Metamaterials (from the Greek *meta* meaning *beyond* and *materia* for *material*) refer to a particular type of material artificially made to interact with a wave, and having properties not found in nature. To obtain such properties, metamaterials are composed of structures much smaller than the wavelength and organized in a 3D lattice with a sub-wavelength spacing.
Metasurfaces, on the other hand, can be defined as the 2D equivalent of metamaterials and are generally composed of a set of very small structures, usually arranged on a substrate. In a metamaterial, the properties of an incoming wave are modified during its propagation through the volume of the material. Conversely, it is the interaction of the incident wave with a single layer of sub-wavelength structures that modifies its properties (amplitude, phase or polarization) in the case of a metasurface [1]. Usually, a necessary condition to optimize the efficiency of metasurfaces is that the distance between two adjacent structures does not exceed $\lambda/2$, λ being the wavelength of the interacting wave [2]. Therefore, by perfectly controlling the properties of the output wave with such a high resolution ($< \lambda/2$), it becomes possible to design very complex and highly efficient ultrathin components. This high level of tunabillity is precisely what makes metasurfaces so popular and attractive today.

1.1.1 Optical metasurfaces

We illustrate here the different types of metasurfaces focusing on optical metasurfaces operating in the visible and near-infrared (NIR) ranges.

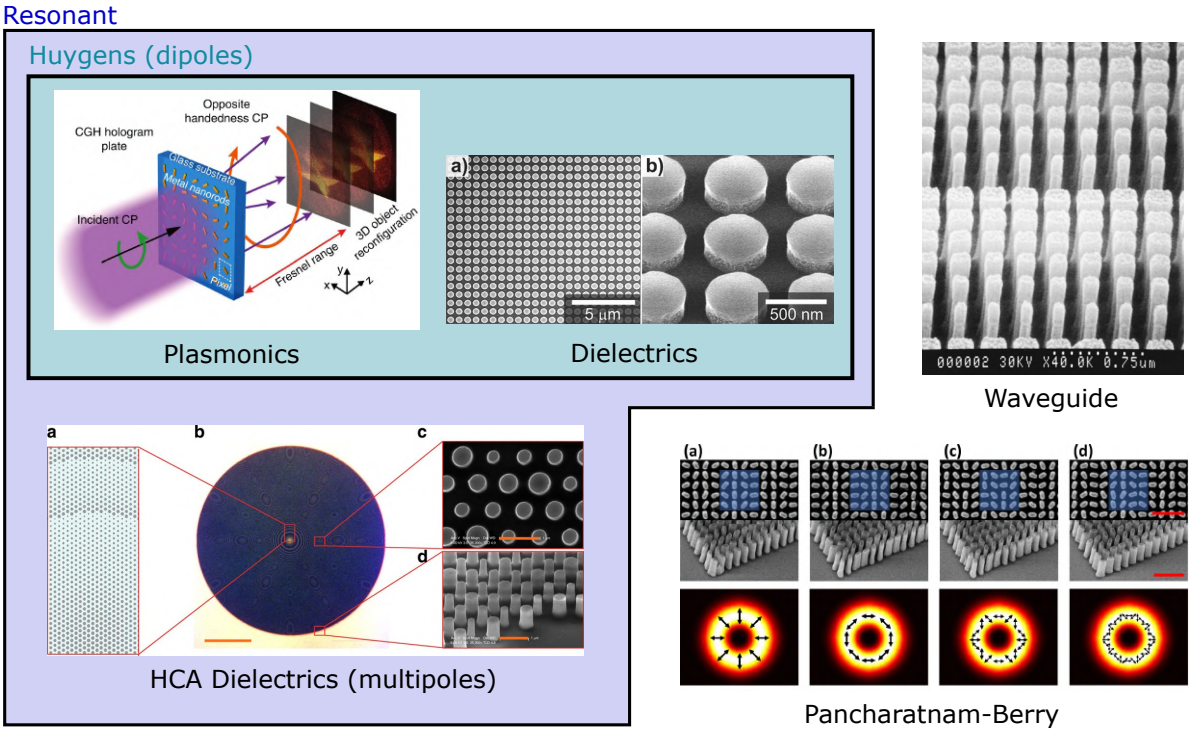

Figure 1.1: Illustration of the different types of metasurfaces: resonant metasurfaces (plasmonic and Huygens dielectrics, HCA dielectrics), waveguide type metasurfaces and Pancharatnam-Berry type metasurfaces.

1.1.1.1 Resonant metasurfaces

A large part of metasurfaces are defined according to the optical resonances of their constitutive nanostructures. Here we list three different types of resonant metasurfaces, based on plasmonic nanostructures, thin dielectric structures ($H << \lambda$), and thick dielectric structures ($\lambda/2 < H < \lambda$).

Resonance of sub-wavelength structures In his famous work, Mie explained that light scattering from sub-wavelength dielectric and metallic nanospheres can be explained by the presence of multipolar electric and magnetic resonances. In the case of dielectric structures, both electric and magnetic resonances are supported, whereas metallic structures support only electrical resonances. Increasing the size of the structure also gives access to higher order resonance modes (quadrupole, octupole, etc.). Although Mie formalism is exclusive to the case of spherical structures, multipole resonances occur in structures of any shapes such as cylinders, rods, cones, etc. [3].
When a subwavelength structure is illuminated, each excited resonance can be considered as equivalent to an harmonic oscillator which can induce a phase shift ranging from 0 to π [4]. As we will see, this property is the foundation of resonant metasurfaces.

Plasmonic metasurfaces When exposed to a plane wave, the free electrons of a subwavelength metal nanostructure oscillate at its surface [5]. For a specific wavelength of the incident field, a localized surface plasmon resonance occurs, enhancing light inside the nanostructure [6, 7]. These metallic structures are also called plasmonic structures because of their plasmonic resonances.
Thus, plasmonic metasurfaces are made of small metallic nanoantennas (such as gold or silver), and generally surrounded by a dielectric environment (such as quartz or silicon) [1, 8–12]. We show an example of a plasmonic metasurface in Fig. 1.1. By modifying the geometry of plasmonic nanostructures (nanorods, nanodiscs, V-shaped, C-shaped, ...), we can precisely control their localized surface plasmon resonances, and thus create metasurfaces with controlled properties.
Plasmonic metasurfaces are most often made of nanostructures that support only one electric dipole mode, the latter being efficiently coupled to far field radiation. The phase shift induced by such nanostructures can then only span the range from 0 to π. However, full control of the outgoing wave from the metasurface requires access to the entire range from 0 to 2π. To achieve this, two different strategies are applied. The first one consists in combining two or more plasmonic structures to create Huygens metallic metasurfaces [13]. The second is to use the Pancharatnam-Berry phase of circularly polarized beams [1, 11]. More information on both approaches (Huygens and Pancharatnam-Berry) will be provided in the following. We note that a new approach based on the encircling of an exceptional point has been recently demonstrated, bringing a new degree of freedom on the control of the phase shift to design metasurfaces [14].

Dielectric Huygens metasurfaces We introduce here the principle of Huygens dielectric metasurfaces. Inspired by Huygens' principle, Huygens' metasurfaces are composed of nanostructures that can be considered as secondary sources of spherical waves. They exploit the superposition of electric and magnetic dipole resonances of the nanostructures to control the direction of light scattering [13, 15]. For example, backward scattering can be canceled when the electric and magnetic dipole coefficients are equal, and when the higher-order modes are negligible, fulfilling the so-called first Kerker condition [16, 17].
Huygens dielectric metasurfaces [15, 18–22], are based on this principle and take advantage of the ability of dielectric nanostructures to support electric and magnetic dipoles. In general, Huygens dielectric metasurfaces are composed of relatively thin dielectric nanostructures (typically $\lambda/10$ to $\lambda/2$), and high refractive index values (n>3). The two supported dipole resonances also provide access to the full 2π phase shift range through modification of the nanostructure geometry. An example of a Huygens dielectric metasurface is shown in Fig. 1.1.

High Contrast Array dielectric metasurfaces High Contrast Array (or HCA) metasurfaces consist of high aspect ratio (height divided by the diameter) dielectric nanostructures (typically, Huygens nanostructures with heights between $\lambda/2$ and λ), and high refractive indices (n>3) [23–28]. Due to their larger size, HCA structures support higher multipole order resonances such as quadrupole, octupole or even higher order modes. The phase shift control is then not from 0 to 2π but from 0 to $2N\pi$, with $N > 1$. Although it may seem unnecessary, the existence of multiple resonances actually gives more flexibility to search for more efficient geometries for each desired phase shift. This explains why HCA metasurfaces are generally

more efficient than Huygens metasurfaces. In addition, the high refractive index contrast between the nanostructures and the environment confines the electromagnetic field inside the nanostructures, minimizing coupling and simplifying the design methods (see Chapter 2 for more information). These properties allow HCA metasurfaces to achieve very high efficiencies for wavefront shaping [28]. An example of a HCA metasurface is shown in Fig. 1.1.

1.1.1.2 Waveguide metasurfaces

Waveguide metasurfaces are made of nanostructures that have a very high aspect ratio (heights are greater than the wavelength), and relatively high refractive index (n>2) [29–31]. In contrast to resonant metasurfaces, the nanostructures here are behaving as vertical nano-waveguides. By increasing the width of one nano-waveguide, its induced local phase shift is increased. We show in Fig. 1.1 an image of a waveguide metasurface [30].

1.1.1.3 Pancharatnam-Berry metasurfaces

Pancharatnam-Berry metasurfaces do not consist of a specific type of nanostructures, but use the Pancharatnam-Berry phase (PB phase). The latter is related to the orientation of the nanostructures when illuminated by circularly polarized light [1, 11, 32–35]. Fig. 1.1 shows an example of a PB metasurface made of gallium nitride (GaN) nanopillars [33–35].
The use of PB phase provides an additional means to control the phase of the output wave and an interesting strategy to design highly efficient metasurfaces with sophisticated polarization properties. However, this means that PB metasurfaces cannot be used to design polarization-insensitive components.

1.1.2 History of metasurfaces

Although metasurfaces are a fairly recent research topic, their implementation is based on relatively old physical principles. In this subsection, we describe the history of metasurfaces, listing the major discoveries and concepts that led their creation, starting from Huygens' principle until now.

1.1.2.1 17^{th} to 19^{th} century: early concepts and studies

Fresnel's lens In 1748, Buffon had for the first time the idea of separating a solid lens into concentric zones to reduce its thickness [37]. This idea was then taken up by Condorcet at the end of the 18^{th} century [38] and Brewster in 1811 [39], but the complexity of the design (biconvex) meant that their lenses could not be used for applications [40]. It is only in 1819 that Fresnel had the same idea and proposed the design of his stepped lens which had the particularity of being plano-convex and therefore more suitable for manufacturing. During three years, Fresnel worked on the fabrication of his lenses and in 1822 is installed for the first time a Fresnel lens inside a lighthouse [36, 41, 42]. Since that time, the Fresnel lens design has inspired many fields of optics [36].

Diffraction In 1690, Huygens elaborated a theory in which he postulated that every point in space reached by an optical disturbance becomes the source of a spherical wave. His idea was then taken up by Fresnel who added the principle of coherence and superposition to explain

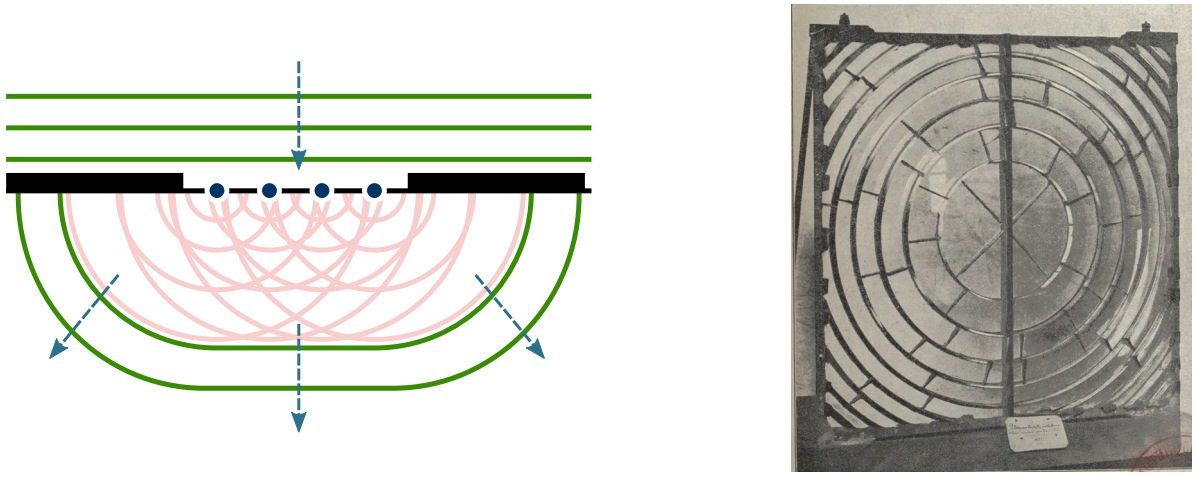

(a) (b)

Figure 1.2: (a) Illustration of the Huygens principle. (b) Image of one of the first circular echelette lenses made by Fresnel in 1821 [36].

the phenomenon of diffraction, which led to the Huygens-Fresnel principle (see Fig. 1.2). During the 18th and 19th centuries, the study and fabrication of diffraction gratings also interested several renowned scientists such as Fraunhofer, Rayleigh or Cornu. In 1865, one of the most important papers in the history of optics was published by Maxwell, introducing Maxwell's equations, describing the relationship between electric charges and currents, and the electric and magnetic fields [43]. At the same time, Rayleigh, following Maxwell's work, gave the first correct interpretation of the scattering of light by structures much smaller than the wavelength, a theory that could explain the blue color of the sky [44]. What is remarkable is that in his paper written in 1899, Rayleigh was already describing an optical component that was very similar to what would become metasurfaces more than a century later: "*Let us suppose then that a large number of small discs are distributed at random over a plane parallel to a wave-front, and let us consider their effect upon the direct light at a great distance behind.*"

1.1.2.2 20th century: from theories to fabrications

Pioneer studies In 1902, Wood first observed what later became known as the "Wood anomalies", and were surface plasmon polariton (SPP) resonances occurring in plasmonic structures [5, 49].
In 1908, Gustav Mie studied the scattering of light by spherical subwavelength particles [46]. Originally, his work aimed at explaining the color of colloidal metallic solutions. As explained earlier, Mie theory revealed the presence of electric and magnetic resonances in illuminated nanospheres (see Fig. 1.3(b)). Although the publication of this theory was almost ignored until 1945 [50], today it has a very large influence and is commonly used in the field of nano-optics.
The beginning of the 20th century saw the advent of several studies inspired by blazed gratings. Among these studies, we find the articles of Cotton in 1901 and Wood in 1910 [45] (Fig. 1.3(a)). Later, in 1946, Brillouin studied in detail wave propagation in periodic structures [51]. In 1968, Goodman's publication of his book on Fourier optics gave the optical community the

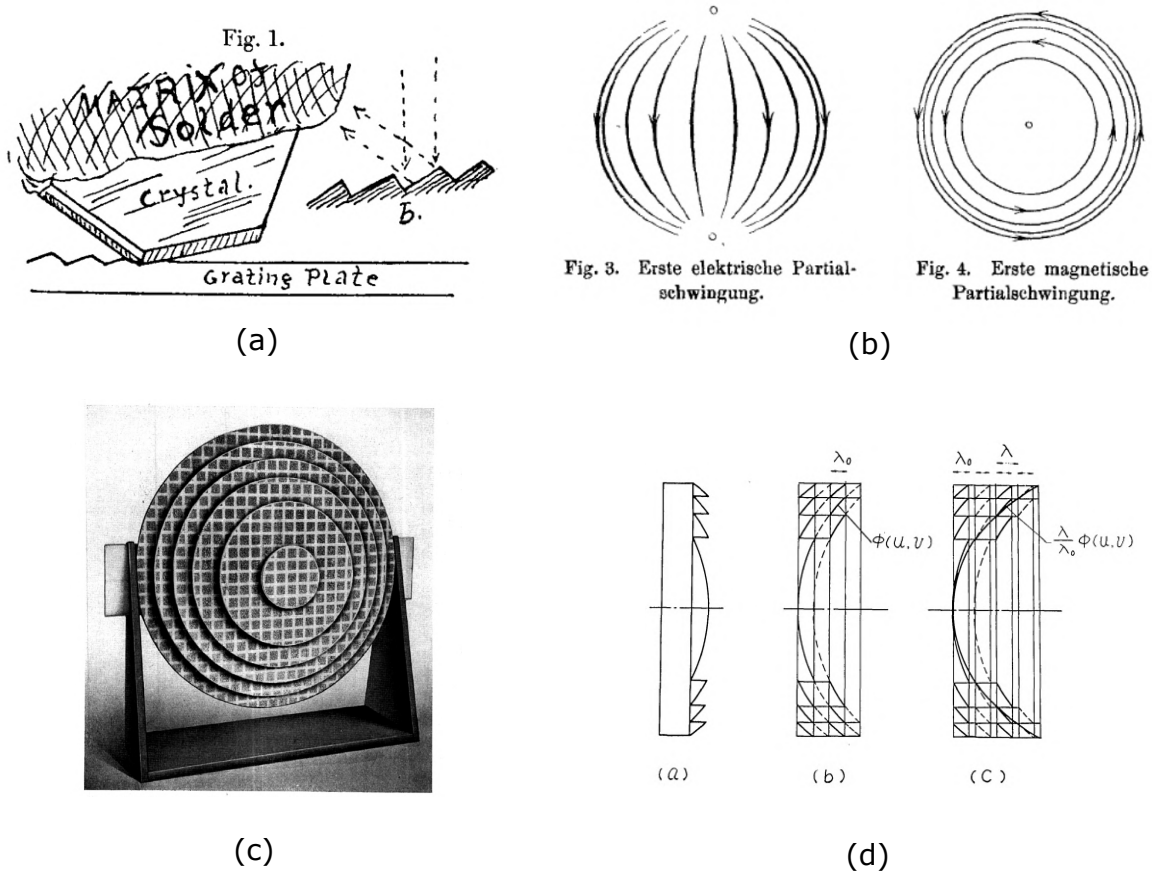

Figure 1.3: (a) Illustration of a blazed grating designed and manufactured by Wood in 1910 [45]. (b) Optical electric and magnetic Mie dipole resonance of a spherical particle [46]. (c) Doped polystyrene lens made by Kock in 1948 [47]. (d) Illustration of the principle of the phase Fresnel lens. [48].

theoretical tools to solve a variety of problems (e.g. the optical properties of periodic structures).
It is also noteworthy that in 1948, Kock made a microwave diffractive lens by doping polystyrene foam sheets with sub-wavelength metallic inserts, locally modifying the effective-index, which can be seen as the first fabrication of a metamaterial [47] (Fig. 1.3(c)).

Technology improvements At the end of the 20$^{\text{th}}$ century, the development of technology provided the research community with new tools, either for the simulation of complex systems or for their fabrication. In particular, with the strong development of computer technology at the end of the century, several numerical methods were developed to solve Maxwell's equations. Among these methods, we can cite the first numerical implementations of Mie theory [52–54], but also the FDTD (Finite Difference Time Domain) method [55], the boundary element method (BEM), the discrete dipole approximation (DDA) [56, 57] and Green's dyadic method [58, 59] which can be used to study the interaction between light and subwavelength structures. Further details on Green's dyadic method and FDTD are provided in the next sections of this chapter.
At the same time, the emergence of new fabrication tools (with the different methods of lithog-

raphy) allowed to reach better and better resolutions, up to sub-micrometer resolutions. These new resources made available to scientists at the end of the 20th century stimulated new ideas for new optical components.

Photonic crystals and plasmonics As example, we can first cite the study of photonic crystals. Photonic crystals are periodic dielectric structures. They allow to control the light by preventing the propagation of photons in certain directions and for certain frequencies (photonic gap). Because of the simplicity of their fabrication, they have been particularly attractive for the study of photonic integrated circuits [60–62].
As another example, in the 1990's, the interest in plasmonics increased exponentially. Indeed, it has been shown that localized surface plasmons can overcome the diffraction limit and concentrate light in regions much smaller than the wavelength [6, 7]. This specificity has enabled many very interesting applications, for example in near-field microscopy or in waveguides [6]. As we will see in the following, the field of plasmonics has played a central role in the development of metasurfaces in the 21st century.

Blazed gratings At that time, the study of blazed gratings also attracted a lot of interest from the optical community. Inspired by the Fresnel lens design, and made possible by the development of new advanced fabrication technologies [63, 64], phase Fresnel lenses (or kinoform optics) were proposed to shape the optical wavefront [48, 65]. These designs pushed the Fresnel lens idea to the highest degree by making periodic jumps for each λ of thickness (see Fig. 1.3(d)). However, although they were very popular and showed high performances, a certain limit capped their efficiencies. As can be seen in Fig. 1.4, as one approaches the 2π phase jump, the light that is deflected interacts with the vertical face of the next portion. The latter phenomenon is called *shadowing effect* and the region where it occurs is called the *shadowing zone*. The shadowing effect reduces the efficiencies of diffractive optics, and makes them very sensitive to the angle of incidence of the light (see Fig. 1.4).

Effective-index Thus, in the 1990s, to improve the efficiency of flat optics, researchers began to seek new design strategies. During this period, with the rise of plasmonics, some laboratories were now able to fabricate sub-micrometer structures. A new idea of flat optical components then appeared, based on the control of the effective-index gradient δn_{eff} (see Fig. 1.4).
With kinoform or blazed optics, the thickness control can actually be considered as a local control of the effective-index gradient. By increasing the thickness, δn_{eff} increases and so does the phase delay. This control of δn_{eff} is based on a vertical gradient, since the control parameter is the thickness.
Therefore, in order to avoid any shadowing effect, the new strategy discussed was to adjust δn_{eff} using a horizontal gradient (at a constant height) rather than a vertical gradient. Thus, in 1991, a first grating consisting of an assembly of lines of the same height and variable width (see Fig. 1.4) was made for water waves [66]. After this result, several optical components (in IR and visible) were fabricated by adjusting the effective-index gradient using rectangular shapes at the nanoscale [67–72]. These optical components can be considered today as the first metasurfaces. We illustrate in particular in figure 1.4 a flat lens fabricated in 1996, using fused quartz nanopillars and operating at 632.8 nm [70]. Nevertheless, all these optical gratings based on the effective-index theory had limited efficiencies.

An explanation for this limitation was provided in 1999 by Lalanne et al. [30]. The effective-index theory also implied the appearance of a shadowing zone, due to the large shift in the refractive index at each 2π phase jump (see Fig 1.4). They then proposed the idea of using nano-waveguides, made of a high refractive index material, to confine and guide light vertically, and thus cancel the shadowing effect [73]. As a proof of concept, they designed several diffractive optical components, including a flat lens operating in the near infrared (see Fig. 1.1) [30, 31]. The gratings were composed of TiO_2 nanopillars on quartz, and were very similar to modern metasurfaces. The grating lens (which we now call metalens) showed an absolute efficiency of 80%.

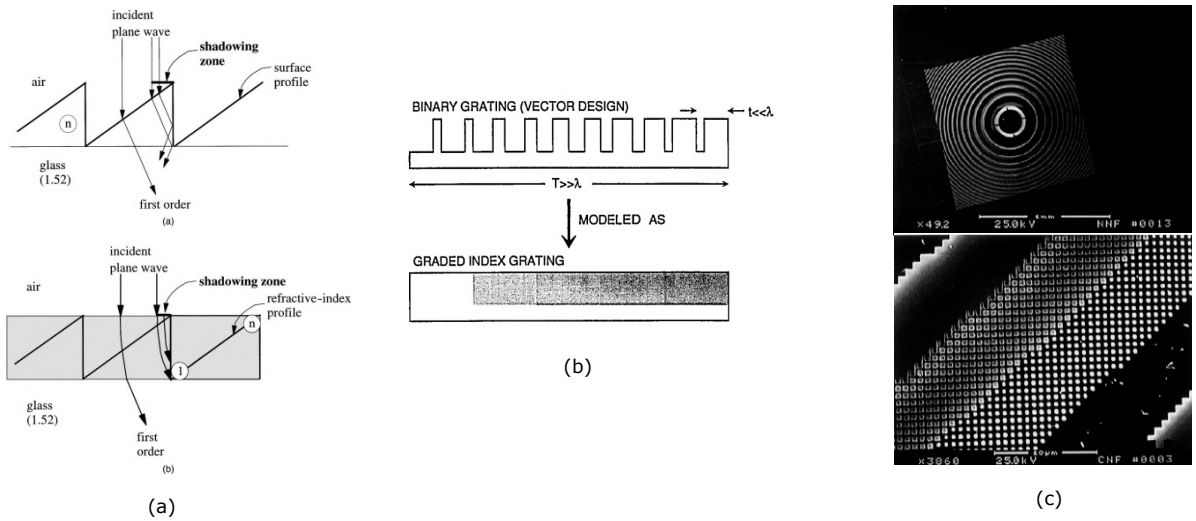

Figure 1.4: (a) Demonstration of the shadowing effect occurring in the echelette gratings and in the components related to the effective-index gradient [30]. (b) Illustration of the idea of describing an assembly of nanoposts by a local effective-index [74]. (c) Illustration of a metalens made from fused quartz nanoposts based on the effective-index gradient theory [70].

1.1.2.3 Beginning of the 21st century: from metamaterials to metasurfaces

The 21st century witnessed the true birth of metasurfaces. First of all, it must be clarified that the research topics discussed in this part motivated a vast litterature. Therefore, it is not possible to give an exhaustive review of the field of metasurfaces in the 21st century. For that reason, the objectives here will be to give a brief description of the most important milestones. In that regard, we will first see how the rise of metamaterials led to the idea of metasurfaces, then we will see how the theory behind metasurfaces was built, and finally how the metasurfaces evolved through the years. This section was largely inspired by many very interesting reviews on the field of metasurfaces [22, 75–79].

Metamaterials As we have just seen, at the end of the 1990s, thanks to the increased performance of fabrication tools and computational methods, several nanoscale components (such as blazed gratings, photonic crystals or plasmonic based components) have been studied and fabricated. The fabrication of materials composed of an artificial 3D lattice with a sub-wavelength

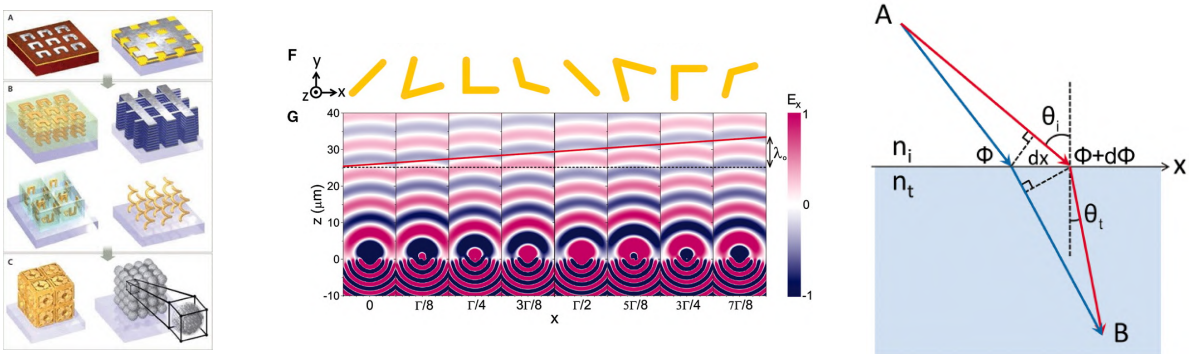

(a) (b) (c)

Figure 1.5: (a) Some examples of metamaterial design for different wavelength ranges [80]. (b) and (c) The generalized law of refraction and diffraction explaining the optical response of metasurfaces [1].

pitch has then attracted increasing interest. In 1999, Pendry *et al* described an artificially magnetic material composed of non-magnetic split metal rings, much smaller than the wavelength, and arranged in a 3D cubic lattice [81]. This material had the particularity to provide a negative effective magnetic permeability μ_{eff} not accessible in natural materials. One year later, a synthetic material was described for the first time with both negative values of effective magnetic permeability and dielectric permittivity in the microwave spectral range [82]. This phenomenon was then demonstrated experimentally in 2001 [83]. This marked the beginning of research on metamaterials and of numerous studies on their potential for complete refractive index control [84, 85]. It should be noted that in the same period, some photonic crystals also showed the potential for negative refractive index [86], and research on photonic crystals for applications in the visible and IR range was also very active [62, 87].
Over the following decade, various research projects have attempted to bring metamaterials closer to the visible range [88]. New ideas for optical components also emerged, such as invisible cloaking components [89], perfect absorbers [90], and gradient index lenses [91, 92]. Unfortunately, due to their large thickness and the use of metallic structures inducing important losses in the visible range, the efficiencies were always low [93]. In addition, the fabrication process of these 3D materials was very challenging.
For these reasons, researchers looked for different solutions to reduce the losses of metamaterials. Among the possible solutions, one was to reduce the propagation of light inside the metamaterial to reduce the losses. This idea pushed researchers to study thin metamaterials and finally 2D metamaterials, first called *metafilms* then *metasurfaces*.

Metasurfaces theory Sophisticated theories have emerged to derive the optical response of optical metasurfaces, as the latter are not particularly periodic and can be composed of many different types of scatterers. One of the first proposals was to derive the generalized sheet transition condition (GSTC) by examining the optical field transition at the interface where the scatterers are positioned [94, 95].
Later, in 2011, Yu *et al* presented a new approach to Snell's law of refraction and reflection, taking into account the presence of discrete and abrupt phase shifts induced by nanoresonators at the interface between two media [1]. The equation extracted from these generalized laws

is the following, and is based on Fig. 1.5:

$$\sin(\theta_t)n_t - \sin(\theta_i)n_i = \frac{\lambda_0}{2\pi}\frac{d\Phi}{dx} \tag{1.1}$$

Where θ_i and θ_t are respectively the angle of the incident and transmitted beams, n_i and n_t the refractive indices of the input and output media, λ_0 the wavelength in vacuum and $\Phi(x)$ the phase shift at the interface between the two media at position x (see Fig. 1.5).
They also demonstrated the usefulness of these generalized reflection and refraction laws by designing and fabricating two metasurfaces made of V-shaped gold nanorods, working at $\lambda = 8$ µm (see Fig. 1.5). The first metasurface induced a constant phase gradient, thus tilting an incoming beam and showing for a certain angle of incidence a negative effective refractive index. The second metasurface induced a vortex beam at the output. As we will see, this paper and the generalized laws of reflection and refraction opened the way to the design of many metasurfaces.

1.1.2.4 Metasurfaces current research directions

In the years that followed, the field of metasurfaces experienced an incredibly strong growth. We show in Fig. 1.6 some examples of different types of metasurfaces. The literature published on metasurfaces generally focuses on one or several of the following four parameters:

- The **material** used (silicon, SiO_2, TiO_2, GaN, gold, ...).
- The **geometry** of the nanostructures (discs, rectangles, ellipsoids with varying aspect ratios, ...).
- The **optical functionalities** implemented by the metasurface (tilt light at an angle of X°, focus light at a distance of Y mm, working wavelengths, multi-functional aspects, tunability, ...).
- The **fabrication** process used (Electron Beam Lithography, Photolithography, Deep UV Lithography, FIB, ...).

In what follows, we will describe the evolution of metasurfaces in terms of each of these characteristics.

Material With the constantly growing interest in plasmonics came the natural idea to fabricate plasmonic metasurfaces, using the plasmonic resonances of small metal nanoantennas. As explained in the previous subsection, the efficiency of plasmonic metasurfaces was limited in the visible range. In fact, the most efficient plasmonic metasurfaces that were fabricated were based on coupled plasmonic structures or PB phases. Moreover, the fabrication of plasmonic metasurfaces was not compatible with the complementary metal oxide semiconductor (CMOS) fabrication process, which made their potential industrial applications more difficult. Nevertheless, it was possible to use plasmonic absorption to design other types of plasmonic metasurfaces, such as absorbers [96].
Because of these constraints, scientists began to use dielectric nanostructures to make Huygens metasurfaces, since dielectric materials like silicon offered high refractive indices and low losses in the NIR/visible range [22, 78]. Due to the low aspect ratio of the nanostructures,

Huygens metasurfaces were very easy to fabricate. In addition, the fabrication of dielectric metasurfaces was compatible with the CMOS fabrication process. Yet, Huygens' metasurfaces have shown limitations in terms of efficiency for wavefront shaping, mainly due to the coupling between their nanostructures [97].

Geometry In 2015, a highly efficient HCA metasurface composed of silicon nanodiscs was designed and fabricated by Arbabi *et al* [24]. In their paper, they also provided a description of a simple design process to fabricate high-efficiency metasurfaces. As discussed earlier, the use of HCA structures has led to very high efficiencies due to the higher order modes that are supported by the nanostructures. Despite being more challenging due to the high aspect ratios involved, the fabrication process is very similar to that of Huygens dielectric metasurfaces and is therefore suitable for industrial applications (CMOS compatible). It is also very interesting to note the great similarity between the HCA metasurfaces and the waveguide metasurfaces fabricated by Lalanne in 1998 and 1999, which had already demonstrated a great efficiency for wavefront shaping in the NIR/visible domain [30, 31, 98]. Since then, the use of high refractive index HCA dielectric structures (such as silicon, GaN or TiO_2) has become very common for the fabrication of efficient metasurfaces.
Nevertheless, all these designs use separate structures to introduce locally discrete phase shifts. Although the distance between the structures is smaller than the wavelength, it is still constrained as the fabricated nanostructures must generally be of comparable size to the wavelength in order to resonate efficiently. [1] This distance then generally oscillates between $\lambda/4$ and $\lambda/2$ for dielectric resonators. As a result, a well known limitation of this type of discrete design is the strong decrease of the efficiency for strong phase shift gradients [99, 100]. This for instance makes the fabrication of high Numerical Aperture (NA) metasurfaces very difficult.
A potential solution to this problem has been provided by the evolution of computer hardware and methods, which have developed very rapidly over the recent years and made possible the computation of increasingly demanding numerical simulations. Optimization algorithms allow for instance the automatic design of non-intuitive geometries that overcome the conventional limits of discretized metasurfaces [99, 101, 102]. In 2017, a high-efficiency metasurface based on an optimized and continuous design, capable of tilting light at 75° with an efficiency of about 80% was fabricated [99].
In addition, the concomitant development of Deep Learning has allowed researchers to predict the optical response of metasurfaces made up of random geometries. Deep Learning and new optimization algorithms are now widely used for designing various types of metasurfaces, pushing their limits in terms of optical transformations [103–110].

Metasurfaces optical functions At the beginning of the 21st century, metamaterials were designed for applications such as wavefront shaping [111], absorbers [90] and polarization control [112, 113]. As we will see, the first metasurfaces targeted the same functionalities.
For example, many metasurfaces with high polarization control have appeared [8, 34, 114–117]. In particular, this capability has been used to realize polarization multiplexed metasurfaces [24, 35, 118, 119]. The first metasurface with high efficiency and high polarization control was designed and fabricated by Arbabi *et al*, demonstrating two distinct optical responses for

[1] Typically $n_{struct} \times S$ must be of comparable size, where n_{struct} and S are respectively the refractive index and the dimension of the structures

two different linear polarizations [24].
Moreover, the multiplexing power of metasurfaces is not only limited to polarization, as demonstrated by the fabrication of an angle-multiplexed metasurface [120], or a spatially mutiplexed metasurface for multiwavelength applications [26].
The fabrication of multiwavelength or broadband metasurfaces has also been a major objective. Indeed, as metasurfaces are typically made of resonant nanostructures, they are expected to operate for a specific wavelength in a narrow bandwidth. As a result, several studies on broadband metasurfaces were done, as well as on achromatic metasurfaces and dispersion control [26, 29, 32, 121–129]. One of the most important studies on this topic was the fabrication of an RGB metalens in 2016 by Capasso *et al*, showing high efficiency for red, green and blue colors, using TiO2 nanopillars and Pancharatnam-Berry phase [32].
In addition, since the optical response of metasurfaces was generally passive, scientists began to look for a way to create active metasurfaces, the optical response of which can be switched by an external stimulus. As examples, we can mention MEMS tunable metasurfaces [130], thermally tunable metasurfaces [131, 132], electrically tunable metasurfaces based on liquid crystals [133–136] or tunable metasurfaces based on elastic substrates [137].
It should also be noted that the field of acoustic metasurfaces has also emerged with the design and fabrication of numerous components [138].
Today, the possibilities offered by metasurfaces continue to develop very rapidly with new design strategies based for example on deep learning.

Fabrication process Most of the metasurface fabrications for visible applications were performed using electron beam lithography (EBL), as EBL allows very high resolutions (< 10 nm). Although variations of the EBL fabrication process are possible (choice of resist, choice of etch material, ...), the overall process usually remains the same (see Chapter 2 for a complete description).
All the metasurfaces that were fabricated by EBL were generally very small (less than 1 mm^2), because the time and cost of fabrication by EBL are proportional to the surface of the component. Moreover the EBL time required for very large metasurfaces makes the fabrication process prone to mechanical or thermal instabilities.
More recently, however, researchers have begun to fabricate efficient metasurfaces using extreme ultraviolet lithography, which is also commonly used for the fabrication of nanoscale computer chips [139–142]. Nano-imprint technology also showed good results for the fabrication of high-performance metasurfaces [143–145]. The use of nano-imprint and extreme UV lithography has enabled the fabrication of metasurfaces that can cover multi-inch plates.

1.1.3 Applications

Metasurfaces represent a research field that has still a lot to offer. Today, some industrial applications are starting to emerge. In this section, we provide some examples of these applications. Then, we highlight the main issues that currently limit the application of metasurfaces and propose an estimation of potential future applications using metasurfaces. [2]

[2] Additional information can be found in the corresponding review article in Ref. [146].

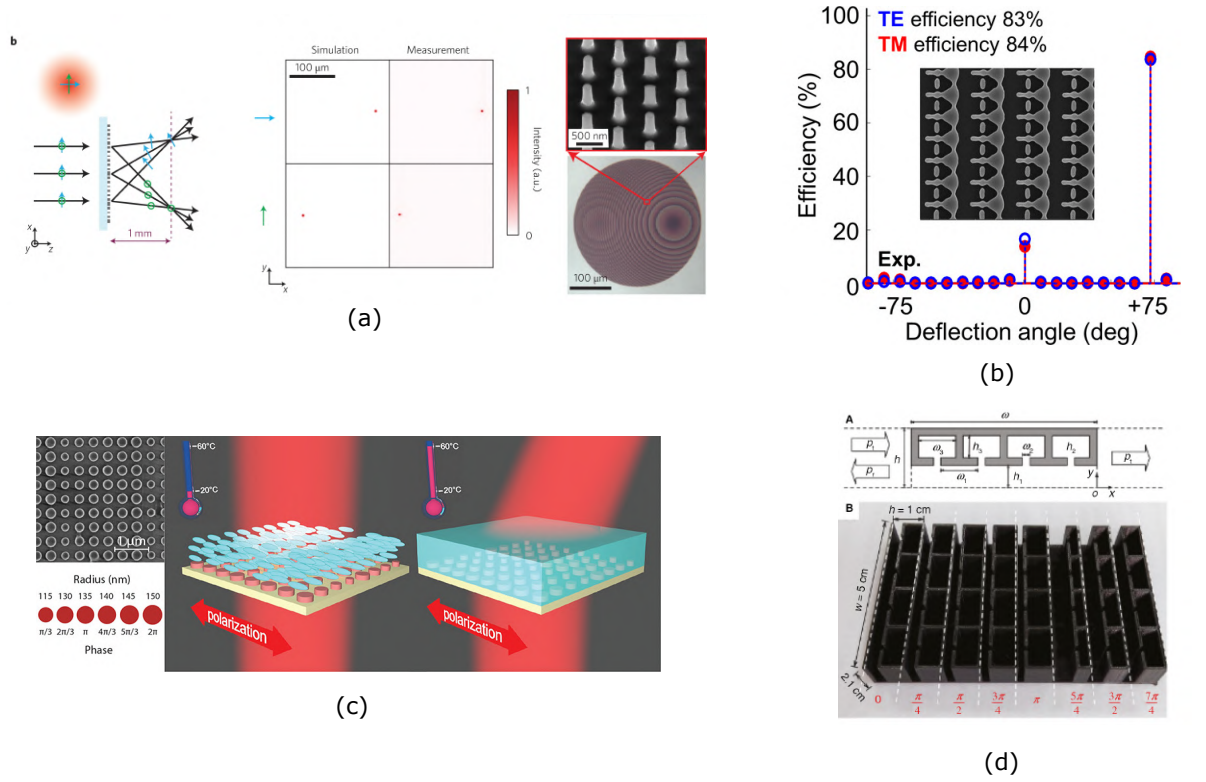

Figure 1.6: (a) Example of a dual metalens focusing light at two different positions depending on the incident polarization state [24]. (b) Example of a metasurface whose computationally optimized design shows high efficiency for a deflection angle of 75° [99]. (c) Example of a tunable metasurface that may or may not deflect light depending on the state of the surrounding liquid crystal [135]. (d) Example of an acoustic metasurface [138].

1.1.3.1 Industrial applications

The industrial applications listed here are all shown in Fig. 1.7. A well-known application is the use of metasurfaces combined with vertical cavity self-emitting lasers (VCSELs) to replace conventional optical components [147, 148]. As an industrial example, we can find a 3D imaging system using a metasurface to create a multipoint pattern, shown in figure 1.7(e) (for facial recognition, or AR applications) [149].
In 2018, the potential of metasurfaces for the fabrication of a miniaturized spectrometer had also been demonstrated [150]. The authors showed the fabrication of a metasurface-based spectrometer of volume 7 mm^3 and that can resolve a spectrum from 760 nm to 860 nm with a resolution of 1.2nm .
Metasurfaces are also currently being studied for applications in very small LIDAR components, allowing to scan entire rooms [151, 152].
Finally, we illustrate in figure 1.7(c) the potential of metasurfaces to recover the full set of Stokes vectors (*i.e.* the polarization state) of different objects [153].

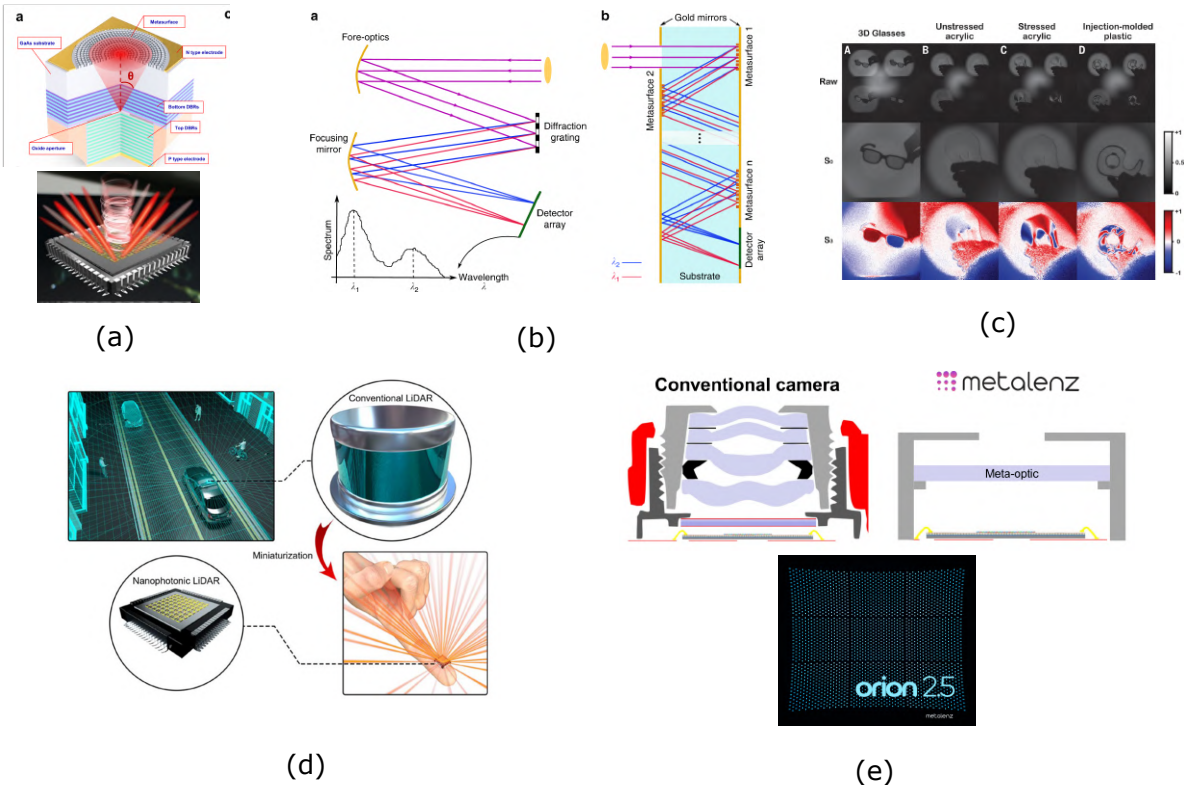

Figure 1.7: Example of industrial applications currently under development. (a) Focusing of a VCSEL beam. (b) Miniaturization of a spectrometer using several metasurfaces. (c) Polarization full-Stokes camera. (d) Miniaturized LIDAR using metasurfaces. (e) 3D imaging by creating a map of more than 10000 points at the output of a VCSEL beam.

1.1.3.2 Current limits

Metasurfaces hold great promise for replacing or improving various optical components. However, today, metasurfaces still suffer from the following limitations.

Efficiency The best efficiencies are now between 80% and 95%. While these are very high numbers, it is worth remembering that conventional bulk optical components, such as lenses used in very demanding industrial or scientic applications, can achieve near perfect efficiencies. In addition, we have also seen that as the NA of the metasurface increases, its efficiency generally decreases.

Multiwavelengths Research on broadband metasurfaces is very active. However, the realization of very efficient achromatic metasurfaces is still very difficult, as the best focusing efficiencies of achromatic metalenses are currently reported around 40% in the visible range [124, 125, 129, 154].

Size Compatible with CMOS fabrication, metasurfaces are expected to be easily replicable on large surfaces, using UV photolithography or nanoimprint technology. However, the design of the original metasurface is still challenging, as the lack of periodic patterns usually requires

the use of EBL technology for fabrication. Fabricating a metasurface greater than one square centimeter is still difficult today.

1.1.3.3 Future applications and perspectives

Metasurfaces are now ready to enter industry, and we are now seeing large high-tech companies taking interest in flat optics conferences [155], as well as many emerging metasurface startups [149, 156–158]. Improvements are constantly being made, and metasurfaces are already very competitive compared to other flat optical components such as diffractive optics [161, 162].

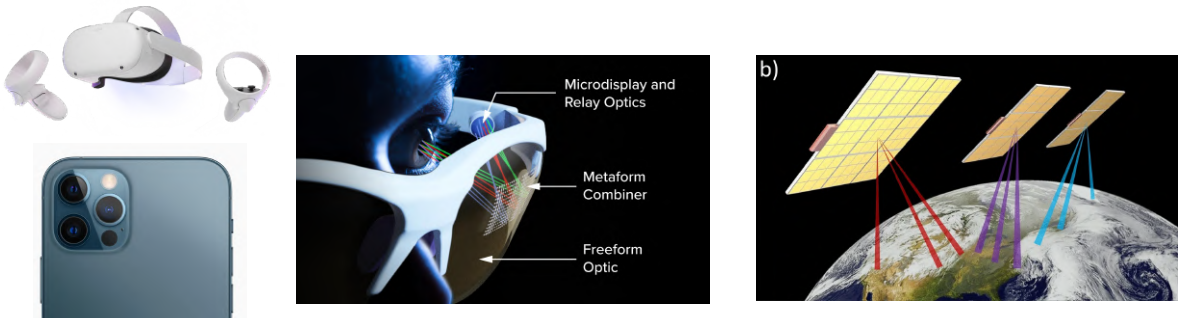

Figure 1.8: Example of future applications of metasurfaces: the miniaturization of optics for smartphones and VR headsets, as well as applications in AR glasses [159] and satellites [160].

Figure 1.8 shows some applications that are most likely to emerge in the near future. The smartphone industry is one of the most promising areas for metasurface applications. Similarly, the VR/AR component industry should soon use metasurfaces, as this would significantly reduce their size and make it much more comfortable and accessible. Space applications would also benefit from the use of metasurfaces : the replacement of heavy and bulky optical systems with thin and light metasurfaces would reduce launch costs. In addition, the multiplexing power of metasurfaces (polarization, angle, wavelength) makes them very suitable for future telecommunication applications, increasing the maximum achievable data rate.

1.2 Optical resonances of Silicon nanostructures

We have seen that the optical properties of metasurfaces are governed by the optical resonances of the nanostructures they are made of. A better understanding of the optical response of such nanostructures is then essential. Concerning wavefront shaping metasurfaces, we can distinguish metasurfaces composed of dielectric nanostructures with high refractive index. Indeed, the latter show high efficiencies while being relatively easy to manufacture. In particular, the use of silicon for metasurfaces seems to be very suitable as it is an abundant resource on Earth and has been already widely used in semiconductor technologies since a long time. Therefore, in the rest of this manuscript, we will mainly focus on the use of silicon nanostructures for the fabrication of metasurfaces.
In this section, we will first introduce Green's Dyadic Method (GDM) [58, 59, 163] as well as its python toolkit pyGDM to simulate the interaction between light and nanostructures [164, 165]. Next, we will focus on the optical resonances of individual silicon nanostructures as a function of their geometries and introduce the dipole approximation. Finally, we will discuss the limits of the dipole approximation and present the quadrupole approximation.

1.2.1 Green Dyadic Method

Green's dyadic method (GDM) describes the interaction of an incoming wave with a structure at the interface between two environments. In what follows, we will briefly develop the GDM formalism used to compute the optical response of a structure surrounded by a homogeneous environment. To simplify the formalism, we consider a monochromatic plane wave illumination in a linear, isotropic, homogeneous and non-magnetic media. Our objective will be to calculate the total electric field excited in the structure.

From Maxwell's equations to Lippman-Schwinger's equation

First, we start with Maxwell's equations using CGS (centimeter gram second) units, and in the frequency domain:

$$\nabla \times \mathbf{E}(\mathbf{r},\omega) = ik_0[\mu_{\text{env}}(\omega)\mathbf{H}(\mathbf{r},\omega) + 4\pi\mathbf{M}(\mathbf{r},\omega)] \tag{1.2}$$

$$\nabla \cdot \mathbf{H}(\mathbf{r},\omega) = -\frac{4\pi}{\mu_{\text{env}}(\omega)}\nabla \cdot \mathbf{M}(\mathbf{r},\omega) \tag{1.3}$$

$$\nabla \times \mathbf{H}(\mathbf{r},\omega) = -ik_0[\epsilon_{\text{env}}(\omega)\mathbf{E}(\mathbf{r},\omega) + 4\pi\mathbf{P}(\mathbf{r},\omega)] \tag{1.4}$$

$$\nabla \cdot \mathbf{E}(\mathbf{r},\omega) = -\frac{4\pi}{\epsilon_{\text{env}}(\omega)}\nabla \cdot \mathbf{P}(\mathbf{r},\omega) \tag{1.5}$$

$$\tag{1.6}$$

where $\mathbf{E}(\mathbf{r},\omega)$ and $\mathbf{H}(\mathbf{r},\omega)$ are the electric and magnetic fields at the position $\mathbf{r}$ for the light frequency $\omega = 2\pi c/\lambda_0$ (c being the speed of light and λ_0 its wavelength in vacuum). $\mathbf{P}(\mathbf{r},\omega)$ and $\mathbf{M}(\mathbf{r},\omega)$ are the electric and magnetic polarizations. ϵ_{env} and μ_{env} are the dielectric permittivity and the magnetic permeability of the surrounding medium and $k_0 = 2\pi/\lambda_0$ is the wavenumber of the incident light in vacuum.
As we consider a non-magnetic medium, we have $\mathbf{M}$ = 0 and $\mu_{\text{env}} = 1$. By applying the curl

operator to Eq. (1.2), using the identity $\nabla(\times\nabla\times\mathbf{A}) = \nabla(\nabla\mathbf{A}) - \Delta\mathbf{A}$ and Eq. 1.4 we find:

$$(\Delta + k^2)\mathbf{E}(\mathbf{r},\omega) = -\frac{4\pi}{\epsilon_{\text{env}}}(\nabla\nabla + k^2)\mathbf{P}(\mathbf{r},\omega) \tag{1.7}$$

with $k = \sqrt{\epsilon_{\text{env}}}k_0$ the wavenumber in the environment.
As we do not take into account non-linear responses, we can define the electric polarization as $\mathbf{P} = \boldsymbol{\chi}_{\text{e}} \cdot \mathbf{E}$. The susceptibility can be expressed as $\boldsymbol{\chi}_{\text{e}} = (\boldsymbol{\epsilon}_{\text{r}} - \boldsymbol{\epsilon}_{\text{env}})/4\pi$, $\boldsymbol{\epsilon}_r$ being the dielectric permittivity of the structure. It should be noted that for dispersive materials, $\boldsymbol{\epsilon}_r = \boldsymbol{\epsilon}_r(\omega)$ and $\boldsymbol{\chi}_{\text{e}} = \boldsymbol{\chi}_{\text{e}}(\omega)$.

Using Green's functions, we can find solutions of equation 1.7 in the form of a single vectorial *Lippmann-Schwinger equation* :

$$\mathbf{E}(\mathbf{r},\omega) = \mathbf{E}_0(\mathbf{r},\omega) + \int_V \mathbf{G}_0(\mathbf{r},\mathbf{r}',\omega)\cdot\boldsymbol{\chi}_{\text{e}}\cdot\mathbf{E}(\mathbf{r}',\omega)\text{d}\mathbf{r}' \tag{1.8}$$

where V is the volume of the structure and $\mathbf{E}_0$ is the incid ent field. $\mathbf{G}_0(\mathbf{r},\mathbf{r}',\omega)$ is the *Green Dyad* function and corresponds to the propagation from position $\mathbf{r}'$ to position $\mathbf{r}$ of the electric field generated by a dipole $\mathbf{p}$, so that $\mathbf{E}(\mathbf{r},\omega) = \mathbf{G}_0(\mathbf{r},\mathbf{r}',\omega)\mathbf{p}(\mathbf{r}',\omega)$. $\mathbf{G}_0$ is thus also called a $propagator$ and has the following expression:

$$\mathbf{G}_0(\mathbf{r},\mathbf{r}',\omega) = \frac{1}{\boldsymbol{\epsilon}_{\text{env}}}\Big(-k^2\mathbf{T}_1(\mathbf{R}) - ik\mathbf{T}_2(\mathbf{R}) + \mathbf{T}_3(\mathbf{R})\Big)e^{ikR} \tag{1.9}$$

and

$$\mathbf{T}_1(\mathbf{R}) = \frac{\mathbf{RR} - \mathbf{I}R^2}{R^3} \tag{1.10}$$

$$\mathbf{T}_2(\mathbf{R}) = \frac{3\mathbf{RR} - \mathbf{I}R^2}{R^4} \tag{1.11}$$

$$\mathbf{T}_3(\mathbf{R}) = \frac{3\mathbf{RR} - \mathbf{I}R^2}{R^5} \tag{1.12}$$

where $\mathbf{R} = \mathbf{r} - \mathbf{r}'$, and $\mathbf{T}_2(\mathbf{R})$, $\mathbf{T}_3(\mathbf{R})$ and $\mathbf{T}_1(\mathbf{R})$ are respectively the far, intermediate and near field contributions to the propagator.

Volume discretization

The Lippman-Schwinger equation written above cannot generally be solved for a structure of arbitrary shape. We describe here the numerical approach which consists in a discretization of the volume of the structure into N cubic (or hexagonal) unit cells of volume Δv. After discretization, Eq. 1.8 becomes :

$$\mathbf{E}(\mathbf{r}_{\text{i}}) = \mathbf{E}_0(\mathbf{r}_{\text{i}}) + \sum_{\text{j}=1}^{\text{N}} \mathbf{G}_{\text{tot}}(\mathbf{r}_{\text{i}},\mathbf{r}_{\text{j}})\cdot\boldsymbol{\chi}_{\text{e}}\cdot\mathbf{E}(\mathbf{r}_{\text{j}})\Delta v \tag{1.13}$$

We can then rewrite Eq. 1.13 as follows:

$$\mathbf{E}_0(\mathbf{r}_{\text{i}}) = \sum_{\text{j}=1}^{\text{N}} (\delta_{ij}\mathbf{I} - \Delta v\boldsymbol{\chi}_{\text{e}}\cdot\mathbf{G}_{\text{tot}}(\mathbf{r}_{\text{i}},\mathbf{r}_{\text{j}}))\cdot\mathbf{E}(\mathbf{r}_{\text{j}}) \tag{1.14}$$

Therefore, we obtain a linear system in which $\forall i$, the incident field $\mathbf{E}_0(\mathbf{r}_\mathrm{i})$ is related to each of the total fields $\mathbf{E}(\mathbf{r}_\mathrm{j})$ $(1 \leq j \leq N)$ by a 3×3 matrix $M_{ij} = \delta_{ij}\mathbf{I} - \Delta v \boldsymbol{\chi}_\mathrm{e} \cdot \mathbf{G}_\mathrm{tot}(\mathbf{r}_\mathrm{i}, \mathbf{r}_\mathrm{j})$. Thus, if we define the total field of the entire structure as a N×3 *supervector* $\hat{\mathbf{E}}_{obj.} = [\mathbf{E}(\mathbf{r}_1), \mathbf{E}(\mathbf{r}_2), ..., \mathbf{E}(\mathbf{r}_\mathrm{N})]$, as well as the incident field as another N×3 *supervector* $\hat{\mathbf{E}}_{0,obj.} = [\mathbf{E_0}(\mathbf{r}_1), \mathbf{E_0}(\mathbf{r}_2), ..., \mathbf{E_0}(\mathbf{r}_\mathrm{N})]$, we can write the following system:

$$\begin{bmatrix} \mathbf{E_0}(\mathbf{r}_1) \\ \mathbf{E_0}(\mathbf{r}_2) \\ . \\ . \\ . \\ \mathbf{E_0}(\mathbf{r}_\mathrm{N}) \end{bmatrix} = \begin{bmatrix} M_{11} & M_{12} & . & . & . & M_{1N} \\ M_{21} & M_{22} & . & . & . & M_{2N} \\ . & . & . & & & . \\ . & . & & . & & . \\ . & . & & & . & . \\ M_{N1} & M_{N2} & . & . & . & M_{NN} \end{bmatrix} \cdot \begin{bmatrix} \mathbf{E}(\mathbf{r}_1) \\ \mathbf{E}(\mathbf{r}_2) \\ . \\ . \\ . \\ \mathbf{E}(\mathbf{r}_\mathrm{N}) \end{bmatrix} \tag{1.15}$$

$$\hat{\mathbf{E}}_{0,obj.} = \mathbf{M} \cdot \hat{\mathbf{E}}_{obj.} \tag{1.16}$$

where $\mathbf{M}$ is a $3N \times 3N$ matrix composed of 3×3 matrices M_{ij}. Finally, the solution of this system can be obtained by inverting the matrix M, which leads to the equation (with $\mathbf{K} = \mathbf{M}^{-1}$):

$$\hat{\mathbf{E}}_{obj.} = \mathbf{K} \cdot \hat{\mathbf{E}}_{0,obj.} = \sum_{\mathrm{i,j}=1}^{\mathrm{N}} \mathbf{K}_{ij} \cdot \mathbf{E}_{0,obj.}(\mathbf{r}_j) \tag{1.17}$$

To conclude, the computations performed in the GDM essentially consist in inverting the matrix $\mathbf{M}$ to obtain $\mathbf{K}$, the latter being also called the *generalized field propagator* [166] (composed of 3×3 matrices K_{ij}).

Computation of the far-field and near-field optical response

The resolution of Eq. 1.17 gives access to the electric field inside the illuminated nanostructure. From the knowledge of the total or *self-consistent* electric field inside the nanostructure, it is possible to compute several quantities that characterize its far-field or near-field optical properties. Among these, we can mention (more information can be found in Ref. [164, 165]):

- the extinction, absorption or scattering spectra;
- the optical near field inside and around nanostructures as well as its chirality;
- the photonic local density of states (LDOS);
- the heat generation and temperature distribution.

GDM is very well suited to calculate the optical response of individual nanostructures. However, some limiting factors appear for the calculation of a large number of nanostructures. Indeed, we have seen with equation 1.16 that we compute the generalized propagator K by inversion of a matrix of size $3N \times 3N = 9N^2$. As the inversion operation is linear, the computation time required is also proportional to N^2. Thus, increasing the number of structures drastically increases the calculation complexity, and the required time rapidly becomes a limiting factor.

In this thesis, I have used the open source python package pyGDM implemented by P.R. Wiecha. pyGDM is based on simulation codes and theoretical models developed over the past 20 years by C. Girard at CEMES (see e.g. [163]), with contributions from G. Colas des Francs, A. Arbouet, R. Marty, C. Majorel, A. Patoux, Y. Brûlé and P.R. Wiecha. It is available online at the following address : https://wiechapeter.gitlab.io/pyGDM2-doc/.

1.2.2 Optical resonances in an individual nano-object

In this section, we will study the optical resonances supported by silicon nanostructures. We will first see that silicon nanodiscs support both magnetic and electric dipole resonances. Then, we will describe the dipole approximation and illustrate it with examples. Finally, we will see the limitations of this approximation.

1.2.2.1 Dipole resonances of a silicon nanodisc

In Fig. 1.9 we show the extinction spectrum of a silicon nanodisc of height 120 nm and diameter 150 nm. Two resonances are clearly visible in the extinction spectrum at $\lambda = 520$ nm and $\lambda = 595$ nm. We also show for these two wavelengths the electric field vectors inside the nanostructure. By observing these vector fields, and based on the description of Mie resonances given in Fig. 1.3, we can clearly identify the electric and magnetic dipole resonances. Therefore, as for the Mie resonances for nanospheres, the optical response of a silicon nan-

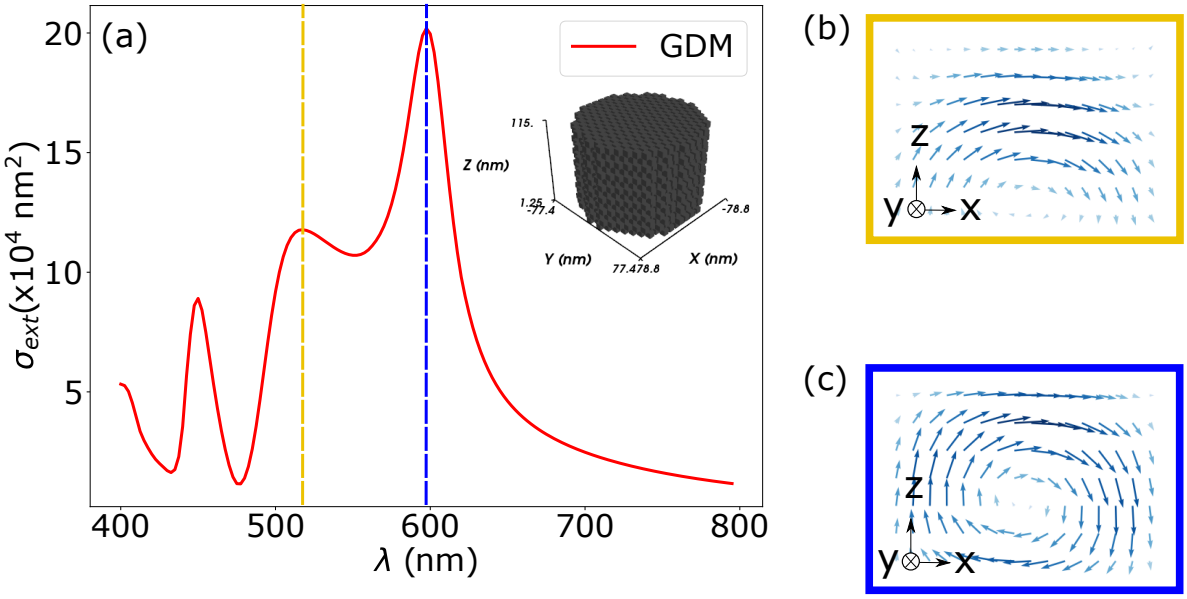

Figure 1.9: (a) Extinction spectrum of a silicon nanodisc of 120 nm height and 150 nm diameter. We can identify for $\lambda = 520$ nm and $\lambda = 595$ nm the electric (b) and magnetic (c) dipole resonances.

odisc can be assimilated to the response of a couple of electric and magnetic dipoles. This is called in the literature the dipole approximation. (see Fig. 1.10). This approximation is in fact very interesting for numerical simulations. Indeed, being able to describe the optical response of a nanostructure as a single pair of dipoles would enable to overcome the limit of the number of structures that can be simulated via the GDM.

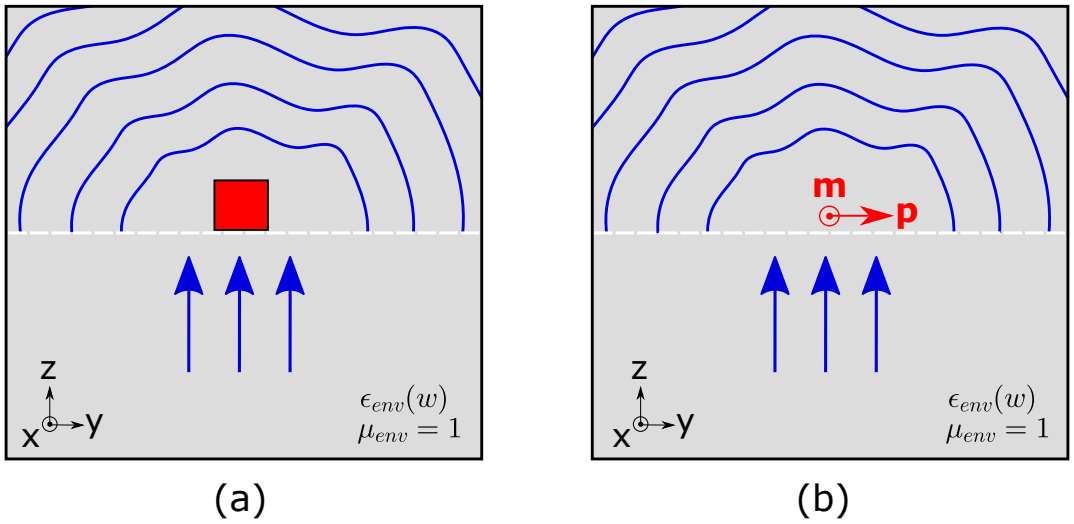

Figure 1.10: Principle of the dipole approximation. (a) Interaction between an incident light and a nanostructure. The nanostructure re-emits a scattered light. (b) Dipolar approximation of the nanostructure represented in (a). The pair of dipoles $\mathbf{p}$ and $\mathbf{m}$ is assumed to have an optical response similar to that of the nanostructure.

1.2.2.2 Dipole approximation

As we have explained, the dipole approximation consists in finding an electric dipole $\mathbf{p}$ and a magnetic dipole $\mathbf{m}$ such that they alone can describe the complete optical response of a nanostructure (see Fig. 1.10). In this section, we will show how we can calculate these dipole moments, based on the extraction of polarizabilities. The presented development is based on the article published in Ref. [167], where more details are given.
We consider an incident and self-consistent electromagnetic field described by two super-vectors: $\mathbf{F}_0(\mathbf{r}) = (\mathbf{E}_0(\mathbf{r}), \mathbf{H}_0(\mathbf{r}))$ and $\mathbf{F}(\mathbf{r}) = (\mathbf{E}(\mathbf{r}), \mathbf{H}(\mathbf{r}))$. $\mathbf{E}$ and $\mathbf{H}$ are respectively the electric and magnetic fields. From eq. 1.16, we define a new generalized field propagator $\mathbb{K} = \sum_{i,j=1}^{N} \mathbb{K}(\mathbf{r_i}, \mathbf{r_j})$ which is now a 6N x 6N matrix and is defined as follows:

$$\mathbf{F}(\mathbf{r}) = \sum_{i,j=1}^{N} \mathbb{K}(\mathbf{r_i}, \mathbf{r_j}) \cdot \mathbf{F}_0(\mathbf{r}_j);. \tag{1.18}$$

For clarity, we denote the superpropagator $\mathbb{K}$ as being composed of four mixed dyadic tensors (3×3) :

$$\mathbb{K}(\mathbf{r_i}, \mathbf{r_j}) = \begin{pmatrix} \mathbf{K}^{EE}(\mathbf{r_i}, \mathbf{r_j}) & \mathbf{K}^{EH}(\mathbf{r_i}, \mathbf{r_j}) \\ \mathbf{K}^{HE}(\mathbf{r_i}, \mathbf{r_j}) & \mathbf{K}^{HH}(\mathbf{r_i}, \mathbf{r_j}) \end{pmatrix} \tag{1.19}$$

The dipole approximation is based on the extraction of the electric and magnetic polarizabilities to simulate the response of a nanostructure as being equal to the response of a pair of electric and magnetic dipoles $\mathbf{p}$ and $\mathbf{m}$:

$$\begin{pmatrix} \mathbf{p}(\mathbf{r}) \\ \mathbf{m}(\mathbf{r}) \end{pmatrix} = \overbrace{\begin{pmatrix} \alpha^{EE} & \alpha^{EH} \\ \alpha^{HE} & \alpha^{HH} \end{pmatrix}}^{\boldsymbol{\alpha}} \cdot \overbrace{\begin{pmatrix} \mathbf{E}_0(\mathbf{r}) \\ \mathbf{H}_0(\mathbf{r}) \end{pmatrix}}^{\mathbf{F}_0(\mathbf{r}_c)} \tag{1.20}$$

where the polarizabilities α^{EE}, α^{EH}, α^{HE} and α^{HH} are four (3×3) dyadic tensors. These polarizabilities have the following expression in non-magnetic materials ($\chi_m = 0$):

$$\alpha^{EE} = \chi_e \Delta v \sum_{i,j}^{N} \mathbf{K}^{EE}(\mathbf{r}_i, \mathbf{r}_j) e^{i\mathbf{k}\cdot\mathbf{r}_j} \tag{1.21a}$$

$$\alpha^{EH} = 0 \tag{1.21b}$$

$$\alpha^{HE} = -\Delta v \sum_{i,j}^{N} \left\{ \frac{ik_0}{2} \chi_e \mathbf{r}_i \wedge \mathbf{K}^{EE}(\mathbf{r}_i, \mathbf{r}_j) \right\} e^{i\mathbf{k}\cdot\mathbf{r}_j} \tag{1.21c}$$

$$\alpha^{HH} = 0 \tag{1.21d}$$

Usually, the polarizabilities extracted via the dipole approximation are only defined from the geometrical parameters of the structures, and do not depend on the illumination. This is why we use here the term *pseudopolarizabilities* because they depend on the illumination direction due to the term $e^{(i\mathbf{k}\cdot\mathbf{r}_j)}$. The preservation of this illumination dependence allows in fact to take into account the magnetic dipole resonance. Indeed, the dipolar magnetic resonance comes from the creation of a vortex of the electric field rotating inside the nanostructure (see Fig. 1.3 for the Mie resonances), which comes from the phase delay of the incident light propagating through the nano-object. Discarding it would imply that the field is constant inside the nanostructure, which means no phase delay, and therefore no magnetic resonance.
However, since they depend on the direction of the incident wave, one can think that these pseudopolarizabilities apply only to very restricted cases. In fact, it is possible to evaluate the pseudopolarizability of a structure for plane waves of any incident angle, after having computed those for the three directions of incidence x, y, z. Indeed, it has been analytically demonstrated in Ref. [167] that:

$$\alpha_\nu^{EE} \approx \left(\frac{k_x}{|\mathbf{k}|}\right)^2 \alpha_x^{EE} + \left(\frac{k_y}{|\mathbf{k}|}\right)^2 \alpha_y^{EE} + \left(\frac{k_z}{|\mathbf{k}|}\right)^2 \alpha_z^{EE} \tag{1.22a}$$

$$\alpha_\nu^{HE} \approx \left(\frac{k_x}{|\mathbf{k}|}\right) \alpha_x^{HE} + \left(\frac{k_y}{|\mathbf{k}|}\right) \alpha_y^{HE} + \left(\frac{k_z}{|\mathbf{k}|}\right) \alpha_z^{HE} \tag{1.22b}$$

where $\mathbf{k} = (k_x, k_y, k_z)$ is the incident wave vector and ν is the incident angle.

1.2.2.3 Spectra and dipole extraction of nanostructures with varying shapes

In this part we will evaluate how much of the far field scattered light corresponds to the electric and magnetic dipoles $\mathbf{p}$ and $\mathbf{m}$. To do so, we apply the dipole approximation for nanostructures of various shapes.
We first calculate $\mathbf{p}$ and $\mathbf{m}$ from the pseudopolarizabilities of the structure. Then, we propagate the scattered electric field emitted by these dipoles and integrate the intensities on a sphere.
To obtain the expressions of the associated Green dyads propagators, we used an analytical approach based on the literature [168].

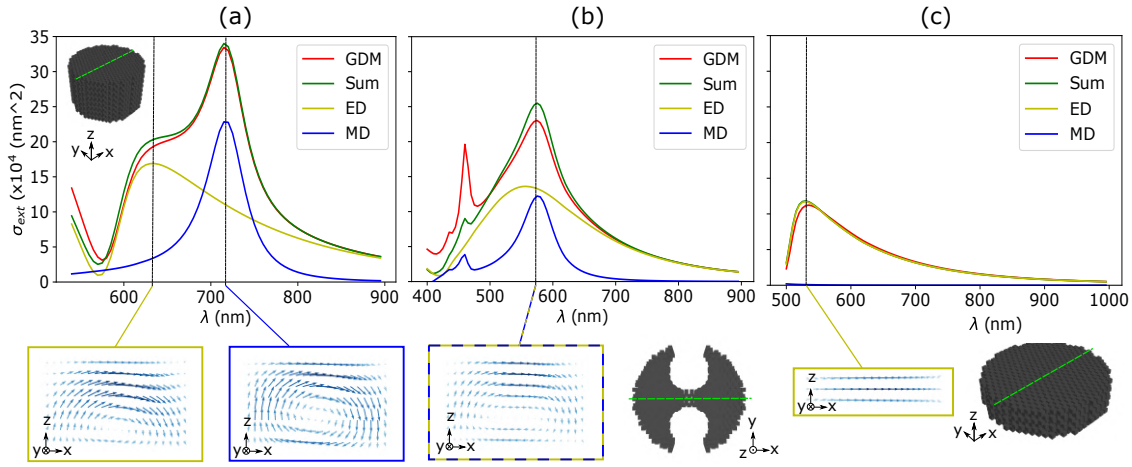

Figure 1.11: (a) Extinction spectra of a silicon nanodisc of 130 nm height and 200 nm diameter. The electric field corresponding to the electric (resp. magnetic) resonance is represented for $\lambda = 630$ nm (resp 715 nm). (b) Extinction spectra of a silicon nanodisc of 130 nm height and 200 nm diameter which was pierced by two holes from top to bottom. The electric field is represented for $\lambda = 580$ nm. (c) Extinction spectra of a silicon nanodisc of 50 nm height and 200 nm diameter. The electric field is represented for $\lambda = 530$ nm.

Silicon nanodisc of low aspect ratio In Fig. 1.11(a), we show the extinction spectrum of a silicon nanodisc of 200 nm diameter and 130 nm height, with its electric and magnetic dipole contributions, and the sum of the contributions. The nanodisc is discretized in a 10 nm hexagonal mesh leading to 6056 mesh points. We also show for each resonance a (Ox, Oz) 2D representation of the electric field inside the structure. First of all, we can observe that the spectrum approximated by the dipoles is in very good agreement with the full GDM calculation. This highlights that the dipole approximation can work very well with dielectric structures. Then, the field representations clearly show the behavior corresponding to each of the resonances. For the electric resonance (at $\lambda = 630$ nm), we can see that the field vectors are mainly going from left to right. For the magnetic resonance (at $\lambda = 715$ nm), we can clearly see the vortex of the electric field, creating the magnetic dipole.

Tuning the magnetic resonance of silicon nanodiscs As we have just seen, the magnetic dipole resonance relies on the creation of an electric vortex inside the nanostructure. Knowing this, it becomes possible to imagine some geometries that could cancel, or at least decrease this magnetic resonance. An example of such a structure is shown in Fig. 1.11(b). This structure is in fact a nanodisc with two holes pierced from the top (see figure). The cylinder has a diameter of 200 nm and a height of 130 nm. The holes have a diameter of 90 nm and are positioned between the center of the disc and the edge of the disc. The extinction spectrum associated with this structure is also shown in Fig. 1.11(b). Comparing this extinction spectrum to that of the complete disc in Fig. 1.11(a), we see that the electric and magnetic resonances are both shifted and are both resonating at $\lambda = 580$ nm. Moreover, we see that although the electric dipole peak is only shifted, the magnetic dipole's amplitude is strongly decreased. In fact, this comes from the fact that the holes prevent the formation of the electric field vortex that creates the magnetic dipole resonance. We also note the presence of another resonance peak

at $\lambda = 460$ nm which comes from a higher order resonance (quadrupole).
Another silicon nanodisc with no magnetic resonance is shown in Fig. 1.11(c). This nanodisc has a very low aspect ratio, as its diameter is 200 nm and its height is 50 nm. For such low aspect ratios, the creation of a field vortex (hence the presence of a magnetic resonance) is not possible, as it relies on the phase delay accumulated by the incident light propagating through the nanodisc. To be more precise, the magnetic resonance actually occurs, but for smaller wavelengths. Indeed, as λ_0 diminishes, the minimum thickness required to support the creation of a vortex also diminishes. On the other hand, as the electric resonance does not depend on this thickness, it is weakly altered.

Silicon nanodisc with varying aspect ratio We now study the influence of the aspect ratio on the efficiency of the dipole approximation. In Fig. 1.12, we show several extinction spectra of nanodiscs of diameter 200 nm and heights ranging from 50 nm to 500 nm. Each nanodisc is discretized in a hexagonal mesh of cell size 15.5 nm. As before, we plot the spectra corresponding to the full GDM calculation, to the sum of the dipole contributions and to each of the dipole moments. The results allow us to set a first limit to the dipolar approximation. Indeed, we can see that the difference between the full GDM spectra and the dipole approximation spectra increases as the aspect ratio increases. This is due to the fact that as the aspect ratio increases, additional multipole orders can be excited inside the structure, such as electric and magnetic quadrupoles. This means that for such structures, the dipole approximation is no longer sufficient, and a better description of the polarization distribution induced inside the optically excited nanostructure requires to take into account the contribution of higher order multipoles.

1.2.3 Beyond the dipole approximation

As we have just seen, the dipole approximation is not sufficient to describe the optical response of high aspect ratio silicon nanostructures. In the following, we take into account electric and magnetic quadrupole moments to improve the description of the induced polarization.

1.2.3.1 Quadrupole approximation

Here we compute, in addition to the electric and magnetic dipoles $\mathbf{p}$ and $\mathbf{m}$ the electric and magnetic quadrupoles $\hat{\mathcal{Q}}$ and $\hat{\mathcal{M}}$.
The implementation of the quadrupole approximation to describe the optical response of silicon nanostructures in this thesis has been done in close collaboration with Peter R. Wiecha (LAAS-CNRS). Initially inspired by the results of Evlyukhin *et al* (Ref. [3]) we tried to re-demonstrate the analytical formulas proposed in their article and implement them in GDM to include the contribution from the electric and magnetic quadrupolar resonances excited in the silicon nanostructures. However, our calculations did not yield the exact same expressions as in the article. It appeared indeed that our quadrupole contributions, although very similar in their forms, were underestimated by a factor close to $\alpha = 4$. Despite considerable efforts, we could not find the origin of this difference. A more fundamental limit on the validity of the expressions proposed by Evlyukhin *et al* was recently pointed out by Alaee *et al* [168]: these expressions, calculated in the long wavelength limit, appear to yield erroneous predictions even in the case of sub-wavelength nanostructures. The authors propose novel expressions for the electric and magnetic dipoles and quadrupoles. These expressions are exact, valid for

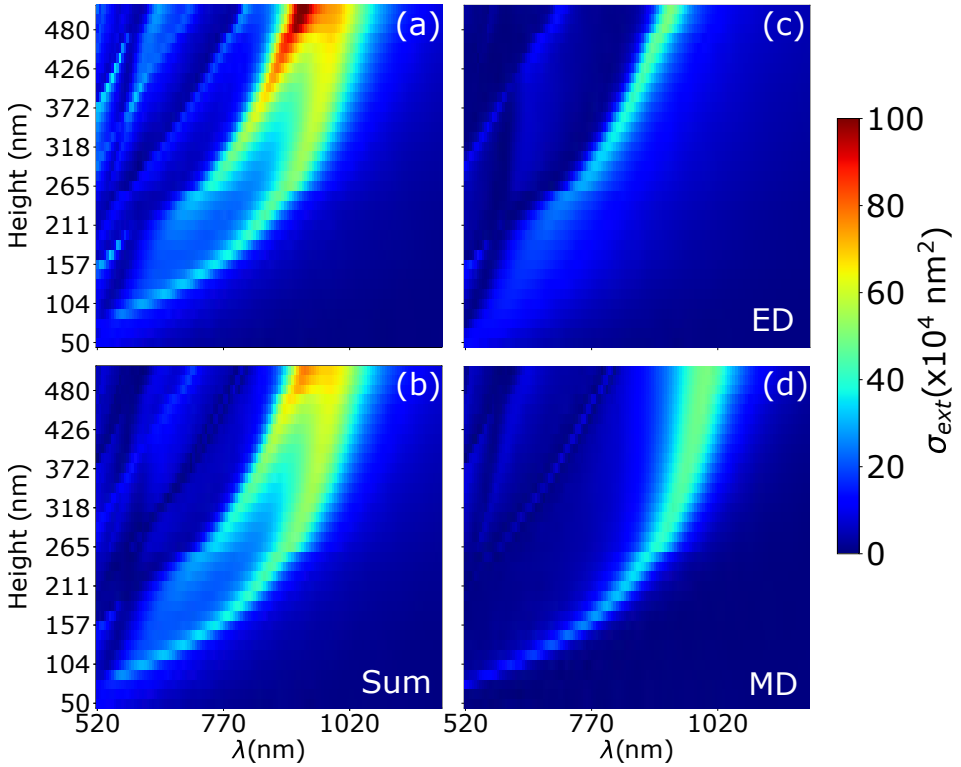

Figure 1.12: Extinction spectra of a set of silicon nanodiscs of fixed diameter ($D = 200$ nm) and increasing height (50 nm < H < 500 nm). For each spectrum, we represent (a) the full pyGDM computation , (b) the total dipole approximation, (c) the electric dipole contribution and (d) the magnetic dipole contribution.

any wavelength and size, and therefore correct the approximated expressions that we used initially.

In order to compare with the previous study, we illustrate on Fig. 1.13 the same calculation as for Fig. 1.12, adding this time the quadrupole contributions calculated using the results of Ref. [168]. We also show in Fig. 1.13(e) (resp. Fig. 1.13 (f)) the difference in intensity between the complete GDM calculation and the sum of the dipoles (resp. dipoles and quadrupoles) contributions. As we can see, the addition of the electric and magnetic quadrupoles improves the agreement between the full GDM result and the multipole approximation. Nevertheless, we note that these results are calculated in the case of isolated nanostructures. Keeping in mind that the objective of this thesis is to simulate the optical response of metasurfaces, *i.e.* dense arrays of nanostructures, an approach based on the quadrupole approximation would require to take into account the electromagnetic coupling between the multipoles induced on neighbouring nanostructures.

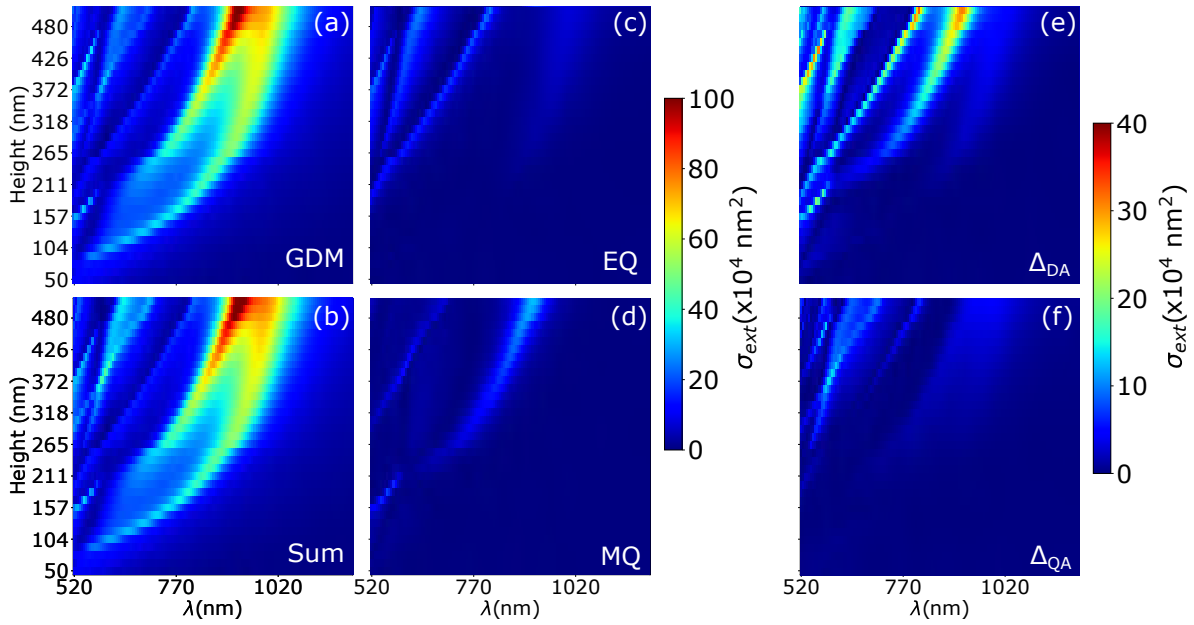

Figure 1.13: Extinction spectra of a set of silicon nanodiscs of fixed diameter ($D = 200$ nm) and increasing height (50 nm < H < 500 nm). For each spectrum, we represent (a) the full pyGDM computation , (b) the total quadrupole approximation, (c) the electric quadrupole contribution, (d) the magnetic quadrupole contribution. In (e) (resp. (f)), we show the difference in intensity between the full GDM map and the sum of the dipoles (resp. of the dipoles and quadrupoles) contributions.

1.3 Optical response of dielectric metasurfaces

In the previous section, we studied the optical response of individual nanostructures, and presented the dipole and quadrupole approximations. In this section, we will see how to simulate the optical properties of metasurfaces. In the latter, coupling effects between neighbouring nanostructures can have a strong influence and make the optical response of the ensemble depart significantly from the one of its isolated constituents. Although the GDM gives a unique physical insight into the nature of the optical resonances excited inside the nanostructures, it appears limited in its basic form to describe such environments. Several approaches to approximate the total optical responses of metasurfaces based on the GDM were studied during this PhD [3]. However, none of them led to satisfactory results. Therefore, in the following, we adopt a different approach based on the Finite Difference Time Domain (FDTD) technique.

1.3.1 FDTD method

1.3.1.1 Description of FDTD formalism

FDTD was originally called *Yee's method*, in reference to Kane S. Yee who introduced the formalism in 1966 [169]. The technique was then studied and developed by Allen Taflov *et al* from 1974 until the beginning of the 21st century [55]. Since its implementation, FDTD techniques

[3] A coupling approach using the pseudopolarizabilities is shown in the Appendix.

have been commonly used to solve many electromagnetic problems for both research and industry. Nowadays, FDTD is also frequently used in nanophotonics, especially for metasurface design.
FDTD is a computational method that solves Maxwell's equations through a discretization in time and space of a volume of interest. This discretization is always associated with a specific grid where the electromagnetic field is reconstructed. As an illustration, we show in Fig. 1.14 *Yee's grid* (widely used for FDTD calculations) where the electric field components are all located on the edges of the elementary cube, while the magnetic field components are located in the center of the faces. In fact, Yee's grid is designed in such a way that each $\vec{E}$ electric field component is surrounded by four $\vec{H}$ circulating components and conversely.
In addition to the spatial separation, there is also a temporal separation. Specifically, if the magnetic field is calculated for each time $t = [\Delta t, 2\Delta t, 3\Delta t, ...]$, then the electric field is calculated at $t = [\Delta t/2, 3\Delta t/2, 5\Delta t/2, ...]$, Δt being the time increment. These temporal and spatial separations are chosen so as to facilitate the resolution of Maxwell's equations. It allows to compute iteratively the electric and magnetic field at each half time step $\Delta t/2$, thus to simulate the propagation of an electromagnetic wave defined in the discretized volume of interest.
We denote Δx, Δy and Δz the space increments in the x, y and z directions. To each of the space and time parameters are generally associated four integers i, j, k and n, so that any space and time function u is defined in Yee's grid as follows:

$$u(i\Delta x, j\Delta y, k\Delta z, n\Delta t) = u^n_{i,j,k} \tag{1.23}$$

Based on the discretization of the system, the spatial and temporal derivatives of such a function u can be written :

$$\frac{\partial u}{\partial x}(i\Delta x, j\Delta y, k\Delta z, n\Delta t) = \frac{u^n_{i+1/2,j,k} - u^n_{i-1/2,j,k}}{\Delta x} + O[(\Delta x)^2] \tag{1.24}$$

$$\frac{\partial u}{\partial t}(i\Delta x, j\Delta y, k\Delta z, n\Delta t) = \frac{u^{n+1/2}_{i,j,k} - u^{n-1/2}_{i,j,k}}{\Delta t} + O[(\Delta t)^2] \tag{1.25}$$

By injecting these relations into Maxwell's equations, we can deduce the relation governing the evolution of the electric and magnetic fields. For example, the E_x component of the electric field, located at position $(i\Delta x, (j+1/2)\Delta y, (k+1/2)\Delta z, n\Delta t)$, can be expressed as follows [55]:

$$\begin{aligned} E_x|^{n+1/2}_{i,j+1/2,k+1/2} = & \left(\frac{1 - \frac{\sigma_{i,j+1/2,k+1/2}\Delta t}{2\epsilon_{i,j+1/2,k+1/2}}}{1 + \frac{\sigma_{i,j+1/2,k+1/2}\Delta t}{2\epsilon_{i,j+1/2,k+1/2}}} \right) E_x|^{n-1/2}_{i,j+1/2,k+1/2} \\ & + \left(\frac{\frac{\Delta t}{\epsilon_{i,j+1/2,k+1/2}}}{1 + \frac{\sigma_{i,j+1/2,k+1/2}\Delta t}{2\epsilon_{i,j+1/2,k+1/2}}} \right) \begin{pmatrix} \frac{H_z|^n_{i,j+1,k+1/2} - H_z|^n_{i,j,k+1/2}}{\Delta y} \\ -\frac{H_y|^n_{i,j+1/2,k+1} - H_y|^n_{i,j+1/2,k}}{\Delta z} \\ -J_{\text{source}_x}|^n_{i,j+1/2,k+1/2} \end{pmatrix} \end{aligned} \tag{1.26}$$

where σ represents the conductivity and J_{source} the current source, both of which are predefined parameters.
The relation described above thus allows to compute E_x at time $t = (n+1/2)\Delta t$ as a function of the environment parameters (σ and J_{source}), of the electric field at $t = (n-1/2)\Delta t$ at the same position, and of the surrounding magnetic field at $t = n\Delta t$. Similar relations relate all the other components of the electric and magnetic fields (they can be found in Ref. [55]).

In conclusion, the algorithm can be summarized as:

1. Discretize all the Maxwell equations in time and space.
2. Solve the equations to get every current fields ($t_{e_c} = (n+1/2)\Delta t$ for the electric field and $t_{m_c} = n\Delta t$ for the magnetic field) as functions of the previous fields ($t_{e_p} = t_{e_c} - 1$, $t_{m_p} = t_{m_c} - 1$).
3. Calculate the $t = n\Delta t$ magnetic field (starting at $n = 0$) for every positions.
4. Get the $t = (n+1/2)\Delta t$ electric field (starting at $n = 1/2$) for every positions.
5. Repeat the latter two steps to increment in time.

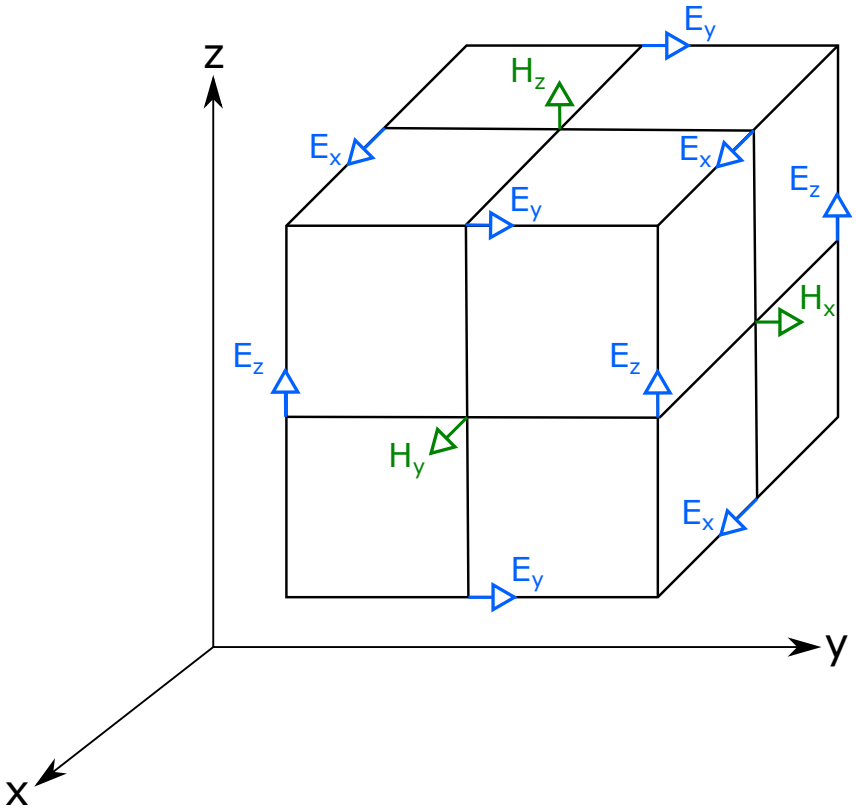

Figure 1.14: Illustration of a cell of Yee's grid. Representation of the positions of the components of the electric and magnetic fields.

It should be remembered that the discretization of the derivatives of Maxwell's equation

is based on a second order limited expansion (see eq. 1.24 and 1.25). This means that FDTD may have some numerical limitations, and that it must generally be optimized depending on the type of problem one wishes to solve. Nevertheless, the FDTD algorithm is very powerful, which explains why it is so popular in optical research. Today, there are more than a dozen commercial or free FDTD softwares. In the next section, we will present **Meep**, the free software that we used for our FDTD simulations.

1.3.1.2 Meep: Python package for FDTD simulations

Meep is an open source python package that performs FDTD calculations. Originally, it was developed in the Massachusetts Institute of Technology in 2009 [170], programmed in C++, and interfaced in Scheme [171]. In 2017, a Python version of Meep was released. Based on the FDTD method, Meep can be used to address many electromagnetic problems including metasurface design.
The different steps of a Meep script can be summarized as follows:

1. Define the environment (resolution, grid volume, materials, boundary conditions)
2. Define the geometry (structures, substrates)
3. Define the incident field (field type, wavelengths, direction, polarization, ...)
4. Define the simulation parameters (duration)
5. Run the simulation
6. Get the desired physical quantities from the compiled simulation (electric field, magnetic field, refractive indexes, ...)

We provide in the appendix section an example of a Meep script and more details on how to perform a MEEP simulation.
In addition to its efficiency, the fact that Meep is open source is a real asset. Moreover, it is supported by a very active community that is ready to provide help for any problem.

1.3.1.3 Example of a FDTD calculation of a cylindrical metalens

Here we provide an example of a complete FDTD simulation of a cylindrical metalens, composed of silicon nanodiscs and designed to focus a λ = 750 nm light at a distance of 5 mm [4]. The FDTD simulation of this metalens is illustrated in Fig. 1.15(a). The total working volume considered is 1 mm $\times$ 10 µm $\times$ 300 nm, for a discretization step of 20 nm. The illumination is a λ = 750 nm X-polarized planewave. Cylindrical lenses are a type of lenses for which the wavefront at the output of the lens has a cylindrical shape (as opposed to spherical for conventional lenses). We show an illustration of a cylindrical lens in Fig. 1.15(c). In our simulation, the cylindrical symmetry of the lens is achieved by imposing a periodic boundary condition on the Y-axis (see Fig. 1.15(b)).
To characterize the performance of the simulated lens, we obtain the amplitude and phase of the field after the metalens (in the plane Z = +3 µm) and repropagate it into the far field. The

[4] More details on the choice of the nanodiscs as well as more FDTD simulations are provided in the following chapters of this manuscript.

corresponding results are shown in Fig. 1.15(c) where we compare the focusing pattern of the simulated metalens with the focusing pattern of a perfect lens at a distance Z = 5 mm.
We can define the wavefront function $W(x)$ of a perfect cynlindrical lens as follows:

$$W(x) = \sqrt{f^2 - x^2} + f \tag{1.27}$$

where f is the focal distance of the lens.
As we can see in Fig. 1.15(c), the agreement between the Meep and ideal focusing patterns is almost perfect. The Strehl ratio of the metalens is evaluated at 98%, which confirms the very good agreement.

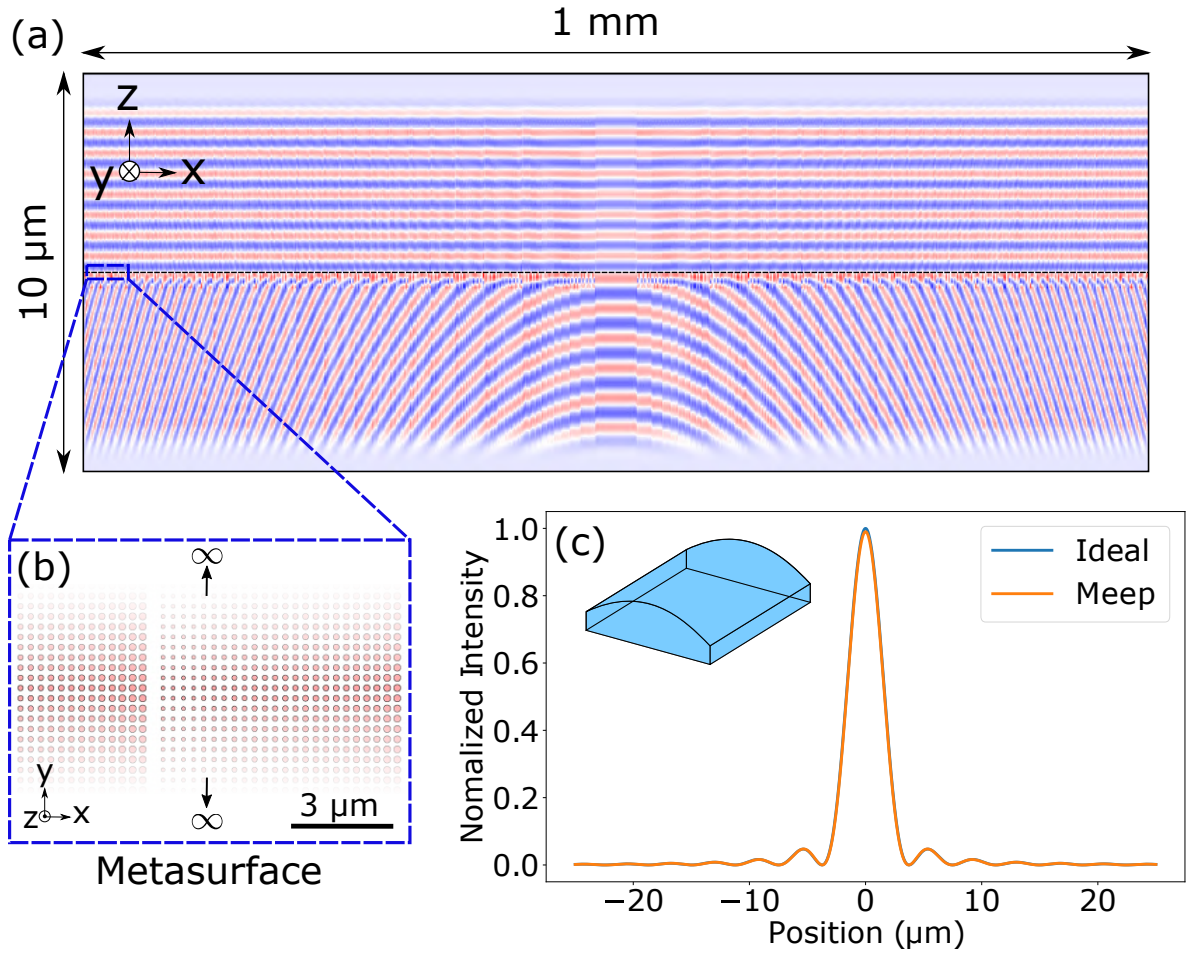

Figure 1.15: FDTD simulation of a cylindrical lens of 1 mm × 10 µm × 300 nm with Meep. In (a) is represented the amplitude of the electric field component E_x at the end of the simulation. A zoom on the metasurface is shown in (b) where we can see a top view of its nanostructures (with infinite and periodic conditions on the Y axis). (c) Far field intensity along the X axis of the metalens and a perfect lens at the focal distance f = 5000 µm.

Conclusion

In this chapter, we introduced the field of metasurfaces. We have seen that the latter inherits from various fields and concepts (plasmonics, Fresnel lenses, diffraction gratings, ...). We have also described how fast the field of research on metasurfaces evolved as well as the very strong potential of metasurfaces for future applications.
Then, we studied the physical properties of metasurfaces. For this purpose, we presented a first simulation tool based on the GDM, as well as its toolkit pyGDM, which proved to be very efficient to simulate the optical responses of isolated nanostructures. Next, with the objective of simulating the response of a large number of nanostructures, we have introduced and studied the dipole and quadrupole approximations. First, we showed that these approximations were efficient to recover the optical response of isolated nanostructures.
In a second step, to perform efficient simulations of metasurfaces, we presented the FDTD method. We then introduced the MEEP package as a FDTD toolkit, and provided an example of a FDTD simulation of a 1 mm cylindrical metalens.
Despite its strong advantage to simulate large structures, performing the simulation of entire metasurfaces via FDTD is too time consuming and does not constitute a good strategy. Thus, the use of FDTD for the design of metasurfaces generally relies on the simulation of infinite and periodic systems. In the next chapter, we will explain how to use the FDTD to design metasurfaces. We will also present the manufacturing process and the tools that are useful to characterize metasurfaces.

2 Conception and fabrication of optical metasurfaces

In this second chapter, we describe the different steps involved in the fabrication of a metasurface. The first section describes the design of a metasurface, presenting the simulation tools as well as the important parameters to be considered to maximize its efficiency. The second section focuses on the fabrication process where we also present the important factors that need to be optimized. Finally, the third section discusses the characterization tools that are used throughout the fabrication process.

2.1 Conception of a metasurface

Designing a metasurface requires to be able to predict the optical response of its nanostructures inside its environment (*i.e.* surrounded by other nanostructures). Indeed, we have seen in the previous chapter that the coupling effects that occur between nanostructures can strongly modify their optical responses. We present here a design strategy that allows to consider the coupling effects, inspired by several research papers: [23, 172, 173].

2.1.1 Simulation approach

2.1.1.1 Periodic and infinite systems approximation

For nanostructures of high refractive index (*e.g.* silicon) surrounded by a low index environment, it has been demonstrated that light is concentrated inside the nanostructures. This phenomenon is increased with high aspect ratio nanostructures. Their optical response inside a metasurface will therefore not vary much if we slightly modify the geometries of the neighboring structures [23, 174]. For a metasurface made of similar nanostrucuctures (such as nanodiscs of varying diameters), we can therefore approximate the response of a nanodisc by that of the same nanodisc surrounded by exactly identical ones. In the case of periodic metasurfaces, for which the structures are positioned on a 2D periodic grid, it means that we can consider periodic and infinite metasurfaces, composed of perfectly identical nanostructures. This approximation is very useful, because the simulation of an infinite and periodic metasurface is very easy using the FDTD method. Indeed, it only requires to create a unit cell of size $p \times p \times L$ (where p is the periodicity, and L is the length of the Z axis for the propagation of light), and add periodic boundary conditions in the X and Y directions. In the following, we will then consider periodic metasurfaces.

2.1.1.2 FDTD Simulation

Now that we know how to approximate the optical response of each nanostructure in its environment within the metasurface, we can begin the design process. The latter consists into

defining which configurations (*e.g.* geometries of nanostructures) will compose the metasurfaces. Since we want to fabricate metasurfaces for wavefront shaping, we calculate for these configurations the induced phase shifts and transmissions.
To do this, we define after the metasurface an output plane (Ox, Oy), outside the near field region, where we compute the electric field for two situations. First, we compute $E_{out,substrate}$, the output electric field without nanostructures (only the substrate). Second, we compute $E_{out,substrate+struct}$, the output electric field taking into account the nanostructure contribution. The phase shift Φ and transmission T induced by a nanostructure are then obtained as follows:

$$T = \left| \frac{E_{out,subtrate+struct}}{E_{out,subtrate}} \right| \tag{2.1}$$

$$\Phi = \arg\left(\frac{E_{out,subtrate+struct}}{E_{out,subtrate}} \right) \tag{2.2}$$

2.1.2 Selection of the geometries

We use the results of this simulation method to choose the configurations used in the metasurface. In order to design highly efficient wavefront shaping metasurfaces, the set of selected configurations must span phase shifts from 0 to 2π while maintaining the highest overall transmission.

Create a dataset

Since metasurfaces are typically fabricated by top-down etching (see next section), the refractive indices, heights, and environments must be identical for all structures. Furthermore, since we are considering periodic metasurfaces, we must keep the same cell-size p for all configurations. Thus, the only remaining parameter that can vary from one structure to another, and that allows to cover the 2π phase shift, is related to the lateral geometry. In the following, we will illustrate a design strategy using silicon nanodiscs. The lateral geometry parameter is therefore the diameter D of the nanodiscs.

Fix the height As we have seen in chapter 1, increasing the height of the nanostructures allows to support higher multipole orders. For magnetic dipole resonance, the electric field vortex corresponds to a phase delay of $\lambda/2$ accumulated by the light passing through the nanostructure (*i.e.* a thickness of $\lambda/2n_s$). Following the same logic, the quadrupole magnetic resonance (two vortices), requires a thickness of at least $2\lambda/2n_s$, and the octupole resonance (three vortices), requires a thickness of $3\lambda/2n_s$, and so on. Looking at the literature, we know that having higher multipole resonances (high aspect ratio nanostructures) increases the efficiency of metasurfaces [79]. Therefore, we aim a using heights greater than or close to $3\lambda/2n_s$, with an upper limit imposed by the increasing constraints of the fabrication as the aspect ratio of the structures increases.
For silicon nanostructures @750 nm ($n_s = 3.7$), this means that we consider heights greater than or close to $H = 300$ nm.

Choose the cell-size and diameter ranges In order to optimize the efficiency, the cell size of the metasurface is limited by the diffraction and must be smaller than $\lambda/2$ [2]. This limit on

the cell size also restricts the possible range of diameters, which are also constrained by the fabrication process (more details after).

2.1.2.1 Transmission and phase-shifts maps

For our first set of simulations, we therefore opted for silicon nanodiscs of height $H = 350$ nm, refractive indexes taken from literature [175], and cell sizes ranging from p = 250 nm to p = 350 nm. The diameters were taken as a fraction of the cell size so that $0.3 \leq \frac{D}{p} \leq 0.8$. As we wanted the metasurface to operate in transmission, we chose a quartz substrate [24, 25]. In Fig. 2.1(a-b), we show the phase shifts and transmissions associated with this dataset. In this figure, each pixel represents the simulation of an entire metasurface, fully periodic and infinite, with periodicity factor (or cell size) p, and composed of perfectly identical nanodiscs of diameter D (see Fig. 2.1(c)). To simulate these metasurfaces, we defined unit cells of size $p \times p \times L$, for which we applied a periodic boundary conditions on the X and Y axis. For the Z axis, however, as we want to avoid any periodicity, we defined Perfect Matched Layers (PML) to absorb the light at each extremity. The upper volume ($Z > 0$) of the unit cell is made of quartz (refractive index $n = 1.45$), the lower volume is vacuum. The nanodisc is positioned at the interface $Z = 0$ (see Fig. 2.1(c)). The resolution step is 10 nm, chosen after ensuring that the results have converged. The illumination is an X-polarized plane wave at $\lambda = 750$ nm, defined in the quartz substrate, propagating towards $Z < 0$. The fact that the illumination originates from the quartz substrate allows to simulate the influence of the latter at the interface on which the metasurface is located. However, this also implies that the Fresnel reflection arising from the second air/glass interface is not taken into account. Considering it would decrease the calculated transmissions by about 4%. Looking at these maps, we see that there are several cell sizes ($p \geq 290$ nm) for which a variation of the diameter allows to cover the 2π phase shift range while maintaining high transmissions.

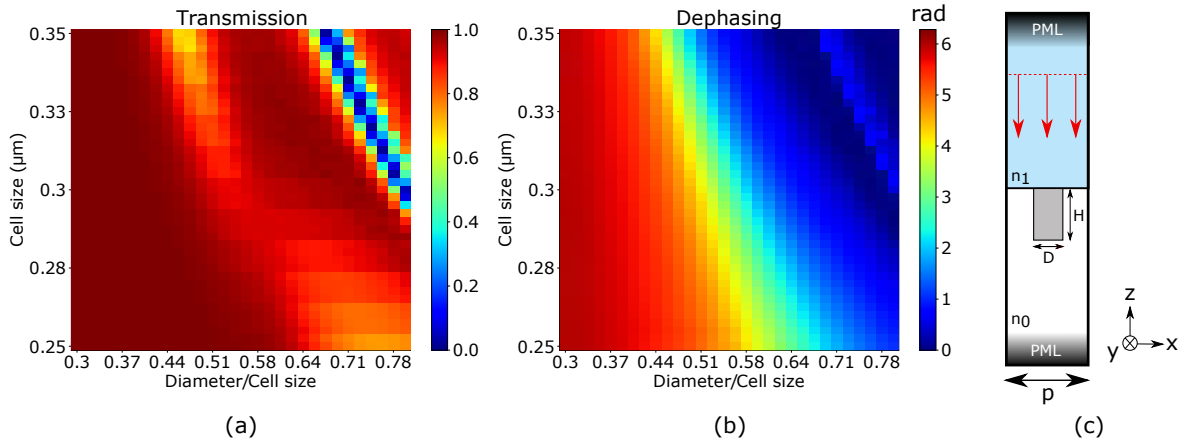

Figure 2.1: (a) Transmission and (b) phase-shift maps associated to different nanodiscs of height $H = 350$ nm, for varying diameters D and cell-sizes p. (c) Illustration of the environment of the FDTD simulation for one configuration.

2.1.2.2 Optimization of the dataset

Therefore, we can now perform the preliminary step of fabrication, which is to produce the wafer from which the metasurfaces will be made. The optimization strategy discussed here consists in measuring some parameters that can then be taken into account to create a new dataset, closer to what will be fabricated.

Height For example, the thickness of the silicon layer deposited by CVD techniques (see next section), which is also equal to the height of the nanocylinders, often differs from the initial target value.
In our case, we deposited a silicon layer with a thickness of $H = 350$ nm. Then, we characterized its real thickness by ellipsometric measurements, which gave a measured value of $H = 370$ nm.

Refractive Index The same is true for the refractive index of the simulated nanostructures, which can also be obtained by ellipsometry. However, one must be careful about the accuracy of the measurement tools when dealing with sub-wavelength thicknesses [176]. For example, our characterization of the refractive index proved to be very inaccurate for its imaginary part. Indeed, we performed two measurements for two different thicknesses and we obtained values of $n_i = 0.043$ and $n_i = 0.034$ for thicknesses of 246 nm and 374 nm respectively. On the other hand, the real part measured showed a very good reproducibility ($n_r = 3.639$ for both thicknesses).

Cell size After making these measurements, we simulated a new dataset by applying corrections to the height and refractive index values. Nevertheless, as the measurement of n_i was very inaccurate, we decided to stay with its theoretical value. The new transmission and phase shift maps are shown in Figure 2.3. Now that the simulation data set is optimized, the only remaining step is to select the cell size.
Since we want to cover the range from 0 to 2π with high transmissions, we can eliminate any cell size $p < 290$ nm. In order to further narrow down the selection, we need to take into account the fabrication limits. First of all, we have to consider the spatial resolution of the machine used for fabrication. Typically, for a chosen cell size, it is necessary to meet the following condition:

$$\delta\Phi_{aim} > \delta R_{fab} \cdot \frac{\partial \Phi}{\partial r} \tag{2.3}$$

Where $\delta\Phi_{aim}$ is the phase shift resolution we desire, δR_{fab} is the spatial resolution limit of the fabrication tools, and r is the size parameter of the geometry (*e.g.* the diameter for nanodiscs). For example, our metasurface fabrications were performed by electron beam lithography (EBL) with a resolution on the nanostructure size close to 5 nm (see the next section for more details). This means that if we want to achieve a resolution on the phase better than $\frac{\pi}{5}$, we have to verify $\frac{\partial \Phi}{\partial r} < 0,12$ rad.nm^{-1}. Typically, we should aim at a cell size allowing to reach the best possible resolution $\frac{\partial \Phi}{\partial r}$.
This resolution limit can also impact the smallest geometry that we can fabricate. In Fig. 2.2(a), we show an example of a nanodisc fabricated by EBL, which is too small in size compared to

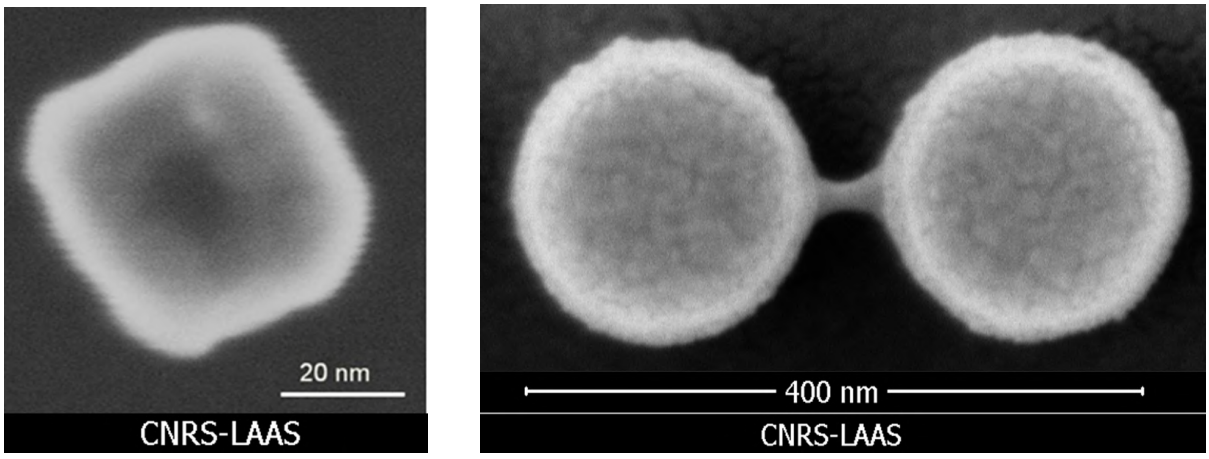

(a) (b)

Figure 2.2: SEM images of two defects examples that occur when manufacturing metasurfaces. (a) Example of a fabrication by EBL of a nanodisc whose size was too close to the resolution limit [177]. (b) Example of the bridging effect linking two nanodiscs with an edge-to-edge distance too small.

the resolution. As we can see, the expected circular shape is completely distorted. As another limit to the minimum size of nanostructures, we can also mention the fact that the thinner a structure is, the more fragile and difficult it is to fabricate.
Finally, there is also a limit in terms of the largest geometry we can fabricate. This is due to the reduction of the edge-to-edge distance between neighboring structures as their respective sizes increase. A consequence of this phenomenon is illustrated in Fig. 2.2, for an EBL fabrication, where we can see a bridge connecting two neighboring structures. This defect is caused by proximity effects and is related to the EBL isolation process (more details in the next section). Since it causes two neighboring structures to merge, this defect can lead to significant changes in optical responses. It is therefore crucial to avoid it as much as possible. In this respect, it may be advantageous to consider the absence of nanostructure as a configuration showing perfect transmission and a phase shift of 0 rad.
To finish, looking at Fig. 2.3, and considering all these factors (optimizing transmission, optimizing phase shift resolution, avoiding very small and very large structures, using no structure as a configuration), we selected the cell size $p = \mathbf{300\ nm}$. This cell size allows us to have a phase shift resolution of $\frac{\pi}{5}$ for a global average transmission of $T_{mean} = 95\%$.

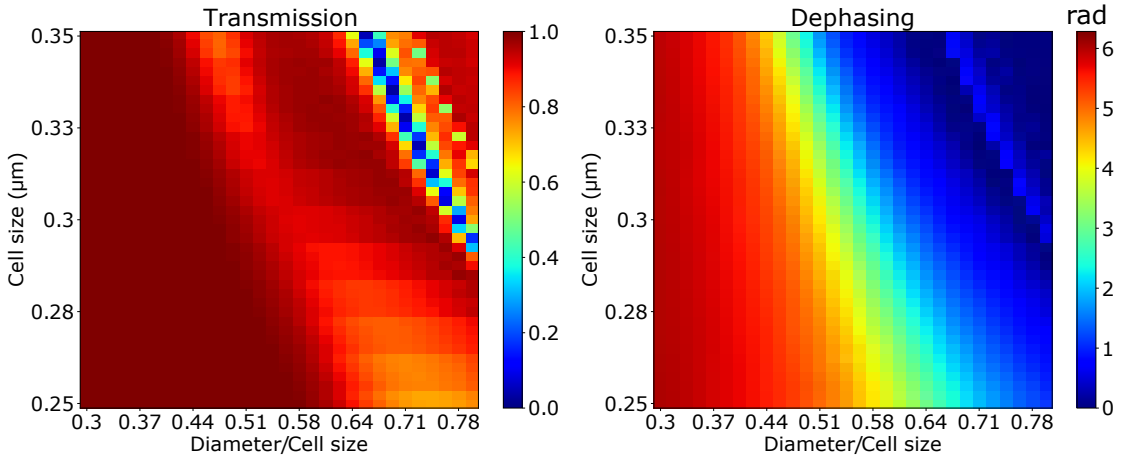

Figure 2.3: (a) Transmission and (b) phase-shift maps associated to different nanodiscs of height $H = 370$ nm, for varying diameters D and cell-sizes p.

2.1.2.3 Summary of the selection steps

To summarize, the selection steps are as follows:

- Find a range of parameters where the configurations are sufficient to cover the $0 - 2\pi$ phase shift range while maintaining high transmission;
- Fabricate the wafer used for the metasurface fabrications;
- Measure the thickness and the refractive index;
- Make a new dataset using the measured values that are enough accurate;
- Identify the fabrication spatial resolution limit;
- Set limits on geometry sizes to avoid strong proximity effects and deformations;
- Find a cell size where the phase-shift variation with geometry is optimized following Eq. (2.3);
- Identify the cell size that gives the best compromise respecting the previous conditions and allowing coverage of $0 - 2\pi$ phase shift range with high transmission;
- If there are still multiple cell sizes available, choose the one with the highest overall transmission.

2.1.3 Creation of a mask for fabrication

To fabricate a metasurface, the fabrication machine software usually requires the use of a GDS file. The .gds format is a specific type of file that will directly contain information about the geometry of the metasurface. To create this file, we need to define a 2D array of geometries

and a 2D array of corresponding positions. In the case of a periodic metasurface, we have for the positions array a 2D square grid of period p.
Thanks to the infinite and periodic approximation, it is possible to associate to each nanostructure a complex amplitude, using the previously chosen dataset. As we want the metasurface to have the highest possible transmission, and as we have chosen our data set according to this condition, we only need to consider the phase shifts. In Fig. 2.4, we show the function ϕ that relates the diameter of the previously chosen nanodiscs to their induced phase shifts. This function is obtained by interpolation of the data of Fig. 2.3, for cell size p = 300 nm.
As it is continuous and strictly decreasing, it is possible to invert this function to define a new one, ϕ^{-1}, associating to any phase shift between 0 and 2π a diameter. We also add to this function the particular case of an absence of structure ($\phi^{-1}(D = 0) = 0$).

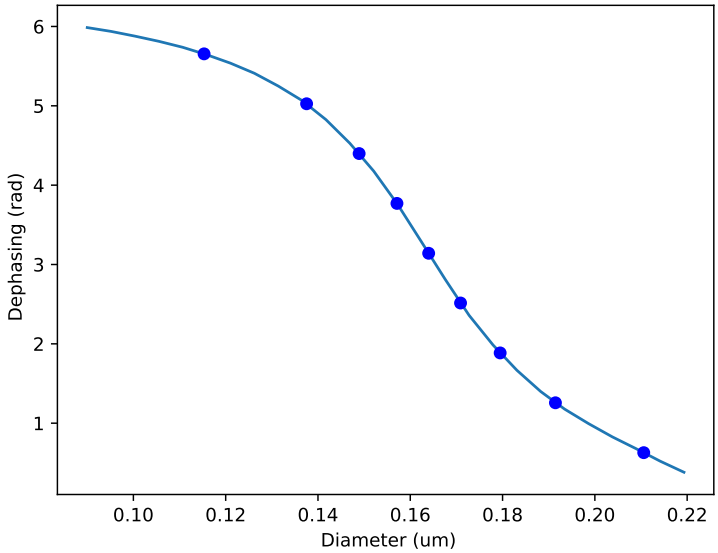

Figure 2.4: Function relating the nanodisc diameter to the corresponding induced phase shifts. This function was calculated from the data of the map shown in Fig. 2.3

The next step is to generate the 2D phase shift array of the metasurface, for which each pixel must be associated to a nanostructure. As an example, we show on figure 2.5(a) the 2D matrix associated to a metalens (metasurface behaving as a lens) of size 500×500 µm^2, where each pixel of indices (i, j) represents the local phase shift at position $(x_i = ip, y_j = jp)$, in an area of 300×300 nm^2. Once this 2D phase shift array is complete, it can be converted to a design using the ϕ^{-1} function.
However, while a direct application of ϕ^{-1} might work, it can also lead to errors related to fabrication accuracy. Indeed, the 2D array we currently have does not necessarily match the best phase shift resolution that we can obtain according to Eq. 2.3. A direct application of ϕ^{-1} could lead us to try to fabricate nanostructures differentiated by less than the fabrication resolution, which may therefore add some uncertainties to their final shapes. Thus, to ensure good agreement between the fabricated and simulated geometries, we first fix a finite number of possible configurations that will compose the metasurface. Likewise, before using the conversion function, the 2D phase shift network must also be discretized so that each pixel can be assimilated, by its position and its phase shift, to one of the chosen configurations.

To follow the example of the metalens design, we also highlight in Fig. 2.4 the selected configurations used to design our metasurface. The objective is to induce a phase shift of $k\frac{\pi}{5}$, with $k \in [|0; 9|]$. We thus consider 10 configurations including 9 diameters and one absence of structure. Similarly, we show in Fig. 2.5(b) the 2D phase array of Fig. 2.5(a) which has been discretized into multiples of $\frac{\pi}{5}$.
At last, we can now apply the ϕ^{-1} function to get the 2D configuration array. To generate the GDS file, we can then use the python module *gdspy*[1], as well as the software *KLayout* to help with visualization. We show in Fig. 2.5(c) the GDS file corresponding to the designed metalens.

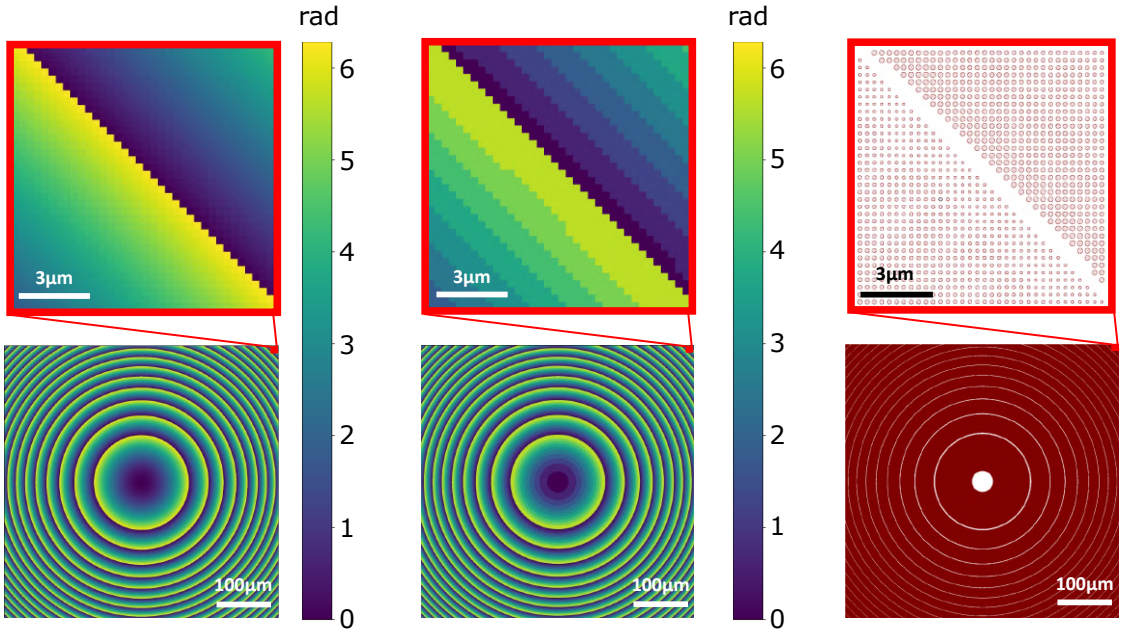

(a) Continuous 2D phase array (b) Discretized 2D phase array (c) Design mask GDS file

Figure 2.5: Illustration of the different steps involved when converting a phase array to its corresponding GDS configuration mask. In (a) is represented the 2D phase shift function of a metalens whose focal length is 500 µm and dimension is 500×500 µm^2 . This function is converted into the 2D phase shift table shown in (b) where all phase shift values are multiples of $\frac{\pi}{5}$. Finally, the corresponding GDS mask is shown in (c). For all the figures, we show a zoom of their upper right corner.

[1] An example of a script to generate a GDS file with *gdspy* is given in appendix.

2.2 Fabrication of a metasurface

In this section we present the different steps of fabrication of a metasurface. At first, we focus on the nanostructuration techniques such as lithography, used to transfer the design of the metasurface to the sample. Then, we provide a guideline for the selection of the resist used for Electron Beam Lithography by justifying our choice for our fabrication process. Finally, we describe the fabrication process used to fabricate metasurfaces. This process starts with the preparation of the sample (material deposition, cleaning, resist deposition), followed by the lithography, and finally with the etching. As an example, we address the process of fabrication used in our paper [28], illustrated in Fig. 2.6.

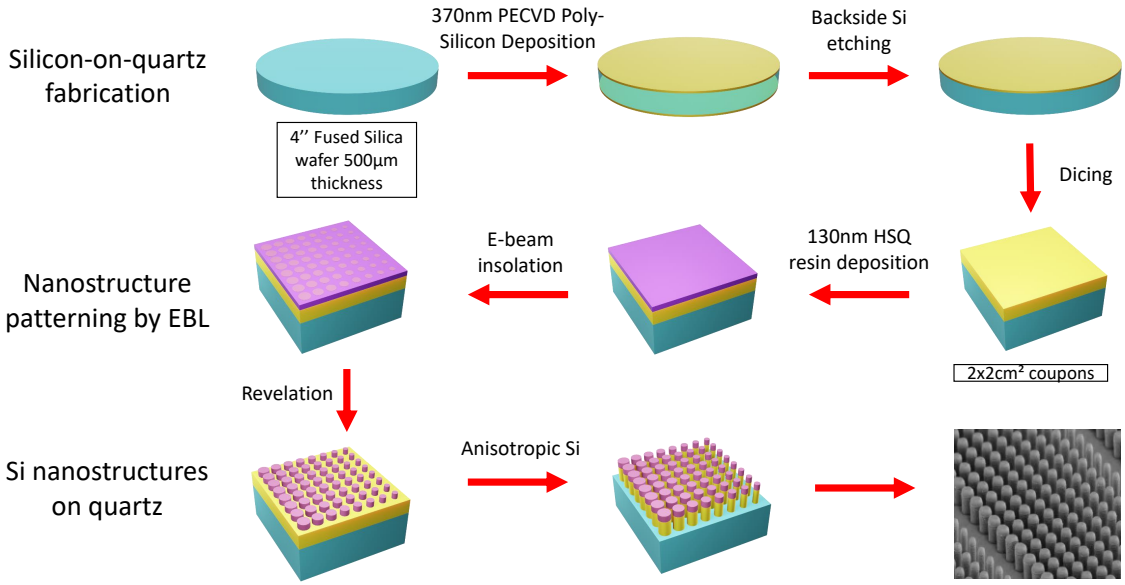

Figure 2.6: All steps of the fabrication process of a metasurface.

2.2.1 Nanostructuration

Nanostructuration refers to the transfer of a mask pattern onto a sample (most often to a resist layer). Several different techniques have been developed in the recent years [178]. Among them, we find direct lithography techniques (like electron beam lithography [63, 179], focused-ion lithography [180]), and pattern-transfer lithography techniques (like deep-UV lithography [139–141, 181], nano-imprint lithography [144]). The fabrication method we will focus on in this manuscript is the Electron Beam Lithography (EBL).

2.2.1.1 Electron Beam Lithography

EBL is a lithography technique where a focused beam of electrons is used to draw a predefined shape on a sample covered by a electron-sensitive film resist, allowing to transfer the drawn shape on the sample. It works very similarly to Scanning Electron Microscopes (see next section), whereas here the electron gun is used to draw the mask onto the sample. Since it uses electrons, it also gives access to very high resolutions (few nanometers). This explains

why it is very suitable for the fabrication of nanostructures for metasurfaces [179, 182–184]. EBL is usually characterized by four main parameters. First there is the energy exposure, or voltage, that relates to the energy of the electron beam, often found in the range between 10 keV to 100 keV depending on the EBL writer used [185, 186]. With the energy exposure, the exposure time also varies. At higher energy, the electrons go deeper into the substrate, which also requires more time.
Next we find the beam current, the dose factor and the grid resolution. The beam current (expressed in pA or nA) is the number of electrons per time unit. The dose factor (expressed in $\mu C/Cm^2$) is, on the other hand, the number of electrons per surface unit. Increasing the dose factor, or reducing the beam current, increases the time the beam has to stay at the same position. The grid resolution is finally the physical grid defining each point where the electron beam is focused. A better resolution involves more points and therefore a longer fabrication time.
Depending on the desired resolution, one has to perform several tests in order to correctly select the values of these three parameters. These tests consist in several exposures with varying parameters. As an example, we performed dose tests for fabricated nanodiscs with varying diameters and dose factors. The characterization of the structures were carried out using Scanning Electron Microscopy.

2.2.1.2 EBL Limits

Although offering high resolution for the structuration of metasurfaces, EBL appears quite limited in some situations.

Resolution, Surface, Time and Cost Because the electron beam is focused for each point of the mask transferred to the resist, the fabrication time is proportional to the exposed surface, and so does the exposition cost. Moreover, although increasing the size of the focused electron beam can reduce the exposure time, it also lowers the resolution. The same compromise comes using resists of higher sensitivity, that usually give access to smaller exposure times (by reducing the dose factor), but at the cost of lower resolutions. More details about the resists properties are given in the following subsection.
Due to these limits, EBL becomes a matter of optimization between the resolution, exposed surface, and exposure time (i.e. cost). Usually, the size of metasurfaces fabricated in the literature ranges between hundreds of micrometers to a few centimeters.

Field Stitching For big surfaces, the electron beam being tilted at large angles can induce distortion effects. The entire surface is therefore divided into small areas more suitable for a high precision exposition. For example, when we fabricated our metasurfaces of total size 500 $\times$ 500 μm^2 and 1 mm^2, we divided them into several 69 $\times$ 69 = 4761 μm^2 working areas. To go from one working area to the other, the stage was shifted mechanically by a distance of 69 μm. Unfortunately, the stage motor does not have a nanoscale mechanical precision, causing what is called *field stitching* errors. SEM images of field stitching errors extracted from our fabrications are shown in Fig. 2.7, where we can clearly identify four different regions shifted in position with respect to the others. From these images, we estimated the field stitching error to be approximately 70 nm.

Proximity effects Finally, during the electron exposure, the point of impact of the beam also induces a low exposure area of some micrometer of diameter due to the scattering of electrons in the substrate. This additional exposure becomes significant for two exposed regions separated by a narrow gap and may induce an additional resist fraction remaining after the development. This effect is called the *proximity effect*, and is one of the principle limitations of the resolution limit for EBL [182, 187, 188]. Notably, we saw in Fig. 2.2 the influence of proximity effects with the formation of bridges between two nanodiscs that are too close. For EBL with higher voltages, the electrons penetrate deeper into the substrate, reducing the low exposure area and thus the proximity effects, but this improvement demands an increased exposure time [189].

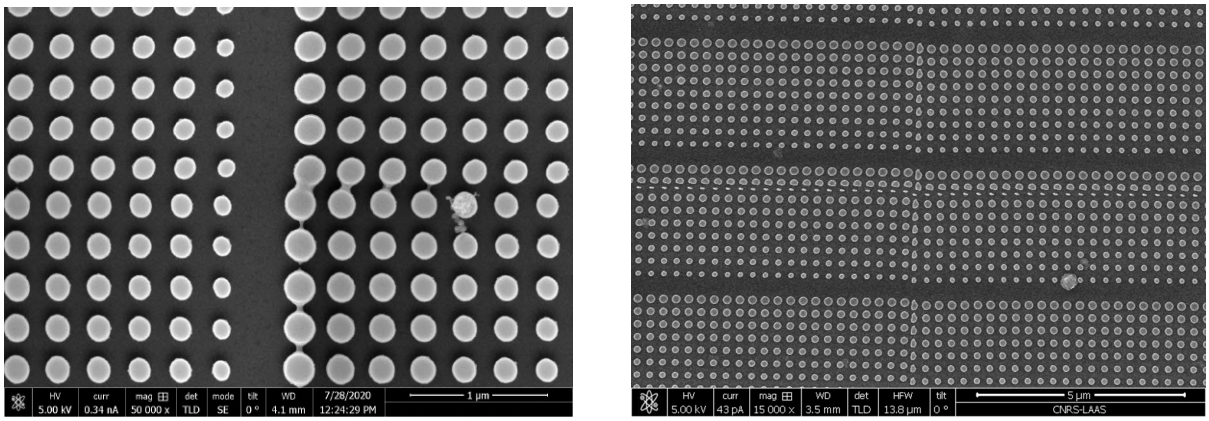

(a) (b)

Figure 2.7: SEM images showing the impact of field stitching error. In (a) the writing field separation was between two structures, whereas in (b) the separation was cutting through the structures.

2.2.2 Resist properties and choice

The choice of the resist for the EBL is one of the most important factor. Here, we provide a description of the resist properties, then give the reason of the choice of the hydrogen silsesquioxane (HSQ) resist used for our fabrications.

Positive and Negative resists

Two different types of resists exist. They are defined by their polarities (negative and positive), and have opposite behavior regarding the resist development step. Negative resists will have the exposed zones remaining after resist development while positive resists will have them removed [185, 190]. Depending on the type of metasurface one wants to fabricate, the choice of a negative or positive resist is usually made to minimize the total surface to expose (i.e. minimize exposition time and cost).

Sensitivity and Contrast

Sensitivity For each resist, two main parameters are always defined, and will influence the EBL resolution. These parameters are the sensitivity and the contrast.

The sensitivity is expressed in Coulomb per unit of surface ($\mu C/cm^2$) and is related to the minimum exposure inducing the necessary chemical action to change the resist structure [186]. Each resist has its own sensitivity to electrons depending on its chemical structure. The higher the sensitivity, the shorter the exposure time required to achieve the same exposed surface. A weak sensitivity allows to reach high resolutions, but requires higher doses (i.e. higher exposure time) [191].

Contrast During the development, there is a threshold exposure from which the resists starts to remain. Above this threshold, the final resist thickness starts to increase rapidly before slowing when getting close to the maximum value. What is called the contrast is the slope of the first thickness increase. Typically, a strong contrast gives access to better defined geometries, as the difference of dose exposition between a non remaining and a totally remaining exposed area is very weak.
In order to enhance the fabrication precision, one should select a resist having a high contrast and a low sensitivity.

Selectivity

As we will show in the following subsection, the selectivity parameter, associated to the etching process, has a strong influence on the final shape of the nanostructures. Optimizing the anisotropy of the etching requires to have a high selectivity. Therefore, in addition to the other described properties, one also needs to look at the selectivity that the resist has regarding the material to etch.

Choice of HSQ

HSQ is a negative resist which, under no exposure, is based on a cage like structure of formula $(HSiO_{3/2})n$. Under electron exposure, the cage-like monomer evolves into a network-like polymer structure, with the Si-H bonds disapearing and Si-O-Si bonds being formed [177, 192]. The exposed HSQ chemical structure then approaches the structure of silicon dioxide, which gives exposed HSQ a very high selectivity for silicon etching. Moreover, HSQ resist has a low sensitivity and high contrast. These typical properties are the reasons of the choice of HSQ for high precision nanofabrication [177].

2.2.3 Fabrication process

We describe here the different steps of the fabrication of a metasurface, following the steps illustrated in Fig. 2.6.

Material Deposition

The process starts with preparation of the substrate (*e.g.* silicon for our process). The deposition is usually performed by Chemical Vapor Deposition (CVD) techniques [193]. During a CVD, the chemical element to be deposited is contained in a gas, heated or/and lowered in pressure, and put in a vacuum chamber with a cold substrate. This chemical element is then aggregating onto the surface of the substrate, similarly as water is condensing on a cold surface during hot days.

We relied on the high resolution and uniformity offered by LPCVD (Low Pressure CVD) for our deposition. The crystallinity of the deposited Silicon (amorphous, poly-crytalline or mono-crystalline) depends on the temperature and pressure during CVD. The optical properties of poly-Si and mono-Si are very close for the NIR range targeted in our project, the main difference being the high cost of mono-Si compared to poly-Si.
Therefore, we deposit a 370 nm poly-Si layer on a 4" quartz wafer through LPCVD, at a temperature of T = 605°C and at a pressure of 240 mTorr (E. Imbernon, LAAS-CNRS). The thickness and the refractive index of the deposited layer were characterized by ellipsometry (E. Scheid, LAAS-CNRS). Then, the back side was selectively etched by plasma etching (A. Lecestre, N. Mallet, LAAS-CNRS). At last, the wafer was diced down to 2 cm $\times$ 2 cm chips (G. Ardit, LAAS-CNRS).

Cleaning

The cleaning of the sample is necessary to prevent dust from disturbing the resist deposition. First, the sample is rinsed with acetone and distilled water. The sample is then dried at 100°C for 2 minutes using a hot plate. Finally, we perform a plasma O_2 exposition to ensure a perfect cleaning.

Resist preparation and deposition

Before starting the EBL process, the resist needs to be applied on the sample. The control on the thickness of the resist layer will also influence the outcome of the fabrication. Indeed, thin resist layers reduce proximity effects (and thus increase the resolution), but they reduce the protection during etching which can possibly induce a deterioration of the etching anisotropy (more details in the following) [194]. We used HSQ resist, diluted in methyl isobutyl ketone (MIBK). The final thickness of the resist layer depends on the dilution ratio between HSQ and MIBK. In our case, for a 130 nm thickness, we had two doses of MIBK for one dose of HSQ.
The deposition is then performed by spin coating using a rotating plate with a maximum speed of 5000 revolutions per minute for one minute, ensuring a homogeneous HSQ application onto the sample. The number of revolutions per minute also affects the HSQ layer thickness [195]. Just after the resist application, we heat the sample at 80°C for one minute with a hot plate to evaporate the remaining MIBK and increase the HSQ contrast [196]. We used a low evaporation temperature in order to avoid reticulations of HSQ that occur at high temperatures.

Lithography

We performed the lithography step using a RAITH 150 EBL writer at 30 keV energy exposure with a dose ranging from 855 to 1260 $\mu C/cm^2$ (varying and optimized for each nanodisc). The beam current was equal to 120 pA and the grid resolution of was 10 nm (F. Carcenac, LAAS-CNRS). Due to the optimization performed with the dose tests, we estimate that the final effective resolution on the size of the nanostructures is close to 5 nm.

Development

Once the EBL is achieved, the resist development consists in the separation between the exposed and non-exposed resist areas. The resist development was achieved through the immersion of the sample in Tetramethylammonium hydroxide (TMAH) at 25% for one minute, then

in distilled water for two minutes and finally in methanol for two minutes. The sample was then dried using a soft blow of dry air. Since the surface tension of methanol is lower than that of water, it prevents nanostructures from tearing off [197]. The high concentration of TMAH increases the contrast, by reducing the influence of the EBL proximity effects, at the cost of an increasing initial dose.

Etching

Finally, the developed HSQ pattern is transferred to the Si layer using etching techniques. We provide here a brief description of top-down plasma etching, which is commonly used for nano-fabrications [194, 197–200].
Plasma etching uses an ionized gas to shoot ionized particles on the sample, inducing two different types of etching. The first one is physical, and is related to the impact between the ions and the molecules of the sample. The second one is chemical, and is due to the chemical reactions occurring between the ions and the molecules of the sample. Typically, physical etching will follow the direction of the ions whereas chemical etching will occur uniformly everywhere.
Three quantities characterize the etching process: the etch rate, the selectivity, and the directionality. The etch rate relates to the speed of the engraving, knowing the etch rate is crucial to anticipate how much time an etching process should last. The selectivity is the ratio of the etch rates between the material we want to engrave and the material of the mask. For our process, we needed a high selectivity between the HSQ and the poly-Silicon to ensure that the HSQ mask was efficiently transferred onto the sample. The choice of the chemical element of the gas is very important, as it also influences the selectivity factor. Finally, regarding the directionality of plasma etching, we find different processes including isotropic and anisotropic ones, the latter referring to a perfectly vertical etching, as illustrated in Fig. 2.8.
In our case, we performed an anisotropic plasma etching by ICP-RIE (Alcatel-AMS4200) using fluorine gases (SF6/C4F8/O2), having a selectivity of approximately 40 [199] (A. Lecestre, D. Ba, L. Bouscayrol, LAAS-CNRS).

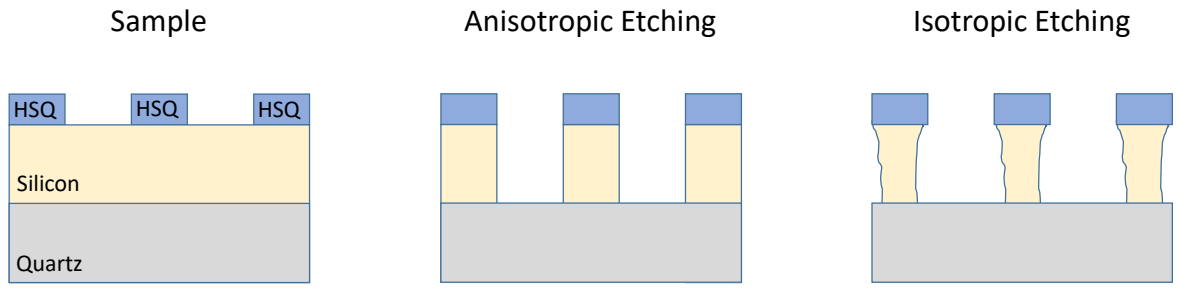

Figure 2.8: Principle of plasma etching. Representation of structures fabricated by perfect anisotropic and isotropic plasma etching techniques.

2.3 Characterization Tools

In this section, we introduce the different characterization tools useful for the design and fabrication of metasurfaces.

2.3.1 Scanning Electron Microscopy

Scanning Electron Microscopy (SEM) is an imaging tool that allows to observe a sample at the nanometer scale with electrons [201, 202]. When a sample is exposed to an electron beam, other electrons are scattered by the sample and collected by a detector. This scattering is highly dependent on the shape and thickness being exposed, allowing SEM images to have a very high resolution of the topology of the sample. One important factor when performing SEM images is to be able to evacuate the incident electrons, otherwise these, stuck on the sample surface, can deflect the scattered electrons due to the electromagnetic force, and alter the image reconstruction. SEM images are by then essentially acquired on conductive substrates, in which electrons are conducted out of the sample. We show examples of images carried out by SEM in Fig. 2.9 (B. Reig, LAAS-CNRS).

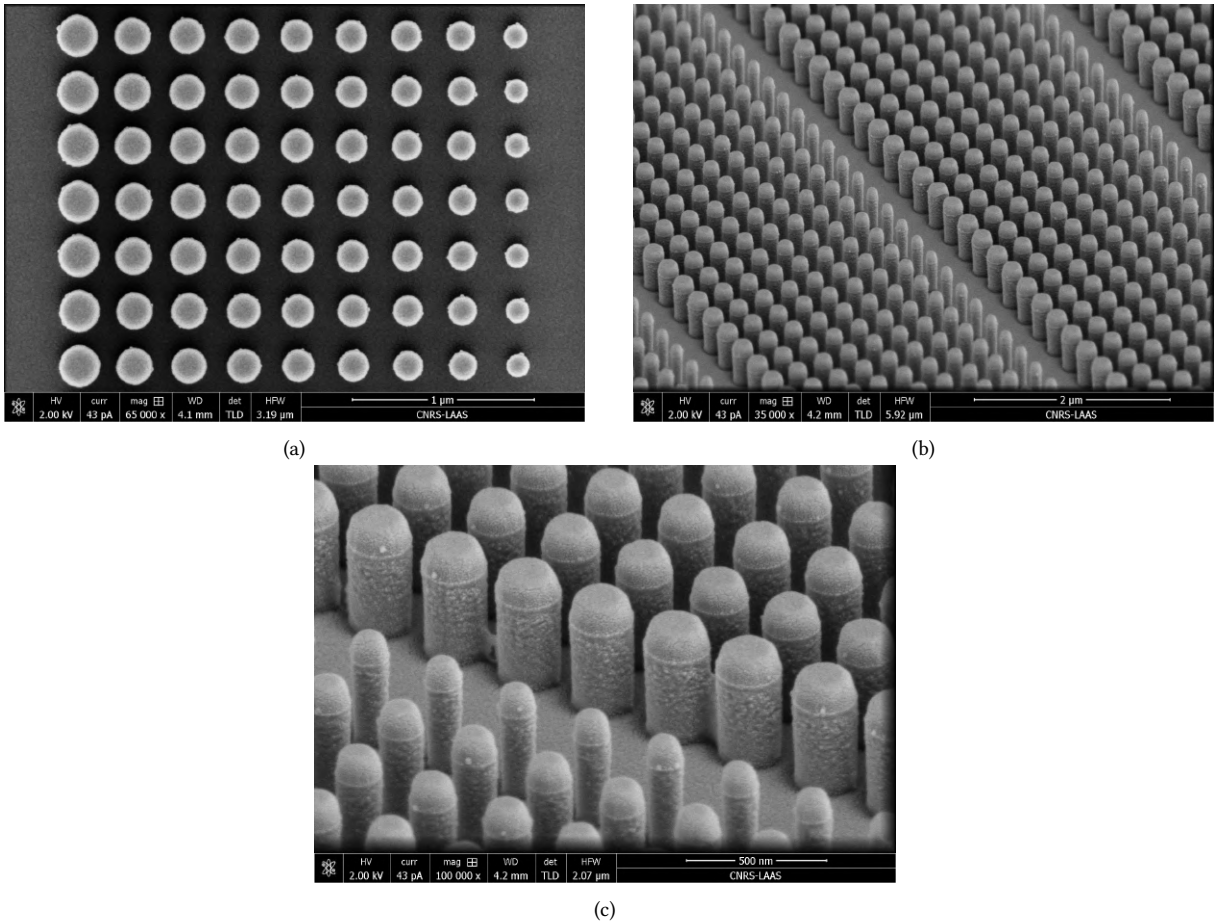

(a) (b)

(c)

Figure 2.9: SEM images of a metadeflector. The images were taken after a deposit of Palladium onto the metasurface to ensure a good conductivity of the electrons. (B. Reig, LAAS-CNRS)

2.3.2 Focused Ion Beam, Transmission Electron Microscope

2.3.2.1 FIB

Focused Ion Beam (FIB) uses ions to prepare a sample for TEM observations [203–205]. We provide in Fig. 2.10 some images of a FIB process with micromanipulation achieved to cut a thin lamella of a metasurface (R. Cours, CEMES-CNRS).
The process starts with the deposition of platinum to protect the zone of interest. Then the cut is made by successively ablating the sample around the zone of interest thanks to the destructive power of the ions. Finally, the lamella is taken away with the micromanipulator, and thinned until reaching a thickness of a few nanometers.

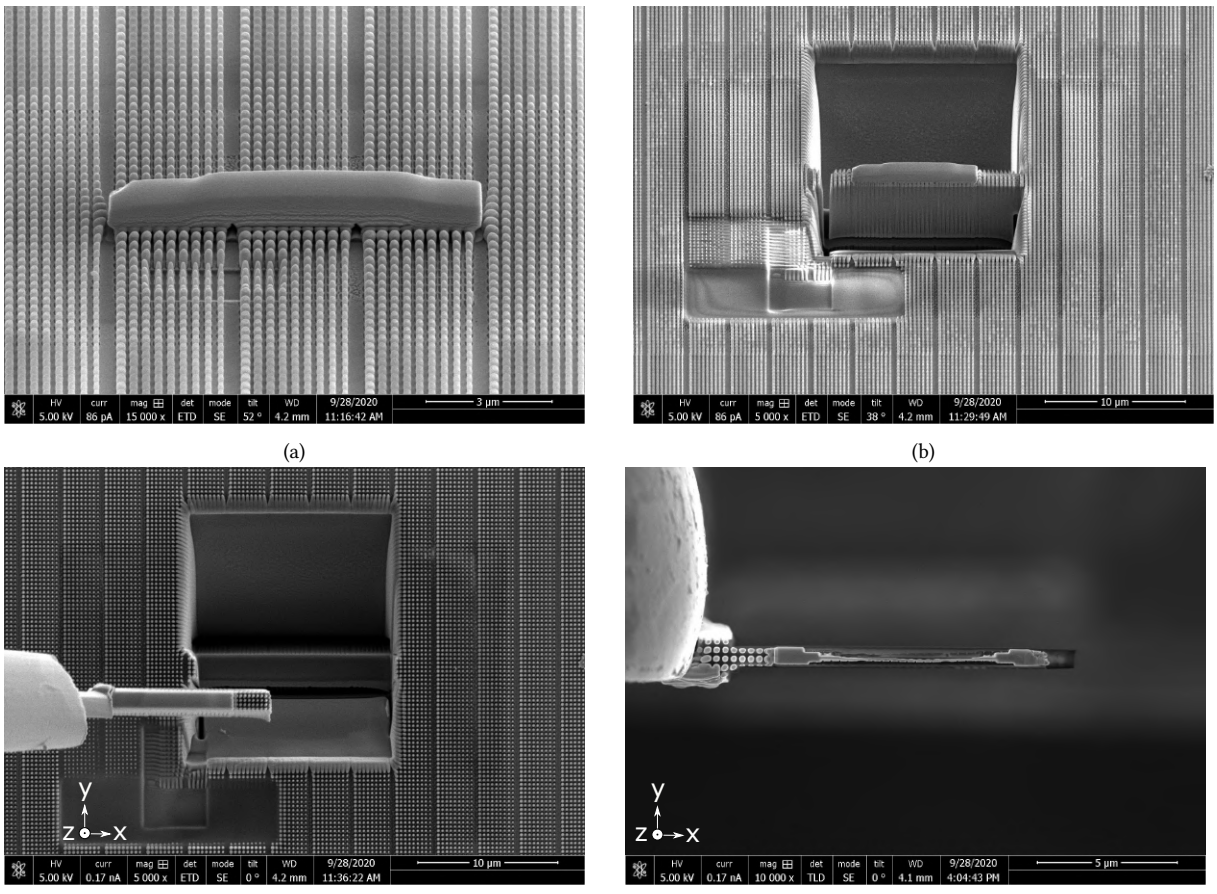

Figure 2.10: FIB sample preparation to extract a fine lamella from the metadeflector. (R. Cours, CEMES-CNRS) (a) Platinum deposit. (b) Cutout of a lamella. (c) Extraction of the lamella from the metasurface. (d) FIB thinning of the lamella. (c) and (d) are images taken from above.

2.3.2.2 TEM

In a Transmission Electron Microscope (TEM) the electrons are passing through the sample and are collected by a detector [206–208]. Usually, the TEM measurements require thin samples to let the electrons go through. These samples can be prepared either mechanically or as

in our case using the FIB. Some TEM observation images of lamella prepared by FIB from a metasurface that we fabricated are shown in Fig. 2.11 (C. Marcelot, CEMES-CNRS).
In addition, it is also possible to analyze the chemical composition of a sample with Energy Dispersive X-ray (EDX) associated to Scanning TEM (STEM-EDX) [202, 209]. In the EDX analysis, X-rays are emitted by the sample due to the electron exposure. The latter are then collected and their analysis gives information about the chemical elements composing the sample. An example of a STEM-EDX analysis in shown in Fig. 3.8 of Chapter 3.

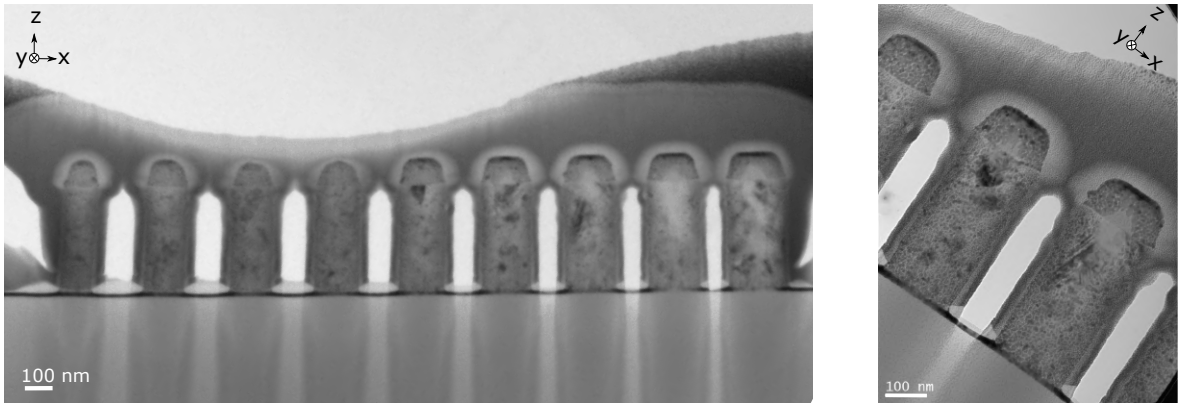

(a) (b)

Figure 2.11: TEM images of a thin lamella of the fabricated metadeflector cut by FIB (see Fig. 2.10). (a) Image of the lamella. (b) Zoomed image of two silicon nanodiscs of the lamella. (C. Marcelot, CEMES-CNRS). The images are taken from the sides. We can identify the silicon nanodiscs with a remaining HSQ cap on a quartz substrate.

2.3.3 AFM

Atomic Force Microscopy (AFM) is a microscopy technique to measure precisely the surface topology of a sample at the atomic scale [210, 211]. A tip, being fixed at the extremity of a cantilever, scans the sample by entering in contact, and is vertically shifted depending on the local thickness scanned. This vertical shift is then measured using a laser reflecting on the top of the cantilever. We show in Fig. 2.12a some AFM images of a metasurface we fabricated, composed of silicon nanodiscs (G. Seine, CEMES-CNRS).

2.3.4 Optical Microscope

During our fabrications, we also used optical microscopy to perform a first inspection of the fabricated metasurfaces. Indeed, each nanostructure of the metasurfaces having different optical resonance properties, we can expect a first glimpse of their optical properties with microscopes. As an example, we show in Fig. 2.12b a bright field image of a fabricated metalens with an optical microscope. We can see that this image is very similar to the simulated metalens phase profile addressed in Fig. 2.5. What is interesting is that we can identify the different regions made of different geometries with the changing colors observed.

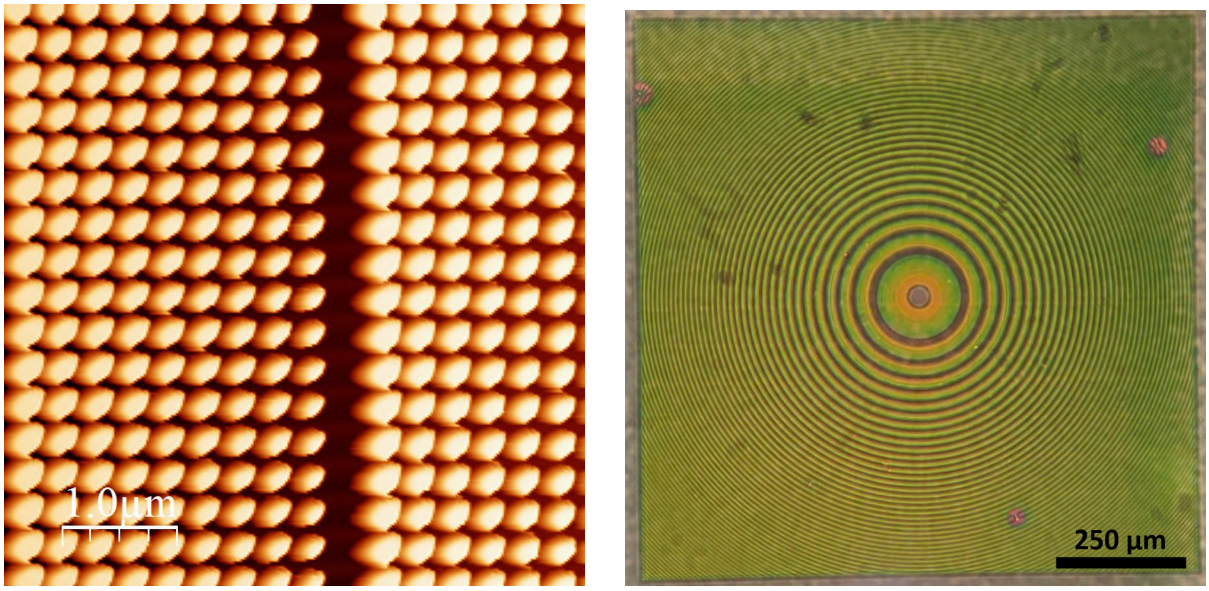

(a) AFM (b) Optical Microscope

Figure 2.12: (a) AFM measurement realized on a fabricated metasurface (G. Seine, CEMES-CNRS, see Fig. 2.9 for SEM images). (b) Bright field image of a fabricated metalens through optical microscope.

Conclusion

In this chapter, we first described a metasurface for which we detailed how to select the configurations to enhance the efficiency, and how to create a GDS mask for the fabrication. Then we presented a fabrication process based on EBL and plasma etching, and gave the main factors to consider (*e.g.* resist choice) to increase the precision of the fabrication. For both parts, we provided examples based on our own designs and fabrications of metasurfaces made of silicon nanodiscs and working at $\lambda = 750$ nm. Finally, we presented the fabrication and characterization tools that were used.
Even though the fabrication tools demonstrate increasing accuracy over the years, nanofabrication discrepancies are often reported in the literature as the origin of alteration of the metasurfaces efficiencies. As the future metasurfaces optical properties will only grow more and more complex, an increasing knowledge and minimization of the nanofabrication errors is required. Following this idea, we provide in the next chapter an analysis of the influence of nanofabrication discrepancies on the efficiency of metasurfaces.

3 Study of metasurfaces optical performance sensitivity to nanofabrication imperfections

In this chapter, we first focus on the optical properties of a simulated and a fabricated metadeflector (metasurface that tilts an incoming light at a specific angle). Then, based on the differences in optical performance between the two cases, and on extensive characterizations of the geometries of the nanostructures by TEM, we investigate the impact of numerous systematic fabrication errors. Finally, we discuss the influence of statistical manufacturing errors on a metadeflector and a metalens. The objective of these studies is to identify the major errors over which it is necessary to have precise control in order to ensure performance close to the expectations of simulations.

3.1 Design, fabrication and characterization of a silicon nanodisc-based metadeflector

In this first section, we describe the conception, fabrication and optical characterization of a metadeflector, working at $\lambda = 750$ nm. As explained in the previous chapter, for simulation and fabrication simplifications, the fabricated metasurface was based on a square and periodic array of nanostructures.

3.1.1 Design and Simulations

Configuration choice

Depending on the intended optical behavior, metasurfaces can be made up of many different types of nanostructures (nanocubes, nanocylinders, elliptical nanocylinders, etc.), and in many types of materials (Silicon, TiO_2, SiO_2, GaN, gold, etc.) [24, 32, 77, 79, 139, 212]. To make a metasurface insensitive to polarization, we choose to use silicon nanocylinders, the efficiency of which has been proven to be very good [18, 25, 27].
First, following the design steps described in chapter 2, we choose from Fig. 2.3 ten configurations to induce phase shifts of $k\frac{\pi}{5}$, with $k \in [|0; 9|]$. The chosen nanostructures are nanocylinders with a height of 370 nm and with the following diameters: 114, 138, 148, 156, 164, 170, 178, 190, 208 nm. The selected cell-size is 300 nm, and the metasurface is placed on a quartz substrate of index n = 1.45. The selected phase shift and transmission configurations are shown in Fig. 3.1. As we can see, they regularly cover the entire range of phase shifts $0 - 2\pi$ with transmissions very close to 1.

Definition of a metadeflector

A metadeflector is a metasurface that tilts an incoming light at a specific angle. Research on metadeflectors is very active in the literature because they serve as a reference base for all metasurfaces [100]. To tilt the incoming light (i.e. the wavefront), a metadeflector must induce a linear phase shift gradient.
The principle of operation of a metadeflector is described in Fig. 3.2. On the left of the figure, we gather several MEEP simulations. Each simulation considers light propagation through an infinite and periodic metasurface composed of identical nanodiscs. The incident light is a plane wave propagating towards -Z and the wavelength is 750 nm. To simulate such metasurface, we first define a computation volume of size $0.3 \times 0.3 \times 10$ μm^3 for X, Y and Z axis, where one nanocylinder is positioned in the center. We then add periodic boundary conditions on X and Y axis. The nanocylinder is put on a glass substrate (Z > 0) of refractive index $n_{glass} = 1.45$, and in vacuum (n = 1, Z < 0).

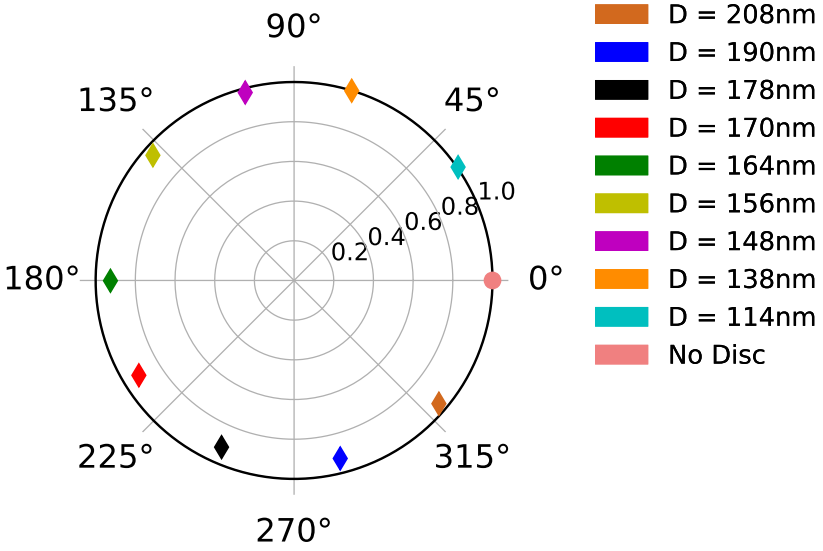

Figure 3.1: Polar representation of the 10 configurations chosen for a metadeflector fabrication. For each configuration, the angle represents the induced phase-shift and the distance to the center is the transmission of the nanodisc array.

By correctly positioning each configuration next to each other, we see that it is possible to create a discrete phase gradient. On the right side of Fig. 3.2, we show the simulation of a metasurface composed of all these nanocylinders gathered together. The simulation now includes the 9 nanocylinders shown on the left side plus an empty space of volume $0.3 \times 0.3 \times 10$ µm^3. Here we can see that the simulated metasurface is effectively tilting the incoming wavefront. By comparing the individual simulations (left) and the full simulation (right), we see a smoothing of the discrete phase shift gradient. This smoothing is due to diffraction phenomena associated with the nanostructures sizes that are smaller than the wavelength [1, 2, 44, 51, 213, 214]. The simulation on the right shows exactly the design we will use in the following for our metadeflector simulations.
According to the generalized laws of reflection and refraction [1], we can establish the follow-

ing relation, for a normally incident plane wave interacting with a metadeflector in vacuum:

$$\sin\theta_d = \frac{\lambda}{2\pi}\frac{d\Phi}{dx} \tag{3.1}$$

Where θ_d is the tilt angle, λ is the vacuum wavelength of the incident plane wave and $\frac{d\Phi}{dx}$ is the phase shift gradient. The metadeflector is designed so that the phase-shift of an incoming plane wave is increased by 2π over the length of the supercell l_c as shown in Fig.3.2. From eq. 6.1, we establish the following relation between the supercell length l_c and θ_d:

$$\theta_d = \arcsin\frac{\lambda}{l_c} \tag{3.2}$$

For our fabricated metadeflector, we have 10 configurations with a cell size of 300 nm. The supercell length l_c is then equal to 3 µm for an operating wavelength of λ = 750 nm yielding a tilt angle θ_d = 14.5°.

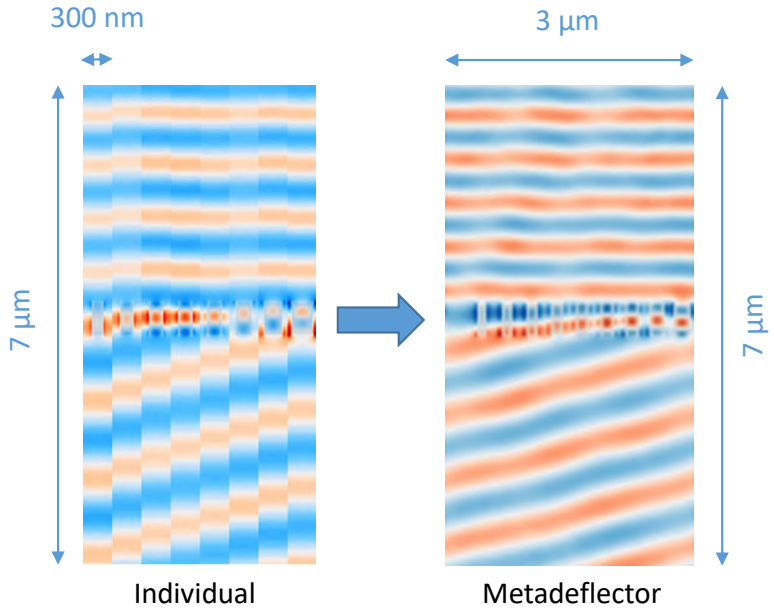

Figure 3.2: FDTD simulation principle of a metadeflector tilting an incoming planewave of λ = 750 nm by an angle of 14.5°. On the left: individual simulations of infinite and periodic metasurfaces composed of identical nanocylinders. Each column is extracted from a 0.3x0.3x10 μm FDTD simulation with periodic boundary conditions on X and Y axis, and PML in the Z axis. On the right: full simulation of a metadeflector composed of the nine geometries from the left with an additional empty space. The volume is 3x0.3x10 μm. Periodic boundary conditions are applied on X and Y axis. PML are applied on Z axis.

3.1.1.1 Expected efficiencies

The last step to validate our design is to perform a full FDTD simulation of its optical response. For metadeflectors, there are generally two quantities characterizing their efficiency: the deflection and diffraction efficiencies. The deflection efficiency η_{defl} is the ratio between the

power P_d of the beam deflected at the nominal tilt angle θ_d to the power of the incident beam P_{inc}. Because the metasurface is perfectly periodic, it diffracts the incident light into several beams propagating in different directions named by their order of diffraction. The deflected beam is diffracted towards the order $+1$. The diffraction efficiency η_{diff} is the ratio between the deflected beam power P_d to the sum of the powers of all the diffracted beams noted P_{diff}. The relation between the deflection and diffraction efficiencies can be defined as follows:

$$\frac{\eta_{diff}}{\eta_{defl}} = \frac{\frac{P_d}{P_{diff}}}{\frac{P_d}{P_{inc}}} = \frac{P_{inc}}{P_{diff}} = \frac{P_{scat} + P_{abs} + P_{diff}}{P_{diff}} = 1 + \frac{P_{scat} + P_{abs}}{P_{diff}} \tag{3.3}$$

Where P_{scat} is the remaining power scattered by the metasurface (i.e. out of the diffracted orders), and P_{abs} is the power absorbed. The scattered power P_{scat} is directly dependent on the periodicity of the metasurface. The more periodic the metasurface, the more P_{scat} decreases [215, 216]. We note that for a perfectly periodic metasurface with no absoption, $\eta_{diff} = \eta_{defl}$. For the fabricated metasurface, we will consider that despite not being perfectly periodic (because of nanofabrication errors), the periodicity precision is high enough to neglect P_{scat}.
We show in Fig. 3.3 the simulated deflection and diffraction efficiencies as a function of the wavelength, for a metadeflector with the nanoresonators chosen previously. As we can see, both efficiencies are at their maximums for the incident wavelength λ = 750 nm, where the maximum diffraction efficiency is 98% and the maximum deflection efficiency is 89%.

3.1.2 Optical Characterization

The metadeflector fabrication is done following the process described in Chapter 2. We can see the SEM images of this metadeflector in Fig. 3.4. These images were acquired after metallization of the metasurface with a small layer of Palladium. We can recognize very well the simulated design, with the 9 nanodiscs and one empty slot.
The following optical characterizations were performed before the metallization, using a Ti:Sa femtosecond laser tunable in the near-infrared range (680-1080 nm). The principle of the characterization is shown in Fig. 3.5. The power P_{diff} is obtained by measuring the power in each output beam using a powermeter. To measure the incident beam power P_{inc}, we translate the sample perpendicularly to the beam until the metasurface is completely out of the incident beam. The transmission losses of 4% from the air/glass interface for the deflection efficiency are therefore not taken into account. We also use a telescope to make the beam smaller than the metasurface. This prevents light that does not go through the metasurface to contribute to the power measured in the order $+0$. An image of the experimental setup is shown in Fig. 3.5.
We measure the deflection and diffraction efficiencies at several wavelengths from 700 nm to 800 nm. The results are presented in Fig. 3.6, as well as the expected values of the simulations in Fig. 3.2. As we can see, the measured diffraction and deflection efficiencies reach 94% and 88%. These values are very close to the ones obtained from the simulations. To our knowledge, these values are among the highest reported in the literature in this wavelength range [27]. However, we can see that the maximum efficiency positions are shifted by 25 nm compared to the simulations (λ = 775 nm instead of 750 nm).

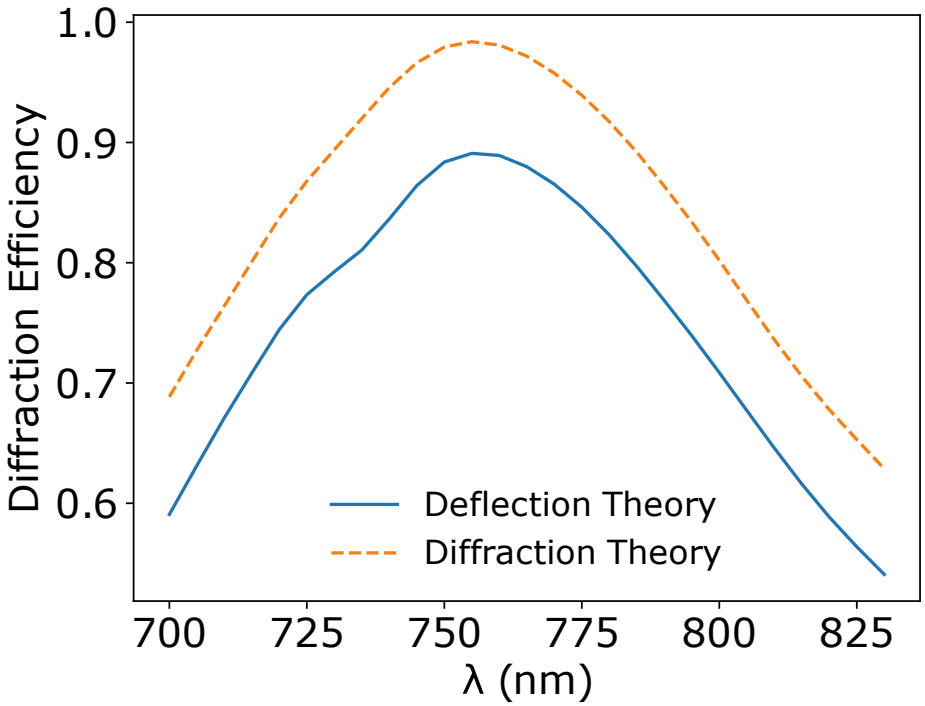

Figure 3.3: FDTD simulated deflection and diffraction efficiencies for a metadeflector. For each wavelength, the far-field optical response of the metasurface is computed in two steps. First, the electric field generated upon interaction of the incident plane wave with the metasurface is computed in a plane parallel to the substrate out of the near-field region. The electric field in this output plane is then used to calculate the far-field intensity distribution using diffraction theory.

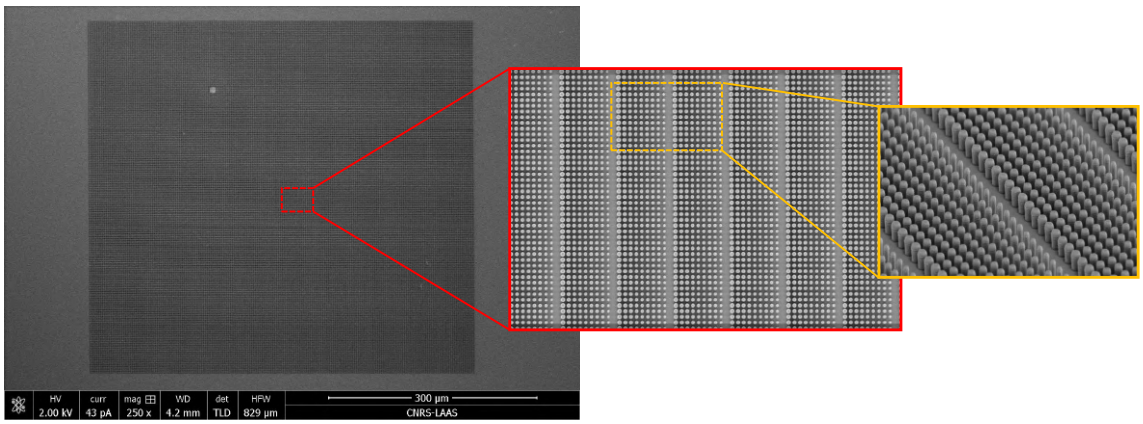

Figure 3.4: SEM images of a fabricated metadeflector designed to tilt an incoming light of λ = 750 nm by an angle of 14.5°. The metadeflector's size is 500x500 μm.

3.1.3 TEM Characterization: Identification of nanofabrication errors

To understand the origin of these differences, we study the impact of nanofabrication errors on the optical response of a metadeflector. First of all, it is necessary to identify the errors that

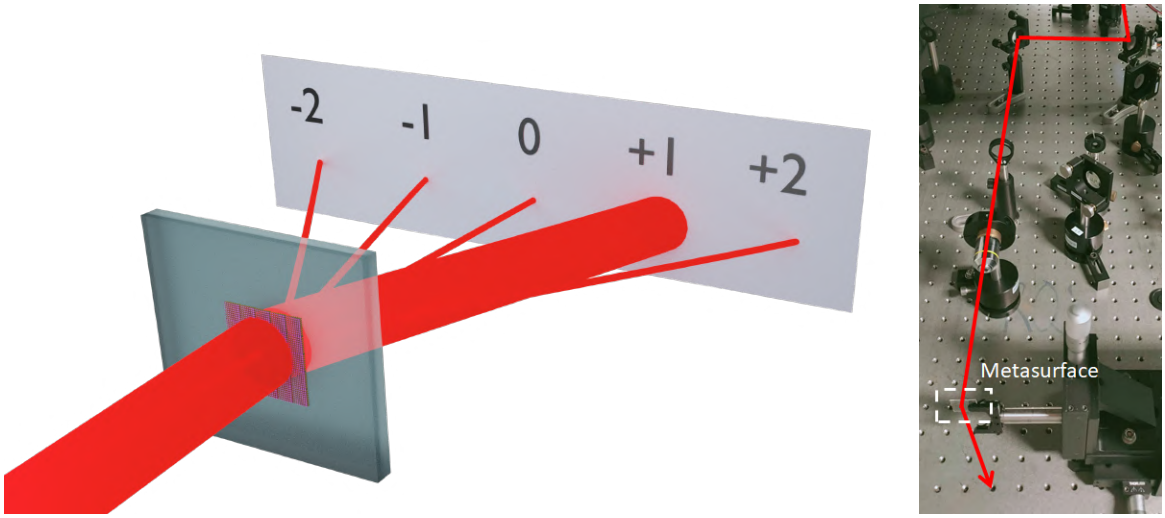

(a) (b)

Figure 3.5: (a) 3D sketch of the optical behavior of the metadeflector illuminated by a normally incident planewave. (b) Optical bench used for the optical characterization of the metadeflector.

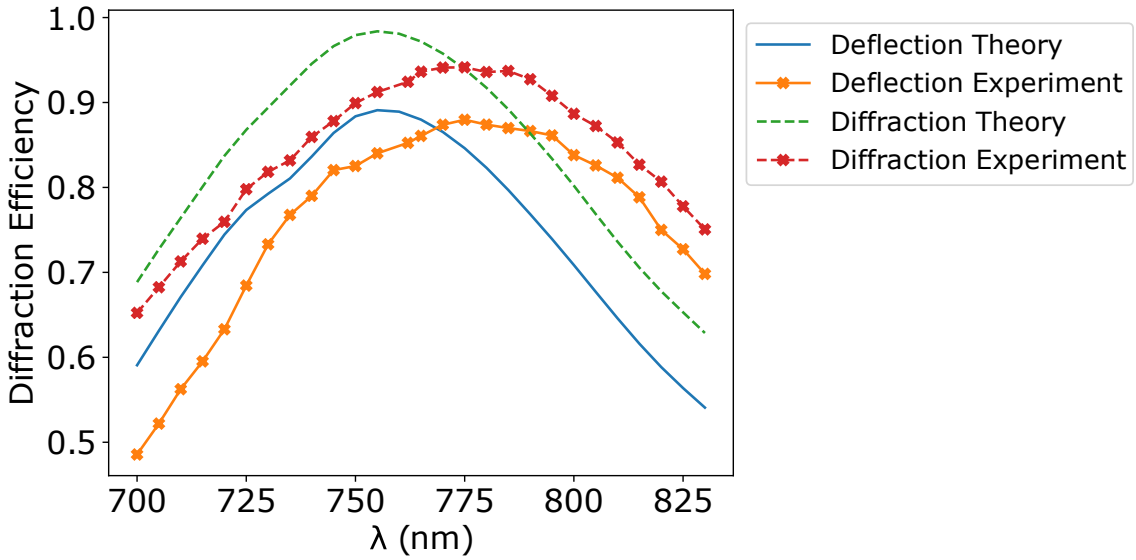

Figure 3.6: Theoretical and experimental deflection and diffraction efficiencies for the simulated metadeflector of Fig.3.2 and fabricated metadeflector of Fig.3.4.

can appear during the nanofabrication process. To do this, we perform TEM measurements to precisely characterize the morphology and environment of the fabricated nanodiscs. These experiments are carried out on a Philips CM20 FEG TEM at 200 keV (collaboration C. Marcelot, CEMES-CNRS).
First, a cross-section lamella of the metadeflector is prepared using a FIB equipped with a micromanipulator (collaboration R. Cours, CEMES-CNRS, Fig.2.10). We show in Fig. 2.11 several TEM bright field images of this lamella. The morphologies of the nanodiscs are extracted from these images using post-processing analysis tools. To improve the measurement accuracy, we

make a calibration using a reference reticle. Using these calibration methods, we report the measured morphologies of the nanocylinders in Fig. 3.7.
As we can see from this table, we can identify several systematic errors. First, the top diameters are always larger than the bottom diameters by around 5 nm to 10 nm. Second, the means of the upper and lower diameters values are always above the expected simulation values by about 5 nm. Third, the height of the nanodiscs is larger than expected, (390 nm against 370 nm).
To go further, we also perform elemental mapping using STEM-EDX mode (see Chapter 2 for more details). We illustrate in Fig. 3.8 an example showing the distribution of silicon and oxygen in the nanostructure. We show the extracted vertical profile in which we can see the presence of oxygen above the nanocylinders with a thickness of about 100 nm. This oxygen is related to the presence of the HSQ resist. Indeed, as we explained in Chapter 2, when exposed to an electron beam, HSQ evolves from a cage-like monomer to a network-like polymer that approaches the structure of silicon dioxide [192].
Due to the presence of dioxigene during the etching, and due to natural oxidation in air, a small oxide layer of a few nanometers thickness is expected all around the nanostructures. To confirm and study this layer, we also show in Fig. 3.8 an horizontal profile of the STEM-EDX analysis, with the proportions of Silicon, Oxygen and Platinum. In this profile, we indeed note the presence of oxygen on the sides of the nanodiscs. However, the curve of Oxigen appears almost superposed to the curve of Platinum. This means that the Oxigen we observe on the side may have been deposited along with the Platinum during the FIB process. Therefore, the only conclusion we can draw is that the oxide layer which was present before the Platinum deposition had a thickness smaller or equal to 40 nm, which is the thickness we retrieve from Fig. 3.8 .

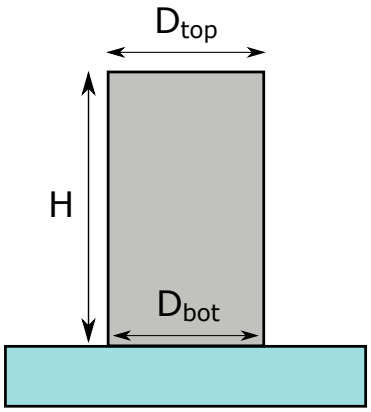

(a)

#	D_{bot}	D_{top}
1	210	224
2	183	194
3	180	185
4	175	183
5	157	167
6	156	160
7	140	150
8	138	146
9	107	121
10	Empty	Empty

(b)

Figure 3.7: (a) Convention used for the nanocylinder geometry parameters. (b) Dimensions of the nanocylinders measured from the TEM images.

To conclude, we can say that the shapes of the fabricated nanostructures are very close to what we expected. Indeed, the mean diameter of the measured nanopillars are all within

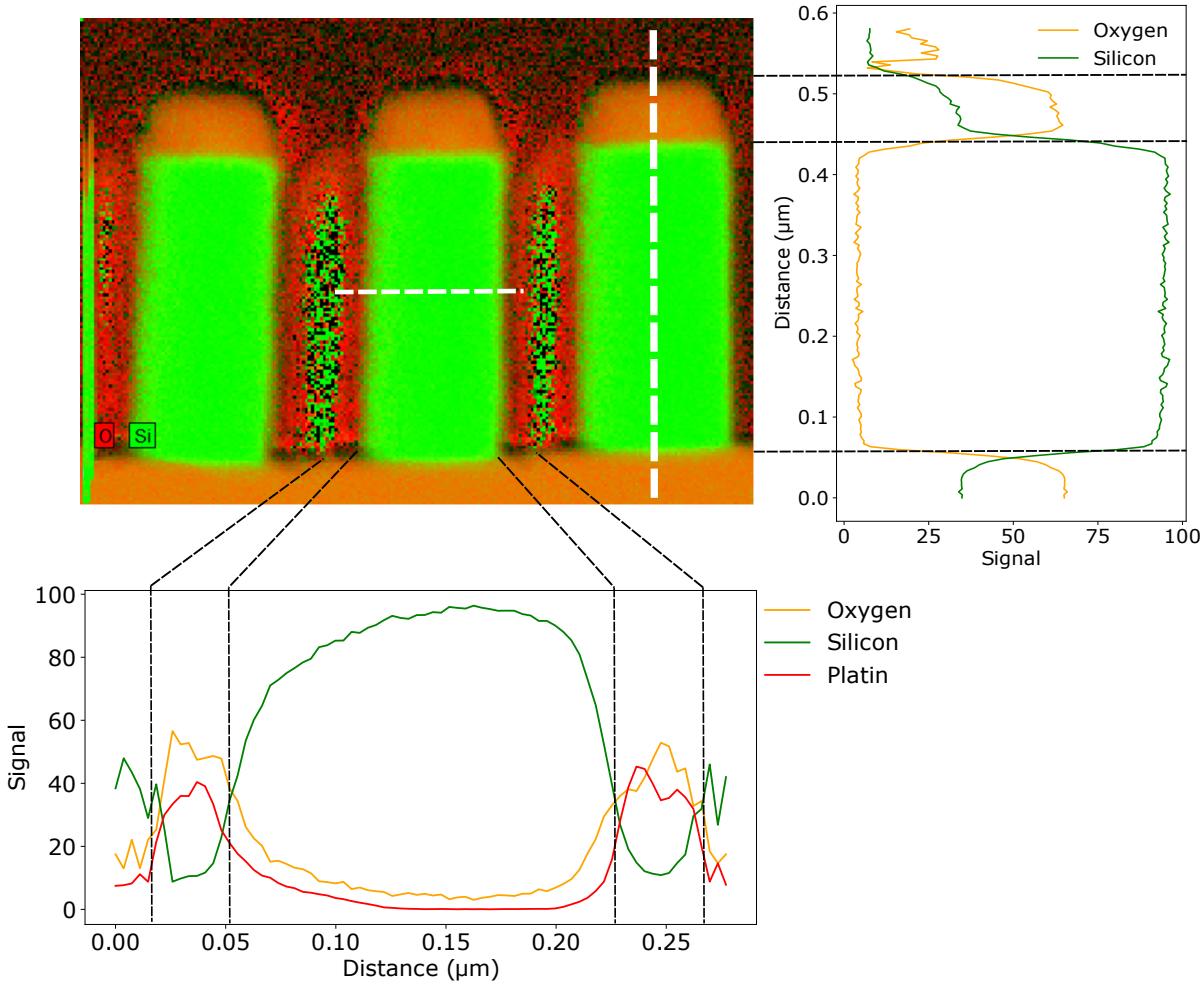

Figure 3.8: Chemical composition of the lamella taken from the metadeflector (see Fig. 2.10). (a) Distribution of Silicon and Oxygen inside and in the vicinity of the nanodiscs. (b) Vertical profile of the distribution along the dotted white vertical line in (a). (c) Horizontal profile of the distribution along the dotted white horizontal line in (a).

the 5% error range from the nominal values. This confirms the high control provided by the fabrication process described in Chapter 2.
Still, as we saw that the performance of the fabricated metadeflector is quite different from the simulated one, we will adress in the next section the influence of the nanofabrication errors we identified through our TEM analysis, which are:

- Diameter error;
- Difference between top and bottom diameters *i.e.* inclination of the nanocylinders sides;
- Presence of a top and lateral oxide layers;

Besides the shape errors that we evidenced with the TEM observations, there is also an additionnal error coming from the refractive index of the silicon which can differ from theoretical values. In the following, we will study the influence on the optical performance of the metadeflector of all the reported errors of this section.

3.2 Impact of systematic nanofabrication errors on the optical performance of a metadeflector

In this section, we analyze in detail the impact of each of the previously reported errors on the optical performance of a metadeflector using FDTD numerical simulations.
We first focus on the morphological errors with diameter, height, and lateral side slope variations. We then study the impact of the environment around the nanostructures, with the residual presence of oxide around the nanocylinders. Finally, we address the impact of a variation of the refractive index of the silicon nanostructures.
We first simulate the modification of the phase-shift and transmission of infinite arrays composed of identical but imperfect nanodiscs. We then consider an entire metadeflector, the nanostructures of which present fabrication errors and compute its diffraction and deflection efficiencies. The FDTD environment is exactly the same as the one used for Fig. 3.1. Each defect is applied identically to each nanopillar of the metadeflector, *i.e.* we consider systematic fabrication errors. The study of statistical fabrication errors which differ from one structure to another is addressed in the next section.

3.2.1 Morphology errors

Diameter Error

Systematic diameter errors occur when the fabricated metasurface nanodiameters are all differing from the nominal design values by the same amount. During the fabrication process, we try to minimize this error by performing dose tests (see chapter 2, section 2). However, this optimization step requires systematic SEM observations. Fig. 3.9 shows an example of a SEM image of one HSQ nanodisc. We notice that it has a blurry contour. It is therefore required to carefully define a criterion on which the diameter measurement will be based. Depending on the selected criterion, as well as on the SEM images resolution, an error in the diameter measurements may occur. Since the metasurface fabrication is relying on these characterizations, this error of measurement will be transferred during fabrication to the metasurface geometries.
Fig. 3.10 represents the change in phaseshift and transmission induced by a diameter error on the 10 selected configurations shown in Fig. 3.1. What we can see is a strong influence on the phase shifts and a weak impact on the transmissions. As we can see, an error as small as 10 nm already changes the phase shift by more than $\frac{\pi}{4}$, which is very important as the phase shift step between two configurations is $\frac{\pi}{5}$. Since we saw in the previous section the great sensitivity on the diameter when choosing the configurations, this result is in fact expected.
We show in Fig. 3.11 the modification of the final optical performance of the metadeflector due to a change in diameter. As the diameter error source is supposed to be the calibration process, the same amount of change in diameter is identically applied for every nanodiscs regardless of their diameters. We thus represent the changes in the deflection and diffraction efficiencies defined in the previous section. Fig.3.11(a) (resp. Fig.3.11(b)) shows the diffraction (resp. deflection) spectra of all the erroneous metadeflectors together with the experimental results. In Fig.3.11(c) (resp. Fig.3.11(d)), we represent the diffraction (resp. deflection) efficiency at the design wavelength of 750 nm. Finally, in Fig.3.11(e) (resp. Fig.3.11(f)), we give the values and the wavelengths of the maximum efficiencies. To simplify the discussion on the results,

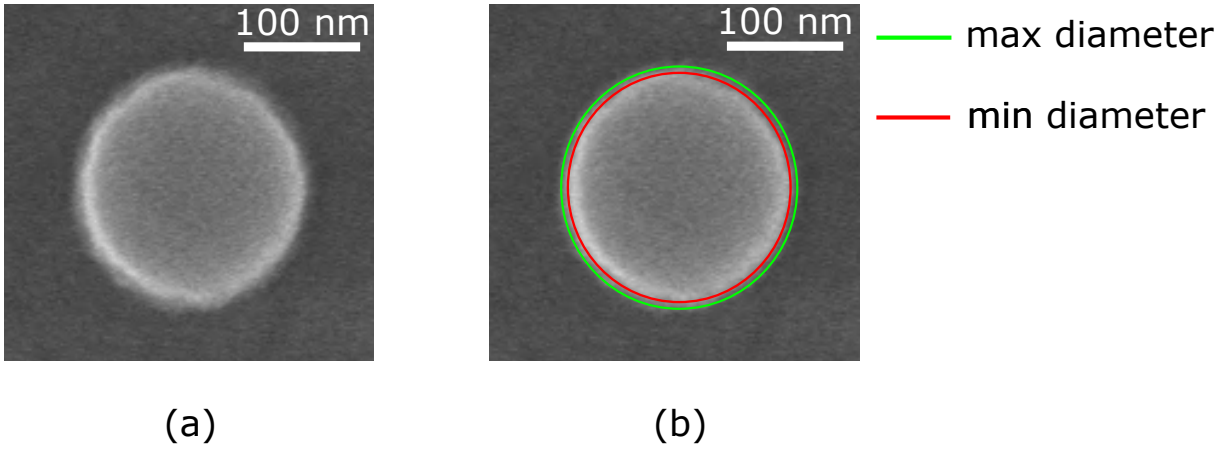

Figure 3.9: Illustration of the accuracy of the diameter measurements using SEM. (a) Top view of a nanodisc with a magnification of 65000. (b) Maximum and minimum diameters that can be extracted from the SEM image (a). The maximum diameter (green circle) is 208 nm and the minimum diameter (red circle) is 195 nm.

the maximum diffraction and deflection efficiency values are noted $\eta_{M_{diff}}$ and $\eta_{M_{defl}}$, and the wavelengths of these maximums are noted $\lambda_{M_{diff}}$ and $\lambda_{M_{defl}}$. The dotted lines represent the measured values.
The results of Fig.3.11(a-b) clearly show the strong influence of a change in diameter on the diffraction and deflection efficiency spectra. Looking at the efficiencies for a 750 nm incident plane wave, we see that a variation of 10 nm induces a loss of 10% to 15% for both the diffraction and deflection efficiencies. However, it seems that this decrease in efficiency is rather due to the shift in the resonance wavelength than to the decrease in efficiency itself. Indeed, looking at Fig.3.11(e-f), we see that for a diameter error of 10 nm, $\eta_{M_{diff}}$ (resp. $\eta_{M_{defl}}$) decreases from 98% (resp. 89%) to 94% (resp. 86%) with both $\lambda_{M_{diff}}$ and $\lambda_{M_{defl}}$ shifted from 730 nm to 780 nm. As we explained in Chapter 2, the precision on the diameters during fabrication is supposed to be close to 5 nm. We can then conclude that the control on the diameter is very important for a good agreement between theory and experiment.

Height error

Systematic height errors are induced during the deposit of silicon on the wafer. First, the deposited silicon layer is inhomogeneous: its thickness varies from the center to the edges of the wafer [193, 217, 218]. Furthermore, ellipsometry characterization accuracy being less precise for thin layers, the measurements of the layer thickness, followed by the refractive index characterization, brings some additional imprecision [176]. Indeed, for our metadeflector, a silicon layer thickness of 370 nm has been measured by ellipsometry whereas the TEM measurements showed that the nanocylinders were 390 nm high.
We illustrate in Fig. 3.12 the influence of a height error on the optical response of the ten selected configurations of Fig. 3.1. A modification of height has clearly a weak influence as a 20 nm thickness increase only induces a phase shift change of $\frac{\pi}{10}$. The transmission is also weakly impacted.
Regarding the impact of a height error on the optical performance of the metadeflector, we

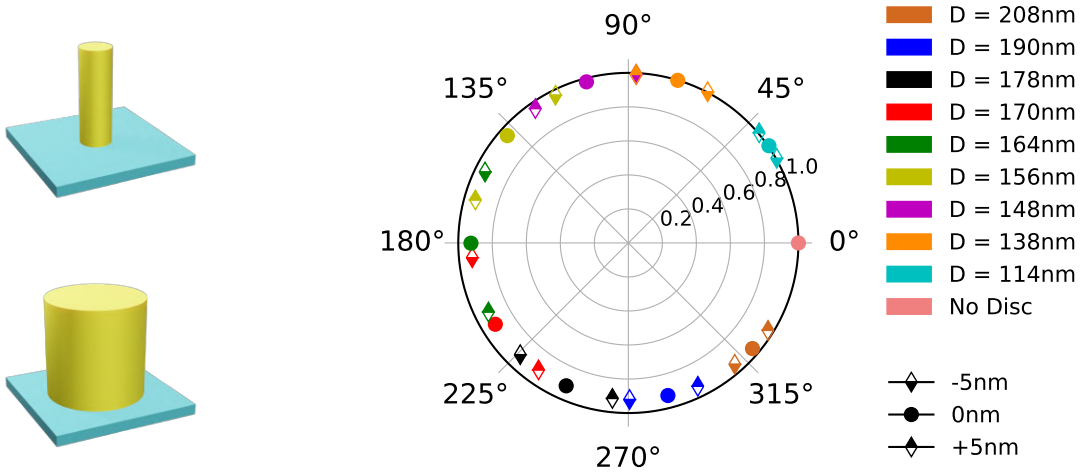

(a) (b)

Figure 3.10: (a) Representation of a diameter modification of nanocylinders. (b) Transmission and dephasing induced by an array of silicon nanocylinders on a normally incident $\lambda = 750$ nm plane wave as a function of a change in diameter for the ten selected geometries.

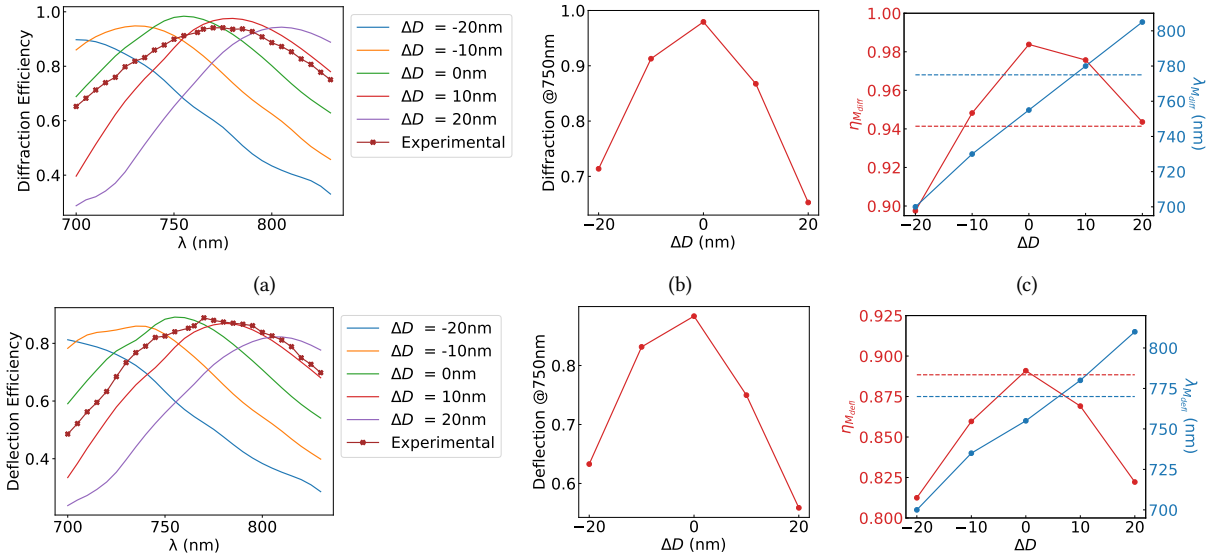

(a) (b) (c)

(d) (e) (f)

Figure 3.11: Influence of an error on the diameters of the nanocylinders used in a metadeflector on the diffraction and deflection efficiencies. (a)(resp (d)) shows the diffraction (resp. deflection) efficiency spectrum for different diameter errors. (b)(resp (e)) shows the variation of the diffraction (resp. deflection) efficiency of an incident light $\lambda = 750$ nm with the diameter error. (c) (resp. (f)) shows the maximum diffraction efficiency (resp. deflection) and the wavelength of the maximum efficiency for different diameter errors. The dotted lines represents the experimental values.

refer to Fig. 3.13, the presentation of which is exactly the same as Fig.3.11. From these results we can clearly see the very small influence of a height error on the spectra for the diffraction

efficiency, since even a 40 nm shift in height does not change $\eta_{M_{diff}}$ and only shifts $\lambda_{M_{diff}}$ by 20 nm. The deflection efficiency appears a little more sensitive, with a 6% decrease of $\eta_{M_{defl}}$ for a height offset by 40 nm. Both $\lambda_{M_{diff}}$ and $\lambda_{M_{defl}}$ follow the same trend gradually shifting to longer wavelengths with increasing height. It can also be noted that increasing the height of the nanodiscs by 40 nm is still not sufficient to bring the computed value close to the one measured on the fabricated device. We see therefore that even without a fine control on the thickness, the optical performances of metasurfaces with nanoresonators shapes similar to the ones we use (*i.e.* high aspect ratio) are not highly impacted by an error in height.

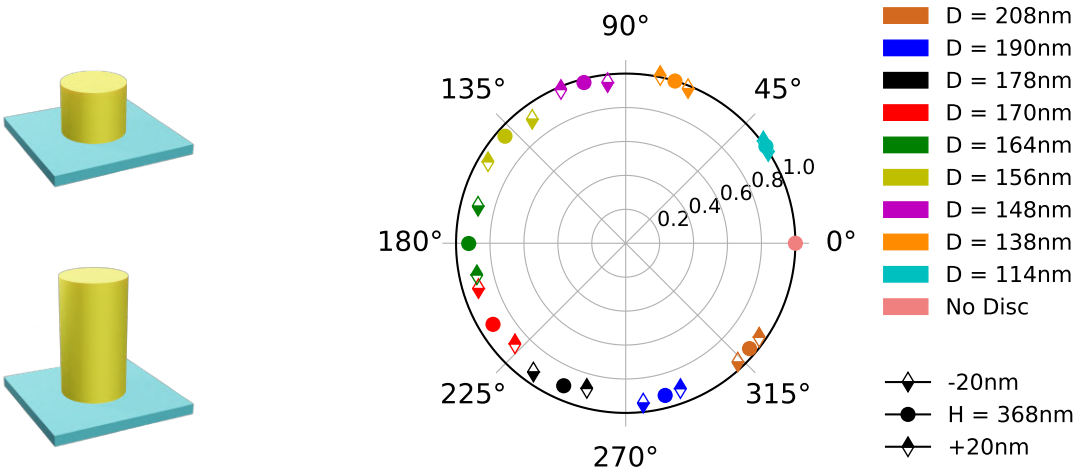

(a) (b)

Figure 3.12: (a) Representation of a height change of nanocylinders. (b) Transmission and dephasing induced by an array of silicon nanocylinders on a normally incident $\lambda = 750$ nm plane wave as a function of a change in height for the ten selected geometries.

Shape error

We study here the influence of a systematic error on the shape of the nanocylinders. We focus on the case of a tilt of the sides of the nanocylinders (see Fig.3.14). This typical error can have two origins. The first one is related to the shape of the HSQ cap cylinders obtained just after the insolation process. Depending on how the resist development is realized, the HSQ cylinders may already have slightly tilted sides. Then, during the etching, the ions trajectories are deviated by the HSQ cap, inducing modified lateral etching on the silicon nanodiscs [194]. The second origin is exclusively related to the etching parameters. As we saw in Chapter 2, in plasma etching, both physical etching and chemical etching occur. The variation of these parameters directly impacts the lateral shapes of the nanocylinders [198, 219].
Fig. 3.14 shows the influence of this error on the optical response of the ten selected configurations of Fig. 3.1. A tilt of the sides as low as 1° induces a phase shift variation of $\frac{\pi}{5}$, showing the very strong influence on the phase shifts. On the other hand, we see that the transmission remains weakly impacted.
Looking at Fig. 3.15, we see the high impact on the optical performance of the metadeflector. At 750 nm, a variation of 2° of the sides slopes causes a drop of the diffraction and deflection

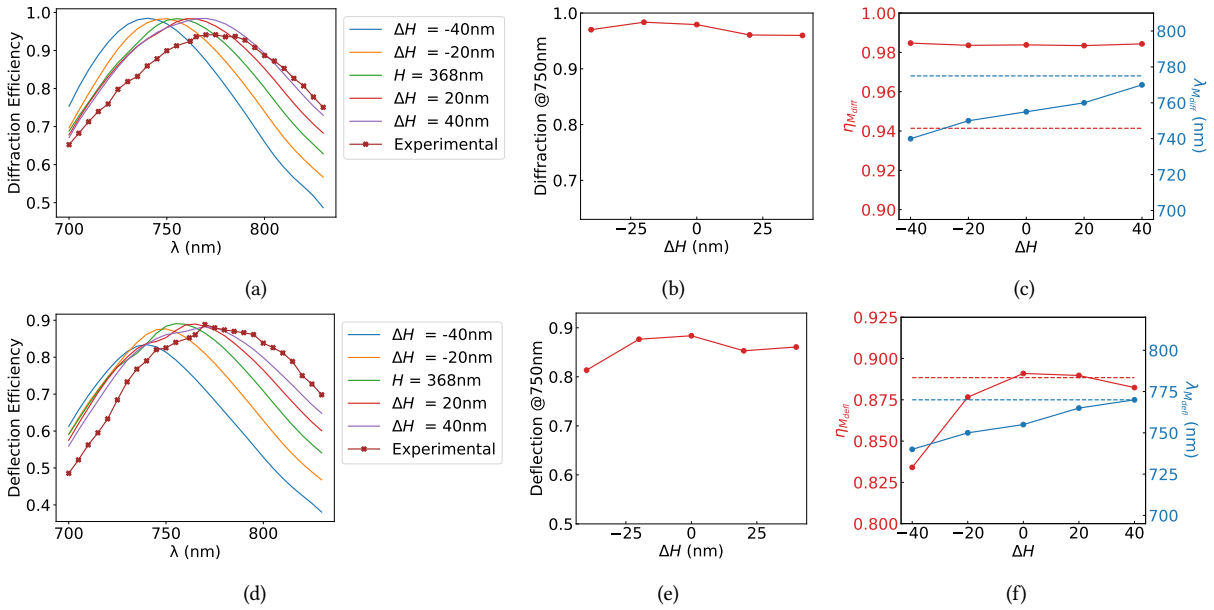

Figure 3.13: Influence of an error on the height of the nanocylinders making up a metadeflector on its diffraction and deflection efficiencies. (a)(resp (d)) shows the diffraction (resp. deflection) efficiency spectrum for different height errors. (b)(resp (e)) shows the variation of the diffraction (resp. deflection) efficiency of an incident light λ = 750 nm with the height error. (c) (resp. (f)) shows the maximum diffraction efficiency (resp. deflection) and the wavelength of the maximum efficiency for different height errors.

efficiencies by 10% to 20%. Then from Fig.3.15(c) and (f), we see that 2° of variation on the slope decreases $\eta_{M_{diff}}$ (resp. $\eta_{M_{defl}}$) efficiency from 98% (resp. 89%) to 94% (resp. 82%). A strong shift of $\lambda_{M_{diff}}$ and $\lambda_{M_{defl}}$ is also noteworthy, as they are shifted by 15 nm per degree. Fig. 3.7 shows that the experimental tilt extracted from the TEM images is of the order of 1°. In [139], the authors measured a tilt angle of 2.85° for their SiO_2 nanopillars. From the previous observations, we see that such angles have a high influence on the optical behavior of metasurfaces. Therefore, the control of this value is crucial to understand the mismatch between the optical performance of simulated and fabricated metasurfaces.

Conclusion on the morphology errors

In Fig. 3.16 we summarize the diffraction and deflection efficiency alterations for all the shape errors we reviewed. Theses results confirm the trend that a modification of the lateral morphology of the nanocylinders induces large deviations, as opposed to a modification of the vertical morphology, especially for the diffraction efficiency.
To explain this difference of impact, we should look at how the electric field behaves inside the nanostructures when changing the lateral or vertical shape. Under the influence of an electric field, there is a separation of the charges that compose a dielectric nanostructure, which is what drives the optical response of the structure. For a normal incident planewave, the polarization state is in the lateral XY plane. Thus, when the lateral shape of the nanopillar changes, the electric charges separation along the polarization axis, induced by the incident electric field, is directly impacted. For instance, the larger the nanodisc's diameter, the larger

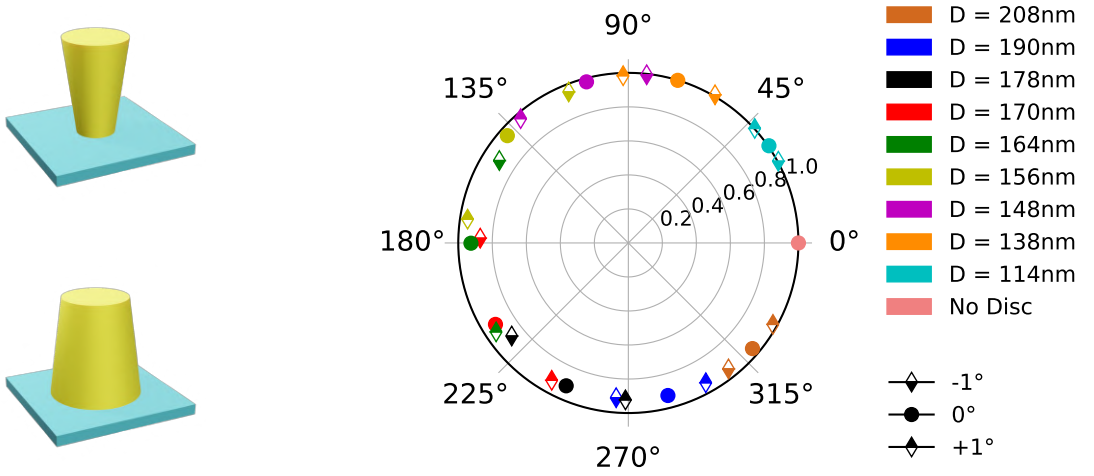

(a) (b)

Figure 3.14: (a) Representation of a lateral slope change of nanocylinders. (b) Transmission and dephasing induced by an array of silicon nanocylinders on a normally incident $\lambda = 750$ nm plane wave as a function of a change in lateral slope for the ten selected geometries.

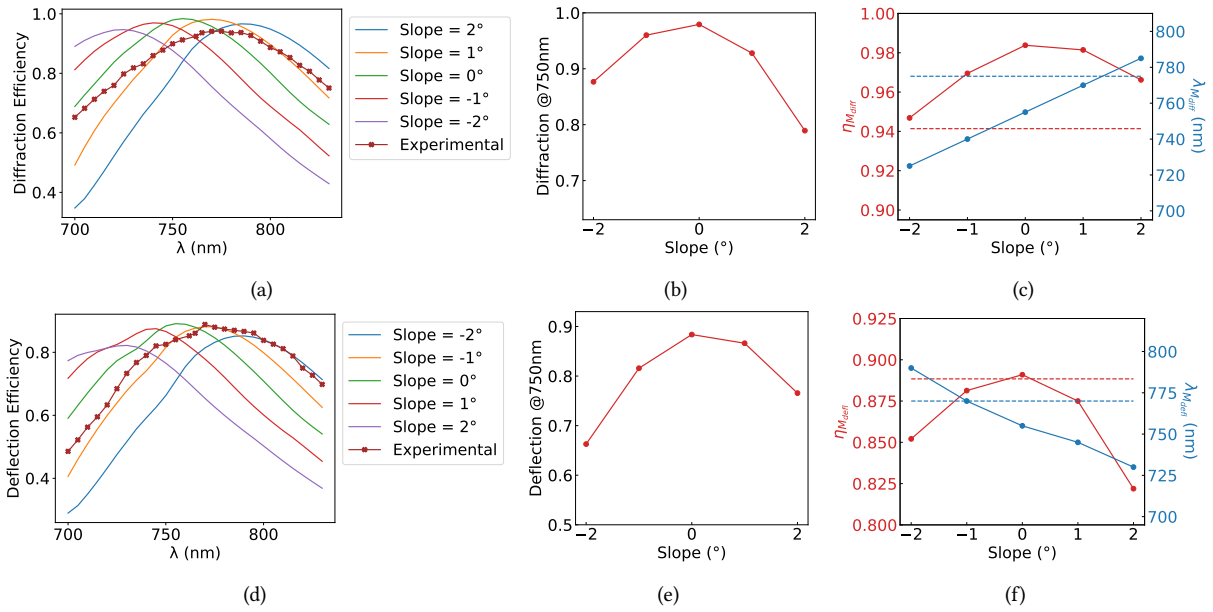

Figure 3.15: Influence of an error on the tilt of the sides of the nanocylinders making up a metadeflector on its diffraction and deflection efficiencies. (a)(resp (d)) shows the diffraction (resp. deflection) efficiency spectrum for different slope errors. (b)(resp (e)) shows the variation of the diffraction (resp. deflection) efficiency of an incident light λ = 750 nm with the slope error. (c) (resp. (f)) shows the maximum diffraction efficiency (resp. deflection) and the wavelength of the maximum efficiency for different slope errors.

the separation distance of the charges. Therefore, increasing the diameter of the nanodisc is equivalent to increasing the phase shift induced to the incident beam. This behavior is exactly

what we observed in Fig. 3.1.
On the other hand, a change in height or of the vertical shape will not directly impact the charge separation inside the nanostructures along the polarization axis, which can give a first explanation of its smaller influence on the optical response. However, it will still slightly directly change the phase delay as the light propagates along the Z axis. The change in height might also alter the transmission if we consider the nanopillars as small Fabry-Perrot cavities. More generally, a modification of the lateral or vertical morphology will change the resonances that are supported by a nanostructure due to its aspect ratio alteration. Indeed, we saw in Chapter 1 that depending on the aspect ratio, higher multipole resonances can be supported, as the volume of the nanostructure becomes sufficient to support them. Therefore, this explains why both lateral and vertical shape affects the optical response of the nanostructures and the metasurface. As the nominal aspect ratios of our nanocylinders are high (diameter smaller than the height), the sensitivity on a diameter modification is enhanced.

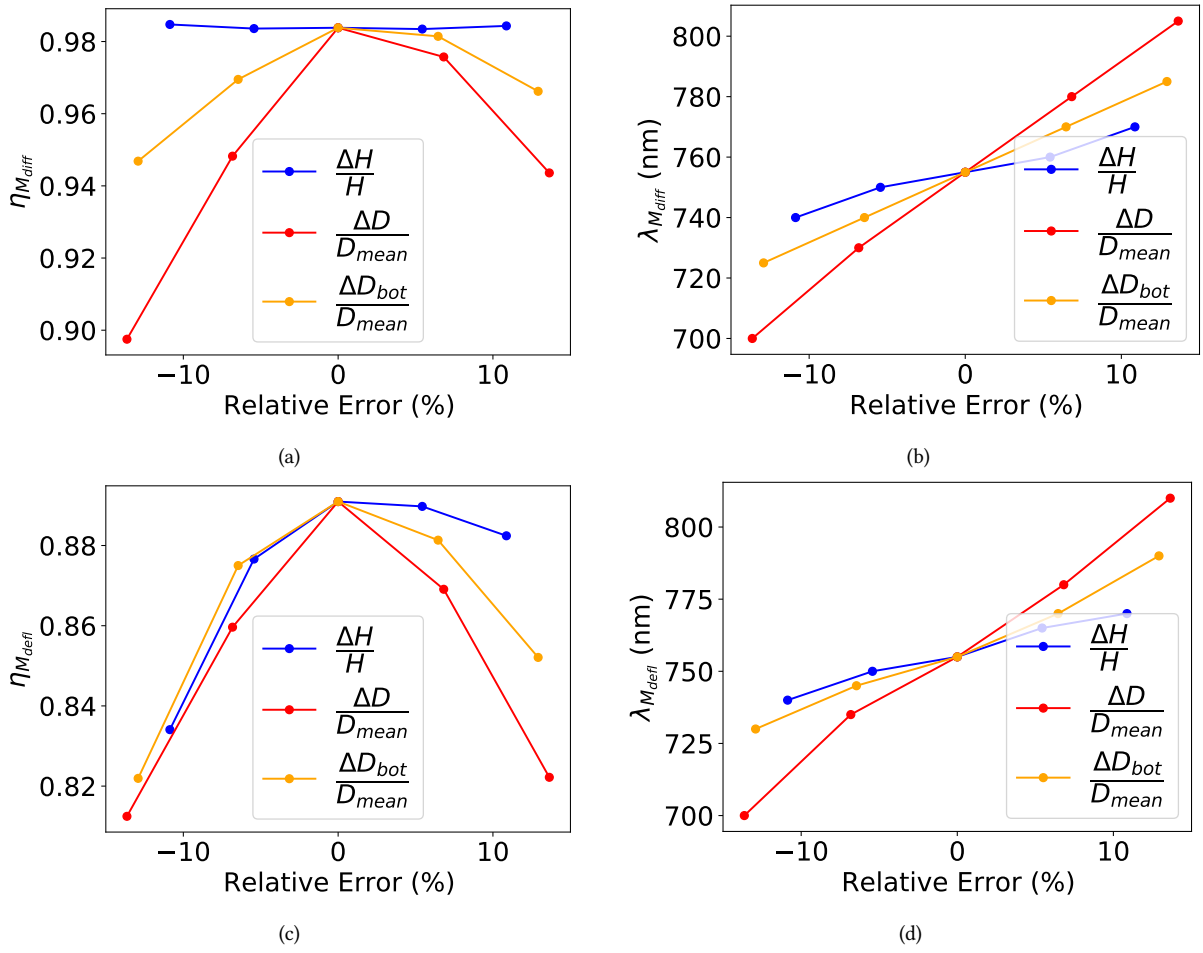

Figure 3.16: Relative impacts of the morphology errors (diameters, height, side slope) on the optical performances of a metadeflector. (a) and (b) show the diffraction efficiency $\eta_{M_{diff}}$ and $\lambda_{M_{diff}}$ evolution with the different relative errors. (c) and (d) show the deflection efficiency $\eta_{M_{defl}}$ and $\lambda_{M_{defl}}$ evolution.

3.2.2 Environment and refractive index errors

As we reported in Fig. 3.8, besides the differences in the morphologies of the nanocylinders, there is also the presence of oxide on the top and potentially on the sides of the nanocylinders. In addition, the refractive index used for the simulations may not exactly match that of the manufactured nanocylinders as the ellipsometry precision decreases for thin layers [176].
The aim of this section is to examine the influence of errors in the dielectric constants of both silicon (material constituting the nanostructures) and the environment (material surrounding the nanostructures).

Oxide layer on top

The presence of oxide above the silicon nanocylinders is due to the HSQ resist remaining after the etching process (see Chapter 2 for more details). We measured a remaining HSQ layer of 100 nm (Fig.3.8). For the FDTD simulations, the presence of HSQ was simulated by adding a layer of index n = 1.45, as the chemical structure of the exposed HSQ is close to SiO_2 [192].
We show in Fig. 3.17 the optical response of the selected configurations with different thicknesses of HSQ added on the top. We notice the weak impact on both the phase shifts and transmissions, as an HSQ layer of 200 nm changes the phase shifts by only $\frac{\pi}{10}$ without changing the transmissions.
In Fig. 3.18, we can clearly see the very weak influence that an additional HSQ layer has on the metadeflector diffraction and deflection efficiencies. Indeed, adding 400 nm of HSQ only decreases the diffraction and deflection efficiencies by 5% at 750 nm. Moreover, the 400 nm HSQ layer only shifts the wavelengths positions $\lambda_{M_{diff}}$ an $\lambda_{M_{defl}}$ by around 10 nm and only changes $\eta_{M_{diff}}$ and $\eta_{M_{defl}}$ by 2%. From this, we can conclude that the HSQ layer remaining after plasma etching can not be the source of large performance discrepancies for a fabricated metasurface.
It is to be noted that the presence of this HSQ on top of the nanocylinders can be removed using fluoridric acid (HF). However, since HF is very toxic, its use can become dangerous for both the metasurface and the user. It may then be advisable to avoid removing the HSQ.

Oxide layers on top and side

We now adress the influence of an oxide layer on both the top and the sides of the nanocylinders. As we have just seen, a residual oxide layer on the top has a very weak influence. The presence of a lateral oxide layer is due to the oxidation of the metasurface. In Section 1, we demonstrated that its corresponding thickness is smaller than 40 nm. As this oxide layer is created in part by natural oxidation in air, its removal would require processes of complete immersion of the entire metasurface after HF cleaning in dry conditions.
For the FDTD simulations, the oxidation taking place in contact with the silicon nanopillars, we simulate the presence of this oxide as if its chemical structure was similar to SiO_2, *i.e.* a refractive index of n = 1.45.
To compare with the previous results, we add the same amount of oxide on the top of the nanocylinders as before, and add 10% of this upper thickness on the sides. Figure 3.19 shows the influence of this layer on the optical response of the ten selected configurations, where we can see the increased sensitivity of the phase shifts. Indeed, a 20 nm layer on the side (with 200 nm on top) causes a variation of phase shift of $\frac{\pi}{4}$ (against $\frac{\pi}{10}$ with the upper oxide layer

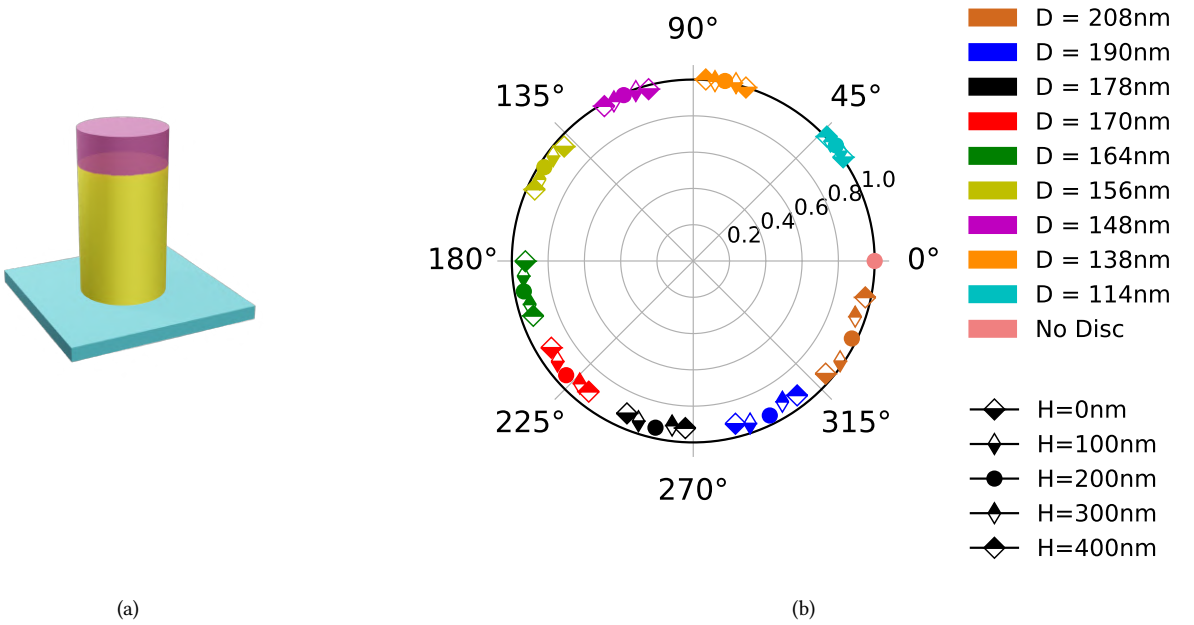

(a) (b)

Figure 3.17: (a) Representation of nanocylinders with a remaining resist layer. (b) Transmission and dephasing induced by an array of silicon nanocylinders on a normally incident $\lambda = 750$ nm plane wave as a function of the thickness of a residual resist layer for the ten selected geometries.

alone). The influence on the transmission remains low.
The impact of this oxide layer on the optical performances of the metadeflector is addressed in Fig. 3.20. What can be clearly noticed is the amplified influence on the spectra for both efficiencies and maximum wavelength positions. At 750 nm, 40 nm of oxide on the sides reduces the deflection and diffraction efficiencies by up to 15%. Regarding the resonances, the addition of a 40 nm oxide layer shifts $\lambda_{M_{diff}}$ and $\lambda_{M_{defl}}$ by around 40 nm and decreases $\eta_{M_{diff}}$ by 6% and $\eta_{M_{defl}}$ by 8%.
To understand this higher sensitivity to a variation of the dielectric environment on the sides, we look at the electric field inside a nanocylinder surrounded by oxide layers. Fig. 3.21 shows the electric field inside an isolated nanocylinder of height 370 nm and diameter 200 nm, with and without oxide layers, excited at its electric or magnetic dipole resonances. These results were obtained using pyGDM [164]. The nano-object is discretized on an hexagonal mesh (20 nm step), and the oxide refractive index is 1.45. We notice that the additional 200 nm oxide layer on top barely modifies the electric and magnetic dipole resonances inside the silicon nanocylinder. On the other hand, the addition of 20 nm on the side has much more influence as it notably increases the amplitude of the electric field at both resonances. The presence of an oxide layer on the sides of the nanocylinders is a relatively important factor that must be taken into account when analyzing the optical response of metasurfaces.

Refractive index : real part

We now study the influence of an error on the refractive index of the nanostructures. We start here with the influence of the real part of the refractive index of Silicon n_r with Fig. 3.22 for the

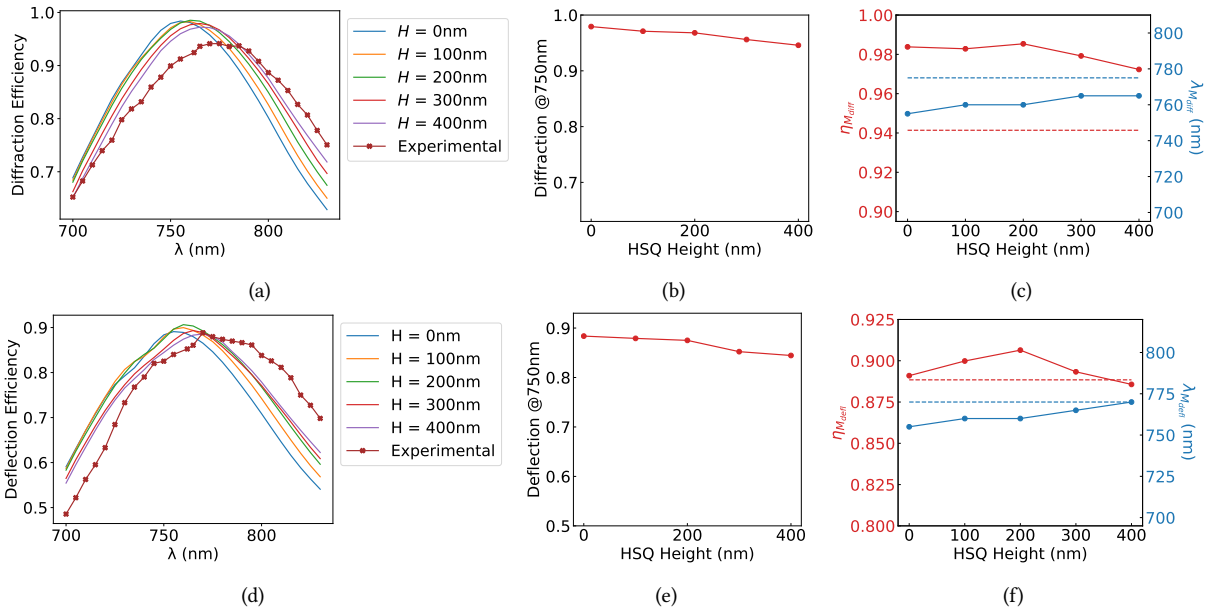

Figure 3.18: Influence of the addition of an HSQ layer above the nanocylinders composing a metadeflector on its diffraction and deflection efficiencies. (a)(resp (d)) shows the diffraction (resp. deflection) efficiency spectrum for different HSQ layer thicknesses. (b)(resp (e)) shows the variation of the diffraction (resp. deflection) efficiency of an incident light λ = 750 nm with the thickness of the HSQ layer. (c) (resp. (f)) shows the maximum diffraction efficiency (resp. deflection) and the wavelength of the maximum efficiency for different HSQ layer thicknesses.

individual configurations, and Fig. 3.23 for the entire metadeflector. As we can see, a modification of n_r has a limited influence on the phase shifts and transmission for each configuration. A typical variation of the index by 0.05 (1.5%) changes the phase shift by about $\frac{\pi}{10}$. This weak influence is confirmed in the metadeflector performances, where the modification of n_r only induces a small wavelength shift and has a low influence on the maximum values. Both the diffraction and deflection efficiencies resonances are indeed shifted by 20 nm and decreased by about 2% for a variation of n_r of 0.1 (3%). We can conclude that the deviation of the silicon refractive index real part, caused by ellipsometry imprecisions, does not alter significantly the optical performance of silicon metasurfaces.

Refractive index: imaginary part

Finally, we look at the influence of a change in the imaginary part of the refractive index n_i. We refer to Fig. 3.24 for the impacts on the individual configurations, and 3.25 for the entire metadeflector. A modification of n_i essentially impacts the transmission for each configuration without changing the induced phase shifts. We notice the same behavior for the metadeflector performances, where the modification of n_i only decreases the maximum deflection efficiency without altering the resonance wavelength. Indeed, a variation of n_i of $2 \cdot 10^{-2}$ leads to a decrease of $\eta_{M_{defl}}$ by 11%, while on the other hand, $\eta_{M_{diff}}$ as well as $\lambda_{M_{diff}}$ and $\lambda_{M_{defl}}$ are not affected at all. This typical behavior is expected as n_i is related to the absorption of Silicon. When n_i increases, P_{abs} increases, inducing a decrease of η_{defl} without changing η_{diff} (see Eq.3.3). Finally, we see that a deviation of the silicon refractive index imaginary part has a

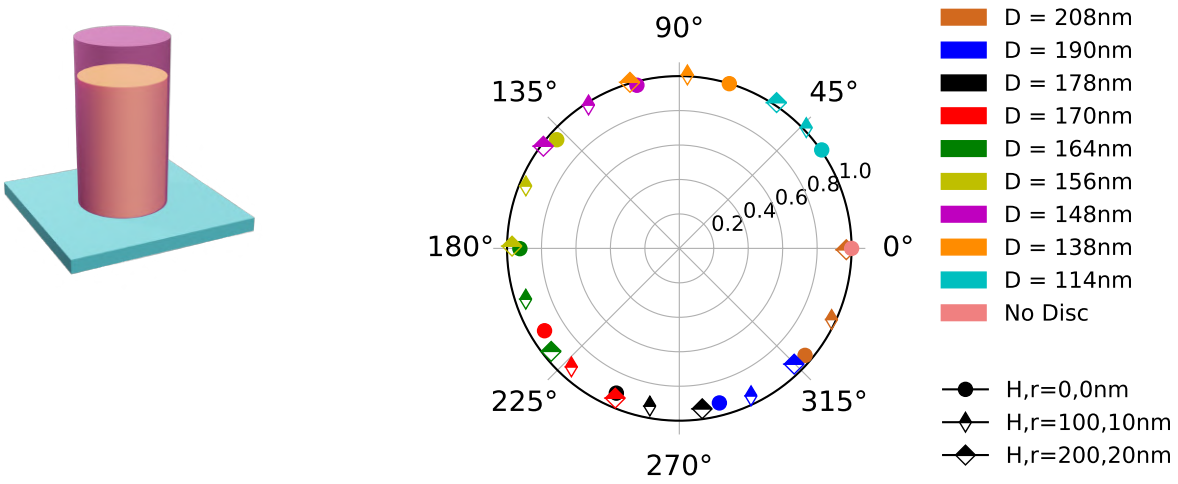

(a) (b)

Figure 3.19: (a) Representation of a nanocylinder with a resist layer and a lateral oxide. (b) Transmission and dephasing induced by an array of silicon nanocylinders on a normally incident $\lambda = 750$ nm plane wave as a function of the thickness of a remaining resist layer and lateral oxide layer for the ten selected geometries.

particular influence on silicon metasurfaces. It only changes the metasurface transmission by increasing the absorption, without modifying the diffraction efficiency. Still, we must keep in mind that this error can explain some divergences between simulated and measured metasurface transmissions.

Conclusion on the systematic errors

Besides the diameter of the nanocylinder, the tilt of the sides and the presence of an oxide layer on the sides are potential sources of the redshift of the efficiency spectra of the fabricated metadeflector with respect to the FDTD simulations. Trying to match the measured diffraction and deflection efficiency spectra of Fig.3.3, we have performed FDTD simulations which take into account the combined influence of all the observed discrepancies (except for the refractive indexes). We refered to the TEM observations shown in Fig. 2.11 of Chapter 2 for the quantification of each discrepancy. The height of the nanocylinders is now H = 390 nm, the HSQ layer on top is 100 nm thick, and the diameters are taken from the values presented in Fig. 3.7. As the only unknown parameter remaining is the oxide thickness on the sides, we made several simulations and found the one showing the best agreement to be 10 nm. The results of this new simulation are shown in Fig.3.26, where we can see a real improvement on the agreement between the simulated and the measured efficiencies. In particular, the spectra have now the same resonance at λ = 775 nm.

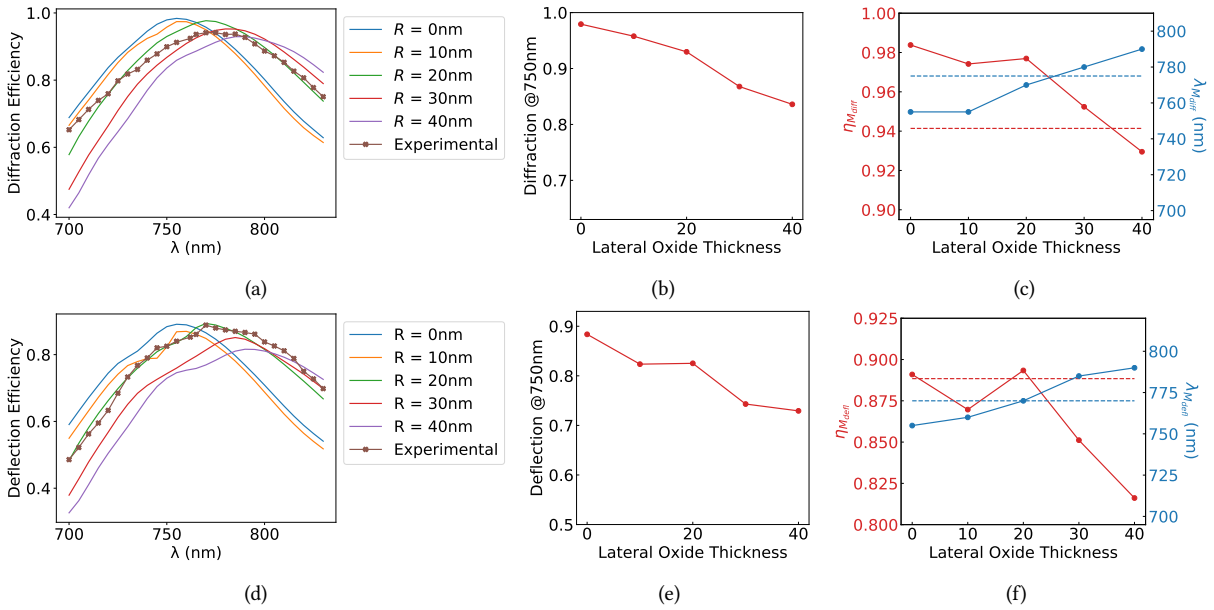

Figure 3.20: Influence of an oxide layer on the top and sides of the nanocylinders composing a metadeflector on its diffraction and deflection efficiencies. (a)(resp (d)) shows the diffraction (resp. deflection) efficiency spectrum for different oxide layer thicknesses. . (b)(resp (e)) shows the variation of the diffraction (resp. deflection) efficiency of an incident light λ = 750 nm with the thickness of the oxide layers. (c) (resp. (f)) shows the maximum diffraction efficiency (resp. deflection) and the wavelength of the maximum efficiency for different oxide layer thicknesses.

.

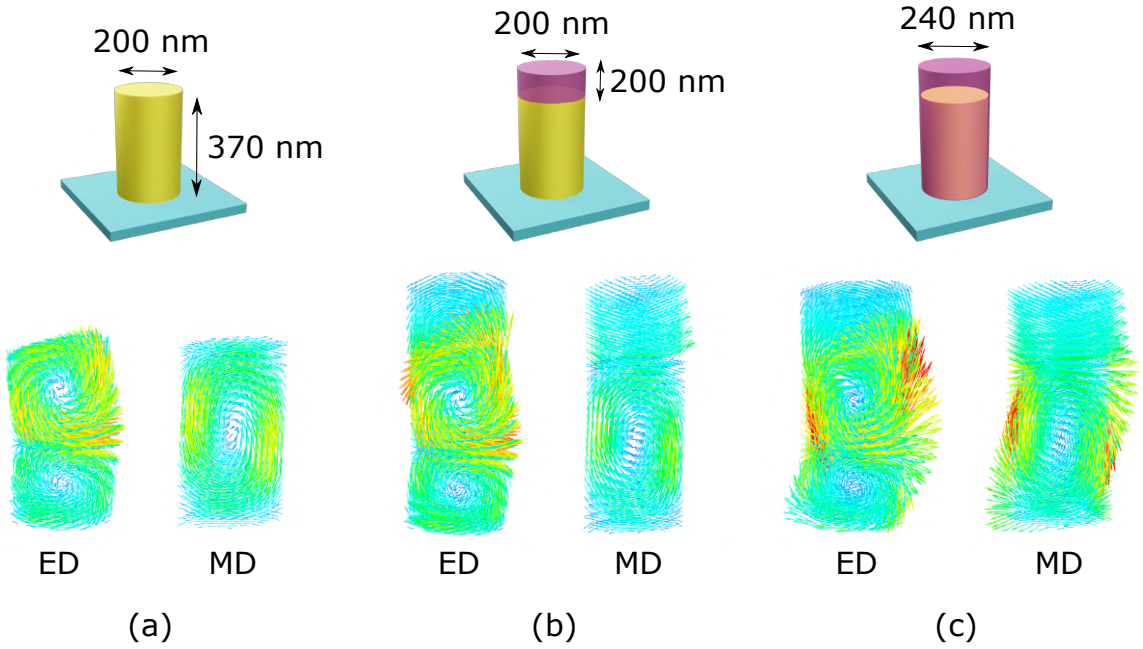

Figure 3.21: Influence of the addition of lateral and vertical oxide layers on the electric and magnetic dipole resonance of an isolated nanocylinder of height 370 nm and diameter 200 nm. (a) 3D representation of the electric field of the electric and magnetic dipole resonances inside the nanocylinder alone (a), with an additional top layer (b), and with additional top and lateral capping (c). For (a) and (b), the resonances are at $\lambda = 830$ nm and $\lambda = 970$ nm. For (c), the resonances are at $\lambda = 850$ nm and $\lambda = 1000$ nm. All plots have the same color scale.

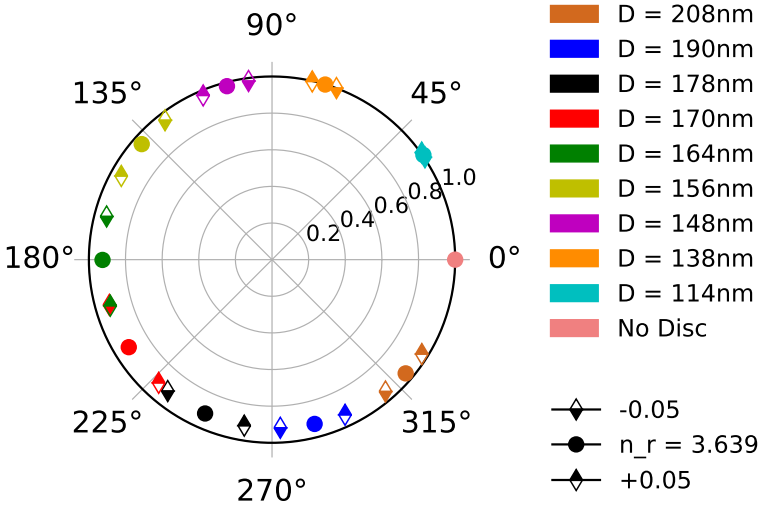

Figure 3.22: Transmission and dephasing induced by an array of silicon nanocylinders on a normally incident $\lambda = 750$ nm plane wave as a function of the real part of the refractive index for the ten selected geometries.

.

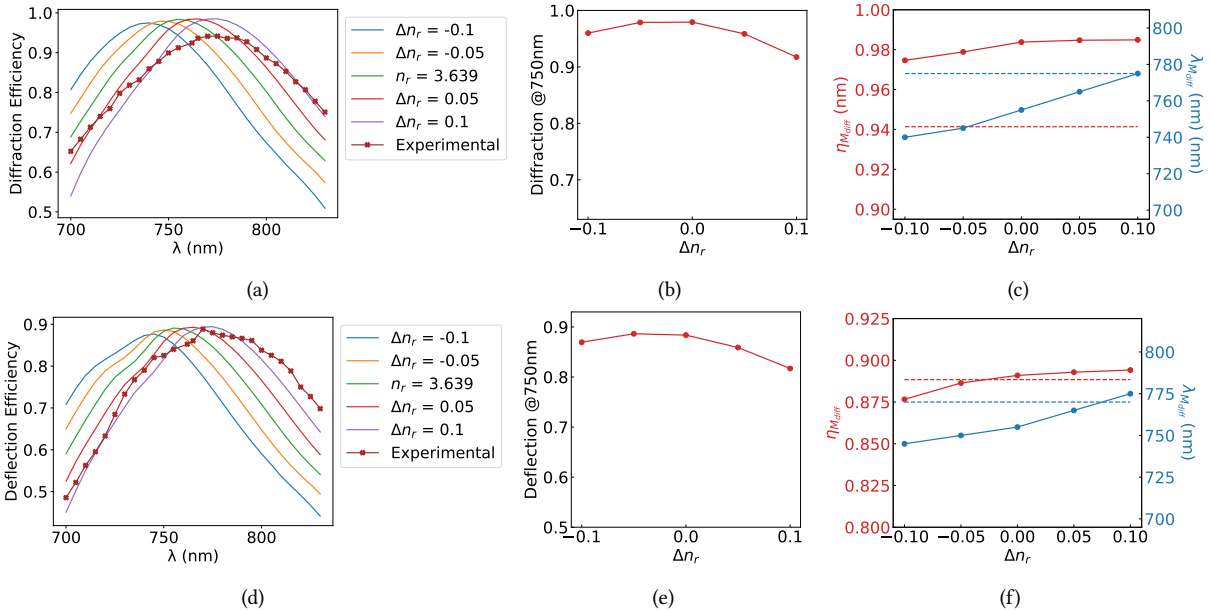

Figure 3.23: Influence of a modification of the real part of the refractive index of the nanocylinders composing a metadeflector on its diffraction and deflection efficiency. (a)(resp (d)) shows the diffraction (resp. deflection) efficiency spectrum for different refractive indexes. (b)(resp (e)) shows the variation of the diffraction (resp. deflection) efficiency of an incident light $\lambda = 750$ nm with the real part of the refractive index. (c) (resp. (f)) shows the maximum diffraction efficiency (resp. deflection) and the wavelength of the maximum efficiency for different refractive indexes.

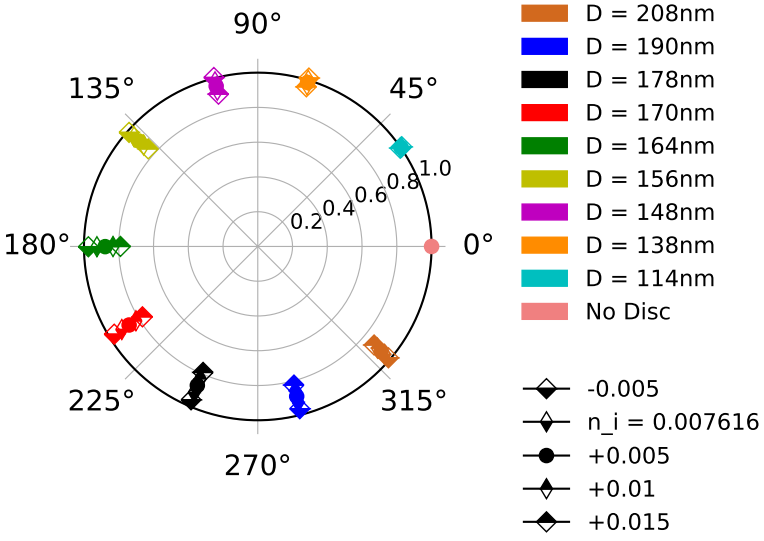

Figure 3.24: Transmission and dephasing induced by an array of silicon nanocylinders on a normally incident $\lambda = 750$ nm plane wave as a function of the imaginary part of the refractive index for the ten selected geometries.

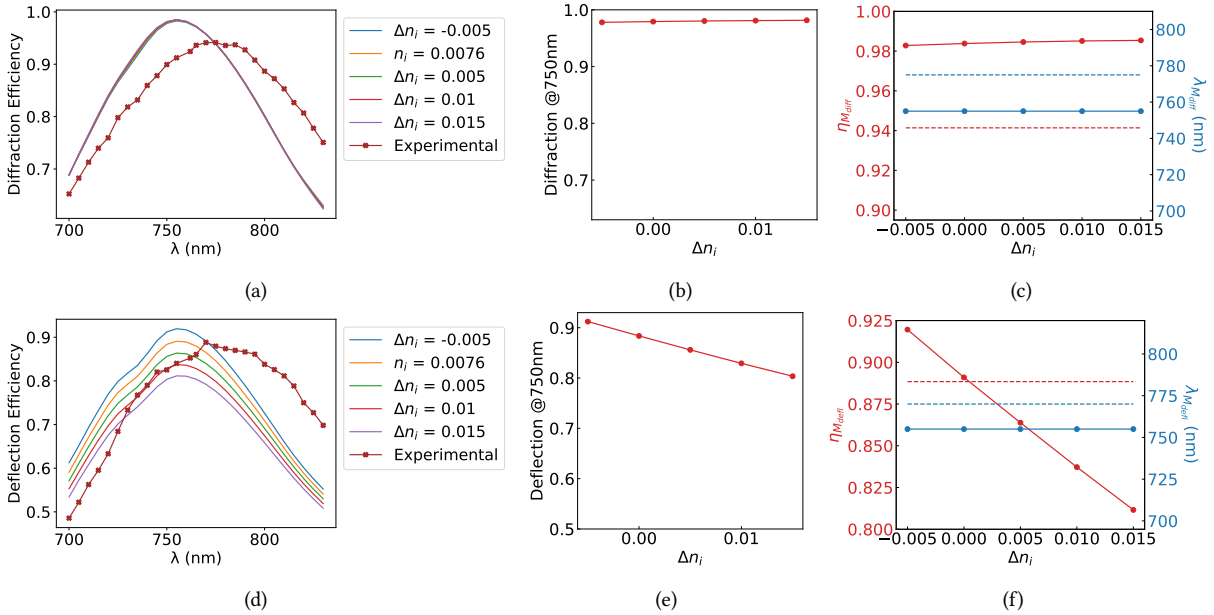

Figure 3.25: Influence of a modification of the imaginary part of the refractive index of the nanocylinders composing a metadeflector on its diffraction and deflection efficiency. (a)(resp (d)) shows the diffraction (resp. deflection) efficiency spectrum for different refractive indexes. (b)(resp (e)) shows the variation of the diffraction (resp. deflection) efficiency of an incident light $\lambda = 750$ nm with the imaginary part of the refractive index. (c) (resp. (f)) shows the maximum diffraction efficiency (resp. deflection) and the wavelength of the maximum efficiency for different refractive indexes.

3.3 Impact of random nanofabrication errors

As opposed to the systematic errors investigated in the previous section, we will consider in the following the impact of statistical errors. We assume that these statistical errors are directly caused by the sensitivity of manufacturing tools to external factors. For example, a variation in temperature or vibrations around the EBL machine have a significant influence on the position of the electron beam on the sample during EBL [63].

3.3.1 Diameter Error

We first consider the influence of a random error on the diameters of nanocylinders on the optical performances of a metadeflector and a metalens.
We assume that the nanocylinders behave like a collection of diffracting elements placed on a square periodic array at locations (x_i, y_j), where $x_i = ia$ and $y_i = ja$, a being the periodicity of the lattice. The entire metasurface is represented by a complex 2D array where each pixel represents a nanostructure. We ascribe to each pixel the transmission and phase shift induced by the represented nanostructure. These transmission and phase shift values are extracted from the simulations shown in Fig. 2.3 of Chapter 2, carried out for an infinite and periodic metasurface using FDTD (MEEP). In order to simulate a random error on the diameter of the nanocylinders, it is necessary to know the transmission and phase shift for every possible value

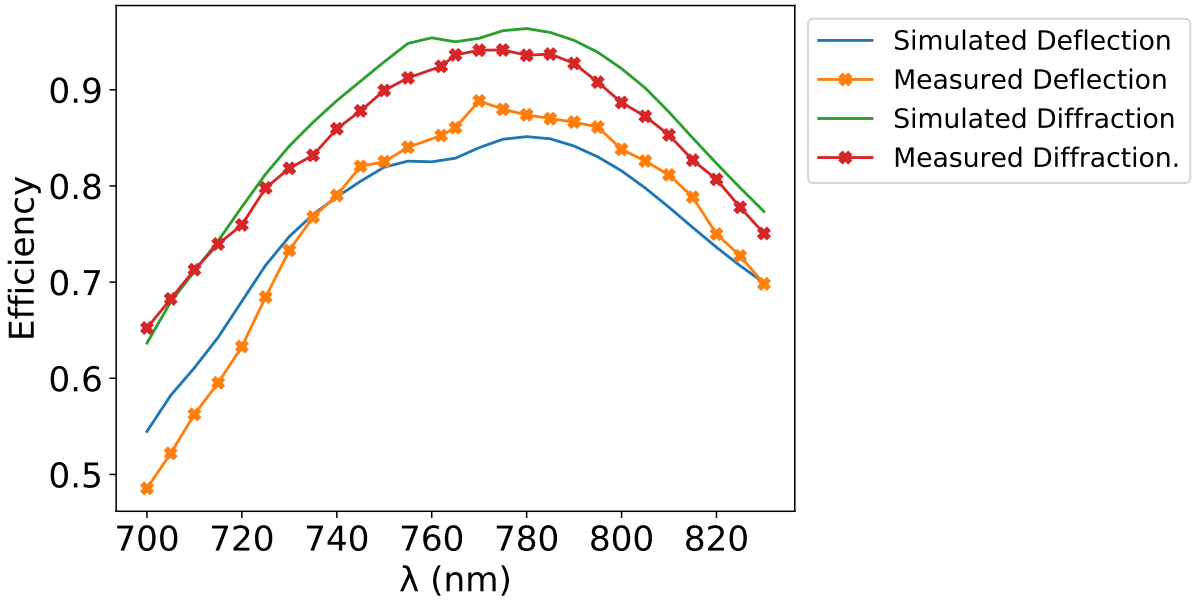

Figure 3.26: Diffraction and deflection efficiencies of a metadeflector where the nanocylinders geometries were adjusted with the values measured using the TEM characterizations (see Fig.2.11 of Chapter 2)

of the diameter. To achieve this, the values relating the diameter to the output transmission and output phase were interpolated. We represent these functions in Fig. 3.27. The far-field response is then calculated using the Fresnel-Kirchhoff theory of diffraction [220]:

$$T(u,v) = \iint_S t(x,y) e^{-2i\pi(ux+vy)} \mathrm{d}x\mathrm{d}y \tag{3.4}$$

Where $T(u,v)$ is the complex diffracted amplitude of the entire metasurface, $t(x,y)$ is the complex amplitude of the metasurface at positions (x,y), and (u,v) are the angular coordinates in the diffracted plane. For our simulations, as we discretized our metasurface in pixels, the amplitude $T(u,v)$ becomes:

$$T(u,v) = a^2 \sum_i \sum_j t(x_i,y_j) e^{-2i\pi(ux_i+vy_j)} \tag{3.5}$$

Diameter error on metadeflector

Here, we study the influence of a random error on the diameters on the optical performance of a metadeflector. The initial design of the metadeflector is the same as the one of the previous sections. For each pixel at position (x_i, y_j), the corresponding nanocylinder has its diameter D_{ij} modified randomly as $D_{ij} = D_{0,ij} + \delta_{ij}$ where $D_{0,ij}$ is the nominal value. The variation δ_{ij} varies randomly from one cylinder to another following a gaussian distribution of standard deviation σ_D.
We show in Fig. 3.28 the influence of a random variation of diameters on the optical performances of a metadeflector of size 100×100 µm^2 and periodic step a = 300 nm. The metadeflector is described by a 2D array of $(100\ \mu\mathrm{m}\ /300\ \mathrm{nm})^2 = 333^2 = 110889$ pixels. For each

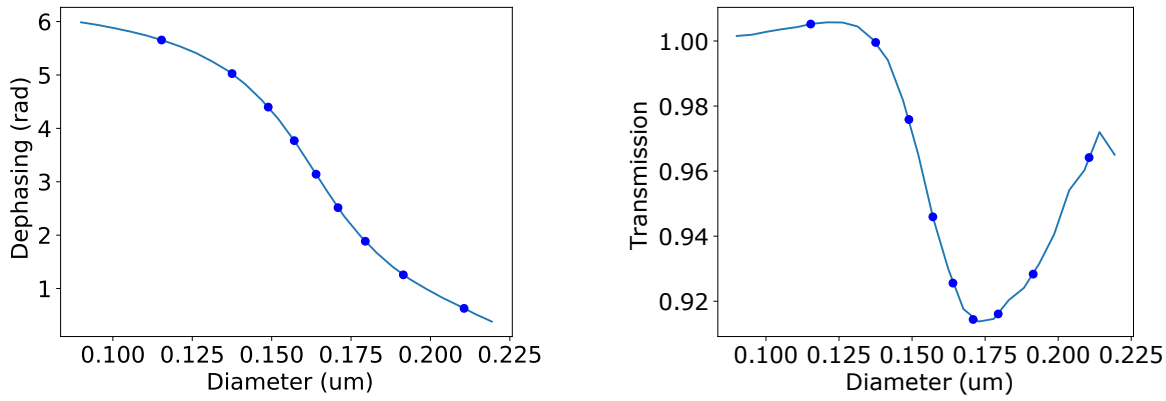

(a) (b)

Figure 3.27: (a) Interpolated function relating the diameter of the nanocylinders and the induced phase shifts. (b) Interpolated function relating the diameter of the nanocylinders and the corresponding transmission.

σ_D, we compute a total of 100 simulations to average the response. Although this number of simulation might seem quite small, in fact, all of the pixels (i.e. 110889 pixels) of the metadeflector are also spatially averaging the random error, which allows to reduce the number of iteration required to have a converged solution.
Fig. 3.28(a) illustrates two different values of the standard deviation σ_D showing the associated phase maps and statistical distributions. The evolution of the diffraction and deflection efficiencies with increasing σ_D is addressed in Fig. 3.28(b). As we can see, the deflection efficiency is strongly impacted by a statistical error of diameters, as it decreases by 20% with $\sigma_D = 10$ nm. A precision on the nanocylinder diameter better than 5 nm is needed to keep the deflection efficiency above 80%.

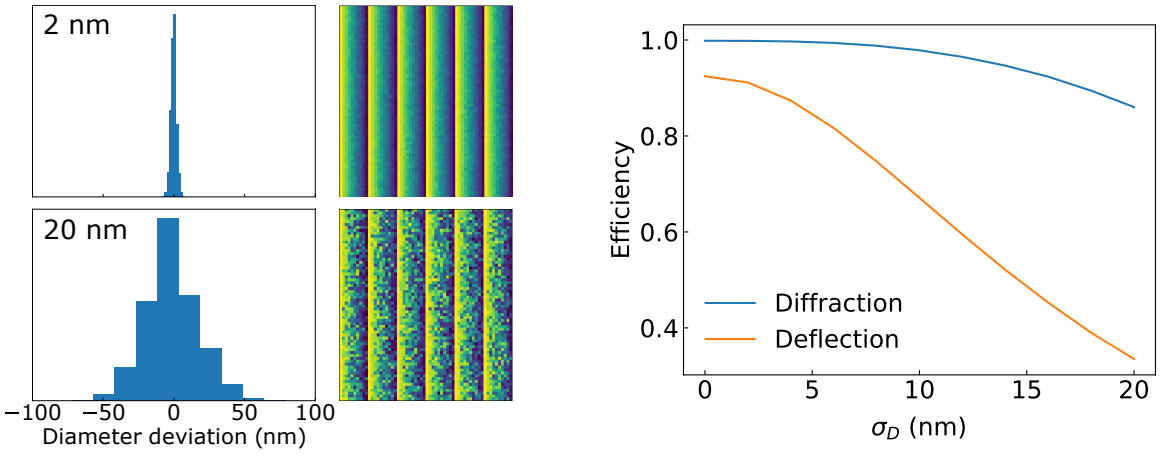

(a) (b)

Figure 3.28: (a) Statistical distribution of a diameter variation δ_{ij} (left) and corresponding map of the dephasing induced by the metadeflector (right) for two different values of σ_D. (b) Deflection and diffraction efficiency of a 100×100 µm^2 metadeflector as a function of σ_D.

Diameter random error on a Metalens

In the same way, we simulate the influence of a random diameter error on the optical response of a metalens. As for the metadeflector, the metalens consists of a square lattice of silicon nanocylinders taken from Fig. 2.3 of Chapter 2, on a quartz substrate, with a regular pitch a = 300 nm. The metalens is circular and has a diameter of 100 µm. Its 2D phase array is represented in Fig. 3.29a. It is designed to focus an incident plane wave of λ = 750 nm at a distance of 500 µm.
A total of 100 simulations were computed for each σ_D to average the response. We represent in Fig. 3.29a the far field diffraction calculations with the 2D phase profiles of each simulated metalens for 4 different values of σ_D. We also provide the variation of the Strehl ratio of the simulated metalens as a function of σ_D in Fig.3.29b.
As expected, these simulations demonstrate the high influence of an increasing σ_D on the efficiency of the metalens. A standard deviation σ_D = 12 nm halves the focused spot intensity at the focal plane, and decreases the Strehl ratio by 30%. We can therefore estimate the accuracy needed to fabricate a metalens showing good performances to σ_D = 10 nm.

3.3.2 Position error on Metadeflector

The influence of a statistical error on the nanocylinders positions is addressed here. As for the random error on the diameters, the statistical error on the positions is the consequence of the thermal, mechanical and electronic instabilities of the manufacturing process.
The calculations are performed here under exactly the same conditions as for the diameter error. In the initial state, each nanostructure is positioned on a regular square grid of pitch a = 300 nm. The error on the position is simulated by the following modification of the coordinates of each pixels:

$$(x_i', y_i') = (x_i + \delta x_i, y_i + \delta y_i) \tag{3.6}$$

Where (x_i', y_i') are the updated positions, and $(\delta x_i, \delta y_i)$ are the random variations of the position. $(\delta x_i, \delta y_i)$ are both following a gaussian distribution of standard deviation σ_{pos}. For each value of σ_{pos}, we perform 100 simulations to average the response. Fig. 3.30a shows the calculated relation between the deflection efficiency and σ_{pos}. We see that a standard deviation as large as σ_{pos} = 50 nm on the positions of the nanocylinders only decreases the deflection efficiency by 1%. This decrease is due to the fact that a part of the energy of the diffracted beam is converted into a diffusive background. Regarding Eq. 3.3, it means that a fraction of the energy accounted for by P_{diff} is now in P_{scat}.
Although the reported influence might be surprisingly low, especially when compared to the error on the diameters, a deeper comparison of each of these errors helps to understand their disparities. We have seen with Fig. 3.10 that a 5-10 nm error on the diameters starts to merge the configurations. This means that a 10 nm error in diameter is similar to a position swap of nanocylinders, which is equivalent to moving them by a distance of at least $a/2$ = 150 nm. This explains why a position shift of 40 nm still has a very weak influence, while a variation of the diameters of 10 nm has a very strong influence.
In addition, it should be noted that our simulations do not involve the EBL proximity effects causing the formation of bridges between two nanostructures that are too close [187] (as we saw in Chapter 2). Our quantification of the impact of the position errors appears then a little underestimated.

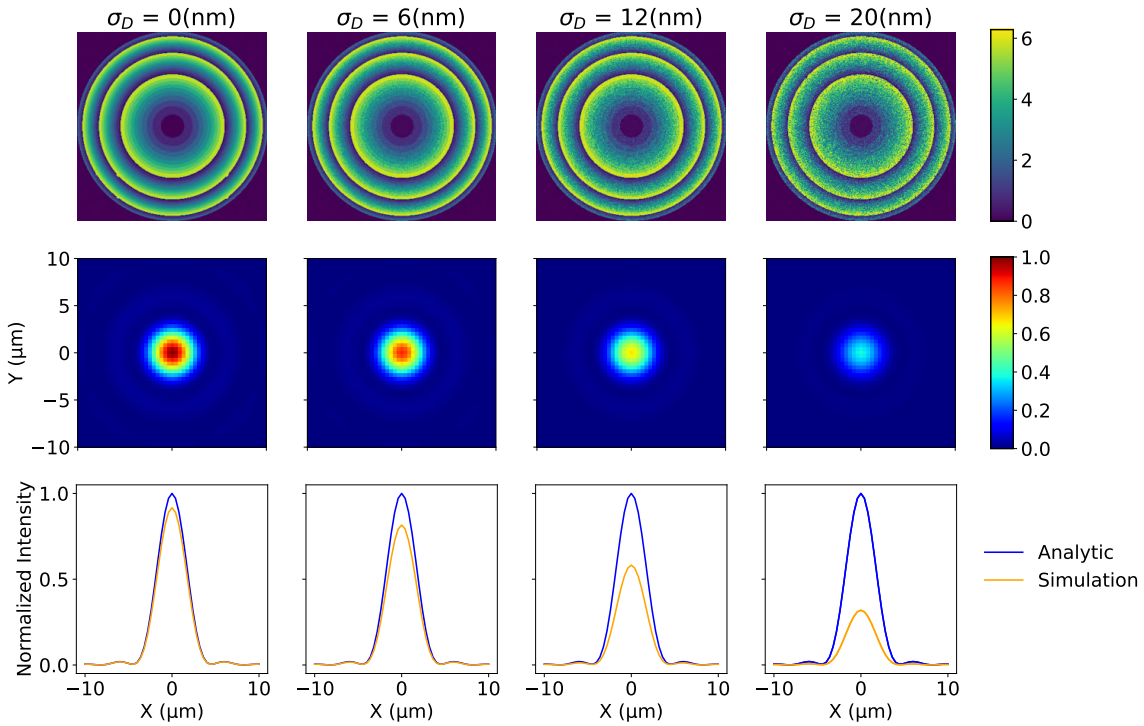

(a)

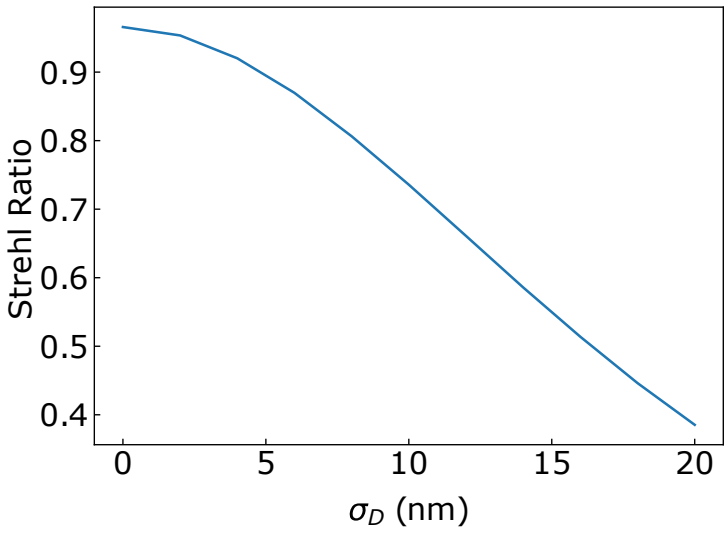

(b)

Figure 3.29: (a) Top: map of the dephasing induced by a metalens (diameter 100 µm, focal distance 500 µm) for different values of σ_D. Middle: corresponding intensity distribution in the focal plane. Bottom: transverse intensity profile in the focal plane of the imperfect metalens (brown line) and of a perfect lens (blue line). (b) Variation of the Strehl ratio of a metalens with the standard deviation σ_D.

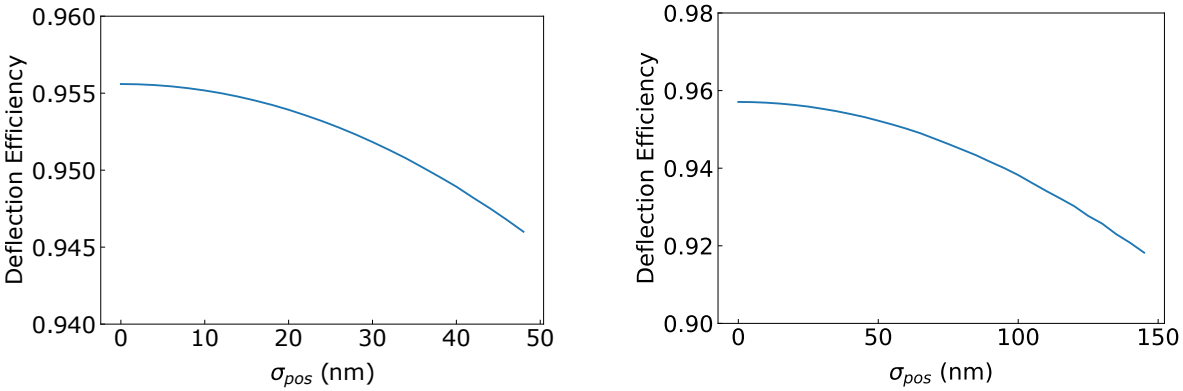

(a) (b)

Figure 3.30: (a) Influence of a random error on the positions of each nanocylinder on the deflection efficiency of a metadeflector. (b) Simulated deflection efficiency of a metadeflector as a function of the field stitching error.

3.3.3 Field Stitching error on Metadeflector

Finally, we look at how field stitching errors alter the optical performance of a metadeflector. We already described the origin of stitching errors in Chapter 2. For the simulations, we start from a metadeflector of size 552×552 µm^2 and split it into 8×8 different writing fields of size 69×69 µm^2 to match our fabrication conditions. Each writing field is then shifted from its reference position by $(\delta^{stit}x_I, \delta^{stit}y_I)$, meaning that all the nanocylinders of one writing field are identically shifted in position by $(\delta^{stit}x_I, \delta^{stit}y_I)$, the variations of which are following a gaussian distribution of standard deviation σ_{pos}. Here, since we calculate only 64 different writing fields, we need to increase the number of simulations up to 2000 (compared to 100 for the previous errors) for each σ_{pos} to average the results.
To compute the entire metasurface response, we start with the simulation of a 69×69 µm^2 metadeflector of complex amplitude $T_{\text{wf}}(u, v)$ following (see Eq. 3.5):

$$T_{\text{wf}}(u, v) = a^2 \sum_i \sum_j t(x_i, y_j) e^{-2i\pi(ux_i + vy_j)} \tag{3.7}$$

The total response $T_{\text{tot}}(u, v)$ of the 552×552 µm^2 metasurface is then derived:

$$T_{\text{tot}}(u, v) = T_{\text{wf}}(u, v) \sum_I e^{-2i\pi(ux'_I + vy'_I)} \tag{3.8}$$

where $(x'_I, y'_I) = (x_I + \delta^{stit}x_I, y_I + \delta^{stit}y_I)$, and (x_I, y_I) are the initial coordinates of each writing field.
The results are shown in Fig. 3.30b in which we show the deflection efficiency as a function of σ_{pos}. The stitching error appears to have a very small influence, as even a standard deviation σ_{pos} of 150 nm only decreases the deflection efficiency by 4%. In Chapter 2, we quantified field stitching errors as being equal to 70 nm. We can then conclude that the field stitching error decreases the fabricated metadeflector deflection efficiency by about 1%.

Conclusion and outputs

In this chapter, we have provided a detailed analysis of the influence of nanofabrication errors on the optical performance of metasurfaces. Our investigation shows that the errors with the strongest influence are a modification of the lateral shapes and environment of the nanostructures. These errors include variations of the diameters and lateral slope of the nanocylinders, as well as the addition of a small oxide layer on the lateral sides. On the other hand, the nanofabrication errors with the weakest influences are the ones altering the nanostructures vertical shapes and environments. These are the variations in height and the addition of an upper oxide layer.
Simulations of a change of the dielectric constant of silicon composing the nanostructures have also been performed. The modification of the real part of the refractive index mainly changes the resonance wavelengths without altering the metasurface's transmission, while the imaginary part only changes the absorption of the metasurface.
Finally, statistical errors on the diameters of the nanocylinders have shown very strong influence. We can generalize this result and infer that random errors on the lateral shapes of the nanostructures will also have a strong impact. On the opposite, position errors, whether on the individual positions of each nanostructure or due to field stitching, induce very weak deterioration of optical performance.

Related to external noise during the fabrication process, random errors are inevitable. Decreasing them goes along with an improvement of the manufacturing conditions, relating to the machines used (EBL, plasma etching) and their environment. On the other hand, systematic errors always occur in the same way for every fabrication iteration. We saw that their presence is partially coming from calibration measurement inaccuracies done by the user (for example diameter measurement).
We can think of two different methods to decrease the influence of these errors. The first implies the use of very precise characterization tools to refine the precision of the calibrations (as we did with TEM observations for instance). However, these tools often come with more constraints to ensure the high precision, and are still related to the user choosing visual criteria for the measurements. Moreover, some complex shape errors can be difficult to measure, and also to address for numerical simulations.
The second solution consists in establishing a direct link between the target geometries (i.e. the GDS mask) and their associated phase shift and transmission. Thus, even if systematic errors occur, they will be automatically taken into account by measuring the optical behavior at the output. All systematic errors can then be bypassed, independently of their complexity. For this purpose, we need to measure the complex amplitudes of manufactured metasurfaces, and use these values as a dataset for further fabrications. This second solution must then be supported by a characterization technique making it possible to recover the phase shift and the transmission of the manufactured metasurfaces. To this end, we describe in the next chapter the implementation of a ptychography technique and its application in metasurface characterization.

4 Characterization of optical metasurfaces with ptychography

In this chapter, we present optical *ptychography*, a phase and amplitude retrieval technique based on the collection of multiple diffraction patterns from an object. First, we introduce its historical background and explain its working principle. Then, we describe the experimental setup and explain how to optimize the resolution. Finally, we show some examples of ptychographic characterizations of metasurfaces. This chapter has been inspired by A. Baroni's thesis work supervised by P. Ferrand at the Fresnel Institute [221].

4.1 Introduction to ptychography

4.1.1 History

The term *ptychography* (*ptycho* means "to fold" in Greek) was first used in 1969 by Hegerl and Hoppe to describe a method for calculating the phase of Bragg reflections from a crystal [222]. Although very different from modern ptychography, and also abandoned, the name and principle have aroused new interest in the late 20^{th} century. At that time, many scientists were concerned about the difficulty of obtaining a direct measurement of the phase of objects, a problem known as the *phase problem*. Some methods based on field interference did work, but their applications were limited to larger wavelengths (visible, IR, ...). Indeed, interference techniques usually require the use of lenses, which, at the end of the 20^{th} century, had very high aberrations for shorter wavelengths (X-rays) and electron illuminations. Therefore, research on lensless techniques to solve the phase problem was very active. As a result, several methods based on coherent diffraction imaging (CDI) techniques emerged, relying on computer algorithms to recover the complex amplitude of objects based on their diffracted intensities.

Coherent Diffraction Imaging CDI refers to lensless computational imaging techniques for the reconstruction of non-periodic objects. The principle is to obtain an interference pattern from the object by illuminating it with a coherent light. From the intensity of the diffracted pattern that results from this illumination, CDI gives access to both the phase and the amplitude of the object [223].
Prior to the implementation of CDI, theoretical models for the resolution of the phase problem using the diffracted intensities have already been studied by Gerchberg and Saxton in 1972 [224], and by Fienup in 1978 [225].
These two techniques use an iterative loop to progressively induce corrections to an initial estimate of an object in order to converge to the correct solution. The corrections are applied from what we already know about the object (in the real domain) and its measured diffraction intensity (in the Fourier domain).

At the end of the 20$^{\text{th}}$ century, CDI was used for X-rays and electrons, either with the Gerchberg-Saxton or the Fienup algorithms. Although CDI is quite easy to implement, it must be used with some restrictions in order to solve the so-called uniqueness problem (several phase/amplitude pairs can have the same diffraction intensity). Among these restrictions, there is for example the Bates condition, which imposes a limit on the sample size (more information are given in the next section).

Rise of the ptychography In 2004, Faulkner and Rodenburg proposed a new technique to solve the phase problem [226, 227], that marks the beginning of modern ptychography. The iterative algorithm used is very similar to that of Fienup's technique. The main difference is that where Fienup's algorithm is applied for a single diffraction intensity for the entire sample, the ptychography algorithm is applied for multiple illumination positions (see Fig. 4.1). In their paper, the authors demonstrated the very high efficiency of the ptychography algorithm. In fact, the strength of ptychography compared to conventional CDI is due to the overlap of illuminations coming from the small shifts between two consecutive positions. The information that gives the complex amplitude of the object is in fact mainly recorded in the overlapping regions, making it a mandatory requirement [228]. In addition, the scanning property of ptychography also allows for the recovery of very large objects.
Over the years, the ptychography algorithm has been updated, improved, and experimentally demonstrated for various applications. Although it was originally designed for X-ray or electron applications, we now find many studies using ptychography for optical applications [228–231], and more specifically for metasurface characterizations [34, 35, 232].
It may be noted that other phase imaging techniques such as Quadriwave Lateral Shearing Interferometry (QLSI) [233, 234], or wavefront sensors [235], have also been used for metasurface characterization. However, ptychography offers the advantage of being easy to implement experimentally, not being limited by the sample size, and also giving the possibility to be updated to image the polarization state of objects (see vectorial ptychography described in the following). These are the reasons why we chose ptychography as our phase recovery technique.

4.1.2 Ptychography algorithms

Ptychography is a computational imaging technique used to recover the complex amplitude of an object. We illustrate its principle in Fig. 4.1. First, we illuminate a small area of an object and collect the resulting diffracted intensity. Then, we move the object relatively to the illumination to illuminate and collect the diffracted intensity of a new area. This last operation is then repeated for several positions, with the condition that the displacement is small enough to ensure an overlap area between two consecutive illuminations. The total number of positions N_{ac} can vary depending on the object we want to characterize, it can go from $N_{ac} = 100$ to $N_{ac} > 5000$. Finally, an iterative algorithm is used to retrieve the complex amplitude of the object from the recorded intensities.

4.1.2.1 PIE algorithm

We describe here the principle of the *Ptychography Iterative Engine* (PIE), implemented by Rodenburg and Faulkner [226, 227, 236], illustrated in figure 4.2.
We define $O(\mathbf{r})$ as the complex transmission function of the object we want to characterize

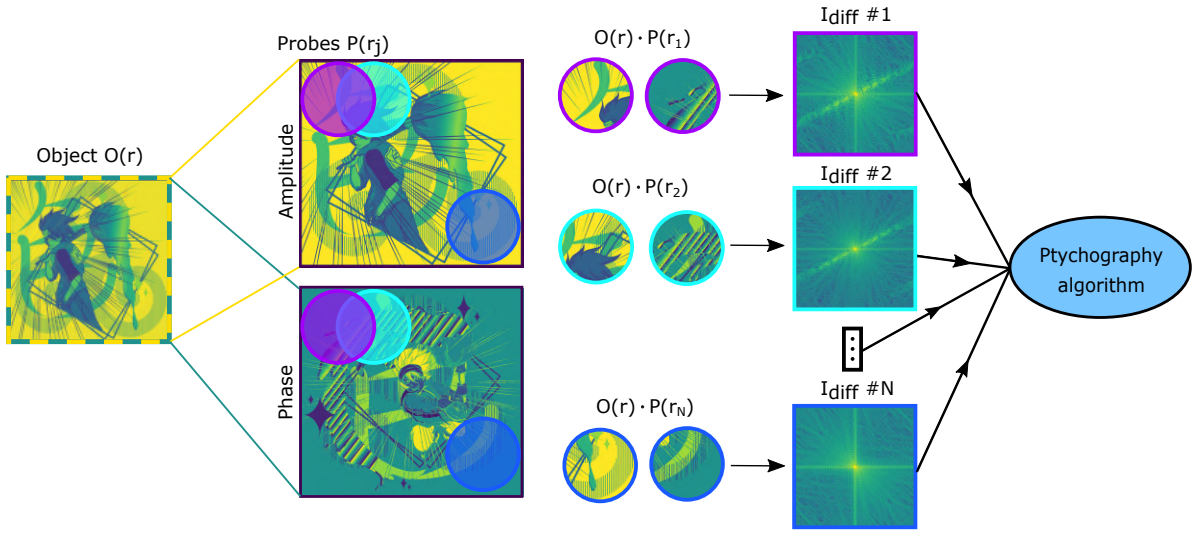

Figure 4.1: Presentation of the ptychography principle. A small area of an object is illuminated at different positions (magenta: position # 1, cyan: position # 2, ... , blue: position # N). The recorded diffracted intensities for every position are the input of the ptychography algorithm.

and $P(\mathbf{r})$ as the complex function associated with the illumination (the probe), where $\mathbf{r}$ is the position vector. The scanning positions are noted $\mathbf{r_j}$, for $1 \leq j \leq N_{ac}$. Since either the probe or the object can be moved while the other is fixed, we use both notations $O(\mathbf{r_j})$ and $P(\mathbf{r_j})$ even if only one of them is moved.
The idea of the PIE algorithm is to simulate the ptychography process illustrated in Fig. 4.1:

- We first define a guessed object $O_g(\mathbf{r_j})$, that we multiply with a known probe $P(\mathbf{r_j})$ to get the output field
$$\Phi_g(\mathbf{r_j}) = O_g(\mathbf{r_j}) \cdot P(\mathbf{r_j}). \tag{4.1}$$
- Then, we apply a Fourier transform to get the diffracted amplitude $\Psi_g(\mathbf{k_j}) = \mathrm{F}(\Phi_g(\mathbf{r_j}))$, where $\mathbf{k_j}$ is the reciprocal space coordinate.
- Comparing the guessed intensity $I_g(\mathbf{k_j}) = |\Psi_g(k_j)|^2$ to the measured intensity $I_m(\mathbf{k_j})$, we can calculate the error function
$$\mathrm{L} = \frac{\sum_j (\sqrt{I_m(\mathbf{k_j})} - \sqrt{I_g(\mathbf{k_j})})^2}{\sum_j (\sqrt{I_m(\mathbf{k_j})}} \tag{4.2}$$
- We then use $I_m(\mathbf{k_j})$ to derive the corrected diffracted amplitude
$$\Psi_c(\mathbf{k_j}) = \sqrt{I_m(\mathbf{k_j})} e^{i\arg(\Psi_g(\mathbf{k_j}))}, \tag{4.3}$$
to which we apply an inverse Fourier transform to get the corrected output field $\Phi_c(\mathbf{r_j}) = \mathrm{F}^{-1}(\Psi_c(\mathbf{k_j}))$.
- Finally, using $\Delta\Phi(\mathbf{r_j}) = \Phi_c(\mathbf{r_j}) - \Phi_g(\mathbf{r_j})$, we apply a correction to the guessed object:
$$O'_g(\mathbf{r_j}) = O_g(\mathbf{r_j}) + \frac{P^*(\mathbf{r_j})}{|P(\mathbf{r_j})|^2_{\max}} \cdot \beta\Delta\Phi(\mathbf{r_j}) \tag{4.4}$$

The step factor β is chosen empirically to allow the algorithm to converge better. A sufficiently strong correction step is needed so that the criterion does not lock into a local minimum, but it is also important to avoid making too large corrections in which case the optimal solution may be missed. The term $\frac{P^*(\mathbf{r_j})}{|P(\mathbf{r_j})|^2_{\max}}$ is the normalization term, which is there to take into account the spatial variation of the illumination energy and avoid divergent behavior. The idea is to weight the correction according to the illumination energy, in order to correct more strongly the most illuminated areas [228].

The PIE algorithm is then applied using the new guessed object until the error function L is small enough to ensure good convergence.

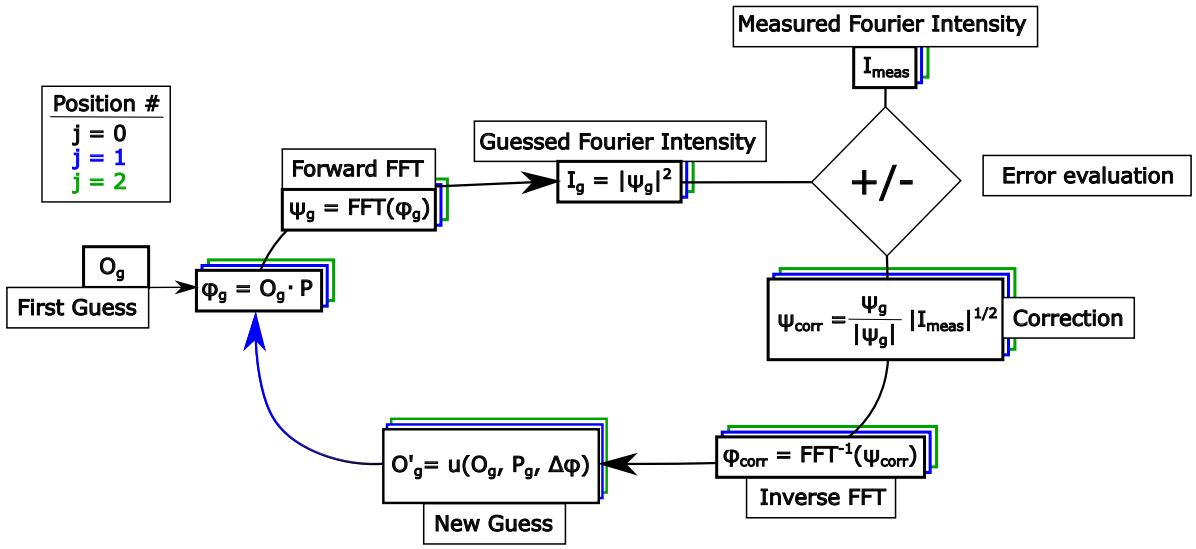

Figure 4.2: Illustration of the PIE algorithm applied for three acquisition positions.

Simulation example We show in Fig. 4.3 the example of a reconstruction using the PIE algorithm [1]. In this example, we first define an arbitrary object having for amplitude and phase two unrelated images of size 1000×1000 pixels. The scanning probe P is a uniform disk of amplitude 1 and radius 90 pixels. The r_j positions are arranged on a square grid of pitch $a = 18$ pixels to ensure an overlap of 80%, corresponding to the optimal value to have a good reconstruction [237, 238]. To prevent the appearance of periodicity artifacts, we also add a small random offset to each position [239, 240].
We first calculate the diffracted intensities $I_m(r_j)$ associated to each position and save them. We then apply the PIE algorithm. The number of iterations N_{it} is equal to 200, and we take β = 1. The initial guessed object O_g is a 2D complex matrix full of zeros. As we can see in Fig. 4.3, the reconstructed phase and amplitude perfectly match the targeted ones. Indeed, the average differences measured are respectively equal to 0.05 rad for the phase and 0.01% for the amplitude.

[1] The corresponding python script is provided in the Appendix.

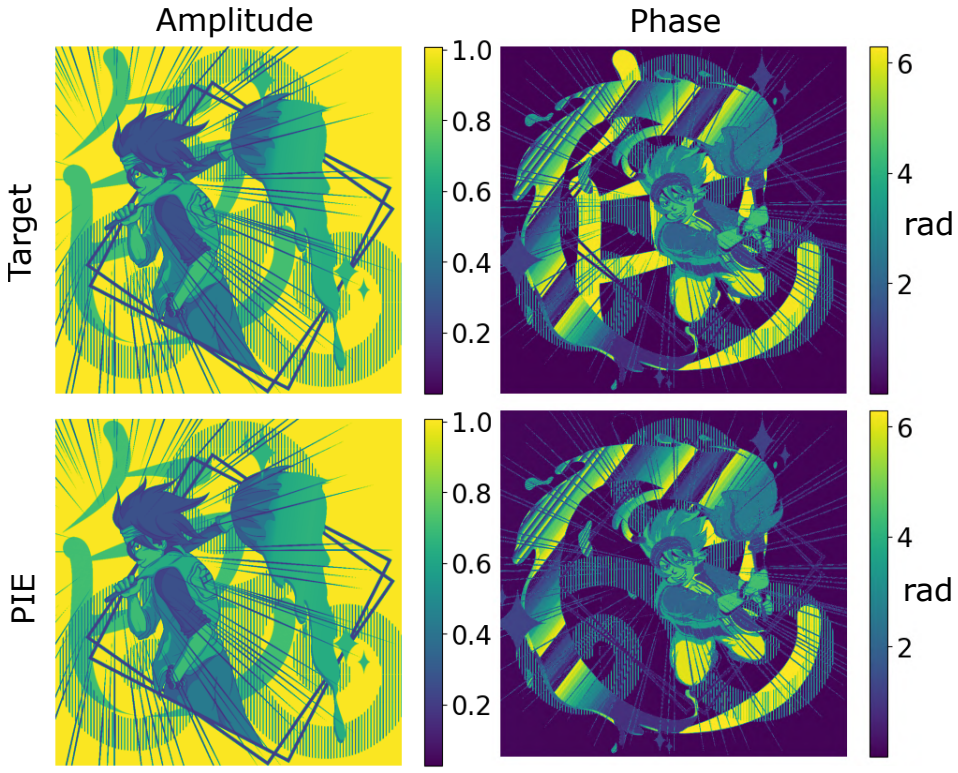

Figure 4.3: PIE reconstruction applied to a theoretical object, for which the phase shift and transmission maps are two unrelated images (drawing by Patoux Alexis).

4.1.2.2 ePIE algorithm

The PIE algorithm assumes that the probe P is perfectly known. However, this is generally not the case for experimental applications.
This ambiguity induces some artifacts in the object reconstruction. We show in Fig.4.5(d-e) the same PIE algorithm than before applied for the same object, but for an assumed illumination (Fig.4.5(f)) that differs from the actual illumination (Fig.4.5(c)). As we can see, the phase and amplitudes recovered are strongly altered.
To solve this problem, in 2009, the *extended ptychographic iterative engine* (ePIE) was demonstrated, allowing to recover the probe as well as the object [241]. Indeed, since the probe is not changing during the scan (for example, when the object is moved while the probe is fixed), the information on its complex amplitude is also hidden in the collected data. The ePIE algorithm (shown in Fig. 4.4) uses this information to find the probe and the object at the same time, without the need for additional information.
Basically, the algorithm is very similar to PIE, except that we also define a guessed probe $P_g(r)$ which is updated as follows:

$$P'_g(\mathbf{r_j}) = P_g(\mathbf{r_j}) + \frac{O^*_g(\mathbf{r_j})}{|O_g(\mathbf{r_j})|^2_{\max}} \cdot \gamma \Delta\Phi(\mathbf{r_j}) \tag{4.5}$$

where $\gamma \in [0, 1]$ is the parameter related to the strength of the probe correction.
The ePIE now involves two different factors: β and γ for the object and probe reconstruction respectively. In some situations, it can be useful to set these factors manually during the algorithm to speed up the convergence.

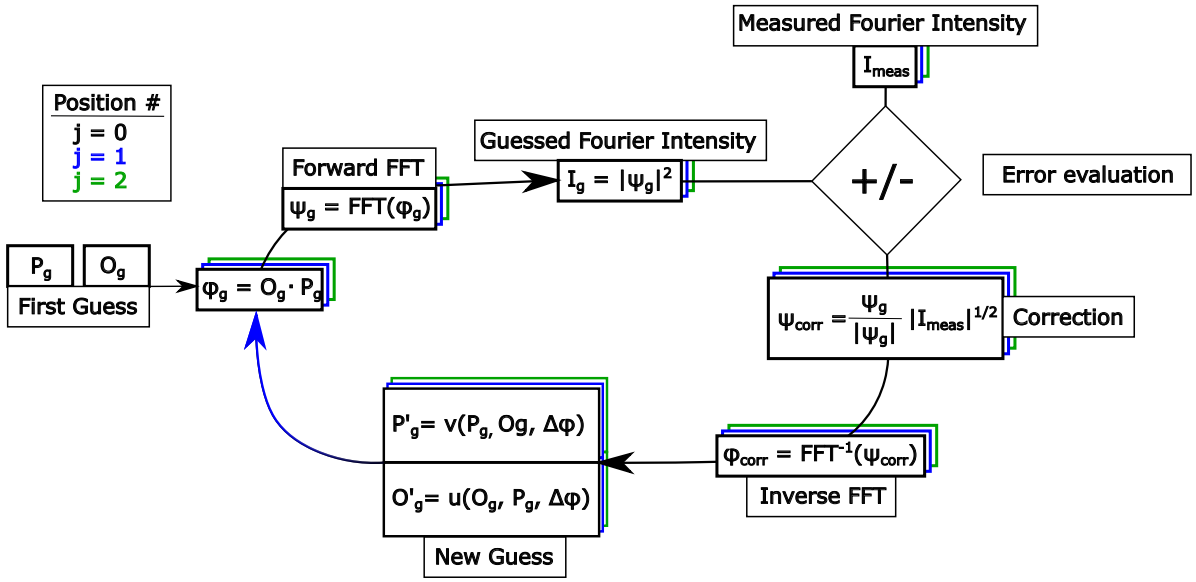

Figure 4.4: Illustration of the ePIE algorithm applied for three acquisition positions.

To illustrate the power of the ePIE algorithm, we apply it to the same problem as before, with the same starting assumptions O_g and P_g, and with $\beta = \gamma = 1$ and N_{it} = 200. We show in Fig. 4.5(f-g) the ePIE reconstructed phase and amplitude of the object, and in Fig. 4.5(h) the reconstructed probe. Here we clearly see the strong improvement of the reconstruction obtained for the same number of iterations for the probe and the object, which are now very close to the targeted values.
We find several variants of the ePIE algorithm in the literature, that usually consists into modifying the update functions (Eq. 4.4 and Eq. 4.5). For example, the *regularized PIE* (rPIE) [230] has the following update functions:

$$O'_g(\mathbf{r_j}) = O_g(\mathbf{r_j}) + \frac{P^*(\mathbf{r_j})\Delta\Phi(\mathbf{r_j})}{(1-\beta)(|P(\mathbf{r_j})|^2 + \beta|P(\mathbf{r_j})|^2_{\max}} \tag{4.6}$$

$$P'_g(\mathbf{r_j}) = P_g(\mathbf{r_j}) + \frac{O^*(\mathbf{r_j})\Delta\Phi(\mathbf{r_j})}{(1-\beta)(|O(\mathbf{r_j})|^2 + \beta|O(\mathbf{r_j})|^2_{\max}} \tag{4.7}$$

This ability of ePIE (and its variants) to reconstruct both the probe and the object makes it very popular and widely used.

4.1.3 Other ptychography developments

In addition to the ePIE algorithm that corrects for the complex amplitude of the probe and object, several other algorithms exist to improve the reconstructions.

4.1.3.1 pcPIE

Usually, the displacement between the probe and the object is obtained by moving the object on a translation stage. However, these displacements usually come with an imprecision on the positions, which add new artifacts that decrease the efficiency of ptychography.

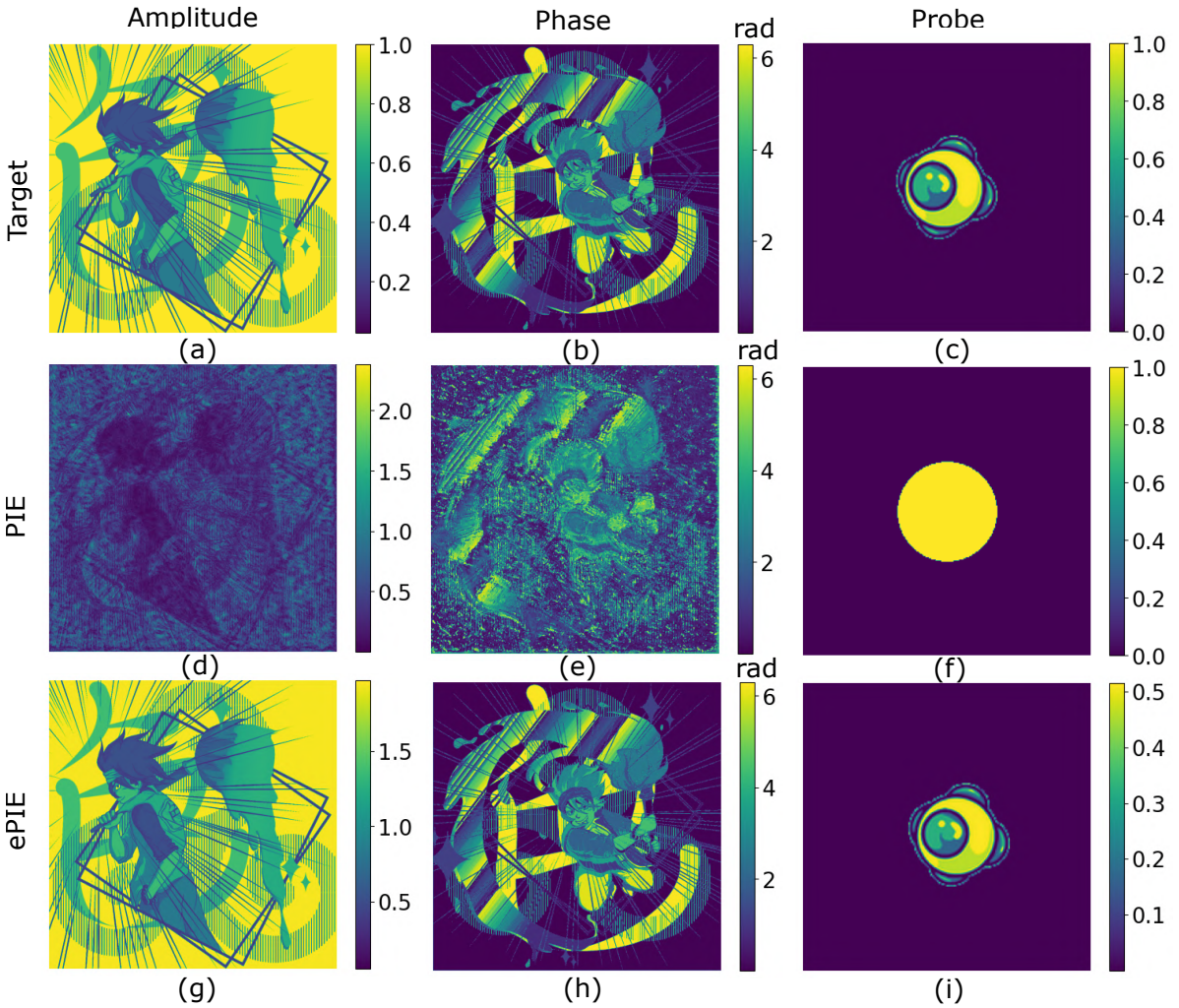

Figure 4.5: PIE and ePIE reconstructions applied to a theoretical object, for which the phase shift and transmission maps are two unrelated images, and an unknown theoretical probe (drawing by Patoux Alexis).

The *position correction PIE* (pcPIE) algorithm was thus implemented by Maiden *et al* [242, 243], and allows, in addition to the probe and object correction, to correct the illumination positions. The principle of pcPIE is illustrated in Fig. 4.6.
For each scan position $\mathbf{r_j}$, N_{pos} test positions $\mathbf{r'_j} = \mathbf{r_j} + \mathbf{\Delta r_n}$ are assumed. The displacement is written $\mathbf{\Delta r_n} = c\mathbf{m}$, where $c = |\mathbf{\Delta r}|$ is the norm of the displacement, and $\mathbf{m} = \dfrac{\mathbf{\Delta r}}{|\mathbf{\Delta r}|}$ is the direction.
We then calculate the error L for every $\mathbf{r'_j}$. The displacement that gives the smallest error then replace the theoretical position. For every iterations, we decrease the norm c of the displacement, allowing to finely correct every position errors of the system.

4.1.3.2 Conjugate Gradient

The use of the conjugate gradient method for ptychography allows to improve the convergence (*e.g.* by improving the noise robustness) [238, 244, 245].

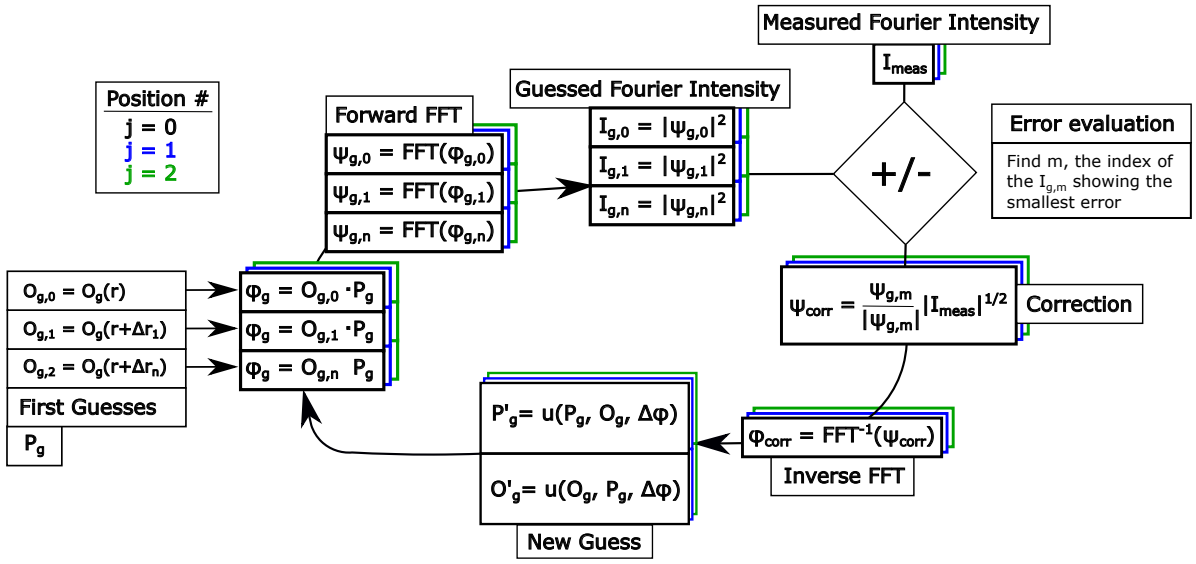

Figure 4.6: Illustration of the pcPIE algorithm applied for three acquisition positions.

The conjugate gradient is usually used to solve the following problem:

$$A \cdot \mathbf{x} = \mathbf{b} \tag{4.8}$$

where we try to find the vector $\mathbf{x}$ knowing A, an operator matrix which is positive definite and $\mathbf{x}$.
For example, a ptychography reconstruction similar to ePIE based on the conjugate gradient would use only one update function for the probe and the object. The corrections would also be applied to all positions simultaneously (as opposed to sequentially for ePIE). A vector $\mathbf{s}$ of dimension $[1 \times N]$ where $N = \dim(Og) \times \dim(P)$ is then defined:

$$\mathbf{s} = [Og, P] \tag{4.9}$$

The update function uses a variable parameter α (similar to β or γ for ePIE) applied to $\mathbf{s}$, which is automatically set for every iterations to control and accelerate the convergence.

4.1.3.3 vPIE

Until now, only the complex amplitudes of objects was reconstructed independently of their birefringences. The *vectorial PIE* (vPIE) algorithm, developed by Ferrand *et al* [246–248], allows to recover the Jones matrices of the object and probe, *i.e.* their total polarization states. This requires adding a polarizer and an analyzer before and after the object, and for each position, making several measurements for the polarization axes (*e.g.* three axes for the polarizer and for the analyzer).

4.2 Experimental application

In the previous section, we described several ptychography algorithms and showed numerical examples of their application. In this section, we describe the experimental setup we used to prepare our data. We also provide details on how the optical components influence the resolution of the reconstruction.

4.2.1 Experimental setup

The experimental setup is shown in Fig. 4.7. For the illumination, we used the same laser source as for the metadeflector characterization in Chapter 3, at λ = 750 nm.
First, the sample is put onto a motorized piezoelectric XYZ stage (Smaract). To control the position of the stage, we used *pymodaq*: an instrumentation software developed at CEMES by S. Weber [249], who helped us for its configuration and more generally in the setting up of the experimental bench.

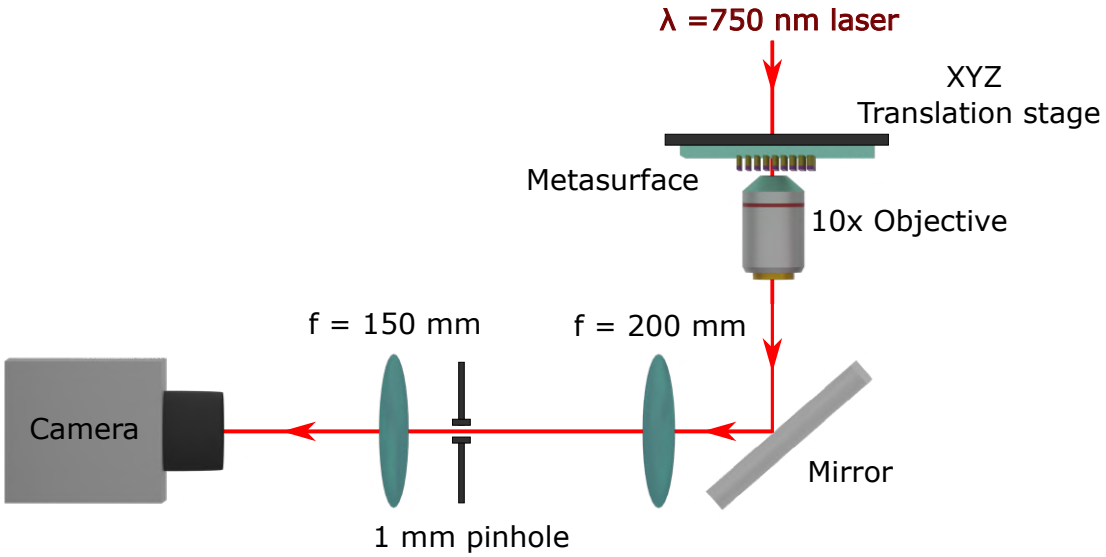

Figure 4.7: Optical bench used to collect diffraction patterns for ptychography reconstruction.

After the sample, a 10× microscope objective (NA_{Obj} = 0.25) collects the light. A mirror is then positioned to tilt the beam, followed by a lens of focal length $f = 200$ mm. The combination of the lens and the microscope objective creates a $4f$ configuration, that reconstructs the image of the object in the focal plane of the lens with a magnification factor $M = 11.1$[2], where we placed a custom 3D-printed pinhole with a diameter of 1 mm.
Thus, in this plane, we have both a magnified image of the sample, and a fixed physical pinhole, which is equivalent to have only a small portion of the magnified sample illuminated. When the sample is moved by a distance δd, the magnified image is moved by a distance $M\delta d$ relatively to the fixed pinhole. The ptychography reconstruction is then performed for this magnified image, enabled by placing a lens of focal length $f = 150$ mm and a camera sensor in the focal plane of this lens. The camera used is an Andor Zyla sCMOS, which has 2048×2048 pixels of size 6.5 µm, and a dynamic range up to 16 bits.

[2]The objective magnification is defined for a lens of $f = 180$ mm, so the effective magnification is $M = 10\times = 200/180 = 11.1$.

4.2.1.1 Alignment method

Since we are reconstructing a magnified image, we must be careful that the latter and the pinhole are in the same plane. To do this, we slightly modify the setup shown in Fig. 4.7 by removing the $f = 150$ mm lens, and placing a $f = 50$ mm lens 100 mm before the camera sensor. The camera now images the inverted intensity of the plane located at a distance $d = 200$ mm. Therefore, to ensure that the pinhole and the image of the sample are in the same plane, we can move them until they are both sharply visualized on the camera. Then, we can put the $f = 150$ mm lens back on, and make the ptychography acquisitions. We are now sure to reconstruct both the right probe and the right object.

4.2.2 Optimization of the resolution

Here we present how to optimize the resolution of ptychography by focusing on the optical components of the setup. More information on the issues related to specific optical components are presented in the Appendix.

4.2.2.1 Numerical Aperture

The relation between the plane of the sample and the plane of the sensor is a Fourier transform. We show in Fig. 4.8 how the spatial resolution δx in the real plane is related to the effective size Δq in the Fourier plane.

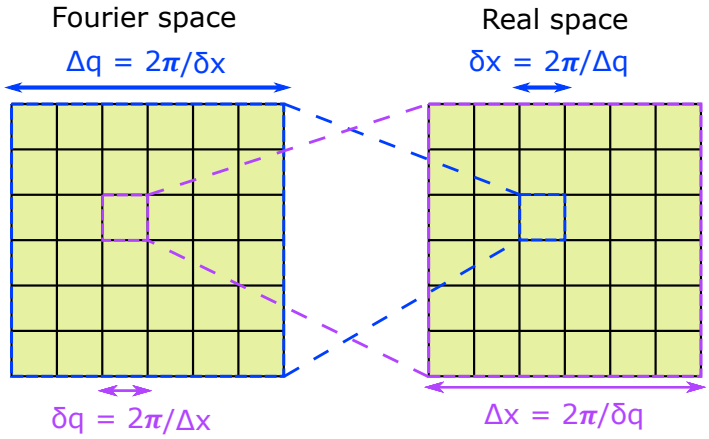

Figure 4.8: Illustration of the dimensional relations between the real space and the Fourier space.

Δq can be calculated from the numerical aperture (NA) of our setup. Usually, the latter comes either from the size of the sensor (NA_{cam}) or from the numerical aperture of the microscope objective we use just after the metasurface (NA_{obj}) [3].
NA_{cam} depends on the size S_{cam} of the sensor, the magnification factor M and the distance d between the camera sensor and the lens:

$$NA_{cam} = \sin(\arctan(\frac{S_{cam}}{2d}))M \tag{4.10}$$

[3] Some sensors have different sizes for the X and Y axes (which is not our case), for which we should distinguish $NA_{cam,X}$ and $NA_{cam,Y}$

δx is then given by:

$$\delta x = \frac{\lambda}{2NA_{cam}} \tag{4.11}$$

This value of δx gives the size in pixels of the object that is reconstructed by the ptychography script. Yet, if $NA_{obj} < NA_{cam}$, the effective resolution of our reconstruction would be $\delta x = \frac{\lambda}{2NA_{obj}}$ (see Fig. 4.9(b)). Therefore, the choice of the microscope objective is important to optimize the spatial resolution of the ptychography. The best configuration would be $NA_O = NA_x$ where no compromise is made.
Depending on the desired resolution, a different microscope objective can be chosen. In our configuration, the sensor has 2048×2048 pixels of size 6.5 µm, which gives NA_{cam} = 0.49 and a pixel size in the real plane of 0.76 µm. Thus, the limiting NA is coming from the objective microscope with NA_{obj} = 0.25 which gives an effective resolution of 1.5 µm.

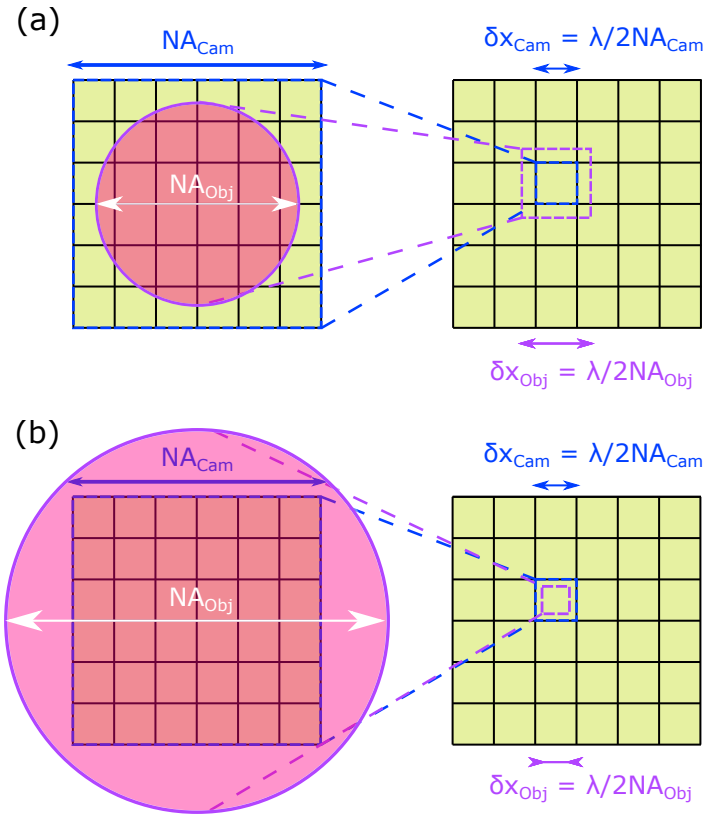

Figure 4.9: Illustration of how the resolution of ptychography is evaluated from NA_{cam} (yellow) and NA_{obj} (pink).

4.2.2.2 Bates Condition

Here we will focus on δq, related to the size of the camera pixels, and see how to adapt to its value. As we can see in Fig. 4.8, increasing δq will reduce the size of the window Δx in the real plane.
For CDI, a well-known condition, called Bates condition, states that the maximum size of the effective object (or probe size in our case) Δu that we want to retrieve must satisfy the

following inequality:

$$\Delta u < \Delta x/2 \tag{4.12}$$

In fact, this last relation is equivalent to having, in the Fourier plane :

$$\delta q_{eff} > 2\delta q \tag{4.13}$$

where δq_{eff} is the pixel size in the Fourier plane corresponding to the effective extension Δu. This condition thus guarantees that the sampling of the information in the Fourier plane is good enough to solve the phase problem.
In ptychography, although the Bates condition is not mandatory (since we find information in the overlapping regions of the probe), it is still advisable to respect it to ensure a good reconstruction. This means that the size of the probe (*i.e.* the pinhole) that we use must be less than half the spatial extension $\Delta x = 2\pi/\delta q$.
The relation between Δx and the pixel size p_{cam} is the following:

$$\Delta x = \frac{\lambda}{2NA_{pixel}} = \frac{\lambda}{\sin(\arctan(\frac{p_{cam}}{2d}))} \tag{4.14}$$

Applying this relation to our configuration (p_{cam} =6.5 µm) we find Δx = 17.3 mm. The upper limit of the pinhole size is therefore 8.65 mm.

4.2.2.3 Pixel binning

Thus, we see that for the 1 mm pinhole that we chose, we largely respect the Bates condition, and this even if the pixels of the camera sensor are 4 times larger (Δx = 4.4 mm).
It is then interesting to study the advantages offered by binning pixels:

- The first advantage is that it reduces the computation time of the algorithm since using smaller matrices;
- The second is that it increases the dynamic range of our data. Indeed, with a binning $n_b \times n_b$, the dynamic range of the data gains n_b bits. We then transform useless information (spatial oversampling) into useful information (dynamic range), which improves the accuracy of the ptychography reconstruction.

Therefore, we used a 4×4 binning for our reconstructions, which means that we have an effective camera sensor of 512×512 pixels with a pixel size p_{cam} = 26 µm, and a dynamic range of 20 bits.

4.3 Characterization of optical metasurface

In this section, we use ptychography to characterize two metasurfaces. We also explain the strategy used to improve the reconstructions.

4.3.1 First characterization of a highly diffractive object

One of the weaknesses of ptychography is the reconstruction of poorly diffracting or periodic elements [250, 251]. Indeed, the less diffracting an object is, the less information we have inside its diffraction pattern, which, for ePIE for example, makes the reconstruction of the probe more difficult.
Therefore, we show here the reconstruction of a highly diffractive object, which will help to finely retrieve the amplitude and phase of the probe of our system that can be used for future reconstructions. This object is a fabricated metalens which has been damaged and has some scratches (see Fig. 4.10(a)). Its size is 1×1 mm^2. Details on its design are provided in the next subsection.

Experimental parameters We measured the diffracted intensities of this broken metalens using the optical bench described previously, at $\lambda = 750$ nm. Between each acquisition, the metasurface is shifted by a distance $d_{step} = 19$ µm. We also added a random shift at each position from 0 to $d_{step}/4$. The total area scanned is 1100×1100 µm^2. There are thus $N_{ac} = 3249$ acquisitions for a mean overlapping value of 79%.

Preparing the reconstruction To facilitate the reconstruction, we first optimized the initial guess for the probe and for the object:
We already have information about the probe alone from its diffracted intensity (*e.g.* when the illumination passes through the substrate only). Moreover, we know that the probe has an nearly circular shape and is uniform. Therefore, we defined an initial probe as a disc of uniform intensity, and we adjust its diameter so that its calculated diffracted intensity is the closest to the one recorded.
For the object, we initiate its phase map as that of a spherical lens whose focal length and size match the values targeted for the metalens design (see next). We also chose a perfect transmission (amplitude of 1).

Noise treatment Since we are now using real data, we have to deal with noise. This is why we previously performed 10 acquisitions of background noise (without any illumination). We then subtracted from each recorded data the average intensity of the noise, and apply a threshold of $t = 0.01\%$ of 20 bits (all values lower than t are set to zero).

Algorithm parameters For the reconstruction, we applied the ePIE algorithm for 50 iterations, followed by a pcPIE correction for 425 iterations, and again ePIE applied for the corrected positions for 25 iterations. The parameters for the ePIE corrections are $\beta = 0.5$ and $\gamma = 20/N_{ac} = 0.006$. The values of β and γ comes from an optimization performed on several tests. For high value of γ, the applied corrections on the probe are too strong, making the ptychography algorithm diverge. For the pcPIE, we try 5 positions for each point, with

a maximum initial step $c_0 = 5$ µm that decreases continuously for each iteration following $c = c - c_0/425$.

Results The results of the ptychography reconstruction are shown in Fig. 4.10. First, we can see the scratches from which the metalens suffer. We also recognize the phase profile of a lens, with concentric rings in the phase shift reconstruction.

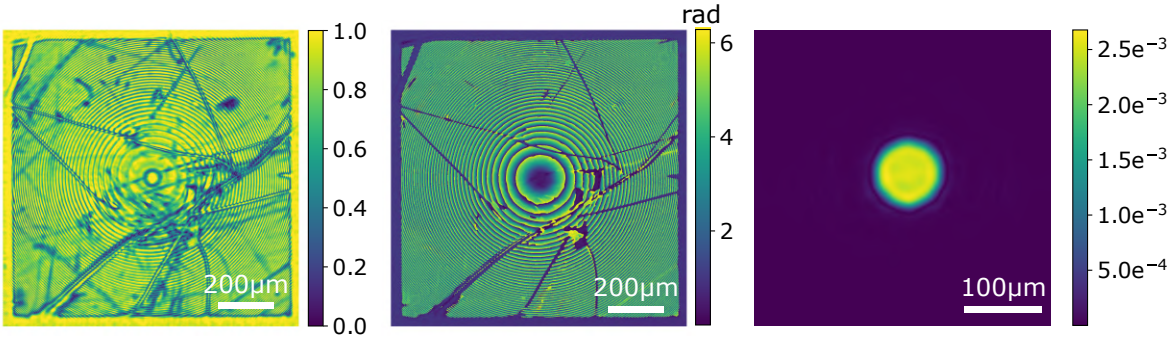

Figure 4.10: (a) Transmission and (b) phase shift of the broken metalens, and (c) probe amplitude obtained by ptychography. We note that the measured pinhole size is close to 90 µm, which is the size we expect to measure in the metasurface plane (1 mm / M = 1/11.1 = 90 µm).

Accuracy evaluation By looking at the reconstructed areas that are uniform (*e.g.* the substrate), we can evaluate the accuracy on the phase and on the transmission. The results show a standard deviations around 0.02 rad on the phase and 1% on the transmission.

4.3.2 Characterization of a metalens

We now show the reconstruction of an undamaged metalens. The latter was designed using the same geometries as those used for the design of the metadeflector in Chapter 3. Its size is 1×1 mm^2 and it is supposed to focus a $\lambda = 750$ nm plane wave at a distance $f = 5$ mm. The fabrication was also done using the process described in Chapter 2. We show in Fig. 4.11(a) a SEM image of this metalens.
The experimental setup and the applied algorithm are the same as the previous ones, except that we now use the recovered probe of Fig. 4.10(d) as an initial guess, and that $\beta = 0.1$ and $\gamma = 0.12/N_{ac}$. The phase and amplitude recovered by ptychography for this metalens are shown in Fig. 4.11(b-c). As for the broken metalens, we recognize here the phase profile of a lens.

4.3.3 Analysis of the metalens performances

Based on the recovered complex amplitude, we can extract information on the metalens efficiency. To do this, we consider three different lenses: (i) an analytically defined perfect (or ideal) simulated lens, (ii) the *Expected From Simulated Dataset* (or EFSD) simulated lens, and (iii) the fabricated and characterized metalens. The ideal lens has a perfect transmission and a

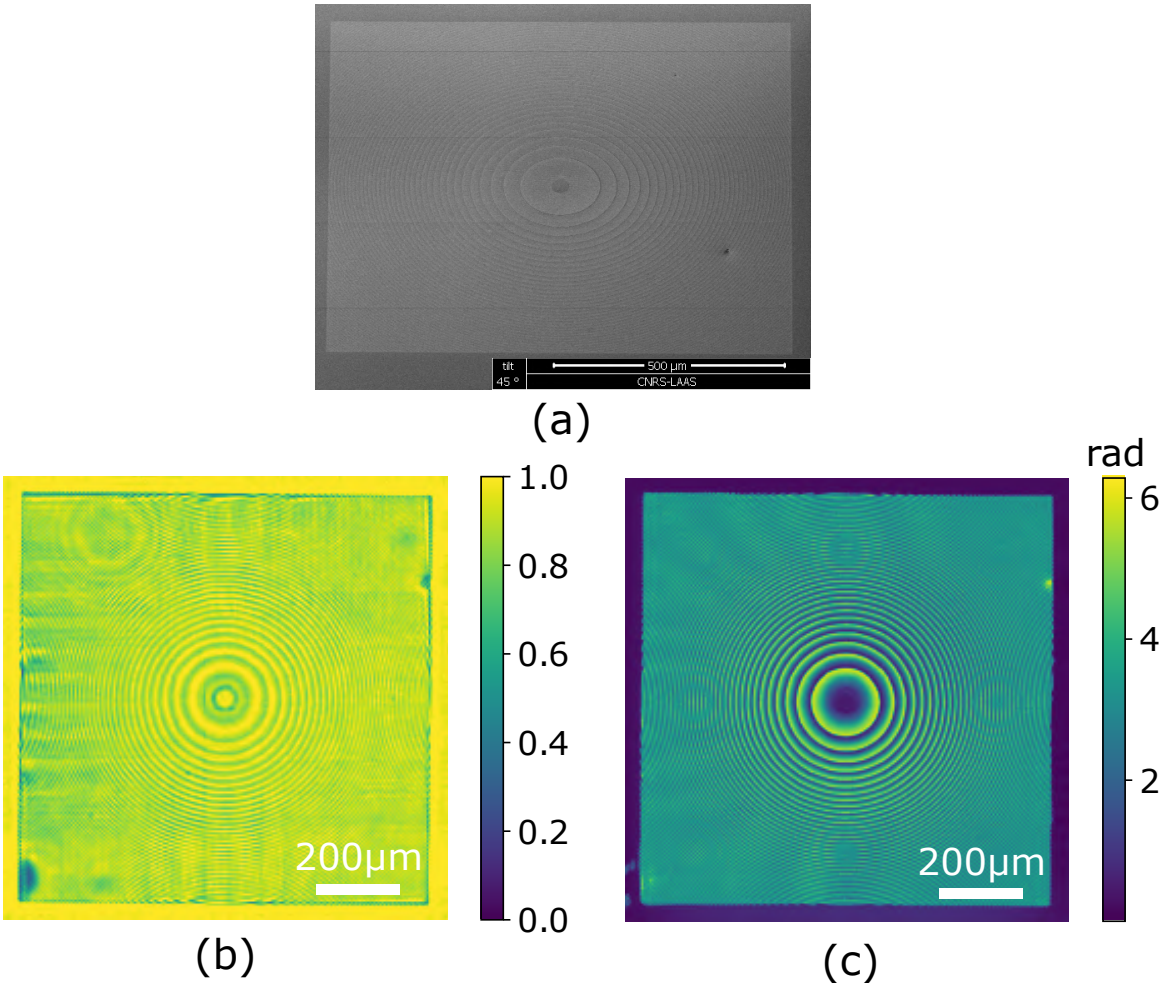

Figure 4.11: (a) SEM image of the fabricated metalens. (b) Transmission and (c) phase shift obtained by ptychography.

spherical wavefront centered on the focal point. The EFSD lens is defined only using the complex amplitudes of the 10 configurations we selected to design of the metadeflector in chapter 3 (Fig. 3.1). Since it takes into account the optical responses induced by the nanostructures, the EFSD lens is expected to perform closely to the fabricated metasurface.
We use the python package *pyoptica* to repropagate the fields corresponding to the complex amplitudes of the three lenses. In Fig. 4.12, we show the focused intensities at the focal distance $f = 5$ mm for (a) the ideal lens, (b) the EFSD lens, and (c) the measured metalens. As can be seen, the diffracted intensity profiles of the three lenses are very close.
We then consider the focusing efficiency, defined as the ratio of the intensity at the focal plane inside a circular aperture of diameter three times the *Full Width at Half Maximum* (FWHM) to the total incident power. The latter are $\eta_{ideal} = 81\%$, $\eta_{EFSD} = 77\%$ and $\eta_{fab} = 75\%$ respectively for the ideal lens, the EFSD lens and the fabricated metalens. We also calculated the ratios between the maximum focalized intensities which are $I_{m,fab}/I_{m,ideal} = 0.74$ and $I_{m,EFSD}/I_{m,ideal} = 0.87$.
Finally, we look at the Strehl ratio. The latter is evaluated equal to $S_{fab} = 92\%$ for the fabricated metalens, against $S_{EFSD} = 96\%$ for the EFSD metalens.
For all calculations, we applied a circular aperture of 1 mm diameter on each lenses profiles,

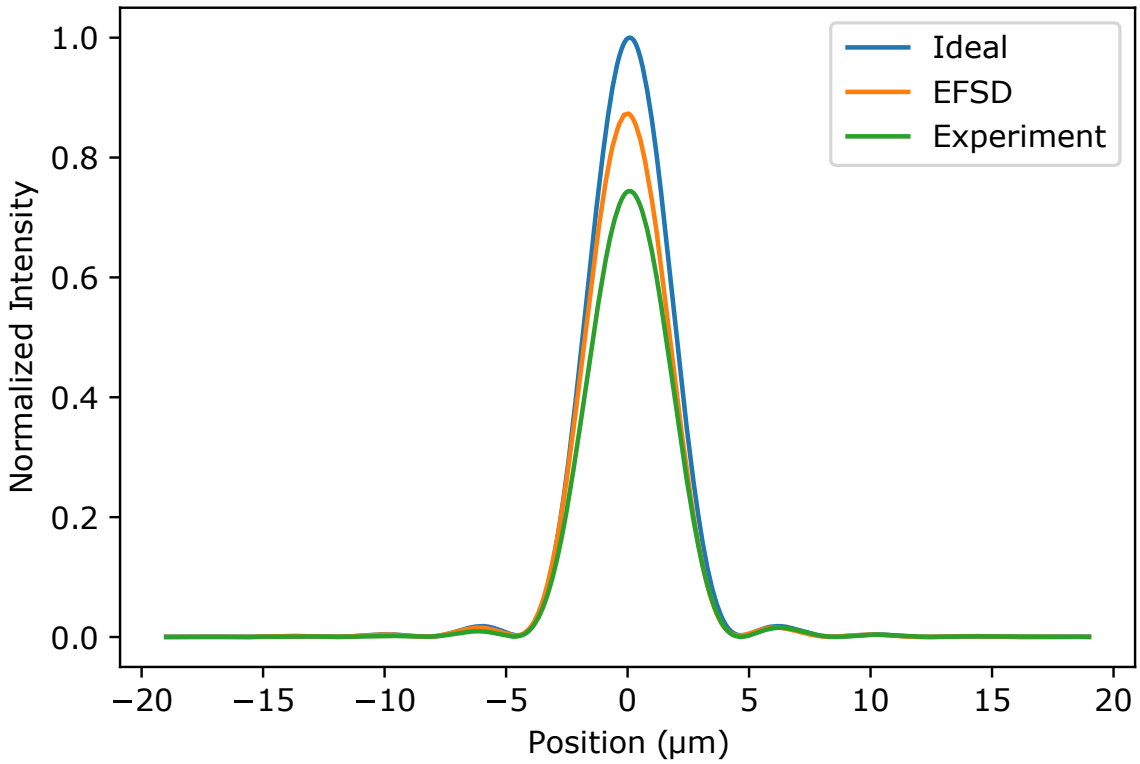

Figure 4.12: Intensities at the focal plane of the ideal lens, the EFSD metalens and the fabricated metalens (at $Y = Y_{max}$).

in order to avoid that defects on the edges of the fabricated metalens have an impact on the results. In particular, this minimize the influence of an error in the orientation of this metasurface in the XY plane. Indeed, the wavefront having a circular symmetry, the application of a circular aperture makes it less sensitive to a XY rotation.
From all these calculated values, we can confirm the high efficiency of the fabricated metalens. However, comparing its performance with that of the EFSD lens, we notice a non-negligible impact of the nanofabrication errors (4% decrease for the focusing efficiency and the Strehl ratio).

Conclusion

In this chapter, we introduced the computational imaging technique of ptychography. We presented our experimental setup, detailed how to calculate its resolution and explained how to optimize the latter. Finally, we have demonstrated the high efficiency of the technique by showing two reconstruction examples, that allowed us to characterize a fabricated metalens. As for the metadeflector, the performances of the fabricated metalens are impaired by the nanofabrication errors we identified in Chapter 3. In the next chapter, we will present a new design strategy that uses ptychography to overcome these errors and improve the performance of our metasurfaces.

5 Mimization of the influence of fabrication errors using a Ptychography-based design method

In this chapter, we present a new method for the design of metasurfaces based on systematic ptychography reconstructions. First, we introduce the latter and contrast it with the traditional numerical simulation-based approach. The design and fabrication of a new metalens is then described, which includes the fabrication and ptychography characterization of a first reference metasurface. Finally, we compare the new metalens' performance to that of the one fabricated in the previous chapter.

5.1 Presentation of the method

5.1.1 Usual design strategy: based on simulations

The standard approach for metasurface design and fabrication, that we used in Chapter 2, is shown in Fig. 5.1(a). At first, it uses numerical simulation techniques to investigate configurations that induce specific optical responses (FDTD, RCWA, FEM, ...). Finding these configurations can be done in a variety of ways. For example, to make the research process easier, one can limit the types of structures to be used (nanodiscs, nanorods, etc.). Other approaches, based on neural networks (Deep Learning), are less constrained and can access the optical response of non-intuitive designs.
Once the metasurface design has been determined, the purpose is to ensure that the dimensions of the fabricated nanostructures are as close to those simulated as possible. Two strategies can be used for this:

- Use SEM, TEM, and ellipsometry characterizations to optimize the fabricated nanostructures (*e.g.* making dose tests).
- Use these characterizations to optimize the simulated structures. For example, during our fabrication process, we used the thickness of the deposited silicon as well as its measured refractive index to generate a new simulation set.

The final metasurface is then fabricated, with optical properties that should be the closest to the simulated ones.
Yet, despite all of these steps, we saw in Chapter 3 that some discrepancies can still exist. The latter are due to the precision limit of the instruments used to characterize and optimize the designs (we had, for example, measured a silicon thickness of 370 nm by ellipsometry and 390 nm by TEM). As a result, there is a clear limit in terms of minimizing the impact of fabrication errors on metasurface performance. It should also be noted that, depending on the desired level

of precision, optimizations involving multiple TEM or SEM characterizations can be very time consuming.

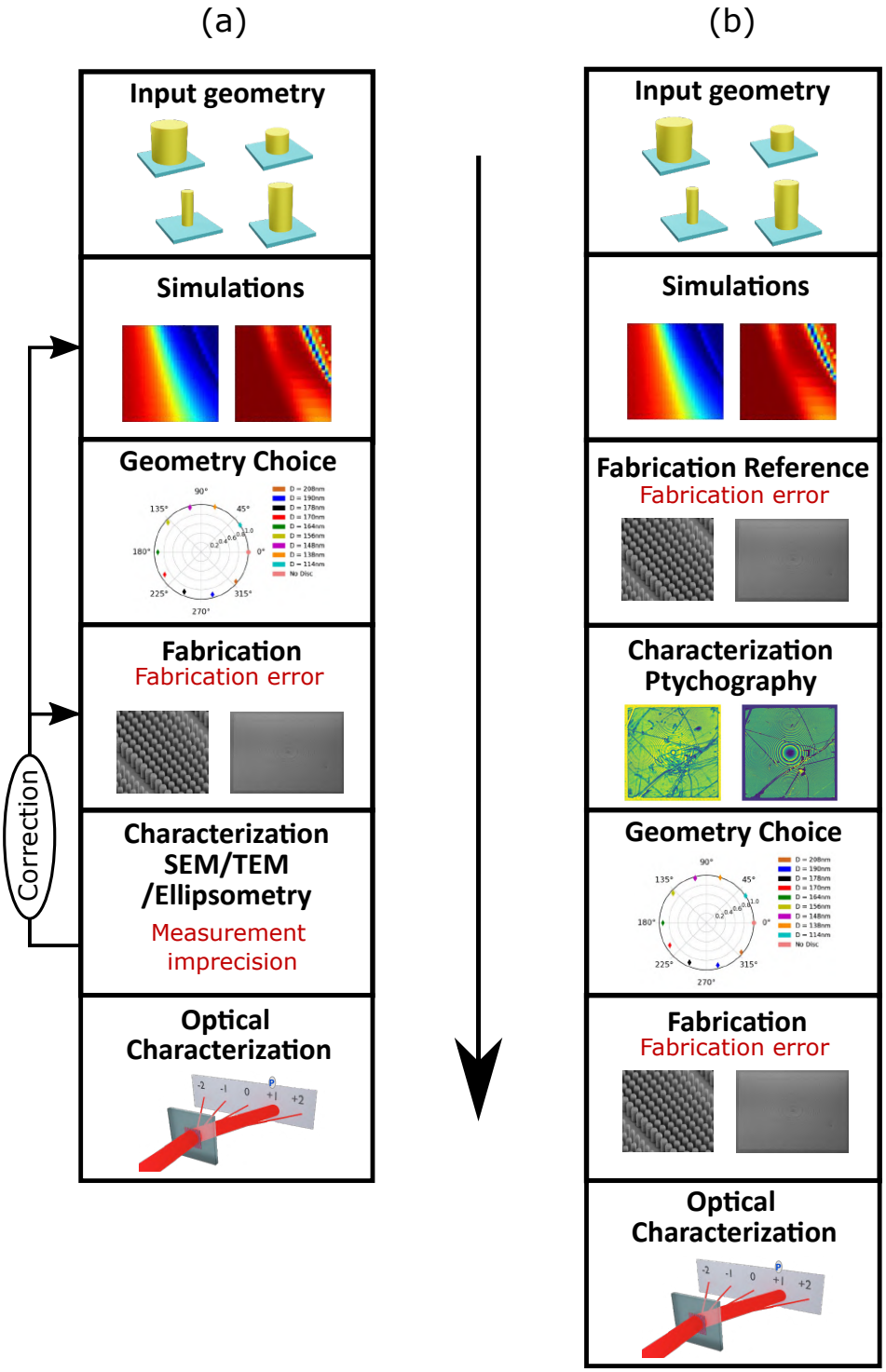

Figure 5.1: Illustration of (a) the conventional strategy based on numerical simulations and (b) the new strategy based on ptychography characterizations used for the design and fabrication of metasurfaces.

5.1.2 New design strategy: based on characterization

Therefore, we present a novel metasurface design approach, illustrated in Fig. 5.1(b). The objective here is to identify the optical properties of nanostructures directly using ptychography rather than performing numerical simulations.
First, to establish the relationship between geometries and optical responses, a *reference metasurface* is designed, fabricated, and characterized by ptychography. Thus, even if the fabricated nanostructures' geometries differ from the expected designs, the measured optical responses will account for these differences. Then, a dataset created from this relationship is used to design and fabricate new metasurfaces. Since the fabrication process does not vary between the reference metasurface and subsequent ones, this method allows to overcome systematic fabrication errors without the need of SEM or TEM measurements, while ensuring optical responses as close to those predicted as possible.

5.2 Fabrication and characterization of a reference metasurface

In this section, we discuss the design and fabrication of a reference metasurface, from which a database of silicon nanodisc optical responses is extracted.

5.2.1 Design of the reference metasurface

We want to create a dataset for this metasurface that is similar to the one generated by the FDTD simulations in Chapter 2 (phase shift and transmission maps shown in Fig. 2.3). The corresponding design is shown in Fig.5.2. The latter consists of several squares of size 30×30 μm^2 composed of silicon nanodiscs of identical diameters D that are arranged on a regular square grid of pitch p. For each different square, the diameters of the nanodiscs and cell sizes vary. From bottom to top, the diameter increases from D = 50 nm to D = 340 nm with a step of 10 nm. From left to right, the cell size increases from p = 200 nm to p = 390 nm with a step of 10 nm. Squares with a nanodisc edge-to-edge distance of less than or equal to 50 nm are not considered (hence the "staircase" shapeof the metasurface). Indeed, if the density of structures inside a square is too high, the proximity effect that occurs during EBL will be too strong, causing the structures to merge. To avoid optical couplings, all of the squares are separated by a 30 µm distance.
Thus, by characterizing the corresponding phase and amplitude for each square, we can recreate new amplitude and phase maps. However, we need to consider only the center region of each square, in which the environment is similar to that of an infinite, periodic metasurface (as in the FDTD simulations of Chapter 2). Indeed, the environment changes in two ways as one approaches the edges. First, the optical coupling is altered, as there are fewer nanostructures surrounding each structure. Second, the proximity effects that occur during EBL are reduced, resulting in smaller nanostructures.

5.2.2 Ptychography of the reference metasurface

The reference metasurface is fabricated using the same process as the one described in Chapter 2, with the exception that the electron dose applied during EBL is the same for all structures and is 900 $\mu C/cm^2$.
Ptychography measurements were taken for a total of N_{ac} = 6566 scanning positions. For the initial probe and object guesses, we used the previously reconstructed probe and a full matrix of 1, respectively, and the same reconstruction process as in the previous chapter.
The reconstructed phase shift and transmission of this metasurface are shown in Fig. 5.3(a-b). We can clearly identify the squares and observe a variation in the measured phase shifts as a function of diameters and cell sizes. We can also see that the squares start to disappear for small diameters and large cell sizes. There are two possible explanations for this phenomenon. First, because the density of structures (the proportion of the surface covered by the nanodiscs) is very low. Second, because thinner and more isolated structures are more fragile, and thus more likely to be torn off during the fabrication process.

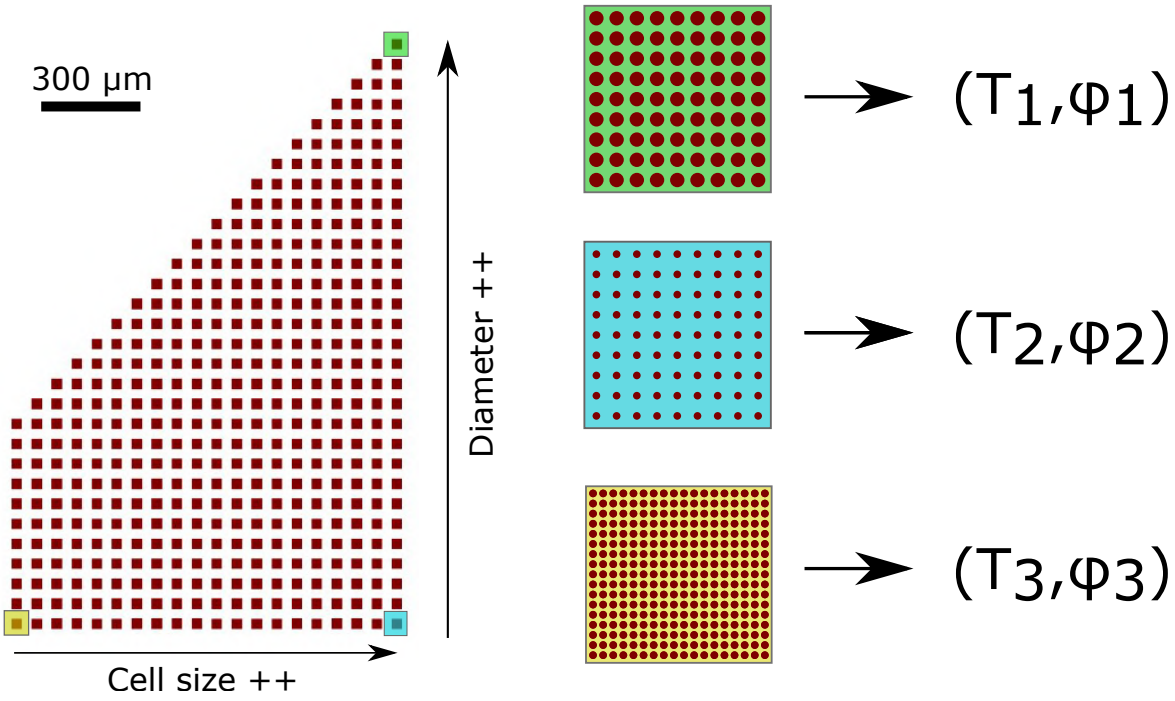

Figure 5.2: Design of the reference metasurface. Each square on the left are 30×30 µm^2 and are made of identical nanodiscs on a periodic grid (see zooms in green, blue and yellow color for three squares). We suppose that each square will induce a uniform phase shift and transmission that will be measurable using ptychography.

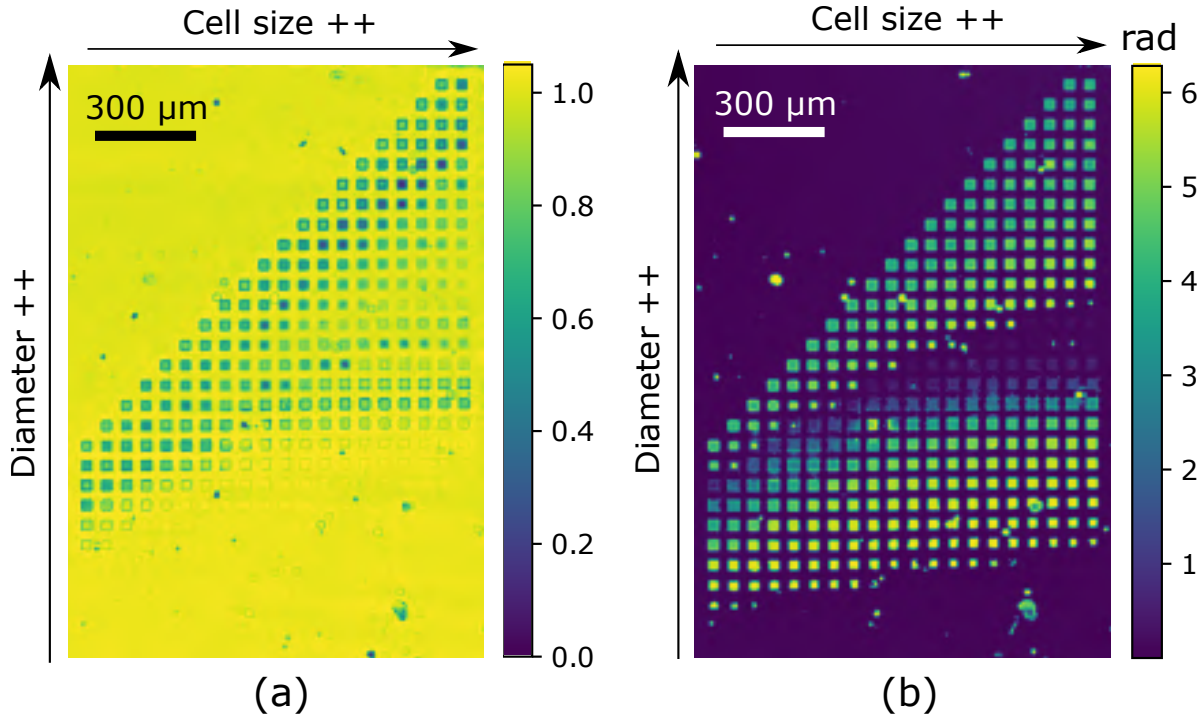

Figure 5.3: Transmission (a) and phase shift (b) of the reference metasurface retrieved by ptychography.

5.2.3 New phase-shifts and transmission maps

5.2.3.1 Construction of phase-shifts and transmission maps from ptychography measurements

Using the ptychography reconstruction shown in Fig. 5.3, new phase shift and transmission maps can now be generated. To do so, we consider a centered surface for each square that corresponds to a 15×15 μm^2 region, from which we extract the average phase shift and transmission value.
We show the extracted phase shift and transmission maps in Fig. 5.4. The white triangles in the upper left corner represent missing data (pairs of (D, p) that were not fabricated). As can be seen, there is a high transmission that decreases as the diameter approaches the cell size, as well as a significant phase shift variation as the diameter increases.

5.2.3.2 Comparison with FDTD simulations

We now compare these maps to the ones created using FDTD in Chapter 2. We show in Fig. 5.5 a direct comparison between the measured and simulated maps for the range of nanodiscs diameter $200\text{ nm} \leq D \leq 400\text{ nm}$ and periodicity (or cell size) $200\text{ nm} \leq p \leq 400\text{ nm}$. As before, the white triangles in the upper left corner of the ptychography maps represent missing data. We can make a number of observations on all these maps:

- The phase shift diminishes as the diameter grows, and for diameters around 150 nm, the decrease is accelerated.
- For small diameters, the transmission is very high but starts to decline around $D = 150$ nm.

However, we find that the measured phase shift and transmission decrease faster than those of the FDTD simulations. In fact, these differences can be explained because the real dimensions of the fabricated nanostructures do not always match the tailored dimensions, due to two factors:

- For our previous fabrications, we applied an exposure dose ranging from 855 to 1260 μC/cm^2 during EBL to be more accurate on the nanodiscs dimensions. As the diameter of the nanodiscs grew larger, the value of the applied dose decreased. For the reference metasurface fabrication, however, we used the same 900 μC/cm^2 dose for all nanodiscs. Thus, the largest structures were overdosed while the smallest ones were underdosed. As a result, after fabrication, the largest structures are actually larger than expected, and the smallest structures are smaller than expected (e.g., a coded diameter of 150 nm may have an actual output diameter of 160 nm). This explains what we see in Fig. 5.5: the decrease in phase shifts and transmissions are faster that the ones observed for the FDTD simulations.
- Furthermore, the fabrication defects discussed in Chapter 3 impact the fabricated nanodiscs' geometries (additional error on diameters, side tilt, oxide layers). These fabrication imperfections are accounted for in the measured data of the reference metasurface, which may also explain why the measured and simulated maps differ.

5.2.4 Selection of the geometries to use for fabrication

Using these new maps, we identify a cell size p that allows to cover a phase shift from 0 to 2π while maintaining the highest transmissions, just as we did in Chapter 2. Based on this cell-size, we then define the interpolated function ϕ_{pty}, which relates the diameters of nanodiscs to their induced phase shifts. Finally, we select ten configurations using ϕ_{pty}^{-1} to induce phase shifts $\Phi_k = k\pi/5$. We still consider the absence of nanostructures to have a phase shift $\Phi_0 = 0$ and a transmission $T_0 = 1$.

Error in the design In fact, I realized while writing this manuscript that I had made a mistake in choosing the appropriate periodicity. Indeed, I unfortunately confused two different columns of the reference sample and chose geometries for the periodicity $p = 350$ nm, thinking that these values were those for the periodicity $p = 300$ nm.
To illustrate the impact of this error, we display in Fig. 5.6 the phases and amplitudes of the 10 selected configurations (diameters chosen from the ptychography results performed on the $p = 350$ nm cell, but later erroneously selected for fabrication with a $p = 300$ nm pitch) in a polar representation. We also show, for comparison, the 10 expected configurations (if we used the periodicity $p = 350$ nm). As we can see, the chosen configurations do not regularly sample the phase shift range of $0-2\pi$, contrary to our expectations, and have transmissions that are also lower. Therefore, we expect the metasurface fabricated with these configurations (which we describe in the following section) to underperform.

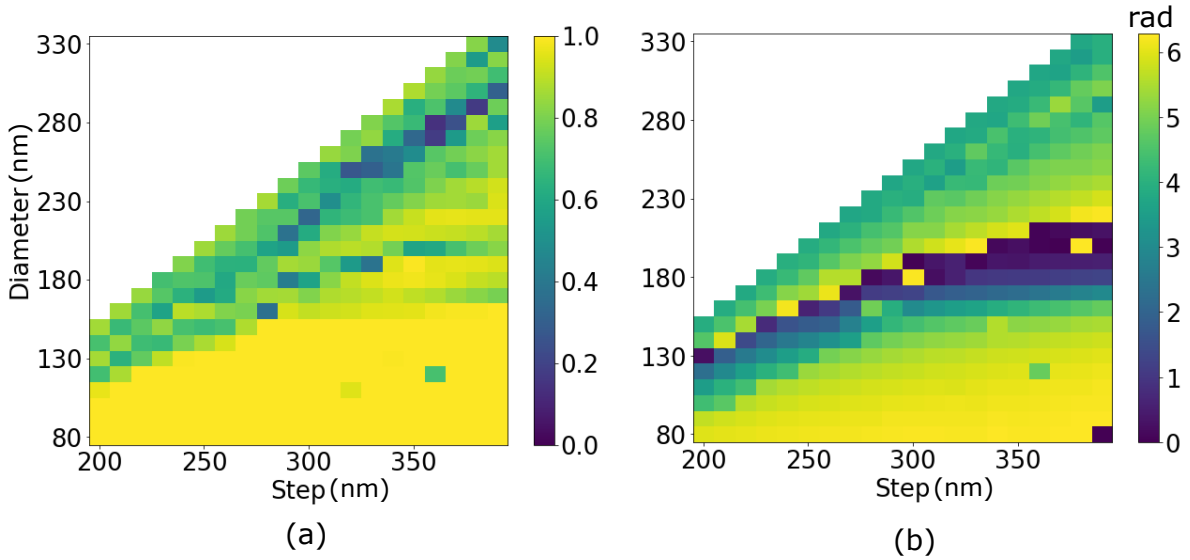

Figure 5.4: Transmission (a) and phase shift (b) maps obtained from the reference metasurface.

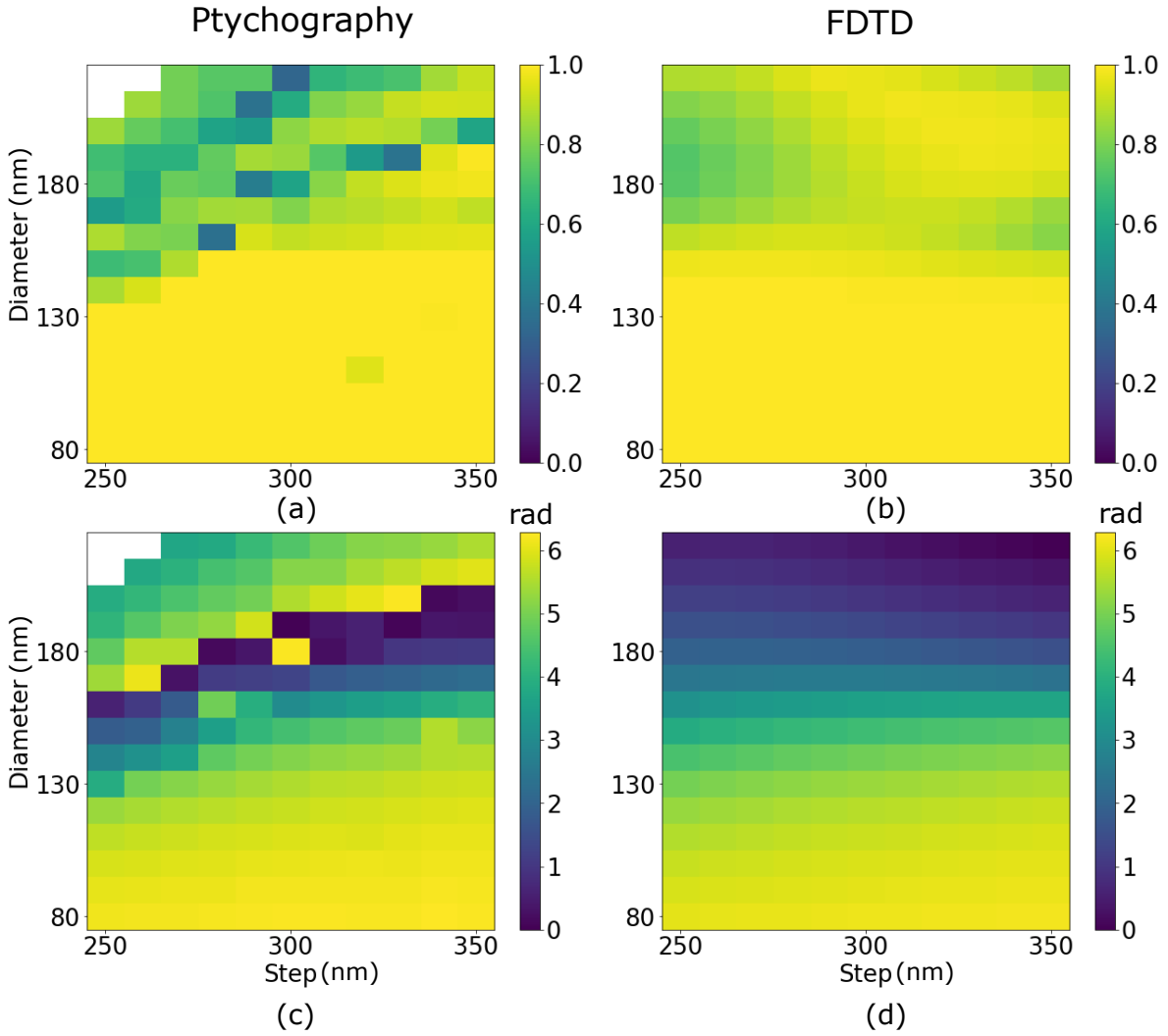

Figure 5.5: Comparison between the amplitude and phase shifts extracted from the reference metasurface ((a,c)) with the FDTD simulations ((b,d)) for corresponding geometries.

5.3 Comparison between the two metalenses

Using the new configurations, we design and fabricate another metalens, with the same targeted focal length as in the previous chapter (f = 5 mm at λ = 750 nm). The fabrication process is identical to the one used for the reference metasurface. An optical microscope image of this metalens is shown in Fig. 2.12b of chapter 2. For simplicity, the two fabricated metalenses are referred to in the following as the *ptychography metalens* and the *FDTD metalens* respectively.

5.3.1 Ptychography characterization of the new metalens

We apply the same ptychography process as the one used for the FDTD metalens. The retrieved phase and transmission profiles are shown in Fig. 5.7.

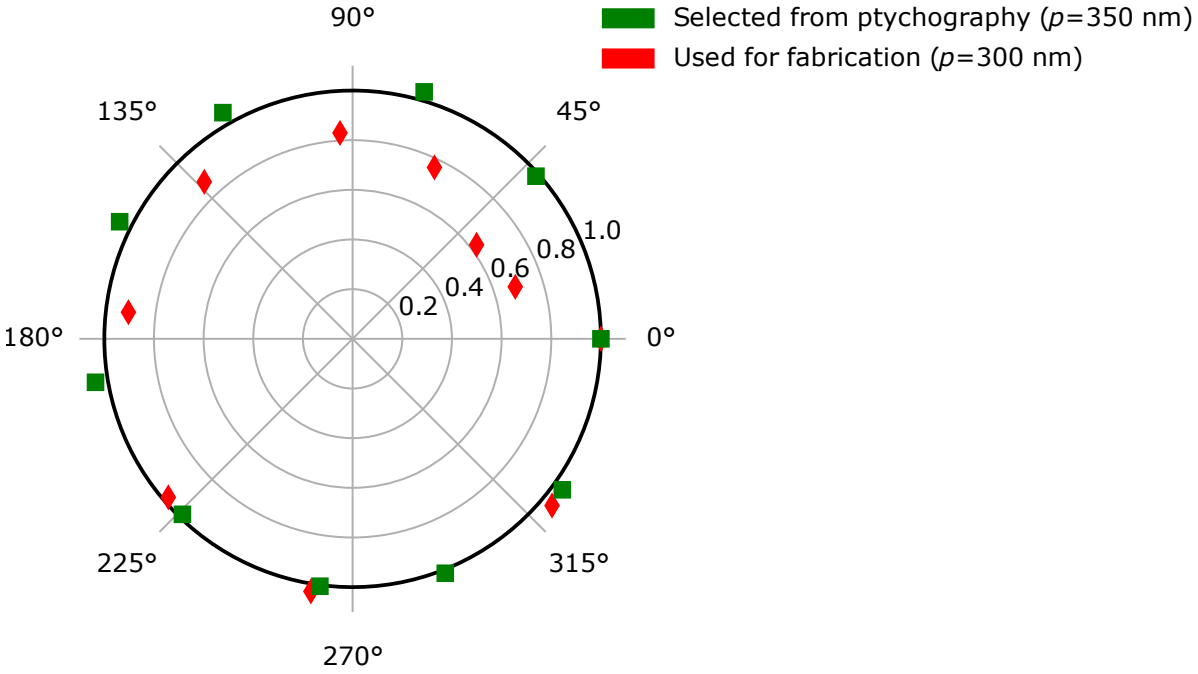

Figure 5.6: In green, we show the expected transmission and phase shifts for the 10 configurations we selected from the reference metasurface (for which we applied ϕ_{pty} and ϕ_{pty}^{-1} for p = 350 nm, thinking that it was for p = 300 nm). In red, we show the true values that were sent for fabrication (same configurations but for which we applied ϕ_{pty}^{-1} for p = 300 nm).

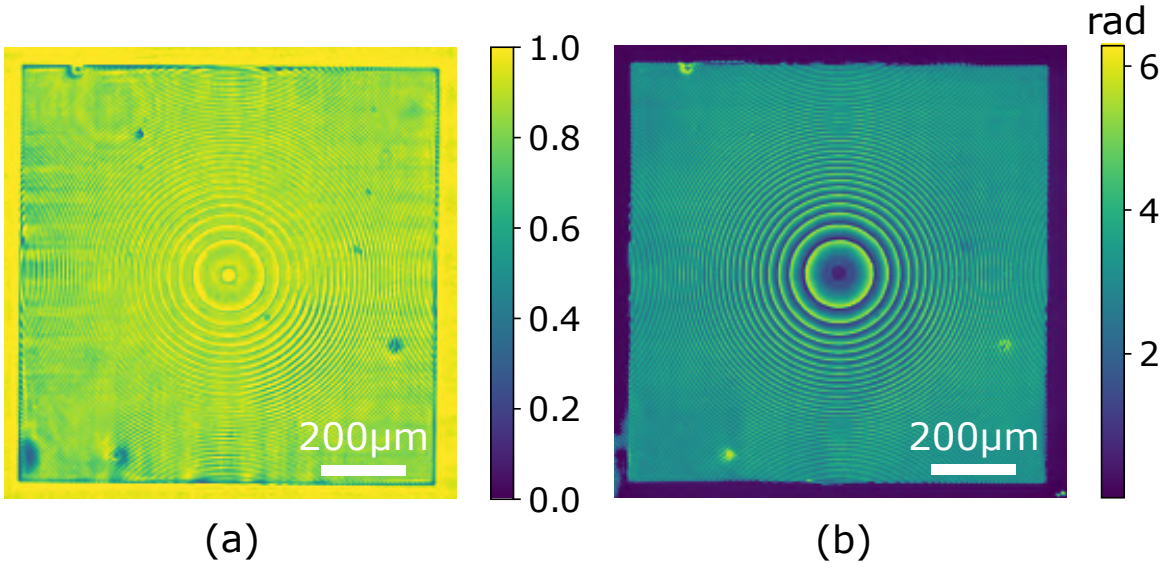

Figure 5.7: Ptychography reconstruction of the metalens that has been designed using the reference metasurface ptychography data. The transmission is shown in (a) and the phase shift in (b).

5.3.2 Optical performances

5.3.2.1 Performances of the metalens designed from the results of ptychography

As for the previous chapter, we compare the measured performance of the fabricated metalens with the calculated performance of two simulated lenses:

- The first is the ideal lens, which has a perfect transmission and a spherical wavefront centered on the focal point.
- The second one is the *Expected From Ptychography Dataset* lens (or EFPD lens). It is defined only using the complex amplitudes of the 10 selected configurations of Fig. 5.6. Thus, its complex amplitude and performance are theoretically the closest to those of the fabricated metalens (if we neglect fabrication errors' influence).

We show in Fig. 5.8 the intensities at the focal plane f = 5000 µm derived using the simulated complex amplitudes for the ideal lens and the EFPD lens, and using the reconstructed complex amplitude for the ptychography metalens.
The calculated focusing efficiencies are respectively $\eta_{fab} = 55\%$, $\eta_{EFPD} = 56\%$ and $\eta_{ideal} = 81\%$, for ratios between the maximum intensities of $I_{m,fab}/I_{m,ideal} = 0.66$ and $I_{m,EFPD}/I_{m,ideal} = 0.70$. The computed Strehl ratios are respectively $S_{fab} = S_{EFPD} = 88\%$.

5.3.2.2 Comparison with the FDTD metalens

Comparing with the FDTD metalens, we find that the one fabricated here is less efficient in both focusing efficiency (55% vs. 75%) and Strehl ratio (87% vs. 92%). However, the agreement between its performance and the EFPD lens is better than the agreement between the FDTD metalens and the EFSD lens (identical Strehl ratio and very close focusing efficiencies). This highlights the main advantage of the new design method, with a better anticipation of the impact of fabrication errors.

5.3.3 Discussion on the results

5.3.3.1 Convergence of the ptychography algorithm

First, the ptychography reconstructions for both lenses may not have converged to their best reconstructions, although we tried to optimize the algorithms (PIE, ePIE, pcPIE, conjugate gradient ePIE) and the parameters used (β, γ,...). It may be possible to improve our results using for example more modern ptychography reconstruction techniques [228].

5.3.3.2 Resolution on the nanodiscs diameters

Second, it should be noted that the FDTD metalens was better optimized for fabrication than the ptychography metalens.
As explained in Chapter 2, prior to the fabrication of our metasurfaces, we performed several dose tests and SEM characterizations to fabricate nanodiscs as close as possible to the theoretical designs. By adjusting the dose applied during the EBL, we could precisely control the exposed surface at each point, improving the precision on the size of the fabricated nanostructures, without having to refine the spatial resolution (distance between two exposure points). This allowed us to achieve a precision on the diameters of the fabricated nanodiscs down to

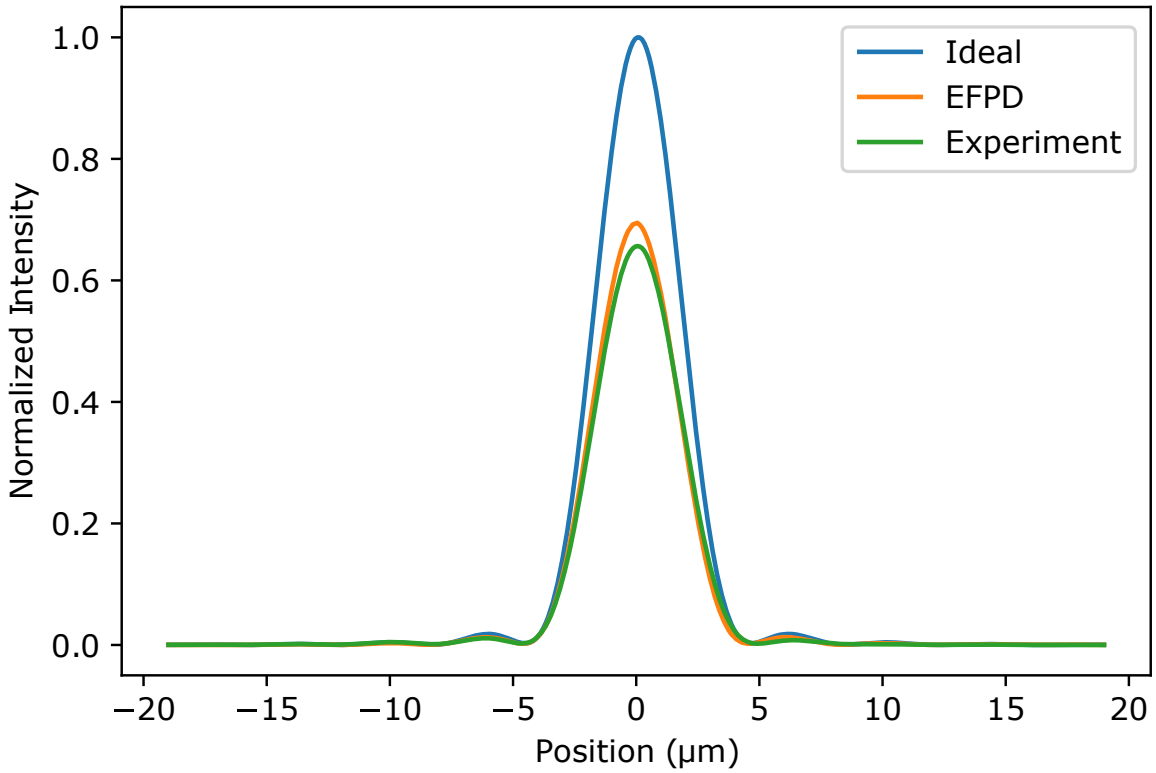

Figure 5.8: Intensities at the focal plane of the ideal lens, the EFPD metalens and the fabricated ptychography metalens (at $Y = Y_{max}$).

about 5 nm, while maintaining a spatial resolution of 10 nm.
However, for the fabrication of the ptychography metalens, we applied the same dose of 900 μC/cm^2 for all nanostructures. This means that the accuracy on the diameters is not optimized and depends only on the spatial resolution we have, equal to 10 nm.
Therefore, as we have less control over its nanostructures sizes (and also because of the error made during its design), it is not surprising that the ptychography metalens performs worse than the FDTD metalens. To further improve the performance, we should fabricate a new reference metasurface that would take into account a variation of the applied doses. As a result, the metasurfaces fabricated from this new reference would benefit from a better resolution on the size of their nanostructures.

Conclusion

In this chapter, we presented a new metasurface design strategy that uses ptychography. We first fabricated a reference metasurface and characterized its phase and transmission. This allowed us to create a database of configurations in the same way as in chapter 2 with the FDTD simulation data. Using this new database, we designed and fabricated a new metalens, and compared its performance with the one presented in Chapter 4. Although being less efficient, we identified that it has a very good agreement with its predicted performances, despite having a poorer resolution on the size of its nanostructures and a non-optimized selection of its geometries.
In conclusion, we can present several advantages regarding the ptychography design approach:

- The first advantages are about the ptychography itself, with the ease of implementation of the optical bench (inexpensive and simple), the possibility of correcting the defects of the probe and positions, and the ability to recover the optical responses of large objects.
- For the design approach presented in this chapter, there is the ability to overcome systematic fabrication errors, and the fact that it does not require multiple SEM or TEM measurements while still being very accurate thanks to the high resolution of ptychography (down to $<\lambda$ for optimized NA).
- Finally, there is a strong potential for improvement of this approach, such as the realization of a reference metasurface accounting for variations on diameters and applied doses.

However, this approach also has limits:

- First, the entire ptychography process takes time. Data acquisition can take several hours and reconstructions can take several days. It should also be noted that the recorded data takes space (for example, the reference metasurface file was 54 GB). Moreover, despite its simplicity, there are some traps to avoid that can deteriorate the good reconstruction of the ptychography (more details in the Appendix). The optimization of the convergence of the algorithm can also be very long: many parameters can be tuned, and the latter depend on the type of objects to be reconstructed.
- Then, the new approach based on ptychography requires the fabrication and characterization of a reference metasurface prior to the fabrication of the final metasurfaces. It also requires the use of simulation tools to guide to the type of nanostructures that are effective for the desired optical behavior. Finally, although being able to overcome the systematic fabrications errors, it does not prevent from the influence of statistical errors.

Therefore, the ptychography design approach brings new interesting perspectives. Once that the ptychography setup is mastered, its very high resolution allows to improve the prediction of the performance of the fabricated metasurfaces, taking into account the influence of the systematic fabrication errors. It also brings new possibilities in terms of designs, which we will discuss in the final conclusion. We are aware that due to the error made on the design of the ptychography metalens, and the low resolution we had for its fabrication, we cannot yet confirm that this new approach is really more efficient than the conventional one. Nevertheless, our results are very encouraging and we believe that this new method will give access to the design of metasurfaces that would be more efficient and more robust to fabrication errors.

Conclusion

As explained in the first chapter, one of the main issues of metasurfaces when compared to conventional optics is their limited efficiency. As a result, over the years, new and more sophisticated design approaches have been developed in order to improve the optical performance and the functionalities they offer. However, these design approaches, based on numerical simulations, still suffer from the impact of nanofabrication errors. This is the context in which we oriented the research work presented in this manuscript.
First of all, in Chapter 1, we studied GDM and FDTD, which are two techniques allowing to simulate the optical response of nanostructures. Then, in chapter 2, we presented an optimized process for the design and fabrication of metasurfaces, based on FDTD for simulation and EBL for fabrication. We then fabricated a metadeflector, from which we were able to identify and study, in Chapter 3, the impact of nanofabrication errors. Among these, we noticed that systematic fabrication errors, related to the lateral geometries of the nanostructures (*e.g.* diameter error for nanodiscs), had a very strong influence. As these errors are due to the imprecision of the characterization tools used on the dimensions of the nanostructures, we considered a new characterization approach that would allow to directly measure the complex amplitudes of metasurfaces.
Therefore, in Chapter 4, we studied the implementation of the ptychography technique, which benefits from a very high resolution, while being relatively easy to implement experimentally. From the latter, we reconstructed the complex amplitude of a fabricated metalens, having a focal length f = 5 mm at λ = 750 nm. We thus evaluated its focusing efficiency and its Strehl ratio, respectively valued at η = 75% and S = 92%. The impact of fabrication errors was also quantified, the latter resulting in a decrease of 4% for the two considered criteria.
After successfully characterizing metasurfaces by ptychography, we investigated in Chapter 5 the implementation of a new design approach based on the latter. We first designed, fabricated and characterized by ptychography a reference metasurface. This allowed us to create a new database, similar in principle to the one established in Chapter 2 (built from FDTD simulations), but this time taking into account systematic fabrication errors. We were then able to select new geometries from which we fabricated another metalens, being then supposed not to be impacted by the nanofabrication errors. Unfortunately, due to an error made during the selection of the geometries, the characterized performances of this metalens were measured lower than those of the metalens fabricated in chapter 4 (η = 55% and S = 88%). However, we noticed that these measured performances were very close to the expected ones (same Strehl ratio and 1% difference in the focusing efficiency), which allowed us to conclude on the efficiency of the new strategy in order to minimize the impact of the fabrication errors.
The work presented in this thesis manuscript opens up many perspectives. It would first be interesting to confirm the relevance of our characterizations based on ptychography, by performing direct measurements of the efficiencies of the fabricated metalenses. Next, although the metasurface fabricated in the last chapter did not perform very well, there are ways of improvement that can be easily achieved in the future. For example, we can fabricate a more

complete reference metasurface, taking into account a variation of the exposure dose applied during EBL.
The implementation of vectorial ptychography for the characterization of metasurfaces is also conceivable as was demonstrated in Ref. [34] and would then allow the design of polarization sensitive components. In addition, we can also consider recently developed simulation strategies that combine sophisticated tools such as optimization algorithms (e.g., evolutionary optimization) or machine learning techniques with computational tools traditionally used for electrodynamic simulations (such as GDM or FDTD). These hybrid simulation approaches have shown immense potential for describing the optical response of non-intuitive metasurface designs. While these approaches are typically driven by simulation data, an exciting continuation of the work presented in this thesis would be to exploit data collected from ptychography measurements. Thus, we can imagine developping a Deep Learning algorithm that would use the measured complex amplitudes of reference metasurfaces. This could even lead to the discovery of interesting new optical properties arising from fabrication defects usually avoided (such as proximity effects during EBL or highly isotropic etching). The ability to obtain data from measurements also makes us less limited in the size of the objects that can be studied. We have indeed been able to characterize metasurfaces as large as 1 mm^2, which is impossible using FDTD simulations due to computing power limitations.
In conclusion, for all these reasons, and also because the results obtained are very encouraging, we believe that this new design strategy has many advantages. We also believe that it would allow to further improve the performances as well as the possible functionalities offered by metasurfaces.

6 Résumé en français : Conception, caractérisation et étude de métasurfaces optiques

6.1 Introduction

6.1.1 Metasurfaces

Le terme *métasurface* hérite directement du nom *métamatériau*. Ce dernier désigne des matériaux conçus artificiellement offrant des propriétés optiques spécifiques allant au delà de ce que l'on retrouve dans la nature. Pour obtenir de telles propriétés, les métamatériaux sont composés de structures beaucoup plus petites que la longueur d'onde organisées en un réseau 3D. Les métasurfaces peuvent être définies comme l'équivalent 2D des métamatériaux et sont généralement composées d'un ensemble de très petites structures, arrangées sur une surface. Dans un métamatériau, les propriétés d'une onde entrante sont modifiées lors de sa propagation dans le volume du matériau. Dans le cas d'une métasurface, c'est l'interaction de l'onde incidente avec une seule couche de structures sub-longueur d'onde qui modifie ses propriétés (amplitude, phase ou polarisation). En contrôlant parfaitement les propriétés de l'onde de sortie, il devient possible de concevoir des composants ultraminces très complexes et très efficaces. Cette versatilité est précisément ce qui rend les métasurfaces si populaires et attrayantes aujourd'hui. Ainsi, plusieurs modèles de métasurfaces sont actuellement étudiés, que ce soit pour le design de composants passifs ou actifs ayant divers objectifs(moduler un front d'onde, multiplexage en polarisation, etc).
Plusieurs approches pour contrôler l'interaction lumière-matière s'opérant au sein des métasurfaces sont utilisées (voir Fig. 6.1). Parmi celles-ci, on retrouve une première approche liées aux résonances optiques supportées par les nanostructures, une seconde liée au design de nano-guides d'ondes, et une troisième liée aux retards de phases de polarisation (Patcharatnam-Berry). Concernant les métasurfaces de mise en forme du front d'onde, nous pouvons distinguer les métasurfaces composées de nanostructures diélectriques à haut indice de réfraction (e.g. silicium). Ces dernières sont particulièrement efficaces et ont l'avantage d'être compatible avec des procédés de fabrication déjà maîtrisés (CMOS). Pour la suite de nos travaux, nous nous sommes donc penchés sur l'approche résonante de nanostructures de silicium, que nous avons d'abord étudiées en utilisant la Méthode Dyadique de Green (ou Green Dyadic Method (GDM)) [58, 59, 163].

6.1.2 Méthode dyadique de Green

La méthode dyadique de Green (GDM) décrit l'interaction d'une onde avec une structure à l'interface entre deux environnements. Cette méthode se base sur une discrétisation des nanos-

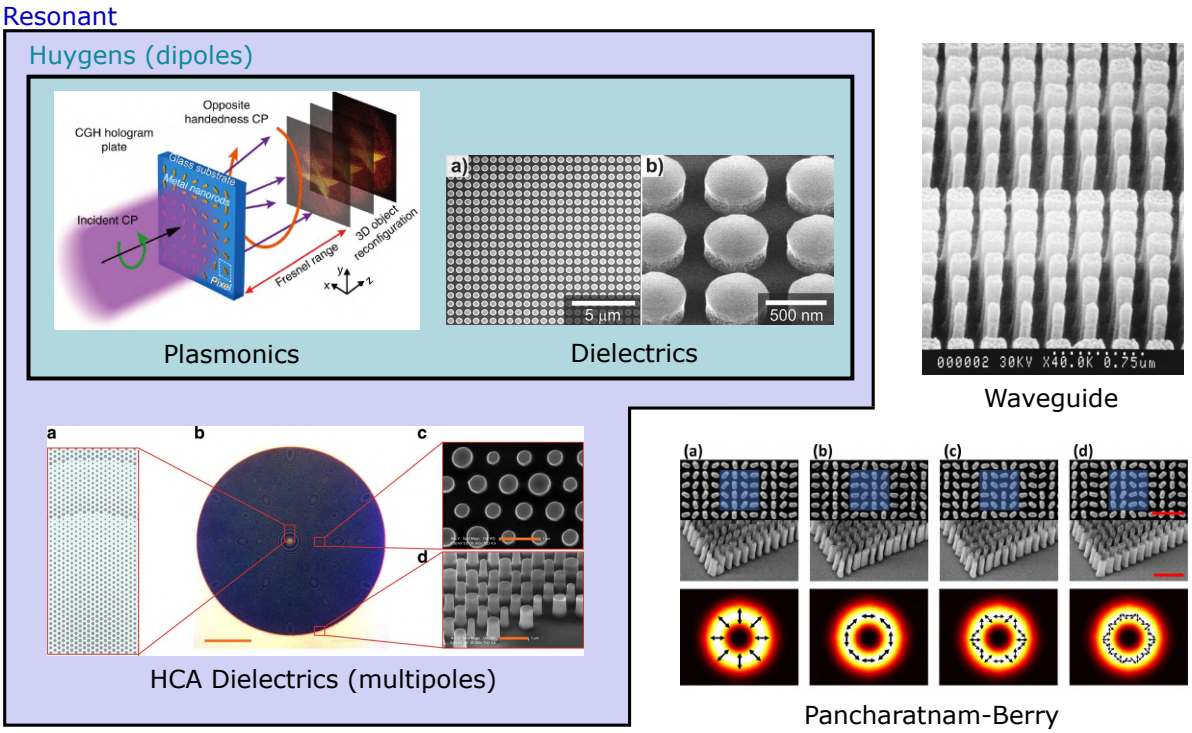

Figure 6.1: Illustration des différents types de métasurfaces : métasurfaces résonantes (diélectriques plasmoniques et de Huygens, diélectriques HCA), métasurfaces de type guide d'ondes et métasurfaces de type Pancharatnam-Berry.

tructures à étudier en une matrice 3D de petits dipoles. La réponse optique alors obtenue est associée à la réponse du système composé de tous les dipoles, couplés entre eux.

6.1.2.1 Décomposition multipolaire via GDM

Lorsque intéragissant avec la lumière, une structure diélectrique va rayonner selon plusieurs résonances multipolaires. Pour des métasurfaces de Huygens par exemple, on associe la réponse optique de chaque nanostructure à celle d'un couple dipole électrique et magnétique ($\mathbf{p}$ et $\mathbf{m}$). C'est ce qu'on appelle l'*approximation dipolaire*.
Via GDM et son formalisme python pyGDM, il est possible de calculer les contributions de ces résonances pour tout type de structures. A titre d'exemple, nous illustrons en Fig. 6.2 plusieurs spectres d'extinction pour plusieurs structures différentes, ainsi que leurs décompositions dipolaires respectives. Comme on peut le voir, il y a un excellent accord entre les extinctions calculées par le calcul GDM complet et la somme des contributions dipolaires. Cette décomposition est très intéressante afin d'observer l'influence d'un changement de la géométrie d'une structure sur sa réponse optique et sur chaque dipole en particulier.
Par exemple, on voit ici qu'en perçant deux trous par le dessus sur un nanodisque de Silicium de hauteur 130 nm et de diamètre 200 nm, le dipole électrique est très peu impacté tandis que le dipole magnétique est fortement changé. De la même manière, on voit qu'affiner un disque de silicium va décaler sa résonance électrique et annuler sa résonance magnétique.

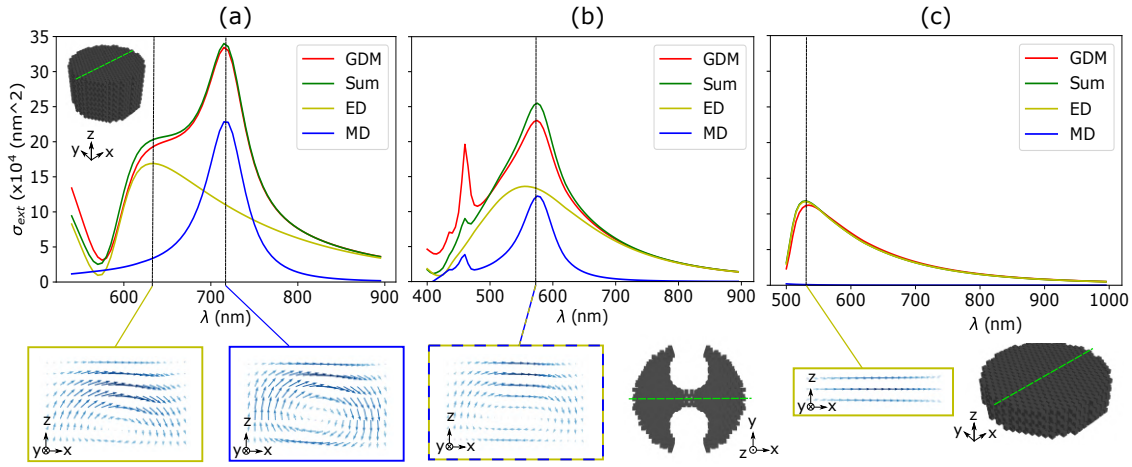

Figure 6.2: (a) Spectres d'extinction d'un nanodisque de silicium de 130 nm de hauteur et de 200 nm de diamètre. Le champ électrique correspondant à la résonance électrique (resp. magnétique) est représenté pour $\lambda = 630$ nm (resp. 715 nm). (b) Spectres d'extinction d'un nanodisque de silicium de 130 nm de hauteur et 200 nm de diamètre qui a été percé de deux trous par le haut. Le champ électrique est représenté pour $\lambda = 580$ nm. (c) Spectre d'extinction d'un nanodisque de silicium de 50 nm de hauteur et de 200 nm de diamètre. Le champ électrique est représenté pour $\lambda = 530$ nm.

6.1.3 Méthode FDTD

La GDM est très intéressante pour l'étude de la physique de l'interaction lumière matière pour des nanostructures. Cependant, il demeure encore aujourd'hui quelques limites fondamentales qui la rendent inefficace pour effectuer la simulation d'un grand nombre de structures, e.g. des métasurfaces. C'est donc pourquoi pour la suite de nos travaux, nous avons étudié la méthode FDTD (Finite Difference Time Domain).
Depuis sa mise en œuvre, les techniques FDTD ont été couramment utilisées pour résoudre de nombreux problèmes électromagnétiques, tant pour la recherche que pour l'industrie. De nos jours, la FDTD est également fréquemment utilisée en nanophotonique, notamment pour la conception de métasurfaces.
La FDTD est une méthode de calcul qui résout les équations de Maxwell par une discrétisation dans le temps et l'espace d'un volume d'intérêt. Cette discrétisation est toujours associée à une grille spécifique où le champ électromagnétique est reconstruit. A titre d'illustration, nous montrons sur la Fig. 6.3 la *Grille de Yee* (largement utilisée pour les calculs FDTD) où les composantes du champ électrique sont toutes situées sur les bords du cube élémentaire, tandis que les composantes du champ magnétique sont situées au centre des faces. La grille de Yee est conçue de telle sorte que chaque composante du champ électrique $\vec{E}$ est entourée de quatre composantes magnétiques circulantes $\vec{H}$ et inversement.
En plus de la séparation spatiale, il existe également une séparation temporelle. Plus précisément, si le champ magnétique est calculé pour chaque temps $t = [\Delta t, 2\Delta t, 3\Delta t, ...]$, alors le champ électrique est calculé à $t = [\Delta t/2, 3\Delta t/2, 5\Delta t/2, ...]$, Δt étant l'incrément de temps. Ces séparations temporelles et spatiales sont choisies de manière à faciliter la résolution des équations de Maxwell. Il permet de calculer itérativement le champ électrique et magnétique à chaque demi-pas de temps $\Delta t/2$, donc de simuler la propagation d'une onde électromagné-

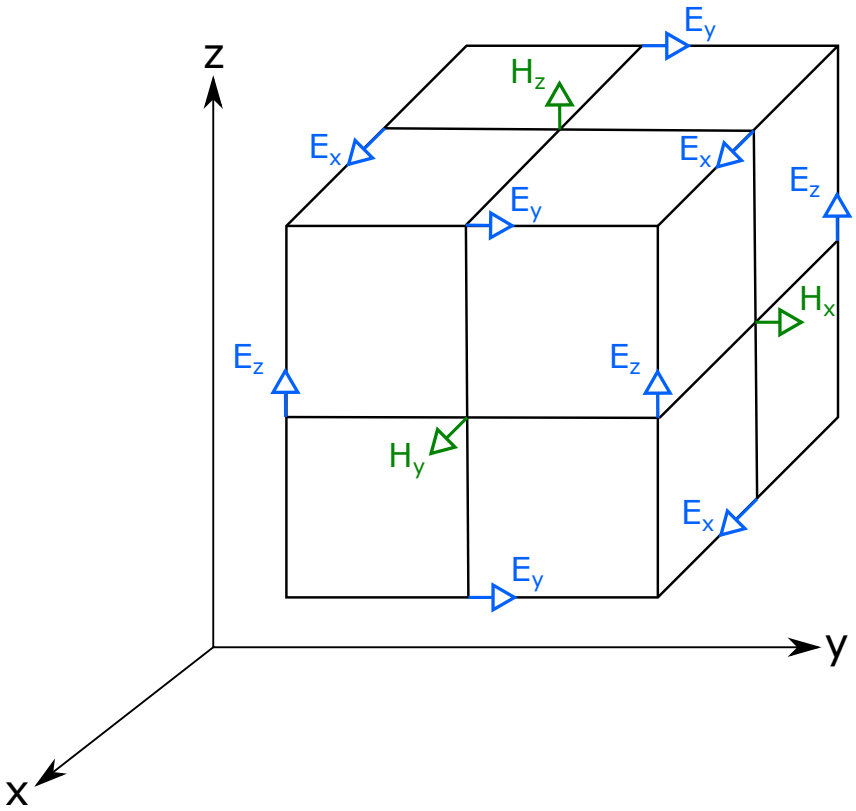

Figure 6.3: Illustration d'une cellule de la grille de Yee. Représentation des positions des composantes des champs électriques et magnétiques.

tique définie dans le volume discrétisé d'intérêt.
L'algorithme FDTD est très puissant, ce qui explique pourquoi il est si populaire dans la recherche optique. Aujourd'hui, il existe plus d'une dizaine de logiciels FDTD commerciaux ou gratuits. Pour nos calculs, nous avons utilisé le module python open source **Meep**.

6.2 Conception, fabrication et caractérisation d'un métadéflecteur

6.2.0.1 Méthode de design par FDTD

Pour designer des métasurfaces à modulation de front d'onde, l'objectif est d'avoir des nanostructures dont une variation sur la géométrie permet de parcourir un déphasage allant de 0 à 2π tout en maintenant une forte transmission.
Ainsi, il faut une approximation permettant d'anticiper la réponse optique qu'aurait individuellement une structure dans l'environnement de la métasurface. Cela nécessite de pouvoir prendre en compte les effets de couplages optiques liés à la forte densité de structures. Une approximation très efficace démontrée dans la littérature consiste à effectuer des simulations de réponses optiques de métasurfaces infinies et périodiques. Ces métasurfaces sont en fait composées d'un nombre infini de structures ayant toutes la même géométrie et étant arrangées sur une grille carrée (ou hexagonale) de période fixée.
Après une première étape d'optimisation, nous avons décidé de designer des métasurfaces

composées de nanodisques de silicium de hauteur $H = 370$. Les paramètres sur lesquels on peut jouer sont donc la périodicité de la grille ainsi que le diamètre des disques. Notre objectif va donc être de trouver une périodicité (ou taille de cellule), pour laquelle une variation de diamètre permet d'avoir des nanostructures induisant des déphasages allant de 0 à 2π, tout en ayant une forte transmission. Pour cela, nous effectuons une série de plusieurs simulations FDTD afin d'obtenir le déphasage et la transmission pour des périodicité de grille et des diamètres variables (voir Fig. 6.4). On fait varier la périodicité de 250 nm à 350 nm et les diamètres sont pris comme une fraction de la taille de la cellule de sorte que $0,3 \leq \frac{D}{p} \leq 0,8$. Comme nous voulions que la métasurface fonctionne en transmission, nous avons choisi un substrat en quartz [24, 25].
Pour simuler les métasurfaces infinies et périodiques, nous avons défini des cellules unitaires de taille $p \times p \times L$, pour lesquelles nous avons appliqué des conditions aux limites périodiques sur les axes X et Y. Le volume supérieur ($Z > 0$) de la cellule est constitué de quartz (indice de réfraction $n = 1,45$), le volume inférieur est sous vide. Le nanodisque est positionné à l'interface $Z = 0$ (voir Fig. 6.4(c)). Le pas de résolution est de 10 nm. L'illumination est une onde plane polarisée en X à $\lambda = 750$ nm, définie dans le substrat de quartz, se propageant vers $Z < 0$. Le fait que l'illumination provienne du substrat de quartz permet de simuler l'influence de ce dernier à l'interface sur laquelle se trouve la métasurface. Cependant, cela implique également que la réflexion de Fresnel provenant de la seconde interface air/verre n'est pas prise en compte. Sa prise en compte diminuerait les transmissions calculées d'environ 4 %.
Ainsi, à partir des cartes, et en essayant d'optimiser également la robustesse liée à l'imprécision de la fabrication (i.e. minimiser l'impact d'une erreur sur le diamètre sur le déphasage), nous avons choisi la périodicité p = 300 nm.

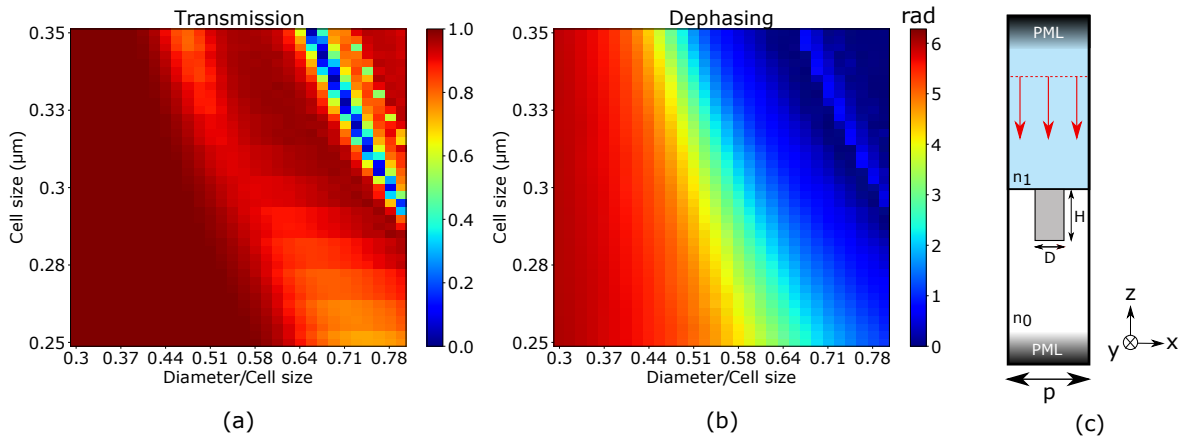

Figure 6.4: (a) Carte de transmission et (b) carte de déphasage associées à différents nanodisques de hauteur $H = 370$ nm, pour des diamètres D et des tailles de cellules p variables. (c) Illustration de l'environnement de la simulation FDTD pour une configuration.

6.2.1 Design d'un métadéflecteur

6.2.1.1 Définition d'un métadéflecteur

Un métadéflecteur est une métasurface qui défléchit une onde plane incidente d'un angle spécifique. La recherche sur les métadéflecteurs est très active dans la littérature car ils servent de base de référence pour toutes les métasurfaces à modulation de front d'onde [100]. Pour incliner la lumière entrante (c'est-à-dire le front d'onde), un métadéflecteur doit induire un gradient de déphasage linéaire.
Selon les lois généralisées de la réflexion et de la réfraction [1], nous pouvons établir la relation suivante, pour une onde plane normalement incidente interagissant avec un métadéflecteur dans le vide:

$$\sin\theta_d = \frac{\lambda}{2\pi}\frac{d\Phi}{dx} \tag{6.1}$$

Où θ_d est l'angle d'inclinaison, λ est la longueur d'onde dans le vide de l'onde plane incidente et $\frac{d\Phi}{dx}$ est le gradient de déphasage. Le métadéflecteur est conçu de manière à ce que le déphasage d'une onde plane incidente soit augmenté de 2π sur la longueur de la supercellule l_c comme le montre la Fig.6.5 (b). D'après l'éq. 6.1, nous établissons la relation suivante entre la longueur de la supercellule l_c et θ_d :

$$\theta_d = \arcsin\frac{\lambda}{l_c} \tag{6.2}$$

A partir des données extraites des cartes de la figure 6.4, nous choisissons dix configurations pour induire des déphasages de $k\frac{\pi}{5}$, avec $k \in [|0;9|]$. Les nanostructures ainsi choisies sont des nanocylindres d'une hauteur de 370 nm et dont les diamètres sont les suivants : 114, 138, 148, 156, 164, 170, 178, 190, 208 nm. La taille de cellule sélectionnée est de 300 nm, et la métasurface est placée sur un substrat de quartz d'indice n = 1,45. Ainsi, la longueur de la supercellule l_c est alors égale à 3 µm pour une longueur d'onde de fonctionnement de λ = 750 nm donnant un angle d'inclinaison θ_d = 14.5°.
Les configurations de déphasage et de transmission sélectionnées sont présentées sur la figure 6.5 (a). Comme on peut le constater, elles couvrent régulièrement toute la gamme des déphasages $0 - 2\pi$ avec des transmissions très proches de 1.

6.2.2 Fabrication

Une fois le design de la métasurface optimisé, on passe à l'étape de fabrication. La méthode de fabrication est décrite dans la Fig. 6.6. Le processus commence par l'ingénierie d'une plaquette de silicium sur quartz. Une couche de Si polycristallin de 370 nm d'épaisseur est déposée par dépôt chimique en phase vapeur à basse pression (LPCVD) sur une plaquette de silice fondue de 4 pouces. L'épaisseur et l'indice de réfraction de la couche déposée sont mesurés par ellipsométrie. La couche de Si sur la face arrière est gravée sélectivement et la plaquette de 4 pouces est découpée en échantillons de 2 cm x 2 cm.
La nanostructuration est réalisée par une approche descendante sur chaque échantillon. Nous utilisons une résine électro-négative, à savoir l'Hydrogène-Silsesquioxane (HSQ). Tout d'abord, une couche de HSQ de 130 nm d'épaisseur est déposée par spin coating, puis recuite sur plaque

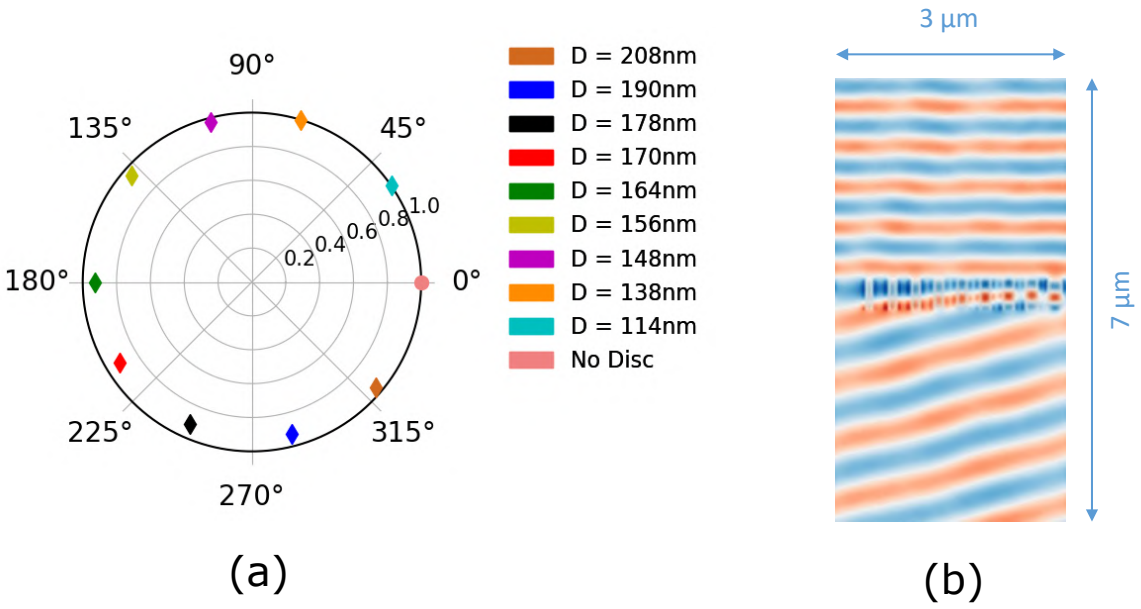

Figure 6.5: (a) Représentation polaire des 10 configurations choisies pour la fabrication d'un métadéflecteur. Pour chaque configuration, l'angle représente le déphasage induit et la distance au centre est la transmission du réseau de nanodisques. (b) Simulation FDTD d'un métadéflecteur inclinant une onde plane entrante de λ = 750 nm d'un angle de 14,5°.

chauffante à 80°C pendant 1 min afin d'évaporer le solvant. La lithographie par faisceau électronique (EBL) a été réalisée avec un graveur RAITH 150 à une exposition d'énergie de 30 keV et une dose allant de 855 à 1260 μC/cm^2 et un courant de faisceau de 120 pA. Le développement de la résine a été effectué dans de l'hydroxyde de tétra-méthyl-ammonium (TMAH) hautement concentré (25 %) afin d'augmenter le contraste du motif. L'échantillon est ensuite rincé dans de l'eau déminéralisée puis dans une solution de méthanol avant un séchage doux avec un flux d'azote afin de réduire la tension de surface et de minimiser l'effondrement des nanopiliers. Enfin, les motifs HSQ sont transférés dans la couche de Si par gravure plasma anisotrope jusqu'à l'interface du quartz ($SF_6/C_4F_8/O_2$). La gravure plasma est réalisée par ICP-RIE (équipement Alcatel-AMS4200) en utilisant des gaz fluorés.
Le métadéflecteur fabriqué a une empreinte carrée avec une longueur de bord de 500 μm. Une image au microscope électronique à balayage (MEB) du métadéflecteur est présentée dans le coin inférieur droit de la figure 6.6.

6.2.3 Caractérisation des performances

Pour les métadéflecteurs, il existe généralement deux grandeurs caractérisant leur efficacité : les efficacités de déflection et de diffraction. L'efficacité de déflection η_{defl} est le rapport entre la puissance du faisceau dévié P_d à l'angle d'inclinaison nominal θ_d et la puissance du faisceau incident P_{inc}. Le métadeflecteur étant périodique, il diffracte la lumière incidente en plusieurs faisceaux se propageant dans des directions différentes nommées par leurs ordres de diffraction. Le faisceau dévié est diffracté vers l'ordre $+1$. L'efficacité de diffraction η_{diff} est le rapport entre la puissance du faisceau dévié P_d et la somme des puissances de tous les

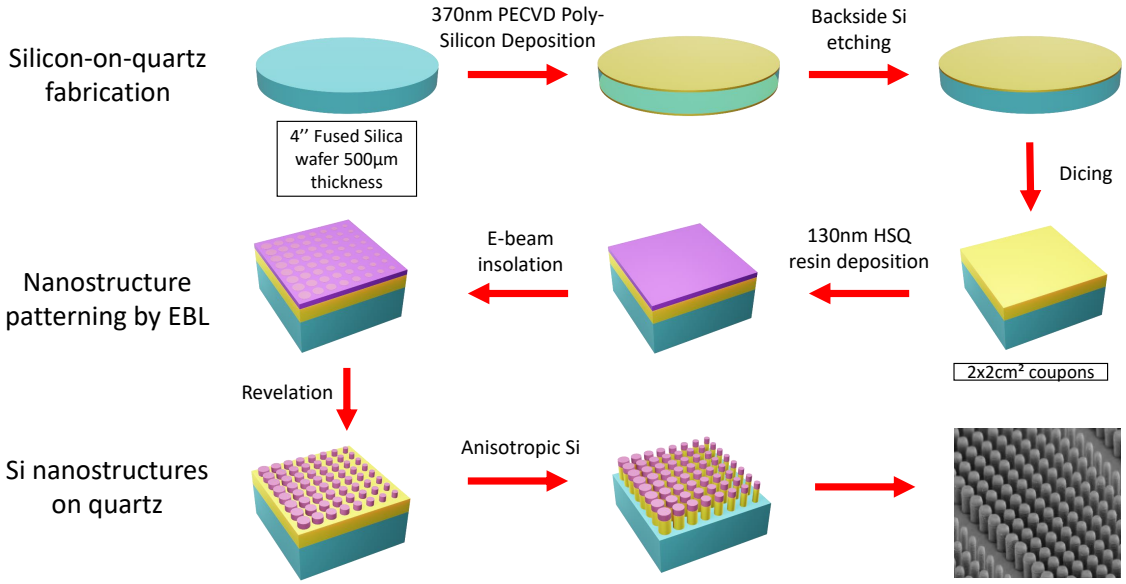

Figure 6.6: Etapes du processus utilisé pour la fabrication de métasurfaces.

faisceaux diffractés notés P_{diff}.

Simulation FDTD Nous montrons sur la Fig. 6.7 les efficacités de déflection et de diffraction simulées en fonction de la longueur d'onde. Comme nous pouvons le voir, les deux efficacités sont maximales pour la longueur d'onde incidente λ = 750 nm, où l'efficacité de diffraction maximale est de 98% et l'efficacité de déflection maximale est de 89%.

Mesures expérimentales Les caractérisations optiques expérimentales ont été réalisées à l'aide d'un laser femtoseconde Ti:Sa accordable dans le domaine du proche infrarouge (680-1080 nm). Le principe de la caractérisation est illustré sur la Fig. 6.7. La puissance P_{diff} est obtenue en mesurant la puissance de chaque faisceau de sortie à l'aide d'un powermètre. Pour mesurer la puissance du faisceau incident P_{inc}, on translate l'échantillon perpendiculairement au faisceau jusqu'à ce que la métasurface soit complètement hors du faisceau incident. Les pertes de transmission de 4% de l'interface air/verre pour l'efficacité de déflection ne sont donc pas prises en compte. Nous utilisons également un objectif de télescope pour rendre le faisceau plus petit que la métasurface. Cela empêche la lumière qui ne traverse pas la métasurface de contribuer à la puissance mesurée de l'ordre $+0$.
Nous mesurons alors les efficacités de déflection et de diffraction à plusieurs longueurs d'onde, de 700 nm à 800 nm. Les résultats sont également présentés dans la Fig. 6.7 (traits pointillés). Comme nous pouvons le constater, les efficacités de diffraction et de déflection mesurées atteignent 94% et 88%. Ces valeurs sont donc très proches de celles obtenues à partir des simulations. A notre connaissance, ces valeurs sont parmi les plus élevées rapportées dans la littérature dans cette gamme de longueur d'onde [27]. Toutefois, nous pouvons constater que les positions de ces efficacités maximales sont décalées de 25 nm par rapport aux simulations (λ = 775 nm au lieu de 750 nm).

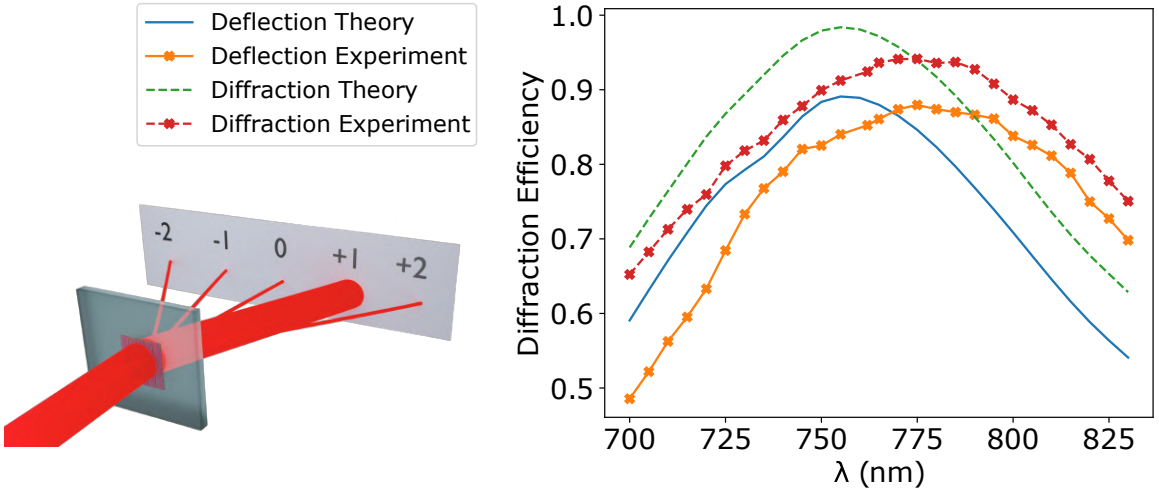

Figure 6.7: Efficacités de diffraction et de déflection théoriques et expérimentales pour le métadéflecteur simulé et le métadéflecteur fabriqué.

6.3 Etude des erreurs de fabrication sur un métadéflecteur

Dans cette partie, nous allons présenter une étude de l'impact d'erreurs de fabrication sur les performances d'un métadéflecteur afin d'expliquer les différences entre les performances que nous avons simulées et mesurées.

6.3.1 Identifications des erreurs de fabrication

Tout d'abord, il est nécessaire d'identifier les erreurs qui peuvent apparaître lors du processus de nanofabrication. Pour cela, nous effectuons des mesures par microscopie électronique en transmission (TEM) afin de caractériser précisément la morphologie et l'environnement des nanodisques fabriqués. Ces expériences sont réalisées sur un TEM FEG Philips CM20 à 200 keV (collaboration C. Marcelot, CEMES-CNRS). Une lamelle de section transversale a été préalablement préparée par faisceau d'ions focalisé (FIB) et micromanipulation (R. Cours, CEMES-CNRS). Plusieurs images TEM de la lamelle extraite sont présentées dans la Fig. 6.8. A partir de ces mesures, nous avons systématiquement remarqué que les diamètres mesurés à la base des nanocylindres sont plus petits que ceux mesurés au sommet, la différence se situant entre 5 et 10 nm. Le diamètre moyen est toujours supérieur de moins de 5 nm aux diamètres ciblés confirmant l'excellent contrôle lors de la fabrication. Finalement, la hauteur des nanodisques est plus importante que prévu (390 nm contre 370 nm).
Pour aller plus loin, nous avons réalisé une cartographie élémentaire en utilisant l'imagerie par rayons X à dispersion d'énergie en mode microscopie électronique à balayage (STEM-EDX). Un exemple des cartes élémentaires est présenté dans la Fig. 6.9 qui montre la distribution du silicium et de l'oxygène dans l'échantillon. Ces cartes et les profils extraits présentés révèlent la présence d'un recouvrement HSQ restant sur le dessus des cylindres. Ce dernier est proche du composé SiO_2 après modification par le faisceau d'électrons, comme le montre la Fig. 6.9. Une valeur de 100 nm pour l'épaisseur de cette couche de résine restante a été extraite des images TEM. Une couche d'oxyde de silicium de quelques nanomètres d'épaisseur est également

visible sur les côtés des résonateurs.

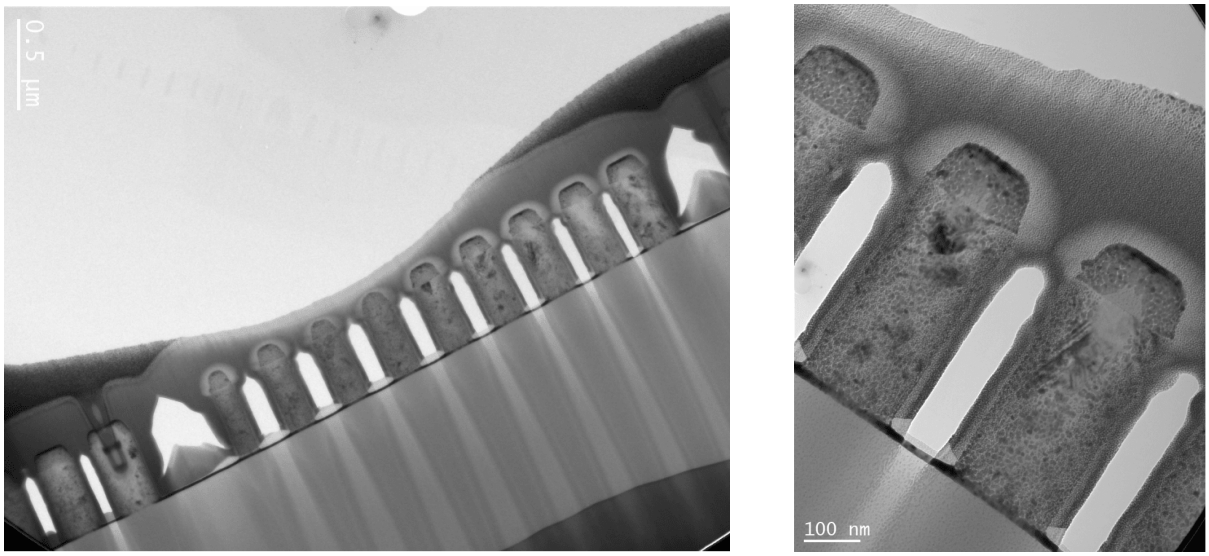

(a) (b)

Figure 6.8: Images TEM d'une fine lamelle du métadéflecteur fabriqué, correspondant à une coupe verticale effectuée par FIB. (a) Image de la lamelle. (b) Image zoomée de deux nanodisques de silicium de la lamelle. (C. Marcelot, CEMES-CNRS). Les images sont prises sur les côtés. Nous pouvons identifier les nanodisques de silicium avec un dôme de HSQ restante sur un substrat de quartz.

6.3.2 Erreurs de fabrication systematiques

Dans la Fig. 6.10 nous résumons les altérations sur les efficacités de diffraction et de déflection pour les erreurs de forme que nous avons identifié (diamètre, hauteur, différence entre diamètre haut et diamètre bas). A gauche, nous montrons pour les trois erreurs relatives l'efficacité maximale de diffraction obtenue. A droite, nous montrons les longueurs d'ondes où ces efficacités maximales sont mesurées.
On peut observer des impacts très divers en fonction de l'erreur concernée. En effet, tout d'abord, il apparaît qu'une variation de la hauteur des nanopilliers n'impacte pas la valeur d'efficacité maximale mais uniquement sa position de résonance. Au contraire, les variations sur le diamètre ou sur la pente des flancs des nanopilliers ont un fort impact sur l'efficacité maximale ainsi que sa résonance.
Ces résultats montrent ainsi la tendance selon laquelle une modification de la morphologie latérale des nanocylindres induit de grandes déviations, contrairement à une modification de la morphologie verticale. Pour comprendre d'où peuvent venir ces différences d'impact, nous pouvons émettre deux hypothèses:

- Premièrement, au sein de chaque nanostructure, plusieurs résonances multipolaires apparaissent. Ces résonances sont fortement dépendantes de la quantité de matière (i.e. volume) au sein de structures. Ainsi, là où le volume varie linéairement avec la hauteur, il varie en fonction du carré du diamètre, ce qui peut expliquer la différence de variation.

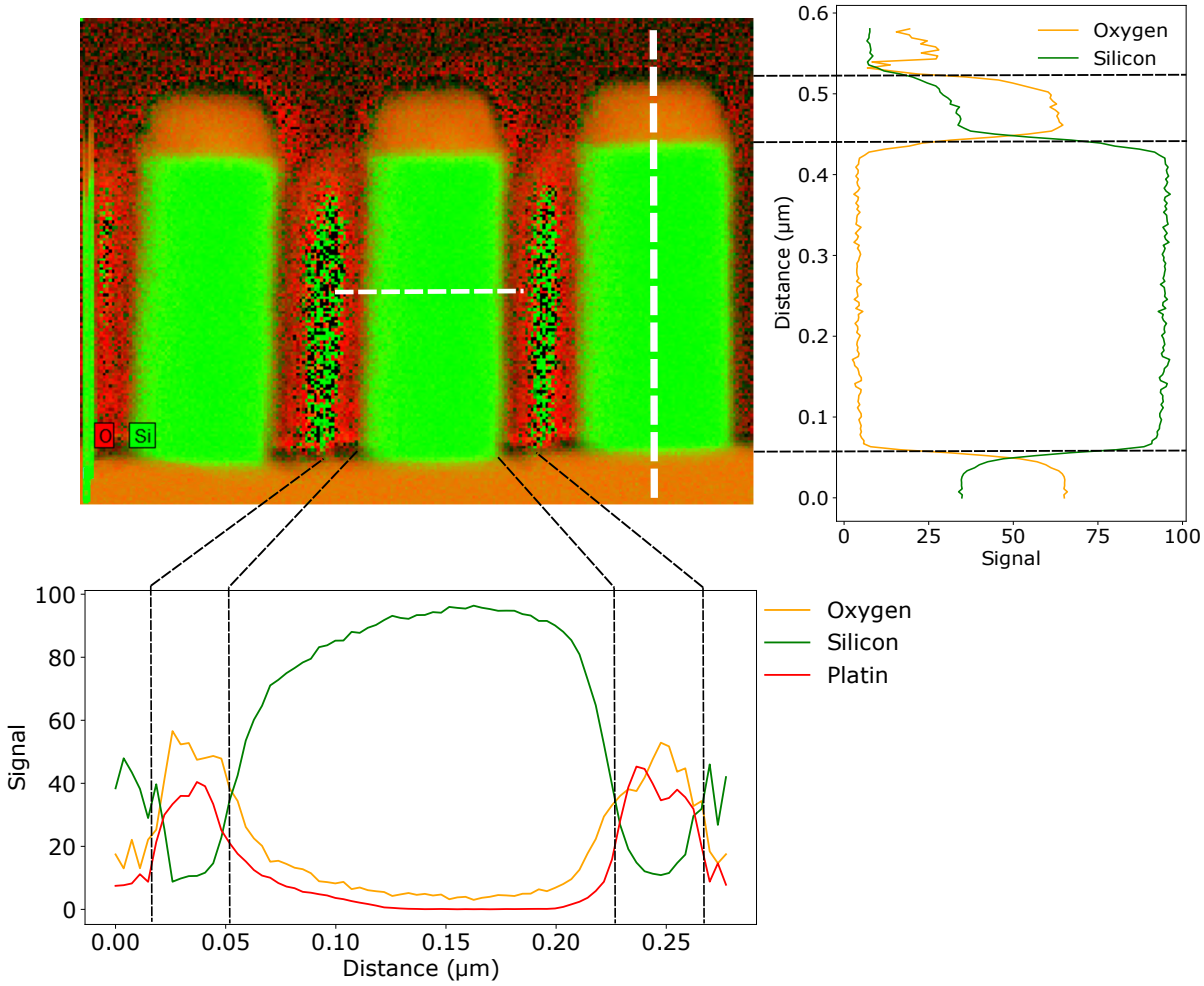

Figure 6.9: Composition chimique de la lamelle prélevée sur le métadéflecteur. (a) Distribution du Silicium et de l'Oxygène à l'intérieur et au voisinage des nanodisques. (b) Profil vertical de la distribution le long de la ligne verticale blanche pointillée en (a). (c) Profil horizontal de la distribution le long de la ligne horizontale pointillée en (a).

- Deuxièmement, les métasurfaces sont des objets très denses où les effets de couplages entre structures voisines sont importants. De ce fait, une variation sur la géométrie latérale des structures va directement impacter la distance bord à bord entre structures voisines et donc aura un fort impact sur le comportement global de la métasurface. Au contraire, une modification de la hauteur ne change pas ces distances bord à bord et donc a une influence plus faible.

Il faut tout de même garder à l'esprit que les variations mises en jeu ici sont très petites (10 % étant 40 nm pour la hauteur et 15 nm pour les diamètres). Ainsi, malgré un excellent contrôle sur les erreurs de fabrication, de très faibles variations auront tout de même un impact important sur les performances finales de la métasurface.

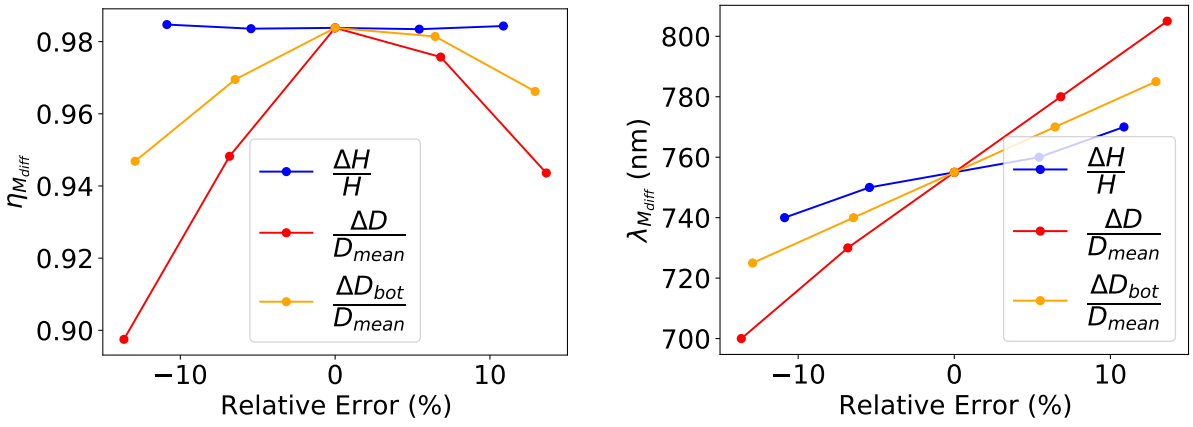

(a) (b)

Figure 6.10: Impacts relatifs des erreurs de morphologie (diamètres, hauteur, pente latérale) sur les performances optiques d'un métadéflecteur. (a) et (b) montrent l'évolution du maximum de l'efficacité de diffraction $\eta_{M_{diff}}$ et de la longueur d'onde résonante $\lambda_{M_{diff}}$ avec les différentes erreurs relatives.

6.4 Nouvelle approche de design utilisant la ptychographie

Dans cette partie, nous allons présenter une nouvelle approche pour designer des métasurfaces permettant de minimiser l'impact d'erreurs de fabrication sur les performances optiques.

6.4.1 Approche conventionnelle

L'approche standard pour la conception et la fabrication de métasurfaces, que nous avons utilisée pour fabriquer le métadéflecteur, est illustrée et détaillée en Fig. 6.11(a). Dans un premier temps, on étudie le comportement optique de nanostructures de différentes géométries via des outils de simulation numériques (FDTD, RCWA, FEM, ...). De ces simulations, une base de données de réponses optiques est générée et permet de sélectionner un set de géométries à utiliser pour le design des métasurfaces à fabriquer. A ce stade, une première optimisation est possible afin d'anticiper l'impact des erreurs de fabrication sur les réponses optiques à considérer. Ainsi, il peut être préférable de viser la fabrication d'une métasurface moins efficace mais plus robuste aux erreurs de fabrication.
Une fois le design de la métasurface déterminé, l'objectif est de s'assurer que les dimensions des nanostructures fabriquées sont aussi proches que possible de celles simulées. Pour cela, deux stratégies peuvent être utilisées:

- Utiliser les caractérisations SEM, TEM et ellipsométriques pour optimiser les nanostructures fabriquées (*e.g.* tests de dose).
- Utiliser ces caractérisations pour optimiser les structures simulées. Par exemple, au cours de notre processus de fabrication, nous avions mesuré l'épaisseur du silicium déposé ainsi que son indice de réfraction pour générer un nouvel ensemble de simulation.

La métasurface finale est alors fabriquée, avec des propriétés optiques optimisées pour être les plus proches de celles simulées.

Il faut toutefois noter que malgré toutes ces étapes, des erreurs de fabrication demeurent, comme nous avons pu l'identifier avec la fabrication et la caractérisation de notre métadéflecteur. Ces dernières sont notamment dues à la limite de précision des instruments utilisés pour caractériser et optimiser les designs (nous avions, par exemple, mesuré une épaisseur de silicium de 370 nm par ellipsométrie et de 390 nm par TEM). Par conséquent, il existe une limite claire en termes de minimisation de l'impact des erreurs de fabrication sur les performances des métasurfaces.

6.4.2 Nouvelle approche

Par conséquent, nous présentons une nouvelle approche de conception de métasurface, illustrée à la Fig. 6.11(b). L'objectif ici est d'identifier les propriétés optiques des nanostructures directement en utilisant une méthode d'imagerie de phase plutôt qu'en effectuant des simulations numériques.
Tout d'abord, afin d'établir la relation entre les géométries et les réponses optiques, une *métasurface de référence* est conçue, fabriquée et caractérisée par imagerie de phase. C'est ensuite à partir de cette caractérisation qu'un ensemble de données est utilisé pour concevoir et fabriquer de nouvelles métasurfaces. Ainsi, même si les géométries des nanostructures fabriquées diffèrent des conceptions prévues, les réponses optiques mesurées tiendront compte de ces différences. De plus, comme le processus de fabrication ne varie pas entre la métasurface de référence et les suivantes, cette méthode permet de surmonter les erreurs systématiques de fabrication sans avoir recours à des mesures SEM ou TEM, tout en garantissant des réponses optiques aussi proches que possible de celles prédites.

6.4.3 Intro sur la ptychography

La nouvelle approche nécessite une méthode d'imagerie de phase très précise qui soit applicable aux métasurfaces. Parmi les méthodes disponibles, nous avons choisi d'utiliser la *ptychographie*, qui est une technique d'imagerie computationnelle utilisée pour récupérer l'amplitude complexe d'un objet. Nous illustrons son principe dans la Fig. 6.12. Tout d'abord, nous illuminons une petite zone d'un objet et enregistrons l'intensité diffractée résultante. Ensuite, nous déplaçons l'objet par rapport à l'illumination pour illuminer et collecter l'intensité diffractée d'une nouvelle zone. Cette dernière opération est ensuite répétée pour plusieurs positions, avec la condition que le déplacement soit suffisamment petit pour assurer une zone de recouvrement entre deux illuminations successives. Le nombre total de positions N_{ac} peut varier en fonction de l'objet que l'on veut caractériser, il peut aller de $N_{ac} = 100$ à $N_{ac} > 5000$. Finalement, un algorithme itératif est utilisé pour retrouver l'amplitude complexe de l'objet à partir des intensités enregistrées.
La ptychographie offre l'avantage d'être facile à mettre en oeuvre expérimentalement, de ne pas être limitée par la taille de l'échantillon, et aussi de donner la possibilité d'être mise à jour pour imager l'état de polarisation des objets (ptychographie vectorielle).

6.4.4 Algorithmes de ptychographie

Il existe plusieurs algorithmes de ptychographie, pouvant être vus comme des extensions, offrant de nouvelles fonctionnalités à la reconstruction:

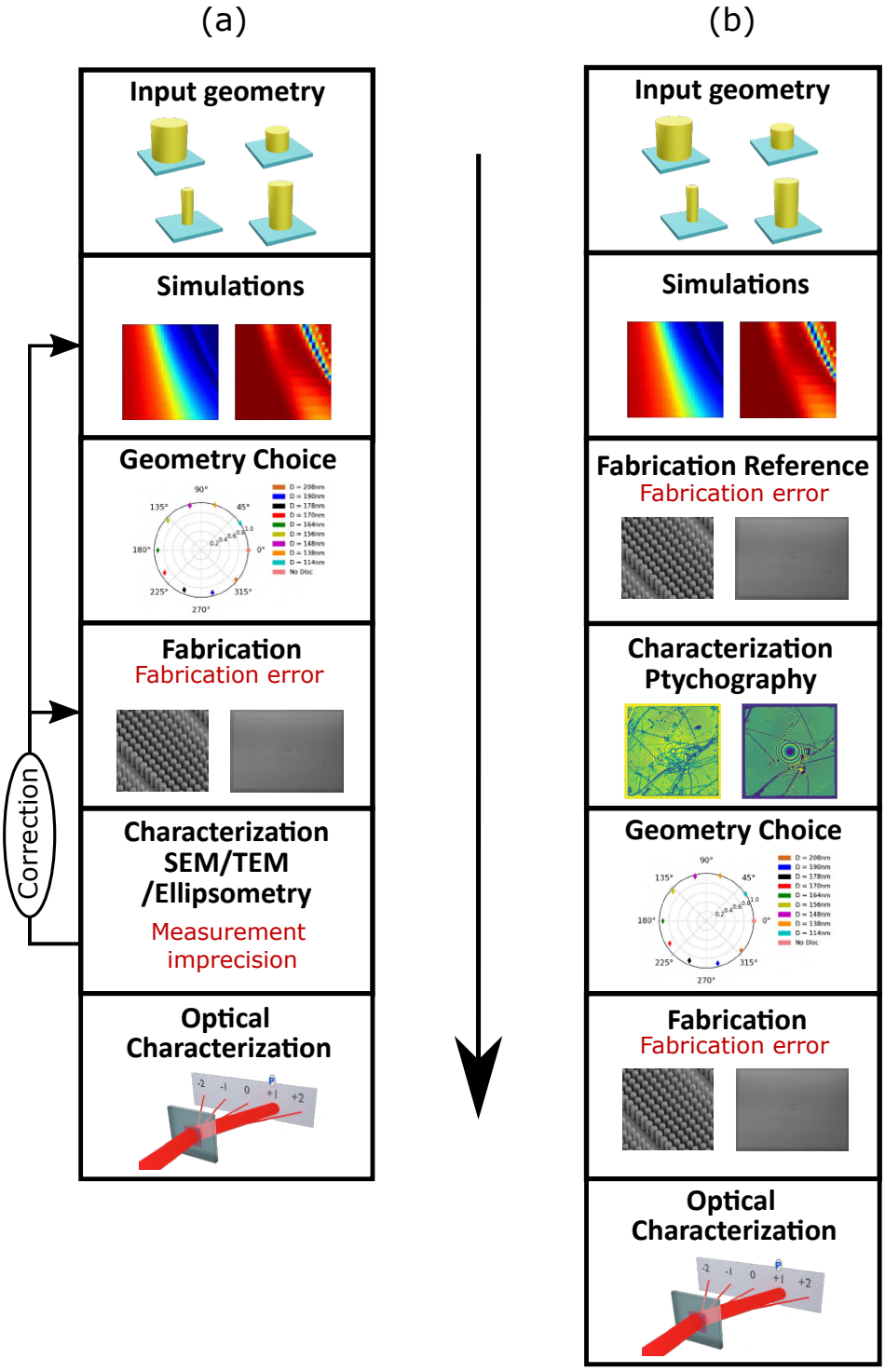

Figure 6.11: Illustration de (a) la stratégie conventionnelle basée sur des simulations numériques et (b) la nouvelle stratégie basée sur des caractérisations par ptychographie utilisées pour la conception et la fabrication de métasurfaces.

- Le PIE (ptychographie Iterative Engine) est l'algorithme de base de la ptychographie, permettant de reconstruire l'amplitude et la phase d'un objet en ayant connaissance de la sonde (de l'illumination).

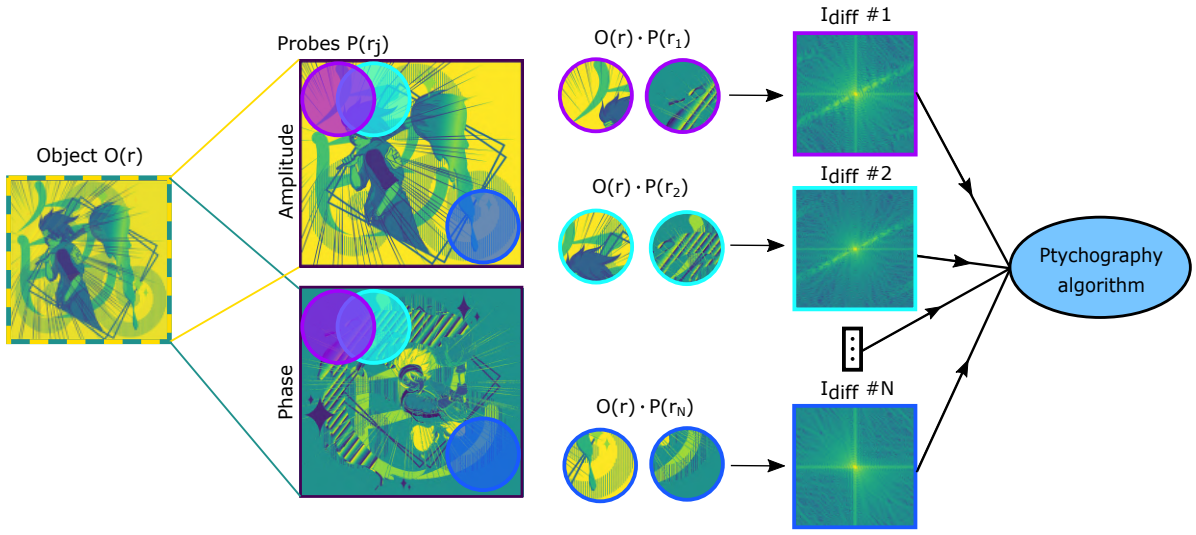

Figure 6.12: Présentation du principe de la ptychographie. Une petite zone d'un objet est éclairée à différentes positions (magenta : position # 1, cyan : position # 2, ... , bleu : position # N). Les intensités diffractées enregistrées pour chaque position constituent l'entrée de l'algorithme de ptychographie.

- L'ePIE (extended PIE) permet en plus de reconstruire l'amplitude complexe de l'objet, de reconstruire également l'amplitude complexe de la sonde sans avoir besoin de plus de données. Ce dernier algorithme est très utilisé car il permet de répondre à l'incertitude sur une illumination expérimentale.
- Le pcPIE (position correction PIE) permet d'apporter une correction sur les positions d'éclairement de la sonde relativement à l'objet. Il permet ainsi d'avoir une meilleure précision sur la reconstruction en répondant aux incertitudes sur les positions d'éclairement (précision d'une platine motorisée par exemple).
- La vPIE (vectorial PIE) permet de reconstruire les états de polarisation d'un objet en reconstruisant ses matrices de Jones. Il donne ainsi accès à des informations très intéressantes pour le design de métasurfaces dépendante de la polarisation.

6.4.5 Caractérisation de la metasurfaces de référence

6.4.5.1 Design de la métasurface de référence

Pour la métasurface de référence, nous voulons créer un ensemble de données qui soit similaire à celui généré par les simulations FDTD pour les précédents designs (cartes de déphasage et de transmission présentées à la Fig. 6.4). La conception correspondante est présentée dans la Fig.6.13(a). On retrouve pour le design plusieurs carrés de taille 30×30 µm^2 composés de nanodisques de silicium de diamètres identiques D qui sont disposés sur une grille carrée régulière de pas p. Pour chaque carré différent, les diamètres des nanodisques et les tailles des cellules varient. De bas en haut, le diamètre augmente de D = 50 nm à D = 340 nm avec un pas de 10 nm. De gauche à droite, la taille des cellules augmente de p = 200 nm à p = 390 nm avec un pas de 10 nm. Les carrés dont la distance bord à bord du nanodisque est inférieure ou égale à 50 nm ne sont pas considérés (d'où la forme en "escalier" de la métasurface).

En caractérisant la phase et l'amplitude correspondantes pour chaque carré, nous pouvons recréer de nouvelles cartes d'amplitude et de phase.

6.4.5.2 Caractérisation

La métasurface de référence est fabriquée selon le même procédé que celui utilisé pour le métadéflecteur, à l'exception de la dose d'électrons appliquée pendant l'EBL qui est cette fois la même pour toutes les structures. Les mesures de ptychographie ont été effectuées pour un total de N_{ac} = 6566 positions de balayage.
Le déphasage et la transmission reconstruits de cette métasurface sont représentés sur la Fig. 6.13(b-c). Nous pouvons clairement identifier les carrés et observer une variation des déphasages mesurés en fonction des diamètres et des tailles des cellules.

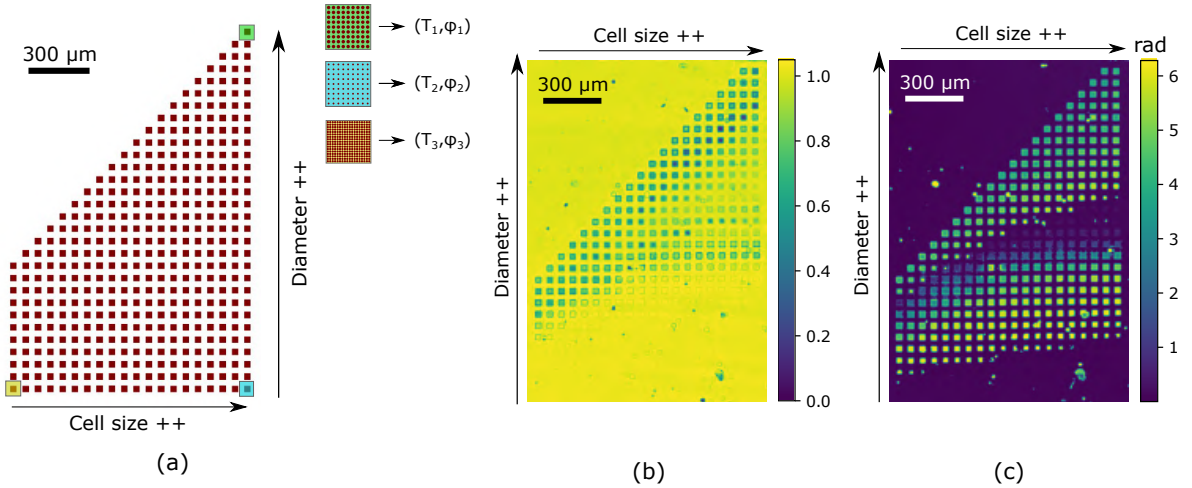

Figure 6.13: (a) Conception de la métasurface de référence. Chaque carré de gauche fait 30×30 µm^2 et est constitué de nanodisques identiques sur une grille périodique (voir les zooms en couleur vert, bleu et jaune pour trois carrés). Nous supposons que chaque carré induira un déphasage et une transmission uniformes qui seront mesurables par ptychographie. (b) Cartes de transmission et (c) de déphasage obtenues à partir de la métasurface de référence.

6.4.5.3 Extraction des données à partir de la métasurface de référence

A partir de ces mesures, nous avons générés de nouvelles cartes de déphasage et de transmission. Pour cela, nous considérons une surface centrée pour chaque carré qui correspond à une région de 15×15 µm^2, dont nous extrayons la valeur moyenne du déphasage et de la transmission. Nous montrons les cartes de déphasage et de transmission extraites sur la Fig. 6.14. Le triangle blanc dans le coin supérieur gauche représente les données manquantes (paires de (D, p) qui n'ont pas été fabriquées). Comme on peut le voir, il y a une transmission élevée qui diminue lorsque le diamètre s'approche de la taille de la cellule, ainsi qu'une variation significative du déphasage lorsque le diamètre augmente.
Maintenant que ces cartes de transmissions et de déphasages sont établies, il nous faut fixer une périodicité pour laquelle une variation sur le diamètre permet de parcourir des déphasages de 0 à 2π tout en maintenant une forte transmission.

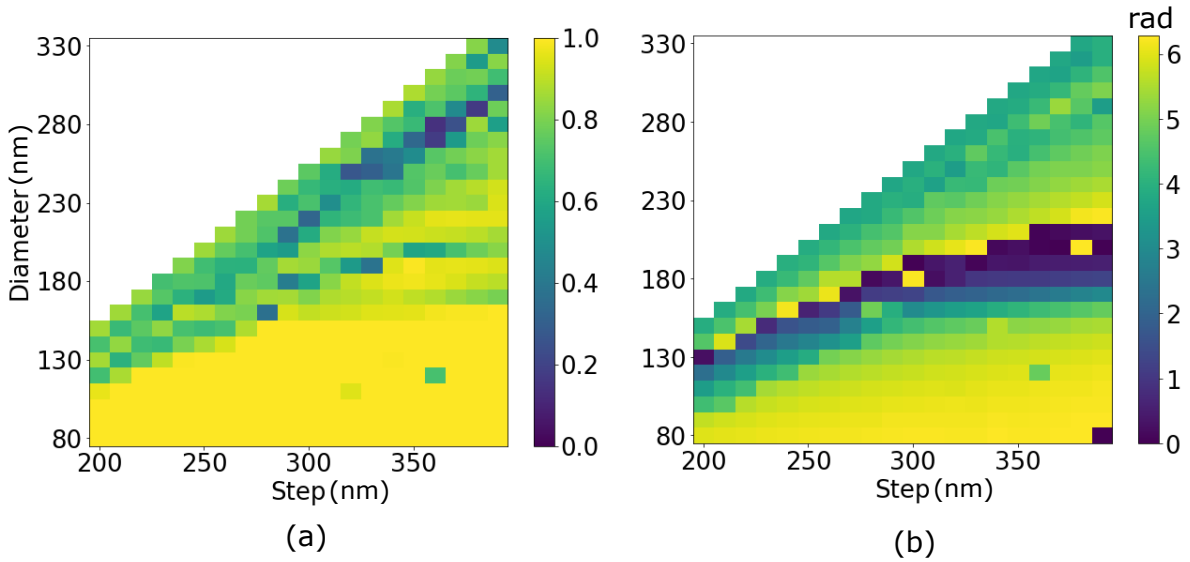

Figure 6.14: Cartes de transmission (a) et de déphasage (b) obtenues à partir de la métasurface de référence.

Erreur dans la conception Lors de la rédaction de ce manuscrit, je me suis aperçu que j'avais fait une erreur dans le choix de la périodicité appropriée. En effet, j'ai malheureusement confondu deux colonnes différentes de l'échantillon de référence et choisi des géométries pour la périodicité $p = 350$ nm, pensant que ces valeurs étaient celles de la périodicité $p = 300$ nm. Comme nous allons le voir dans ce qui suit, cela a eu un impact sur les performances de la métasurface fabriquée à partir de ces données.

6.4.6 Design, fabrication et caractérisation d'une métalentille

Suite à cela, nous avons conçu et fabriqué une métalentille, avec le même principe que pour le métadéflecteur, mais en utilisant les données extraites de la métasurfaces de référence. Cette lentille a un motif carré de 1 mm de largeur et doit focaliser une onde plane normalement incidente de longueur d'onde 750 nm à une distance de 5 mm.
La phase et l'amplitude de cette métalentille fabriquée sont mesurées par ptychographie et sont représentées en Fig. 6.15 Sur la base de l'amplitude complexe récupérée, nous pouvons extraire des informations sur l'efficacité de la métalentille. Pour cela, nous considérons trois lentilles différentes: (i) une lentille simulée parfaite (ou idéale) définie analytiquement, (ii) une lentille simulée à partir des données théoriquement accessibles et (iii) la métalentille fabriquée et caractérisée.
La lentille idéale a une transmission parfaite et un front d'onde sphérique centré sur le point focal. La lentille simulée est définie uniquement à l'aide des configurations extraites des cartes de transmission et de déphasage mesurées par ptychographie sur l'échantillon de référence. Puisqu'elle prend en compte les réponses optiques induites par les nanostructures, la lentille simulée représente les performances attendues de la métasurfaces fabriquée. En comparant les performances entre ces trois lentilles, nous allons donc pouvoir déterminer l'efficacité de la métalentille fabriquée et comparer ses performances mesurées avec celles attendues par simulation.
Enfin, afin de comparer la nouvelle approche de design avec l'approche conventionnelle, nous

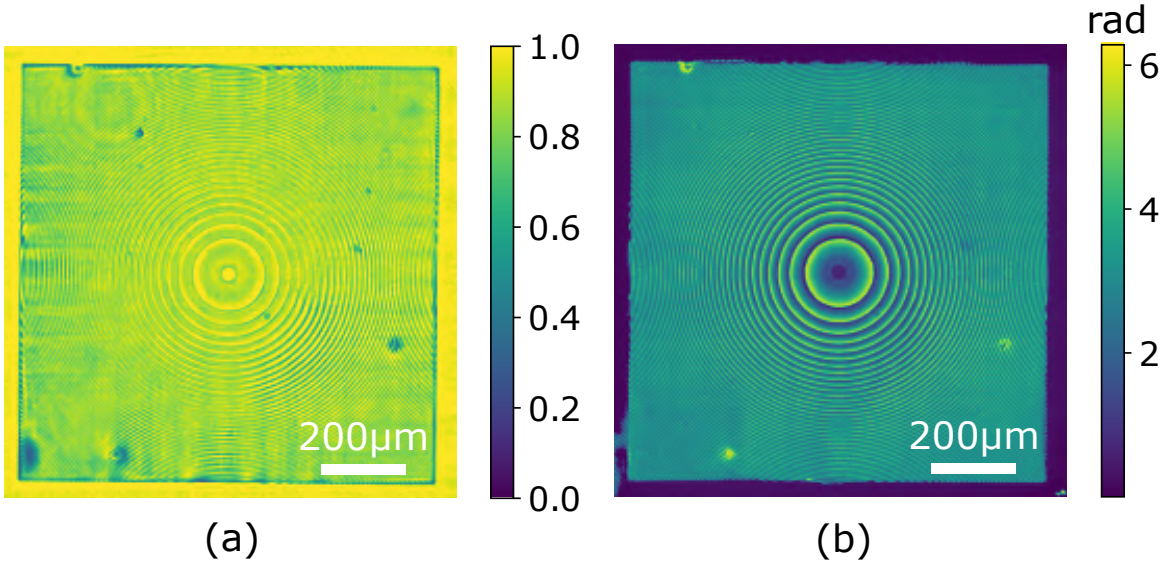

Figure 6.15: Reconstruction par ptychographie de la métalentille qui a été conçu à partir des données de ptychographie de la métasurface de référence. La transmission est représentée en (a) et le déphasage en (b).

avons également designé et fabriqué une autre métalentille uniquement à partir des données FDTD utilisées pour le métadéflecteur. Dans ce cas, nous comparons également la métalentille fabriquée avec une lentille simulée (à partir des données FDTD) et la lentille idéale.

6.4.7 Caractérisation des performances

A partir des cartes de champs complexes de toutes ces lentilles, nous utilisons le module python *pyoptica* afin de propager les champs correspondants et de regarder les profils d'intensité au niveau du plan focal ($f = 5$ mm). Les résultats sont affichés en Fig. 6.16. A gauche (resp. droite) sont montrés les résultats pour l'approche classique (resp. nouvelle approche).
De ces courbes, nous voyons tout d'abord que la métalentille obtenue par l'approche classique est plus efficace que celle obtenue par la nouvelle approche. Ceci n'est pas surprenant compte tenu de l'erreur qui a été faite lors de la conception avec la nouvelle approche (détaillée ci-dessus). Cependant, nous remarquons que les courbes des métasurfaces simulées et fabriquées obtenues par la nouvelle approche ont un meilleur accord que celles obtenues par l'approche classique. Cela signifie un meilleur accord entre la simulation et les mesures pour la nouvelle approche.
Pour confirmer ces observations, nous avons calculé le rapport entre les intensités maximales des lentilles simulées et fabriquées par rapport à la lentille idéale. Nous avons également examiné les rapports de Strehl et les efficacités de focalisation.
Pour l'approche conventionnelle, nous obtenons des ratios d'intensités de 87% et de 74% pour la métasurface simulée et la métasurfaces fabriquée, des rapports de Strehl de 96% et 92% et des efficacités de focalisation de 77% et 75%. Pour l'approche utilisant la ptychographie, nous mesuront cette fois des ratios d'intensité de 70% et de 66%, des rapports de Strehl de 88% pour les deux et des efficacités de diffraction de 56% et 55%. Ainsi, à partir de ces résultats, nous voyons que malgré la plus faible efficacité obtenue avec l'approche utilisant la ptychographie (due à l'erreur de sélection de la géométrie), nous avons un meilleur accord entre les simula-

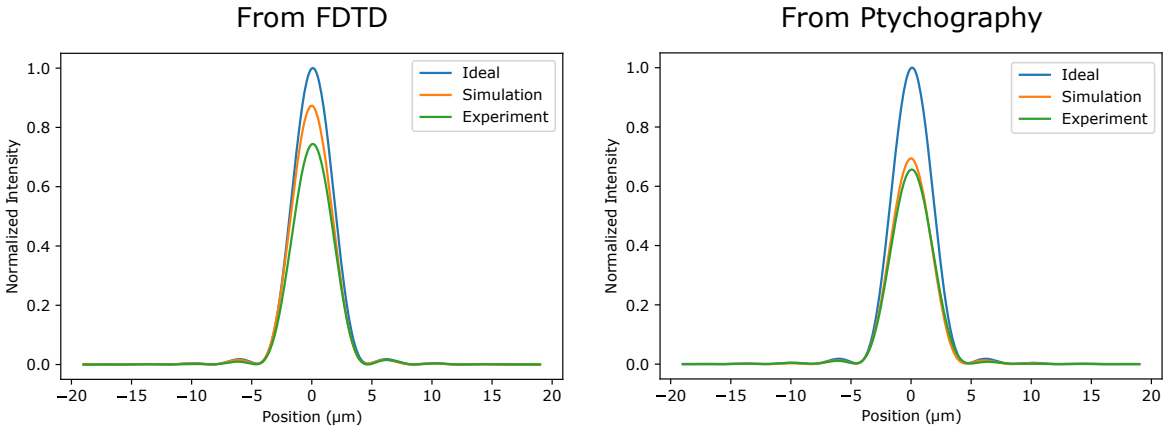

Figure 6.16: Profils d'intensités au plan focal ($f = 5$ mm) pour la lentille idéale (en bleu), les lentilles simulées à partir des bases de données (en orange) , et les métalentilles fabriquées (en vert). Les résultats obtenus pour l'approche conventionnelle (resp. nouvelle approche) sont représentés à gauche (resp. droite).

tions et l'expérience que celui obtenu avec l'approche classique. Cela nous permet de conclure sur la pertinence de cette nouvelle approche de conception afin de mieux prévenir l'impact des erreurs de nanofabrication sur les performances des métasurfaces.

6.5 Conclusion et perspectives

Ainsi, dans ce manuscrit, nous avons d'abord étudié les limites en termes d'efficacités de métasurfaces fabriquées selon une approche conventionnelle optimisée. Pour cela, nous avons fabriqué un métadéflecteur et étudié l'impact des erreurs de nanofabrication sur les performances optiques. En vue de diminuer ces impacts, nous avons présenté et mis en place une nouvelle approche pour le design et la fabrication de métasurfaces se basant sur une caractérisation préalable d'une métasurface de référence par ptychographie. Nous avons ainsi conçu et fabriqué une métalentille et pu observer un très bon accord en simulations et mesures, accord meilleur que celui observé pour l'approche conventionnelle. Cela nous a permis de conclure sur la pertinence de cette nouvelle approche et sur son fort potentiel pour améliorer les performances des métasurfaces.
Dans le prolongement de ce travail, nous prévoyons de refabriquer une nouvelle métasurface de référence en utilisant différents facteurs de dose électroniques pour obtenir une meilleure précision de fabrication. Cela nous permettra de fabriquer une nouvelle métalentille dont l'efficacité sera comparable à celle de la lentille fabriquée à partir des données FDTD. Deuxièmement, nous envisageons également d'utiliser la ptychographie vectorielle pour pouvoir fabriquer des métasurfaces plus complexes impliquant différents comportements par rapport à la polarisation de la lumière. Finalement, une autre possibilité excitante offerte par l'approche de la ptychographie est la possibilité de faire fonctionner un réseau neuronal avec des métasurfaces de très grande taille. En effet, la ptychographie permet de caractériser des objets dont les tailles sont trop grandes pour être simulées.

Appendix A: Coupled systems with dipole approximation

The GDM tool is technically limited to simulate the optical response of metasurfaces. This limitation led us to consider the dipole and quadrupole approximations. Here, we exploit the dipole approximation to simulate the coupling effects present for systems of several nanostructures.

In Fig. .17, we study the influence of the electromagnetic coupling between nano-objects on the example of a system of 5 gold nanorods of size $100 \times 50 \times 50$ nm using the dipolar approximation and the pseudopolarizabilities formalism. The scattering spectra and near-field intensity maps predicted by the full GDM simulations, the coupled static polarizations and the Born approximation are compared. In the Born approximation, the scattering of each dipole is calculated separately, so only interference effects in the far-field are taken into account, while near-field coupling or multi-scattering events are not considered. The incident light is Y-polarized.

As we can see, the agreement between the full simulations and the approximation deteriorates when the nanostructures get closer. The Born approximation only works for large spacing values (Fig. .17(e)), *i.e* cases in which the coupling effects are negligible. The pseudopolarizability approach, on the other hand, improves the agreement for shorter spacings (Fig. .17(d)) but is not sufficient when the structures become too close. This breakdown for small distances can be explained by the fact that pseudopolarizabilities are defined specifically for plane wave illumination. When the structures are sufficiently separated, the field scattered by a given nano-object at the location of its neighbors resembles very closely the one of a plane wave (also because the structures are very small). However, when the structures are very close, this plane wave approximation is no longer correct, and the pseudopolarizability approximation is strongly impaired.

Moreover, we consider here only the dipole moments, which is not sufficient to describe precisely the near field close to the nanostructures. Indeed, higher order multipolar contributions, such as quadrupoles, although only weakly radiating in far field can substantially modify the near field intensity. Therefore, the quadrupole approximation gives better results as it refines the coupling interactions. Unfortunately, the implementation of a quadrupolar approximation based on the same principle as for pseudopolarizabilities would still rely on plane wave illuminations, and would therefore not be compatible with near-field coupling.

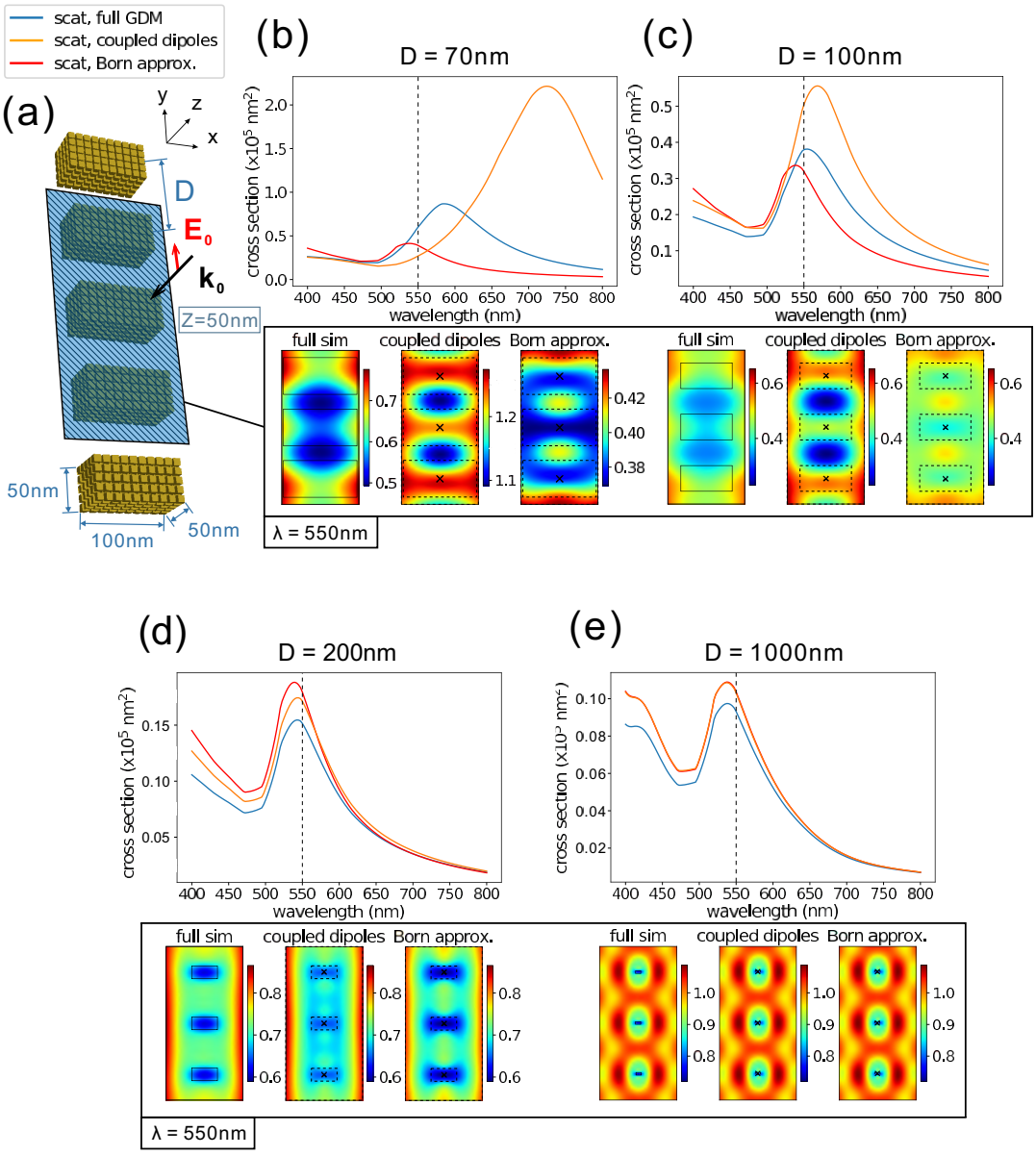

Figure .17: Coupling of five gold nanorods of dimensions 100 × 50 × 50 nm^3 ($X \times Y \times Z$), aligned along the OY axis. As illustrated in (a), the rods are separated by a variable distance D (center-to-center) and are illuminated by a plane wave of linear polarization along Y. (b-e) For different distances D between the nanorods, comparison of: scattering spectra (on top) and near-field intensity $|E|^2/|E0|^2$ in a plane parallel to XY at a height Z = 50 nm above the rod's top surface (on bottom). The shown area in the near-field intensity maps is $3D/2 \times 3D$, the wavelength of the illumination is 550 nm. Note that in (b) the near-field maps are not on the same color scale.

Appendix B: Meep script and detailed description

We detail here how to perform a FDTD simulation with Meep, based on an example script provided below.

Define the volume First, we parameterize in which volume we perform the simulations. Thus, we define the size of the volume in the X, Y and Z directions respectively using the parameters s_x, s_y and s_z. The values chosen in our example are s_x = 3 µm, s_y = 0.3 µm, s_z = 10 µm.
Next, we set the resolution parameter, usually defined as a number of pixels per micrometer. In our example, we set a resolution of 100, which gives a pixel size of 10 nm.
Finally, we set the Perfectly Matched Layers (PML). PMLs are in fact layers that absorb the field, thus allowing to fix the boundaries of a system. Without PMLs in the Z axis, for example, a plane wave that propagates toward +Z beyond the boundary of $Z = s_z/2$ would arrive at $Z = -s_z/2$ and continues its propagation. To work effectively, the thickness of the PMLs must always be greater than the wavelength of the illumination. In our example, since the wavelength used is λ = 750 nm, we defined a PML layer of 1 µm thickness in Z. In the X and Y directions, we did not add any PML, in order to obtain periodic boundary conditions.

Define the environment Now that the volume is set, we can start to design what it is made of. To do this, we first need to specify the materials that will be used (quartz, silicon, ...). Some values are already available in the Meep library, but it can be more accurate to define your own values (as we did in the example, taking values from ellipsometry measurements). By default, the environment is vacuum (n = 1).
Then we can select which geometries to use by creating a list object. When we add a geometry to this list, we inform on its shape, size, material and position. In Meep, several types of shapes are already available such as cylinders, cones, spheres, ellipses, etc. If two objects are defined at the same position, the last one added will overwrite the previous one.
In the example script, we first defined a quartz substrate as a block occupying half the volume. Then, we added 9 cylinders of height 370 nm and variable diameters for positions $X = k \times 300$ nm ($1 \leq k \leq 9$).

Set illumination source Then we define the illumination source. We set its frequency (in μm^{-1}), its polarization, its starting position, and its size.
In our example, we used a *Continuous Source* which refers to a plane wave. Its starting position is $(0, 0, -s_z/2 + 1,5$ µm$)$ and its size is $(s_x, s_y, 0)$. The plane wave propagates towards $+Z$ and $-Z$, but is immediately absorbed by the PML set up at $-s_z/2$. Thus, the only useful plane wave is the one propagating towards $+Z$, interacting with the structures.

Run the simulation The simulation object gathers all the parameters defined previously (volume, resolution, PML, geometries, illumination). Then it runs with the only tuning parameter being its duration. The latter must be long enough to reach the steady state (the field has propagated through the entire volume). In order to optimize the calculation time, it is advisable to limit the duration so as not to calculate too long after reaching the steady state.

Get the desired parameters output Finally, we extract the output parameters we want. In the attached script below, we extract the dielectric environment and the E_x component of the electric field.

```
import meep as mp
import numpy as np
import matplotlib.pyplot as plt
mp.quiet(quietval = True)# Desactivate prints info from Meep
#%%*************************************************************************
#                            DEFINE THE VOLUME
#*************************************************************************
sx = 3 # size of cell in X direction in um
sy = 0.3 # size of cell in Y direction in um
sz = 10. # size of cell in Z direction in um
cell = mp.Vector3(sx,sy,sz)  # computational cell
resolution = 100 # pixels/um
dpml = 1. # PML thickness in um
pml_layers = [mp.PML(dpml, direction=mp.Z)]

#%%*************************************************************************
#                            DEFINE THE ENVIRONMENT
#*************************************************************************
# definition of the refractive index of Silicium at 750 nm
lbda = 0.750 # wavelength used in um
n = 3.639+0.0076156j # refractive index measured
epsilon_imag = (n**2).imag
epsilon_ref = (n**2).real
d_cond_ref = 2 * np.pi * 1/lbda * epsilon_imag / epsilon_ref
# meep object containing information on the defined material
cSi = mp.Medium(epsilon=epsilon_ref, D_conductivity=d_cond_ref)

#%%*************************************************************************
#                            DEFINE THE GEOMETRIES
#*************************************************************************
# Glass substrate for Z<0
nsubstrate2 = 1.45
substrate2 = mp.Block(mp.Vector3(1e20,1e20,sz/2),
                      center=mp.Vector3(0,0,-sz/4.),
                      material=mp.Medium(index=nsubstrate2))

# nanodiscs geometries
H = 0.370 # height in um
# radius in um
rad = np.array([104, 95, 89, 85, 82, 78, 74, 69, 57, 0])/1000
NX = len(rad) # number of disks in X
NY = 1 # number of disks in Y
ax = sx / float(NX) # distance between two neighbors disks in X
```

```
ay = sy # distance between two neighbors disks in Y

# Set the geometry obect
geometry = []
geometry.append(substrate2)
for i in range(0,NX):
  for j in range(0,NY):
      Xc = (i-(NX-1)/2)*ax
      Yc = (j)*ay
      print('Xc =',Xc, 'Yc =',Yc,' rad[i] =',rad)
      geometry.append(mp.Cylinder(radius=rad, height = H,
                                  center=mp.Vector3(Xc,Yc,H/2),
                                  material=cSi))
#%%*************************************************************************
#                           LIGHT SOURCES
#*************************************************************************
fcen = 1/lbda # frequency

# Plane wave illumination
sources = [mp.Source(mp.ContinuousSource(fcen),
                     component=mp.Ex,
                     center=mp.Vector3(0,0,-sz/2 + 1.5 * dpml),
                     size=mp.Vector3(sx,sy,0))]
#%%*************************************************************************
#                             SIMULATION
#*************************************************************************
# set the simulation object
sim = mp.Simulation(cell_size=cell,
                    boundary_layers=pml_layers,
                    geometry=geometry,
                    k_point = mp.Vector3(),
                    sources=sources,
                    resolution=resolution)

# Set the periodicity condition
kx = 1./sx
ky = 1./sy
sim.k_point = mp.Vector3(kx,ky,0)

# run the simulation
sim.run(until=10)

#%%*************************************************************************
#                             EXPORT DATA
#*************************************************************************

# Get the dielectric environment
eps_data = sim.get_array(center=mp.Vector3(),
                         size=mp.Vector3(sx,0,sz),
                         component=mp.Dielectric)
eps_data_z = sim.get_array(center=mp.Vector3(0,0,H/2),
                           size=mp.Vector3(sx,sy,0),
                           component=mp.Dielectric)

# Get the computed field
ex_data = sim.get_array(center=mp.Vector3(),
```

```
                                size=mp.Vector3(sx,0,sz),
                                component=mp.Ex)
```

Appendix C: Script example using gdspy to generate a .gds mask

```
import numpy as np
from gdsii.library import Library
from gdsii.structure import Structure
from gdsii.elements import Boundary, SRef, RaithCircle
from gdsii.utils import circle, v
import gdspy
#%%
nm = 1
um = 1000 * nm
mm = 1000 * um
#%%
# load the geometries of the structures used
fname_npz = 'List_radius_lens_1mmm_foc_is_5000um.npz'
#%%
# list of the 10 selected configurations (nanodiscs of varying diameters)
list_10_radius = np.load(fname_npz)['list_10_radius']

# electron exposure doses applied for the corresponding nanostructures

doses = [2800,2500,2200,2200,2050,2050,2050,1900,1900,0][::-1]

# arranged list of all the geometry used for the design of the metasurface
matrix_all_radius = np.load(fname_npz)['matrix_all_radius'].ravel()

# positions of the structures, arranged to work with matrix_all_radius
X = np.array([np.load(fname_npz)['X'].ravel()]) * um
Y = np.array([np.load(fname_npz)['Y'].ravel()]) * um
#%%
############################
##### IF RAITH CIRCLE #####
############################
# Raith circles to use with Raith EBL
# create the first layout of the disc structures
NAME = "Test_Lentille"
lib = Library(3, NAME, 1e-9, 0.001)
disks_structs = []
for i in range(10):
    if i >0:
        disks_structs.append(Structure("Cercle_"+str(i)))
        lib.append(disks_structs[i-1])
        center = [0,0]
        disks_structs[i-1] += [RaithCircle(12, doses[i], center,
                                           list_10_radius[i]),]

```

```
############################
##### IF NORMAL CIRCLE #####
############################
# For easy visualization with KLayout
# create the first layout of the disc structures
NAME = "Test_Lentille"
lib = Library(3, NAME, 1e-9, 0.001)
disks_structs = []
for i in range(10):
    if i >0:
        disks_structs.append(Structure("Cercle_"+str(i)))
        lib.append(disks_structs[i-1])
        circlee = circle(list_10_radius[i]) + v(0*nm, 0)
        disks_structs[i-1] += [Boundary(12, 1000, circlee),]
#%%
# Call the structures from the first layout to make the metasurface design
struct_top = Structure("TOP")
lib.append(struct_top)
XY_top = np.concatenate((X,Y), axis = 0).T
print(XY_top.shape)
for i in range(len(list_10_radius)):
    if i >0:
        indexes_rad = np.where(matrix_all_radius == list_10_radius[i])[0]
        for j in indexes_rad:
            struct_top += [SRef("Cercle_"+str(i),[XY_top[j]]), ]

#%%
# save to file
fname = "lentille_PTYCHO.gds"
with open(fname, 'wb') as outfile:
    lib.save(outfile)

    #%%
# show data
poly_cell = gdspy.Cell('Deflecteur')
poly_cell.add(struct_top)
gdspy.LayoutViewer()
```

Appendix D: Example of a ptychography script

```
import numpy as np
import cupy as cp  # use cupy to accelerate the calculations
import matplotlib.pyplot as plt
import cv2

def FT(x):
    # Fourier transform and shift
    return cp.fft.fftshift(cp.fft.fft2(x))

def iFT(x):
    # inverse Fourier transform and shift
    return cp.fft.ifft2(cp.fft.ifftshift(x))

#%% Create Object numpy image
Norx =  1000
Nory =  1000

#%% Load the image that makes the taget phase and the amplitude
def rgb2gray(rgb):
    # transform a rgb defined image into a grayscale image
    return np.dot(rgb[...,:3], [0.2989, 0.5870, 0.1140])

# load target phase of shape (1000,1000)
img = cv2.imread('Image_phase.png')
phase = rgb2gray(img)
phase -= np.min(phase) # put the minimum at zero

# load target amplitude of shape (1000,1000)
img = cv2.imread('Image_amp.png')
trans = rgb2gray(img)
trans /= np.max(trans) # normalization

# define taget object coplex amplitude
image_i = trans*np.exp(1j*phase)

#%%  Fourier plane
# number of pixels on the "camera"
Nx, Ny = 256, 256
# coordinates on the camera
x = np.arange(0, Nx)
y = np.arange(0, Ny)
X,Y = np.meshgrid(x,y)

#%% To make the product between the object and the probe possible for all
```

```
    positions,
## we add bands of size Nx and Ny (size of probe) around the image
image = np.ones((Norx+Nx, Nory+Ny), dtype = complex)
image[int(Nx/2):-int(Nx/2), int(Ny/2):-int(Ny/2)] = image_i

#%% Probe definition
probe = np.ones((Nx,Ny), dtype = complex)
p_size = 90 # diameter in pixel

# Put every pixels out of the circle of diameter p_size to zero
probe[np.where(np.sqrt(((X-int(Nx/2)))**2
                       +((Y-int(Ny/2)))**2)> p_size/2)] = 0
P = cp.asarray(probe)

#%% Define the illumination positions
step = 18 # step between two positions in in pixel

POS_X, POS_Y = np.meshgrid(np.arange(0,Norx,step), np.arange(0,Nory,step))
pos_x, pos_y = np.ravel(POS_X), np.ravel(POS_Y)

# number of positions
Nmx, Nmy = len(pos_x), len(pos_y)

# add random to positions, +/- 10% of the probe size
rand_x = np.random.rand(Nmx)*p_size*0.1
rand_y = np.random.rand(Nmx)*p_size*0.1

# Get the final illumination positions (in pixel coordinates)
pos_xp = (pos_x + Nx/2 + rand_x).astype(int)
pos_yp = (pos_y + Ny/2 + rand_y).astype(int)

#%% Make as if we were using an experimental bench to record the
    intensities of
## the product of the probe and the object for all positions on the camera
data = [] # list of intensities to record
for i in range(Nmx):
    # define the window of size Nx in which we make product probe * object
    ix0, ix1 = int(pos_xp[i]-Nx/2), int(pos_xp[i]+Nx/2)
    iy0, iy1 = int(pos_yp[i]-Ny/2), int(pos_yp[i]+Ny/2)
    # product probe * object
    Phi_r = cp.asarray(image[ix0:ix1,iy0:iy1] * probe)
    # make the fourier transform and get the intensity
    I_r = cp.asnumpy(cp.abs(FT(Phi_r))**2)
    # save the intensity for the position
    data.append(I_r)

data = np.array(data)

#%% Define the ptychography loop function

# shuffle the position scan order to improve the reconstruction
list_pos_index = np.arange(Nmx)
np.random.shuffle(list_pos_index)

def ptycho_classic(Og, P):
    SSE_tot = 0 # total error
```

```
    for i in list_pos_index:
        # window of size Nx to make product probe * object
        ix0, ix1 = int(pos_xp[i]-Nx/2), int(pos_xp[i]+Nx/2)
        iy0, iy1 = int(pos_yp[i]-Ny/2), int(pos_yp[i]+Ny/2)
        # take a portion of the object using the defined window
        O = Og[ix0:ix1, iy0:iy1]
        # real intensity from the "recorded" data
        I_r = cp.asarray(data[i])
        # product probe * object
        Phi_g = O * P
        # fourier transform guessed
        Psi_g = FT(Phi_g)
        # error estimation
        SSE = cp.sum(((I_r-np.abs(Psi_g)**2)**2))
        SSE_tot += float(SSE)
        # correction with measured intensity value
        Psi_c = cp.sqrt(I_r)*cp.exp(1j*np.angle(Psi_g))
        # inverse fourier transform
        Phi_c = iFT(Psi_c)
        # Correction of the object
        O = (O + ((cp.conj(P)/(cp.max(cp.abs(P))**2 + alpha))
                  * (beta*(Phi_c-Phi_g))))
        Og[ix0:ix1, iy0:iy1] = O

        # If correction of the probe
        # P = (P + ((cp.conj(O)/(cp.max(cp.abs(O))**2 + alpha))
        #           * (gamma*(Phi_c-Phi_g))))

    return Og, P, SSE_tot

#%% Apply the algorithm

N_it = 200 # number of iterations

beta = 1 # strength for the object reconstruction
alpha = 1e-10 # value added to avoid division by zero in the algorithm
SSE_list = [] # list where the error values are saved

# define the initial guess for the object
Og = cp.ones((Norx+Nx, Nory+Ny), dtype = complex)

# If correction of the probe
# gamma = 1 # strength for the probe reconstruction

# Apply the ptychography iteration algorithm
for k in range(N_it):
    print('Interation #', k)
    # do the ptycho
    Og, P, SSE_tot = ptycho_classic(Og,P)
    # print error value to control convergence
    print("SSE = ", "{:e}".format(SSE_tot))
    SSE_list.append(SSE_tot)

#%%  Show results

# reconstructed object phase
```

```
plt.figure()
plt.imshow(cp.asnumpy(np.angle(Og))%(2*np.pi))
plt.colorbar()
plt.axis('off')

# reconstructed object amplitude
plt.figure()
plt.imshow(cp.asnumpy(np.abs(Og)))
plt.colorbar()
plt.axis('off')

# target object phase
plt.figure()
plt.imshow((np.angle(image))%(2*np.pi))
plt.colorbar()
plt.axis('off')

# target object amplitude
plt.figure()
plt.imshow(np.abs(image))
plt.colorbar()
plt.axis('off')
```

Appendix E: Common experimental issues of ptychography

We list here some common issues of the experimental ptychography setup that can deteriorate the accuracy of reconstructions.

Fixation of the sample In the case where the sample is not properly fixed on the translation stage, it can move relatively to the stage during the acquisition. This would corrupt the validity of the positions defined for the acquisition, which would affect the reconstruction. Therefore, the sample must be properly fixed, and it is also advisable to isolate the ptychography bench from external vibrations.

Power stability In our setup, we used a very powerful laser source. Therefore, we added absorbers to decrease the laser power so as not to damage the camera sensor. However, we noticed that due to the high power of the laser, the absorption rate varied over time. In the same way, we also noticed that the laser power itself took time to stabilize.
Thus, we had to wait until the measured intensity was stabilized before making the acquisitions. Indeed, otherwise, the intensity of the laser would vary during the acquisition of the data, which would deteriorate the reconstructions.

Saturation If the laser power is not stabilized, it can also saturate the measurements carried out. In that case, information would be lost due to the saturation, and the ptychography would not work properly.

Exposition time To avoid saturation, we can either adjust the power of the laser (using absorbers or reflectors), or adjust the exposure time of our camera. In the latter case, we must be careful with the frequency of the laser used. Indeed, if the data acquisition frequency is of the same order or higher than the laser frequency, the measured signal will be strongly altered (the measured intensity is not averaged), and so will the reconstructions.

Spatial coherence When we record the diffraction patterns, we have to make sure that all the beams crossing the pinhole can interfere (control the spatial coherence). Otherwise, there would be no interference, therefore no information on the diffracted intensities, and the reconstruction by ptychography would not be valid.

Imperfect Fourier transform In our configuration, we used a lens to get the intensities of the Fourier transform on the sensor of the camera. However, all the defects of the lens, or the presence of optical elements positioned between the lens and the camera sensor can alter the transformation induced. The latter would therefore not be an exact Fourier transform, which

would deteriorate the results of the ptychography.
A solution to this problem would be to remove the lens and record the intensities induced after a Fresnel propagation on the sensor. Thus, no optical element can alter the transformation since the propagation operates in free space. Although having several advantages on paper, during our tests, we did not succeed in obtaining satisfactory results using this method.

Bibliography

[1] Nanfang Yu et al. “Light Propagation with Phase Discontinuities: Generalized Laws of Reflection and Refraction”. *Science* 334.6054 (Oct. 21, 2011), pp. 333–337.

[2] Dale C. Flanders. “Submicrometer periodicity gratings as artificial anisotropic dielectrics”. *Applied Physics Letters* 42.6 (Mar. 15, 1983), pp. 492–494.

[3] Andrey B. Evlyukhin, Carsten Reinhardt, and Boris N. Chichkov. “Multipole light scattering by nonspherical nanoparticles in the discrete dipole approximation”. *Physical Review B* 84.23 (Dec. 20, 2011), p. 235429.

[4] Paolo Biagioni, Jer-Shing Huang, and Bert Hecht. “Nanoantennas for visible and infrared radiation”. *Reports on Progress in Physics* 75.2 (Jan. 2012), p. 024402.

[5] Stefan Enoch and Nicolas Bonod. *Plasmonics: From Basics to Advanced Topics*. Springer, June 30, 2012. 331 pp.

[6] T. W. Ebbesen et al. “Extraordinary optical transmission through sub-wavelength hole arrays”. *Nature* 391.6668 (Feb. 1998), pp. 667–669.

[7] Byoungho Lee et al. “Review on subwavelength confinement of light with plasmonics”. *Journal of Modern Optics* 57.16 (Sept. 20, 2010), pp. 1479–1497.

[8] Yang Zhao and Andrea Alù. “Manipulating light polarization with ultrathin plasmonic metasurfaces”. *Physical Review B* 84.20 (Nov. 16, 2011), p. 205428.

[9] Patrice Genevet et al. “Ultra-thin plasmonic optical vortex plate based on phase discontinuities”. *Applied Physics Letters* 100.1 (Jan. 2, 2012), p. 013101.

[10] Anders Pors et al. “Broadband Focusing Flat Mirrors Based on Plasmonic Gradient Metasurfaces”. *Nano Letters* 13.2 (Feb. 13, 2013), pp. 829–834.

[11] Ebrahim Karimi et al. “Generating optical orbital angular momentum at visible wavelengths using a plasmonic metasurface”. *Light: Science & Applications* 3.5 (May 2014), e167–e167.

[12] Jihua Zhang et al. “Plasmonic metasurfaces with 42.3% transmission efficiency in the visible”. *Light: Science & Applications* 8.1 (June 12, 2019), p. 53.

[13] Carl Pfeiffer and Anthony Grbic. “Metamaterial Huygens’ Surfaces: Tailoring Wave Fronts with Reflectionless Sheets”. *Physical Review Letters* 110.19 (May 6, 2013), p. 197401.

[14] Qinghua Song. *Plasmonic topological metasurface by encircling an exceptional point*. 2021. URL: https://www.science.org/doi/10.1126/science.abj3179 (visited on 02/06/2022).

[15] Manuel Decker et al. “High-Efficiency Dielectric Huygens’ Surfaces”. *Advanced Optical Materials* 3.6 (2015), pp. 813–820.

[16] M. Kerker, D.-S. Wang, and C. L. Giles. “Electromagnetic scattering by magnetic spheres”. *JOSA* 73.6 (June 1, 1983), pp. 765–767.

[17] Raquel Gomez-Medina et al. "Electric and magnetic dipolar response of germanium nanospheres: interference effects, scattering anisotropy, and optical forces". *Journal of Nanophotonics* 5.1 (Jan. 2011), p. 053512.

[18] Ye Feng Yu et al. "High-transmission dielectric metasurface with 2π phase control at visible wavelengths". *Laser & Photonics Reviews* 9.4 (2015), pp. 412–418.

[19] Katie E. Chong et al. "Polarization-Independent Silicon Metadevices for Efficient Optical Wavefront Control". *Nano Letters* 15.8 (Aug. 12, 2015), pp. 5369–5374.

[20] Katie E. Chong et al. "Efficient Polarization-Insensitive Complex Wavefront Control Using Huygens' Metasurfaces Based on Dielectric Resonant Meta-atoms". *ACS Photonics* 3.4 (Apr. 20, 2016), pp. 514–519.

[21] Lei Wang et al. "Grayscale transparent metasurface holograms". *Optica* 3.12 (Dec. 20, 2016), pp. 1504–1505.

[22] Arseniy I. Kuznetsov et al. "Optically resonant dielectric nanostructures". *Science* 354.6314 (Nov. 18, 2016), aag2472.

[23] Amir Arbabi et al. "Subwavelength-thick lenses with high numerical apertures and large efficiency based on high-contrast transmitarrays". *Nature Communications* 6.1 (May 7, 2015), p. 7069.

[24] Amir Arbabi et al. "Dielectric metasurfaces for complete control of phase and polarization with subwavelength spatial resolution and high transmission". *Nature Nanotechnology* 10 (Nov. 1, 2015), pp. 937–943.

[25] Zhenpeng Zhou et al. "Efficient Silicon Metasurfaces for Visible Light". *ACS Photonics* 4.3 (Mar. 15, 2017), pp. 544–551.

[26] Ehsan Arbabi et al. "Multiwavelength metasurfaces through spatial multiplexing". *Scientific Reports* 6.1 (Dec. 2016), p. 32803.

[27] Rifat Ahmmed Aoni et al. "High-Efficiency Visible Light Manipulation Using Dielectric Metasurfaces". *Scientific Reports* 9.1 (Apr. 24, 2019), p. 6510.

[28] Adelin Patoux et al. "Challenges in nanofabrication for efficient optical metasurfaces". *Scientific Reports* 11.1 (Mar. 10, 2021), p. 5620.

[29] Wei Ting Chen et al. "A broadband achromatic metalens for focusing and imaging in the visible". *Nature Nanotechnology* 13.3 (Mar. 2018), pp. 220–226.

[30] Philippe Lalanne et al. "Design and fabrication of blazed binary diffractive elements with sampling periods smaller than the structural cutoff". *JOSA A* 16.5 (May 1, 1999), pp. 1143–1156.

[31] Philippe Lalanne et al. "Blazed binary subwavelength gratings with efficiencies larger than those of conventional échelette gratings". *Optics Letters* 23.14 (July 15, 1998), pp. 1081–1083.

[32] Mohammadreza Khorasaninejad et al. "Metalenses at visible wavelengths: Diffraction-limited focusing and subwavelength resolution imaging". *Science* 352.6290 (June 3, 2016), pp. 1190–1194.

[33] Zhanjie Gao et al. "Revealing topological phase in Pancharatnam–Berry metasurfaces using mesoscopic electrodynamics". *Nanophotonics* 9.16 (Nov. 2, 2020), pp. 4711–4718.

[34] Qinghua Song et al. "Ptychography retrieval of fully polarized holograms from geometric-phase metasurfaces". *Nature Communications* 11.1 (May 27, 2020), p. 2651.

[35] Qinghua Song et al. "Broadband decoupling of intensity and polarization with vectorial Fourier metasurfaces". *Nature Communications* 12.1 (June 15, 2021), p. 3631.

[36] *Centenaire d'Augustin Fresnel (10 mai 1788-4 juillet 1827)*. 1928.

[37] *Lighthouse. 1911 Encyclopædia Britannica*. Ed. by Hugh Chisholm. Vol. Volume 16. 1911.

[38] Marie Jean Antoine Nicolas CARITAT (Marquis de Condorcet. *Éloge de M. le comte de Buffon*. 1790. 110 pp.

[39] *Brewster, Sir David. 1911 Encyclopædia Britannica*. Vol. Volume 4. 1911.

[40] *Augustin-Jean Fresnel. Wikipedia*. Aug. 31, 2021.

[41] Augustin (1788-1827) Auteur du texte Fresnel. *Mémoire sur un nouveau système d'éclairage des phares lu à l'Académie des sciences, le 29 juillet 1822 / par M. A. Fresnel,...* 1822.

[42] Tag Thomas. *The Fresnel Lens by Thomas Tag \textbar US Lighthouse Society*. URL: https://uslhs.org/fresnel-lens (visited on 08/19/2021).

[43] Maxwell. *VIII. A dynamical theory of the electromagnetic field \textbar Philosophical Transactions of the Royal Society of London*. 1865. URL: https://royalsocietypublishing.org/doi/10.1098/rstl.1865.0008 (visited on 08/18/2021).

[44] Lord Rayleigh. "XXXIV. On the transmission of light through an atmosphere containing small particles in suspension, and on the origin of the blue of the sky". (Apr. 1, 1899).

[45] R.W. Wood. "LXXXV. The echelette grating for the infra-red". *The London, Edinburgh, and Dublin Philosophical Magazine and Journal of Science* 20.118 (Oct. 1, 1910), pp. 770–778.

[46] Gustav Mie. *Beiträge zur Optik trüber Medien, speziell kolloidaler Metallösungen - Mie - 1908 - Annalen der Physik - Wiley Online Library*. 1908. URL: https://onlinelibrary.wiley.com/doi/abs/10.1002/andp.19083300302 (visited on 08/18/2021).

[47] Kock. *Metallic Delay Lenses - Kock - 1948 - Bell System Technical Journal - Wiley Online Library*. 1948. URL: https://onlinelibrary.wiley.com/doi/abs/10.1002/j.1538-7305.1948.tb01331.x (visited on 08/18/2021).

[48] Kenro Miyamoto. "The Phase Fresnel Lens". *JOSA* 51.1 (Jan. 1, 1961), pp. 17–20.

[49] R.W. Wood. "XLII. On a remarkable case of uneven distribution of light in a diffraction grating spectrum". *The London, Edinburgh, and Dublin Philosophical Magazine and Journal of Science* 4.21 (Sept. 1, 1902), pp. 396–402.

[50] Wolfram Hergert. *Mie Theory: A Review \textbar SpringerLink*. 2012. URL: https://link.springer.com/chapter/10.1007/978-3-642-28738-1_2 (visited on 08/18/2021).

[51] L. Brillouin. *WAVE PROPAGATION IN PERIODIC STRUCTURES : Electric filters and crystal lattices. Second edition with corrections and additions*. New York NY: Dover publications, 1953. xii–255 p.

[52] W. J. Wiscombe. "Improved Mie scattering algorithms". *Applied Optics* 19.9 (May 1, 1980), pp. 1505–1509.

[53] Warren Wiscombe. “Mie Scattering Calculations: Advances in Technique and Fast, Vector-speed Computer Codes”. (Jan. 1, 1979).

[54] V.E. Cachorro and L.L. Salcedo. “New Improvements for Mie Scattering Calculations”. *Journal of Electromagnetic Waves and Applications* 5.9 (Jan. 1, 1991), pp. 913–926.

[55] Allen Taflove and Susan C. Hagness. *Computational electrodynamics : the finite-difference time-domain method*. 2005. URL: https://cds.cern.ch/record/1698084 (visited on 03/09/2021).

[56] Purcell. *Scattering and Absorption of Light by Nonspherical Dielectric Grains - NASA/ADS*. 1973. URL: https://ui.adsabs.harvard.edu/abs/1973ApJ...186..705P/abstract (visited on 08/19/2021).

[57] Bruce T. Draine and Piotr J. Flatau. “Discrete-Dipole Approximation For Scattering Calculations”. *JOSA A* 11.4 (Apr. 1, 1994), pp. 1491–1499.

[58] Christian Girard. *Phys. Rev. Lett. 74, 526 (1995) - Generalized Field Propagator for Electromagnetic Scattering and Light Confinement*. 1995. URL: https://journals.aps.org/prl/abstract/10.1103/PhysRevLett.74.526 (visited on 08/19/2021).

[59] Christian Girard. *Near-field optics theories - IOPscience*. 1996. URL: https://iopscience.iop.org/article/10.1088/0034-4885/59/5/002/meta (visited on 08/19/2021).

[60] Sajeev John. “Strong localization of photons in certain disordered dielectric superlattices”. *Physical Review Letters* 58.23 (June 8, 1987), pp. 2486–2489.

[61] Eli Yablonovitch. “Inhibited Spontaneous Emission in Solid-State Physics and Electronics”. *Physical Review Letters* 58.20 (May 18, 1987), pp. 2059–2062.

[62] John D. Joannopoulos et al. *Photonic Crystals*. Princeton University Press, Oct. 30, 2011.

[63] Gemma Rius Suñé. “Electron beam lithography for Nanofabrication”. PhD thesis. Universitat Autònoma de Barcelona, Mar. 10, 2008.

[64] Marc J. Madou. *Manufacturing Techniques for Microfabrication and Nanotechnology*. CRC Press, June 13, 2011. 672 pp.

[65] L. B. Lesem, P. M. Hirsch, and J. A. Jordan. “The Kinoform: A New Wavefront Reconstruction Device”. *IBM Journal of Research and Development* 13.2 (Mar. 1969), pp. 150–155.

[66] W. Stork et al. “Artificial distributed-index media fabricated by zero-order gratings”. *Optics Letters* 16.24 (Dec. 15, 1991), pp. 1921–1923.

[67] H. Haidner et al. “Diffraction grating with rectangular grooves exceeding 80% diffraction efficiency”. *Infrared Physics* 34.5 (Oct. 1, 1993), pp. 467–475.

[68] H. Haidner, J. T. Sheridan, and N. Streibl. “Dielectric binary blazed gratings”. *Applied Optics* 32.22 (Aug. 1, 1993), pp. 4276–4278.

[69] F. T. Chen and H. G. Craighead. “Diffractive phase elements based on two-dimensional artificial dielectrics”. *Optics Letters* 20.2 (Jan. 15, 1995), pp. 121–123.

[70] Frederick T. Chen and Harold G. Craighead. “Diffractive lens fabricated with mostly zeroth-order gratings”. *Optics Letters* 21.3 (Feb. 1, 1996), pp. 177–179.

[71] Zhiping Zhou and Timothy J. Drabik. "Optimized binary, phase-only, diffractive optical element with subwavelength features for 1.55 um". *JOSA A* 12.5 (May 1, 1995), pp. 1104–1112.

[72] M. E. Warren et al. "High-efficiency subwavelength diffractive optical element in GaAs for 975 nm". *Optics Letters* 20.12 (June 15, 1995), pp. 1441–1443.

[73] Philippe Lalanne. "Waveguiding in blazed-binary diffractive elements". *JOSA A* 16.10 (Oct. 1, 1999), pp. 2517–2520.

[74] Farn. *Binary gratings with increased efficiency*. 1992. URL: https://www.osapublishing.org/ao/abstract.cfm?uri=ao-31-22-4453 (visited on 01/11/2022).

[75] Nanfang Yu and Federico Capasso. "Flat optics with designer metasurfaces". *Nature Materials* 13.2 (Feb. 2014), pp. 139–150.

[76] Alexander Y. Zhu et al. "Traditional and emerging materials for optical metasurfaces". *Nanophotonics* 6.2 (2016), pp. 452–471.

[77] Philippe Lalanne and Pierre Chavel. "Metalenses at visible wavelengths: past, present, perspectives". *Laser & Photonics Reviews* 11.3 (2017), p. 1600295.

[78] Patrice Genevet et al. "Recent advances in planar optics: from plasmonic to dielectric metasurfaces". *Optica* 4.1 (Jan. 20, 2017), pp. 139–152.

[79] Seyedeh Mahsa Kamali et al. "A review of dielectric optical metasurfaces for wavefront control". *Nanophotonics* 7.6 (June 27, 2018), pp. 1041–1068.

[80] Costas M. Soukoulis and Martin Wegener. "Optical Metamaterials—More Bulky and Less Lossy". *Science* (Dec. 17, 2010). Publisher: American Association for the Advancement of Science.

[81] J.B. Pendry et al. "Magnetism from conductors and enhanced nonlinear phenomena". *IEEE Transactions on Microwave Theory and Techniques* 47.11 (Nov. 1999), pp. 2075–2084.

[82] D. R. Smith et al. "Composite Medium with Simultaneously Negative Permeability and Permittivity". *Physical Review Letters* 84.18 (May 1, 2000), pp. 4184–4187.

[83] R. A. Shelby, D. R. Smith, and S. Schultz. "Experimental Verification of a Negative Index of Refraction". *Science* (Apr. 6, 2001).

[84] D. R. Smith, J. B. Pendry, and M. C. K. Wiltshire. "Metamaterials and Negative Refractive Index". *Science* 305.5685 (Aug. 6, 2004), pp. 788–792.

[85] J. B. Pendry, D. Schurig, and D. R. Smith. "Controlling Electromagnetic Fields". *Science* 312.5781 (June 23, 2006), pp. 1780–1782.

[86] M. Notomi. "Theory of light propagation in strongly modulated photonic crystals: Refractionlike behavior in the vicinity of the photonic band gap". *Physical Review B* 62.16 (Oct. 15, 2000), pp. 10696–10705.

[87] Ya-nan Zhang, Yong Zhao, and Ri-qing Lv. "A review for optical sensors based on photonic crystal cavities". *Sensors and Actuators A: Physical* 233 (Sept. 1, 2015), pp. 374–389.

[88] Costas M. Soukoulis, Stefan Linden, and Martin Wegener. "Negative Refractive Index at Optical Wavelengths". *Science* (Jan. 5, 2007).

[89] Wenshan Cai et al. "Optical cloaking with metamaterials". *Nature Photonics* 1.4 (Apr. 2007), pp. 224–227.

[90] N. I. Landy et al. "Perfect Metamaterial Absorber". *Physical Review Letters* 100.20 (May 21, 2008), p. 207402.

[91] R. B. Greegor et al. "Simulation and testing of a graded negative index of refraction lens". *Applied Physics Letters* 87.9 (Aug. 29, 2005), p. 091114.

[92] Smith. "Gradient index metamaterials". (2005).

[93] Alexandra Boltasseva and Harry A. Atwater. "Low-Loss Plasmonic Metamaterials". *Science* 331.6015 (Jan. 21, 2011), pp. 290–291.

[94] E.F. Kuester et al. "Averaged transition conditions for electromagnetic fields at a metafilm". *IEEE Transactions on Antennas and Propagation* 51.10 (Oct. 2003), pp. 2641–2651.

[95] Christopher L. Holloway et al. "An Overview of the Theory and Applications of Metasurfaces: The Two-Dimensional Equivalents of Metamaterials". *IEEE Antennas and Propagation Magazine* 54.2 (Apr. 2012), pp. 10–35.

[96] Na Liu et al. "Infrared Perfect Absorber and Its Application As Plasmonic Sensor". *Nano Letters* 10.7 (July 14, 2010), pp. 2342–2348.

[97] Carlo Gigli et al. "Fundamental Limitations of Huygens' Metasurfaces for Optical Beam Shaping". *Laser & Photonics Reviews* 15.8 (2021), p. 2000448.

[98] Philippe Lalanne et al. "A transmission polarizing beam splitter grating". *Journal of Optics A: Pure and Applied Optics* 1.2 (Jan. 1999), pp. 215–219.

[99] David Sell et al. "Large-Angle, Multifunctional Metagratings Based on Freeform Multimode Geometries". *Nano Letters* 17.6 (June 14, 2017), pp. 3752–3757.

[100] Amir Arbabi et al. "Increasing efficiency of high numerical aperture metasurfaces using the grating averaging technique". *Scientific Reports* 10.1 (Apr. 28, 2020), p. 7124.

[101] Ke Wang et al. "Broadband and Broad-Angle Low-Scattering Metasurface Based on Hybrid Optimization Algorithm". *Scientific Reports* 4.1 (Aug. 4, 2014), p. 5935.

[102] Jianji Yang and Jonathan A. Fan. "Topology-optimized metasurfaces: impact of initial geometric layout". *Optics Letters* 42.16 (Aug. 15, 2017), pp. 3161–3164.

[103] Zhaocheng Liu et al. "Generative Model for the Inverse Design of Metasurfaces". *Nano Letters* 18.10 (Oct. 10, 2018), pp. 6570–6576.

[104] Tianshuo Qiu et al. "Deep Learning: A Rapid and Efficient Route to Automatic Metasurface Design". *Advanced Science* 6.12 (2019), p. 1900128.

[105] Mahmoud M. R. Elsawy et al. "Numerical Optimization Methods for Metasurfaces". *Laser & Photonics Reviews* 14.10 (2020), p. 1900445.

[106] Jiaqi Jiang and Jonathan A. Fan. "Simulator-based training of generative neural networks for the inverse design of metasurfaces". *Nanophotonics* 9.5 (May 1, 2020), pp. 1059–1069.

[107] Mingkun Chen. "Physics-augmented deep learning for high-speed electromagnetic simulation and optimization \textbar Research Square". (2021).

[108] Peter R. Wiecha et al. “Deep learning in nano-photonics: inverse design and beyond”. *Photonics Research* 9.5 (May 1, 2021), B182–B200.

[109] Jiaqi Jiang, Mingkun Chen, and Jonathan A. Fan. “Deep neural networks for the evaluation and design of photonic devices”. *Nature Reviews Materials* 6.8 (Aug. 2021), pp. 679–700.

[110] Thaibao Phan et al. “High-efficiency, large-area, topology-optimized metasurfaces”. *Light: Science & Applications* 8.1 (May 29, 2019), p. 48.

[111] J. B. Pendry. “Negative Refraction Makes a Perfect Lens”. (2000).

[112] Nathaniel K. Grady et al. “Terahertz Metamaterials for Linear Polarization Conversion and Anomalous Refraction”. *Science* (June 14, 2013).

[113] Jiaming Hao et al. “Manipulating Electromagnetic Wave Polarizations by Anisotropic Metamaterials”. *Physical Review Letters* 99.6 (Aug. 10, 2007), p. 063908.

[114] J. P. Balthasar Mueller et al. “Metasurface Polarization Optics: Independent Phase Control of Arbitrary Orthogonal States of Polarization”. *Physical Review Letters* 118.11 (Mar. 14, 2017), p. 113901.

[115] Shuai Wang et al. “Arbitrary polarization conversion dichroism metasurfaces for all-in-one full Poincaré sphere polarizers”. *Light: Science & Applications* 10.1 (Jan. 27, 2021), p. 24.

[116] Yueqiang Hu et al. “All-dielectric metasurfaces for polarization manipulation: principles and emerging applications”. *Nanophotonics* -1 (ahead-of-print June 29, 2020).

[117] H. L. Zhu et al. “Linear-to-Circular Polarization Conversion Using Metasurface”. *IEEE Transactions on Antennas and Propagation* 61.9 (Sept. 2013), pp. 4615–4623.

[118] Dandan Wen et al. “Helicity multiplexed broadband metasurface holograms”. *Nature Communications* 6.1 (Sept. 10, 2015), p. 8241.

[119] Liangui Deng et al. “Malus-metasurface-assisted polarization multiplexing”. *Light: Science & Applications* 9.1 (June 12, 2020), p. 101.

[120] Seyedeh Mahsa Kamali et al. “Angle-Multiplexed Metasurfaces: Encoding Independent Wavefronts in a Single Metasurface under Different Illumination Angles”. *Physical Review X* 7.4 (Dec. 6, 2017), p. 041056.

[121] Ehsan Arbabi et al. “Multiwavelength polarization-insensitive lenses based on dielectric metasurfaces with meta-molecules”. *Optica* 3.6 (June 20, 2016), pp. 628–633.

[122] Ehsan Arbabi et al. “Two-Photon Microscopy with a Double-Wavelength Metasurface Objective Lens”. *Nano Letters* 18.8 (Aug. 8, 2018), pp. 4943–4948.

[123] Ehsan ARBABI et al. “Dispersionless and dispersion-controlled optical dielectric metasurfaces”. Pat. 10670782B2. Type: patentus. June 2, 2020.

[124] Wei Ting Chen, Alexander Y. Zhu, and Federico Capasso. “Flat optics with dispersion-engineered metasurfaces”. *Nature Reviews Materials* (June 19, 2020), pp. 1–17.

[125] Shuming Wang et al. “A broadband achromatic metalens in the visible”. *Nature Nanotechnology* 13.3 (Mar. 2018), pp. 227–232.

[126] Ehsan Arbabi et al. “Controlling the sign of chromatic dispersion in diffractive optics with dielectric metasurfaces”. *Optica* 4.6 (June 20, 2017), p. 625.

[127] Sajan Shrestha et al. "Broadband achromatic dielectric metalenses". *Light: Science & Applications* 7.1 (Nov. 7, 2018), p. 85.

[128] Abdoulaye Ndao et al. "Octave bandwidth photonic fishnet-achromatic-metalens". *Nature Communications* 11.1 (June 25, 2020), p. 3205.

[129] Wei Ting Chen et al. "A broadband achromatic polarization-insensitive metalens consisting of anisotropic nanostructures". *Nature Communications* 10.1 (Jan. 21, 2019), p. 355.

[130] Ehsan Arbabi et al. "MEMS-tunable dielectric metasurface lens". *Nature Communications* 9.1 (Feb. 23, 2018), p. 812.

[131] Mohsen Rahmani et al. "Reversible Thermal Tuning of All-Dielectric Metasurfaces". *Advanced Functional Materials* 27.31 (2017), p. 1700580.

[132] Khosro Zangeneh Kamali et al. "Reversible Image Contrast Manipulation with Thermally Tunable Dielectric Metasurfaces". *Small* 15.15 (2019), p. 1805142.

[133] Jingbo Wu et al. "Liquid crystal programmable metasurface for terahertz beam steering". *Applied Physics Letters* 116.13 (Mar. 30, 2020), p. 131104.

[134] Manuel Decker et al. "Electro-optical switching by liquid-crystal controlled metasurfaces". *Optics Express* 21.7 (Apr. 8, 2013), pp. 8879–8885.

[135] Andrei Komar et al. "Dynamic Beam Switching by Liquid Crystal Tunable Dielectric Metasurfaces". *ACS Photonics* 5.5 (May 16, 2018), pp. 1742–1748.

[136] Oleksandr Buchnev et al. "Electrically Controlled Nanostructured Metasurface Loaded with Liquid Crystal: Toward Multifunctional Photonic Switch". *Advanced Optical Materials* 3.5 (2015), pp. 674–679.

[137] Seyedeh Mahsa Kamali et al. "Highly tunable elastic dielectric metasurface lenses". *Laser & Photonics Reviews* 10.6 (2016), pp. 1002–1008.

[138] Bin Liang, Jian-chun Cheng, and Cheng-Wei Qiu. "Wavefront manipulation by acoustic metasurfaces: from physics and applications". *Nanophotonics* 7.6 (June 1, 2018), pp. 1191–1205.

[139] Joon-Suh Park et al. "All-Glass, Large Metalens at Visible Wavelength Using Deep-Ultraviolet Projection Lithography". *Nano Letters* 19.12 (Dec. 11, 2019), pp. 8673–8682.

[140] Nanxi Li et al. "Large-area metasurface on CMOS-compatible fabrication platform: driving flat optics from lab to fab". *Nanophotonics* 9.10 (Sept. 2, 2020), pp. 3071–3087.

[141] Ting Hu et al. "Demonstration of color display metasurfaces via immersion lithography on a 12-inch silicon wafer". *Optics Express* 26.15 (July 23, 2018), pp. 19548–19554.

[142] Zhengji Xu et al. "CMOS-compatible all-Si metasurface polarizing bandpass filters on 12-inch wafers". *Optics Express* 27.18 (Sept. 2, 2019), pp. 26060–26069.

[143] Dong Kyo Oh et al. "Nanoimprint lithography for high-throughput fabrication of metasurfaces". *Frontiers of Optoelectronics* (Apr. 13, 2021).

[144] Simona Checcucci. *Multifunctional Metasurfaces Based on Direct Nanoimprint of Titania Sol–Gel Coatings - Checcucci - 2019 - Advanced Optical Materials - Wiley Online Library*. 2019. URL: https://onlinelibrary.wiley.com/doi/full/10.1002/adom.201801406 (visited on 06/11/2021).

[145] Vincent J. Einck et al. "Scalable Nanoimprint Lithography Process for Manufacturing Visible Metasurfaces Composed of High Aspect Ratio TiO2 Meta-Atoms". *ACS Photonics* 8.8 (Aug. 18, 2021), pp. 2400–2409.

[146] Wei Ting Chen and Federico Capasso. "Will flat optics appear in everyday life anytime soon?" *Applied Physics Letters* 118.10 (Mar. 9, 2021), p. 100503.

[147] Qiu-Hua Wang et al. "On-Chip Generation of Structured Light Based on Metasurface Optoelectronic Integration". *Laser & Photonics Reviews* 15.3 (2021), p. 2000385.

[148] Yi-Yang Xie et al. "Metasurface-integrated vertical cavity surface-emitting lasers for programmable directional lasing emissions". *Nature Nanotechnology* 15.2 (Feb. 2020), pp. 125–130.

[149] *Metalenz – Transforming light via breakthrough flat-lens technology*. URL: https://www.metalenz.com/?gclid=CjwKCAjwvuGJBhB1EiwACU1AidHknmJNsW1MhpQhp5UNJ1PkI8B7lRoCNywQAvD_B (visited on 09/08/2021).

[150] MohammadSadegh Faraji-Dana et al. "Compact folded metasurface spectrometer". *Nature Communications* 9.1 (Oct. 10, 2018), p. 4196.

[151] Inki Kim et al. "Nanophotonics for light detection and ranging technology". *Nature Nanotechnology* 16.5 (May 2021), pp. 508–524.

[152] Junghyun Park et al. "All-solid-state spatial light modulator with independent phase and amplitude control for three-dimensional LiDAR applications". *Nature Nanotechnology* 16.1 (Jan. 2021), pp. 69–76.

[153] Noah A. Rubin et al. "Matrix Fourier optics enables a compact full-Stokes polarization camera". *Science* 365.6448 (July 5, 2019).

[154] F. Balli et al. "A hybrid achromatic metalens". *Nature Communications* 11.1 (Aug. 4, 2020), p. 3892.

[155] *OSA Incubator on Flat Optics: Recent Advances and Future Opportunities \textbar Unique, Focused Experiences \textbar The Optical Society*. URL: https://www.osa.org/en-us/meetings/incubator_meetings/past_incubator_meetings/2020/flatopticsinc/ (visited on 09/08/2021).

[156] *META - Smart Materials and Nanocomposites*. URL: https://metamaterial.com/ (visited on 09/08/2021).

[157] *Lumotive*. URL: https://www.lumotive.com (visited on 09/08/2021).

[158] *Tunoptix – Emerging leader in meta- optics*. URL: https://www.tunoptix.com/ (visited on 09/08/2021).

[159] Daniel K. Nikolov et al. "Metaform optics: Bridging nanophotonics and freeform optics". *Science Advances* 7.18 (Apr. 1, 2021), eabe5112.

[160] Michael Boyarsky et al. "Electronically steered metasurface antenna". *Scientific Reports* 11.1 (Feb. 25, 2021), p. 4693.

[161] Manuel Decker et al. "Imaging Performance of Polarization-Insensitive Metalenses". *ACS Photonics* 6.6 (June 19, 2019), pp. 1493–1499.

[162] Jacob Engelberg and Uriel Levy. "The advantages of metalenses over diffractive lenses". *Nature Communications* 11.1 (Apr. 24, 2020), p. 1991.

[163] Christian Girard. "Near fields in nanostructures". *Reports on Progress in Physics* 68.8 (July 2005), pp. 1883–1933.

[164] Peter R. Wiecha. "pyGDM—A python toolkit for full-field electro-dynamical simulations and evolutionary optimization of nanostructures". *Computer Physics Communications* 233 (Dec. 1, 2018), pp. 167–192.

[165] Peter R. Wiecha et al. ""pyGDM" - new functionalities and major improvements to the python toolkit for nano-optics full-field simulations". *Computer Physics Communications* 270 (Jan. 1, 2022), p. 108142.

[166] Olivier J. F. Martin, Christian Girard, and Alain Dereux. *Generalized Field Propagator for Electromagnetic Scattering and Light Confinement*. 1995. URL: https://journals.aps.org/prl/abstract/10.1103/PhysRevLett.74.526 (visited on 11/02/2021).

[167] Adelin Patoux et al. "Polarizabilities of complex individual dielectric or plasmonic nanostructures". *Physical Review B* 101.23 (June 8, 2020), p. 235418.

[168] Rasoul Alaee, Carsten Rockstuhl, and I. Fernandez-Corbaton. "An electromagnetic multipole expansion beyond the long-wavelength approximation". *Optics Communications* 407 (Jan. 15, 2018), pp. 17–21.

[169] Kane Yee. "Numerical solution of initial boundary value problems involving maxwell's equations in isotropic media". *IEEE Transactions on Antennas and Propagation* 14.3 (May 1966), pp. 302–307.

[170] Ardavan F. Oskooi et al. "Meep: A flexible free-software package for electromagnetic simulations by the FDTD method". *Computer Physics Communications* 181.3 (Mar. 1, 2010), pp. 687–702.

[171] R. Kent Dybvig. *The Scheme Programming Language, fourth edition*. Google-Books-ID: bL_xCwAAQBAJ. MIT Press, July 31, 2009. 504 pp.

[172] Diego R. Abujetas et al. "High-Q transparency band in all-dielectric metasurfaces induced by a quasi bound state in the continuum". *arXiv:2006.12258 [physics]* (June 10, 2020).

[173] Khaled Ahmed et al. "Light field display for head mounted apparatus using metapixels". Pat. 20200135703A1. Type: patentus. Apr. 30, 2020.

[174] Philippe Lalanne. "Metasurfaces for light shaping: a look into the past to better appreciate the present and future". *Webinar series on acoustic, mechanical and thermal metamaterials*. event-place: London, United Kingdom. Nov. 2020.

[175] Carsten Schinke et al. "Uncertainty analysis for the coefficient of band-to-band absorption of crystalline silicon". *AIP Advances* 5.6 (June 1, 2015). Publisher: American Institute of Physics, p. 067168.

[176] Eugene A. Irene. "A Brief History and State of the Art of Ellipsometry". *Ellipsometry at the Nanoscale*. Ed. by Maria Losurdo and Kurt Hingerl. Berlin, Heidelberg: Springer, 2013, pp. 1–30.

[177] Y. Guerfi, F. Carcenac, and G. Larrieu. "High resolution HSQ nanopillar arrays with low energy electron beam lithography". *Microelectronic Engineering* 110 (Oct. 1, 2013), pp. 173–176.

[178] Vin-Cent Su et al. "Advances in optical metasurfaces: fabrication and applications [Invited]". *Optics Express* 26.10 (May 14, 2018), pp. 13148–13182.

[179] Matteo Altissimo. "E-beam lithography for micro-/nanofabrication". *Biomicrofluidics* 4.2 (June 1, 2010), p. 026503.

[180] Maxim V. Gorkunov et al. "Chiral visible light metasurface patterned in monocrystalline silicon by focused ion beam". *Scientific Reports* 8.1 (Aug. 2, 2018), p. 11623.

[181] Qize Zhong et al. "Large-area Metalens Directly Patterned on a 12-inch Glass Wafer using Immersion Lithography for Mass Production". *Optical Fiber Communication Conference (OFC) 2020 (2020), paper Th2A.8*. Optical Fiber Communication Conference. Optical Society of America, Mar. 8, 2020, Th2A.8.

[182] C. Vieu et al. "Electron beam lithography: resolution limits and applications". *Applied Surface Science*. Surface Science in Micro & Nanotechnology 164.1 (Sept. 1, 2000), pp. 111–117.

[183] E. Kratschmer et al. "Quantitative analysis of resolution and stability in nanometer electron beam lithography". *Journal of Vacuum Science & Technology B: Microelectronics Processing and Phenomena* 6.6 (Nov. 1, 1988), pp. 2074–2079.

[184] L. Pain et al. "Resolution limit of negative tone chemically amplified resist used for hybrid lithography: Influence of the molecular weight". *Journal of Vacuum Science & Technology B: Microelectronics and Nanometer Structures Processing, Measurement, and Phenomena* 18.6 (Nov. 1, 2000), pp. 3388–3395.

[185] Zhiping James Zhou. "Electron Beam Lithography". *Handbook of Microscopy for Nanotechnology*. Ed. by Nan Yao and Zhong Lin Wang. Boston, MA: Springer US, 2005, pp. 287–321.

[186] R. F. W. Pease. "Electron beam lithography". *Contemporary Physics* 22.3 (May 1, 1981), pp. 265–290.

[187] T. H. P. Chang. "Proximity effect in electron-beam lithography". *Journal of Vacuum Science and Technology* 12.6 (Nov. 1, 1975), pp. 1271–1275.

[188] Mihir Parikh. "Corrections to proximity effects in electron beam lithography. I. Theory". *Journal of Applied Physics* 50.6 (June 1, 1979), pp. 4371–4377.

[189] Erik H. Anderson et al. "Influence of sub-100 nm scattering on high-energy electron beam lithography". *Journal of Vacuum Science & Technology B: Microelectronics and Nanometer Structures Processing, Measurement, and Phenomena* 19.6 (Nov. 1, 2001), pp. 2504–2507.

[190] Harry J. Levinson. *Principles of Lithography*. SPIE Press, 2005. 446 pp.

[191] Yifang Chen. "Nanofabrication by electron beam lithography and its applications: A review". *Microelectronic Engineering* 135 (Mar. 5, 2015), pp. 57–72.

[192] Hideo Namatsu et al. "Three-dimensional siloxane resist for the formation of nanopatterns with minimum linewidth fluctuations". *Journal of Vacuum Science & Technology B: Microelectronics and Nanometer Structures Processing, Measurement, and Phenomena* 16.1 (Jan. 1, 1998), pp. 69–76.

[193] Hugh O. Pierson. *Handbook of Chemical Vapor Deposition, 2nd Edition: Principles, Technology and Applications*. William Andrew, Sept. 1, 1999. 507 pp.

[194] Xiang-Lei Han, Guilhem Larrieu, and Emmanuel Dubois. "Realization of Vertical Silicon Nanowire Networks with an Ultra High Density Using a Top–Down Approach". *Journal of Nanoscience and Nanotechnology* 10.11 (Nov. 1, 2010), pp. 7423–7427.

[195] Szymon Lis et al. "Application of flowable oxides in photonics". *Materials Science-Poland* 26 (Jan. 1, 2008), pp. 189–194.

[196] M. Häffner et al. "Influence of temperature on HSQ electron-beam lithography". *Journal of Vacuum Science & Technology B: Microelectronics and Nanometer Structures Processing, Measurement, and Phenomena* 25.6 (Nov. 1, 2007), pp. 2045–2048.

[197] Xiang-Lei Han et al. "Realization of ultra dense arrays of vertical silicon nanowires with defect free surface and perfect anisotropy using a top-down approach". *Microelectronic Engineering*. Proceedings of the 36th International Conference on Micro- and Nano-Engineering (MNE) 88.8 (Aug. 1, 2011), pp. 2622–2624.

[198] Christophe Cardinaud, Marie-Claude Peignon, and Pierre-Yves Tessier. "Plasma etching: principles, mechanisms, application to micro- and nano-technologies". *Applied Surface Science*. Surface Science in Micro & Nanotechnology 164.1 (Sept. 1, 2000), pp. 72–83.

[199] Riccardo d'Agostino and Daniel L. Flamm. "Plasma etching of Si and SiO2 in SF6–O2 mixtures". *Journal of Applied Physics* 52.1 (June 4, 1998), p. 162.

[200] C. J. Mogab and H. J. Levinstein. "Anisotropic plasma etching of polysilicon". *Journal of Vacuum Science and Technology* 17.3 (May 1, 1980), pp. 721–730.

[201] K. D. Vernon-Parry. "Scanning electron microscopy: an introduction". *III-Vs Review* 13.4 (July 1, 2000), pp. 40–44.

[202] Joseph I. Goldstein et al. *Scanning Electron Microscopy and X-Ray Microanalysis*. Springer, Nov. 17, 2017. 554 pp.

[203] C. A. Volkert and A. M. Minor. "Focused Ion Beam Microscopy and Micromachining". *MRS Bulletin* 32.5 (May 2007), pp. 389–399.

[204] John Melngailis. "Focused ion beam technology and applications". *Journal of Vacuum Science & Technology B: Microelectronics Processing and Phenomena* 5.2 (Mar. 1, 1987), pp. 469–495.

[205] L. A. Giannuzzi and F. A. Stevie. "A review of focused ion beam milling techniques for TEM specimen preparation". *Micron* 30.3 (June 1, 1999), pp. 197–204.

[206] Marc De Graef. *Introduction to Conventional Transmission Electron Microscopy*. Cambridge University Press, Mar. 27, 2003. 741 pp.

[207] Ludwig Reimer. *Transmission Electron Microscopy: Physics of Image Formation and Microanalysis*. Springer, Nov. 11, 2013. 532 pp.

[208] Brent Fultz and James M. Howe. *Transmission Electron Microscopy and Diffractometry of Materials*. Springer Science & Business Media, Oct. 14, 2012. 775 pp.

[209] Z. Chen et al. "Energy dispersive X-ray analysis on an absolute scale in scanning transmission electron microscopy". *Ultramicroscopy* 157 (Oct. 1, 2015), pp. 21–26.

[210] Franz J. Giessibl. "Advances in atomic force microscopy". *Reviews of Modern Physics* 75.3 (July 29, 2003), pp. 949–983.

[211] Franz J. Giessibl. "Atomic Resolution of the Silicon (111)-(7x7) Surface by Atomic Force Microscopy". *Science* 267.5194 (Jan. 6, 1995), pp. 68–71.

[212] Haoran Ren et al. "Metasurface orbital angular momentum holography". *Nature Communications* 10.1 (July 19, 2019), p. 2986.

[213] Lord Rayleigh Sec R. Rayleigh. "XVII. On the maintenance of vibrations by forces of double frequency, and on the propagation of waves through a medium endowed with a periodic structure". *The London, Edinburgh, and Dublin Philosophical Magazine and Journal of Science* 24.147 (Aug. 1, 1887), pp. 145–159.

[214] Hisao Kikuta, Hiroshi Toyota, and Wanji Yu. "Optical Elements with Subwavelength Structured Surfaces". *Optical Review* 10.2 (Mar. 1, 2003), pp. 63–73.

[215] Denis Langevin et al. "Study of disordered metallic groove arrays with a one-mode analytical model". *Optics Express* 28.15 (July 20, 2020), pp. 22549–22561.

[216] A. Rahimzadegan et al. "Disorder-Induced Phase Transitions in the Transmission of Dielectric Metasurfaces". *Physical Review Letters* 122.1 (Jan. 9, 2019), p. 015702.

[217] F. Fau-Canillac and F. Maury. "Control of the uniformity of thickness of Ni thin films deposited by low pressure chemical vapor deposition". *Surface and Coatings Technology* 64.1 (Apr. 1, 1994), pp. 21–27.

[218] Youngsu Noh et al. "Applications of vertical cavity surface emitting lasers for low-pressure chemical vapor deposition reactors". *International Journal of Heat and Mass Transfer* 141 (Oct. 1, 2019), pp. 245–255.

[219] Muhammad M. Mirza et al. "Nanofabrication of high aspect ratio (˜50:1) sub-10 nm silicon nanowires using inductively coupled plasma etching". *Journal of Vacuum Science & Technology B* 30.6 (Sept. 27, 2012), 06FF02.

[220] Max Born and Emil Wolf. *Principles of Optics: Electromagnetic Theory of Propagation, Interference and Diffraction of Light*. Elsevier, June 1, 2013. 871 pp.

[221] Arthur Baroni. "Développement de la ptychographie vectorielle pour la microscopie quantitative de matériaux anisotropes." PhD thesis. Aix Marseille Université, Oct. 22, 2020.

[222] R. Hegerl and W. Hoppe. "Dynamische Theorie der Kristallstrukturanalyse durch Elektronenbeugung im inhomogenen Primärstrahlwellenfeld". *Berichte der Bunsengesellschaft für physikalische Chemie* 74.11 (1970), pp. 1148–1154.

[223] J. Miao, D. Sayre, and H. N. Chapman. "Phase retrieval from the magnitude of the Fourier transforms of nonperiodic objects". *JOSA A* 15.6 (June 1, 1998). Publisher: Optical Society of America, pp. 1662–1669.

[224] R. Gerchberg. "A practical algorithm for the determination of phase from image and diffraction plane pictures". *undefined* (1972).

[225] J. R. Fienup. "Reconstruction of an object from the modulus of its Fourier transform". *Optics Letters* 3.1 (July 1, 1978). Publisher: Optical Society of America, pp. 27–29.

[226] Rodenburg. *A phase retrieval algorithm for shifting illumination: Applied Physics Letters: Vol 85, No 20*. 2004. URL: https://aip.scitation.org/doi/10.1063/1.1823034 (visited on 01/22/2022).

[227] H. M. L. Faulkner and J. M. Rodenburg. "Movable Aperture Lensless Transmission Microscopy: A Novel Phase Retrieval Algorithm". *Physical Review Letters* 93.2 (July 9, 2004). Publisher: American Physical Society, p. 023903.

[228] John Rodenburg and Andrew Maiden. "Ptychography". *Springer Handbook of Microscopy*. Ed. by Peter W. Hawkes and John C. H. Spence. Springer Handbooks. Cham: Springer International Publishing, 2019, pp. 819–904.

[229] J. M. Rodenburg. "Ptychography and Related Diffractive Imaging Methods". *Advances in Imaging and Electron Physics*. Ed. by Hawkes. Vol. 150. Elsevier, Jan. 1, 2008, pp. 87–184.

[230] Andrew M. Maiden. *Further improvements to the ptychographical iterative engine*. 2017. URL: https://www.osapublishing.org/optica/fulltext.cfm?uri=optica-4-7-736&id=368463 (visited on 01/23/2022).

[231] Manuel Guizar-Sicairos and Pierre Thibault. "Ptychography: A solution to the phase problem". *Physics Today* 74.9 (Sept. 1, 2021). Publisher: American Institute of Physics, pp. 42–48.

[232] Arthur Baroni et al. "Analyzing full-polarized metasurface holograms by vectorial ptychography". *Focus On Microscopy 2020 (FOM 2020) (Canceled Covid-19)*. Osaka, Japan, Apr. 2020.

[233] Samira Khadir et al. "Metasurface Optical Characterization Using Quadriwave Lateral Shearing Interferometry". *ACS Photonics* 8.2 (Feb. 17, 2021). Publisher: American Chemical Society, pp. 603–613.

[234] Samira Khadir et al. "Optical Imaging and Characterization of Graphene and Other 2D Materials Using Quantitative Phase Microscopy". *ACS Photonics* 4.12 (Dec. 20, 2017). Publisher: American Chemical Society, pp. 3130–3139.

[235] Romain Laberdesque et al. "Metasurfaces characterization by quantitative phase imaging with SID4 wavefront sensor". *High Contrast Metastructures X*. High Contrast Metastructures X. Vol. 11695. SPIE, Mar. 5, 2021, 116951H.

[236] J. M. Rodenburg, A. C. Hurst, and A. G. Cullis. "Transmission microscopy without lenses for objects of unlimited size". *Ultramicroscopy* 107.2 (Feb. 1, 2007), pp. 227–231.

[237] Oliver Bunk et al. "Influence of the overlap parameter on the convergence of the ptychographical iterative engine". *Ultramicroscopy* 108.5 (Apr. 1, 2008), pp. 481–487.

[238] Ashish Tripathi, Ian McNulty, and Oleg G. Shpyrko. "Ptychographic overlap constraint errors and the limits of their numerical recovery using conjugate gradient descent methods". *Optics Express* 22.2 (Jan. 27, 2014). Publisher: Optical Society of America, pp. 1452–1466.

[239] Andrew M. Maiden. *Superresolution imaging via ptychography*. 2011. URL: https://www.osapublishing.org/josaa/fulltext.cfm?uri=josaa-28-4-604&id=211003 (visited on 01/22/2022).

[240] Pierre Thibault et al. "Probe retrieval in ptychographic coherent diffractive imaging". *Ultramicroscopy* 109.4 (Mar. 1, 2009), pp. 338–343.

[241] Andrew M. Maiden and John M. Rodenburg. "An improved ptychographical phase retrieval algorithm for diffractive imaging". *Ultramicroscopy* 109.10 (Sept. 1, 2009), pp. 1256–1262.

[242] A. M. Maiden et al. "An annealing algorithm to correct positioning errors in ptychography". *Ultramicroscopy* 120 (Sept. 1, 2012), pp. 64–72.

[243] Zhang. *Translation position determination in ptychographic coherent diffraction imaging*. 2013. URL: https://www.osapublishing.org/oe/fulltext.cfm?uri=oe-21-11-13592&id=255524#articleFigures (visited on 01/22/2022).

[244] Pierre Godard et al. "Noise models for low counting rate coherent diffraction imaging". *Optics Express* 20.23 (Nov. 5, 2012). Publisher: Optical Society of America, pp. 25914–25934.

[245] Manuel Guizar-Sicairos and James R. Fienup. "Phase retrieval with transverse translation diversity: a nonlinear optimization approach". *Optics Express* 16.10 (May 12, 2008). Publisher: Optical Society of America, pp. 7264–7278.

[246] Patrick Ferrand et al. "Quantitative imaging of anisotropic material properties with vectorial ptychography". *Optics Letters* 43.4 (Feb. 15, 2018). Publisher: Optical Society of America, pp. 763–766.

[247] Arthur Baroni et al. "Joint estimation of object and probes in vectorial ptychography". *Optics Express* 27.6 (Mar. 18, 2019). Publisher: Optical Society of America, pp. 8143–8152.

[248] Patrick Ferrand, Marc Allain, and Virginie Chamard. "Ptychography in anisotropic media". *Optics Letters* 40.22 (Nov. 15, 2015). Publisher: Optical Society of America, pp. 5144–5147.

[249] S. Weber. "PyMoDAQ: An open-source Python-based software for modular data acquisition". *Review of Scientific Instruments* 92.4 (Apr. 2021). Publisher: American Institute of Physics, p. 045104.

[250] Xiaojing Huang et al. "Artifact mitigation of ptychography integrated with on-the-fly scanning probe microscopy". *Applied Physics Letters* 111.2 (July 10, 2017). Publisher: American Institute of Physics, p. 023103.

[251] Frederik Tuitje et al. "Reliability of ptychography on periodic structures". *OSA Continuum* 3.6 (June 15, 2020). Publisher: Optical Society of America, pp. 1691–1702.